SYNTHETIC ANALOGUES OF THE DIIRON HYDROGENASE ENZYME

ACTIVE SITE

AND POSSIBLE PRIMORDIAL H$_2$-PRODUCING CATALYSTS

A Dissertation

by

DANIELLE CROUTHERS

Submitted to the Office of Graduate and Professional Studies of
Texas A&M University
in partial fulfillment of the requirements for the degree of

DOCTOR OF PHILOSOPHY

Chair of Committee,	Marcetta Y. Darensbourg
Committee Members,	Perla B. Balbuena
	David P. Barondeau
	Timothy R. Hughbanks
	Manuel P. Soriaga
Head of Department,	Francois P. Gabbai

August 2015

Major Subject: Chemistry

ABSTRACT

Nature has developed enzymes that utilize the base metals, iron and nickel, in sulfur-rich environments, capable of performing the reversible interconversion of protons and electrons into hydrogen under mild conditions. Recent studies of hybrid enzymes, in which the apo-[FeFe]-hydrogenase protein was loaded with synthetic diiron units, found that the synthetic active site with an azadithioate bridge was fully active at a rate comparable to the native enzyme.

In order to compare the carbon to nitrogen-based bridgehead derivatives, dynamic NMR (^{13}C and ^{1}H) studies of a series of simple diiron models, (μ-SCH$_2$XCH$_2$S)[Fe(CO)$_3$]$_2$ complexes, X = CR$_2$ or NR, were utilized to examine the fluxional processes that are important in the [FeFe]-hydrogenase active site models. Energy barriers for the CO site exchange in Fe(CO)$_3$ rotors were determined to interrogate the effects of fluxional mobility on the electrochemical response to added acid. The nitrogen-based bridgehead derivatives displayed a 2-fold increase in catalytic activity indicating the proton-directing effect of the pendent base. Also to investigate the effects of an azadithiolate linker (-SCH$_2$NHCH$_2$S-), a series of ligand substituted azadithiolate complexes were synthesized and characterized so that the Bengali laboratory at TAMU-Qatar could explore the photochemical reactions.

In another study water-soluble functionalities were introduced into [FeFe]-H$_2$ase active site models by virtue of a sulfonate group incorporated into the –SCH$_2$NRCH$_2$S-dithiolate unit, in order to possibly replace platinum in hydrogen fuel cells that operate in

an aqueous media. Advantages of the aryl sulfonate approach include entry into a variety of water-soluble derivatives that are stable in O_2-free aqueous solutions. The water solubility of a series of phosphine substituted diiron sulfonate complexes were analyzed leading to one of the first systems where the electrochemisty was studied in water without any organic co-solvents.

Finally to help better understand the origin of the [FeFe]-hydrogenase, possible intermediates in the biosynthetic pathway were examined. Evidence that metal sulfide/carbonyl clusters were formed through modifications of a mineral surface were investigated through reactivity studies of various discrete polymetallic compounds. It was demonstrated that the polymetallic compounds were capable of conversion into azadithiolate derivatives through the release of the exogenous metal in the presence of a strong acid.

DEDICATION

This dissertation is dedicated to my mom for supporting me in all my endeavors. To my brother who brings laugher into my life. To my husband who has offered endless encouragement and support for the past 10 years.

ACKNOWLEDGEMENTS

Graduate school has been a huge chapter in my life. It has provided me with many life lessons and allowed me to develop into the scientist I am today. I would like to first thank my advisor, Marcetta Y. Darensbourg, for allowing me to join her group. Thank you for your dedication to all your students and always pushing me to be better. I have grown so much in the past five years because of you. Thank you for providing letters for various award and job applications. Also thank you for the opportunity to travel to conferences and symposiums.

I would like to thank my committee members, Professors Perla B. Balbuena, David P. Barondeau, Timothy R. Hughbanks, and Manuel P. Soriaga, for taking time out of their schedules to serve on my committee. I would also like to thank Prof. Hughbanks for letters of recommendation.

I need to also thank all of the teachers that had a hand in leading me to the path I am on today. I would like to acknowledge Mr. Meekins, my high school Advanced Placement chemistry teacher. If it was not for you, I never would have majored in chemistry at Centenary. To Dr. Lawrence, I am eternally grateful for all the effort and time you spent with Sam Timpa and me. We would not be the people we are today without you. Thank you for allowing me to work in your lab for two summers and teaching me all the air-sensitive techniques that helped me in my graduate career. I would also like to thank the rest of the chemistry department at Centenary, Dr. Ticich, Dr. Blakeney, and Dr. Garret.

brought you into my life. Thank you for always encouraging me to stay on this path even

when times were hard and we were in separate states. I love you so much!

NOMENCLATURE

H_2ase	Hydrogenase
edt	Ethanedithiolate
pdt	Propanedithiolate
o-xdt	O*rtho*-xylyl-α,α'-dithiolate
adt	2-Aza-1,3-propanedithiolate
odt	2-Oxa-1,3-propanedithiolate
dmpdt	2,2-Dimethylpropanedithiolate
depdt	2,2-Diethylpropanedithiolate
dcbdt	Dicarboxyl benzenedithiolate
PTA	1,3,5-triaza-7-phosphaadamantane
Fc	Ferrocene
Fc^+	Ferrocenium
ax	Axial
eq	Equortial
TEA	Tetraethylammonium
dmpe	Dimethylphosphino ethane
dppe	Diphenylphosphino ethane
dppv	Diphenylphosphino ethylene

NH $\qquad$ (μ-SCH$_2$N(H)CH$_2$S)[Fe(CO)$_3$]$_2$

NMe $\qquad$ (μ-SCH$_2$N(Me)CH$_2$S)[Fe(CO)$_3$]$_2$

NtBu $\qquad$ (μ-SCH$_2$N(^{t}Bu)CH$_2$S)[Fe(CO)$_3$]$_2$

1-PPh$_3$ $\qquad$ (μ-SCH$_2$N(Me)CH$_2$S)[Fe(CO)$_3$][Fe(CO)$_2$PPh$_3$]

2-PPh$_3$ $\qquad$ (μ-SCH$_2$N(^{t}Bu)CH$_2$S)[Fe(CO)$_3$][Fe(CO)$_2$PPh$_3$]

3-PPh$_3$ $\qquad$ (μ-SCH$_2$N(Ph)CH$_2$S)[Fe(CO)$_3$][Fe(CO)$_2$PPh$_3$]

1-PTA $\qquad$ (μ-SCH$_2$N(Me)CH$_2$S)[Fe(CO)$_3$][Fe(CO)$_2$PTA]

2-PTA $\qquad$ (μ-SCH$_2$N(^{t}Bu)CH$_2$S)[Fe(CO)$_3$][Fe(CO)$_2$PTA]

3-PTA $\qquad$ (μ-SCH$_2$N(Ph)CH$_2$S)[Fe(CO)$_3$][Fe(CO)$_2$PTA]

1-P(OMe)$_3$ $\qquad$ (μ-SCH$_2$N(Me)CH$_2$S)[Fe(CO)$_3$][Fe(CO)$_2$P(OMe)$_3$]

2-P(OMe)$_3$ $\qquad$ (μ-SCH$_2$N(^{t}Bu)CH$_2$S)[Fe(CO)$_3$][Fe(CO)$_2$P(OMe)$_3$]

3-P(OMe)$_3$ $\qquad$ (μ-SCH$_2$N(Ph)CH$_2$S)[Fe(CO)$_3$][Fe(CO)$_2$P(OMe)$_3$]

1-[PMe$_3$]$_2$ $\qquad$ (μ-SCH$_2$N(Me)CH$_2$S)[Fe(CO)$_2$PMe$_3$]$_2$

2-[PMe$_3$]$_2$ $\qquad$ (μ-SCH$_2$N(^{t}Bu)CH$_2$S)[Fe(CO)$_2$PMe$_3$]$_2$

[1H]$^+$ $\qquad$ (μ-SCH$_2$N(Me)(H)CH$_2$S)[Fe(CO)$_2$PMe$_3$]$_2$$^+$

[2H]$^+$ $\qquad$ (μ-SCH$_2$N(^{t}Bu)(H)CH$_2$S)[Fe(CO)$_2$PMe$_3$]$_2$$^+$

[1Hy]$^+$ $\qquad$ (μ-H)(μ-SCH$_2$N(Me)CH$_2$S)[Fe(CO)$_2$PMe$_3$]$_2$$^+$

[2Hy]$^+$ $\qquad$ (μ-H)(μ-SCH$_2$N(^{t}Bu)CH$_2$S)[Fe(CO)$_2$PMe$_3$]$_2$$^+$

[1HHy]$^{2+}$ $\qquad$ (μ-H)(μ-SCH$_2$N(Me)(H)CH$_2$S)[Fe(CO)$_2$PMe$_3$]$_2$$^{2+}$

[2HHy]$^{2+}$ $\qquad$ (μ-H)(μ-SCH$_2$N(^{t}Bu)(H)CH$_2$S)[Fe(CO)$_2$PMe$_3$]$_2$$^{2+}$

1Na	$Na(\mu\text{-}SCH_2N(C_6H_4SO_3)CH_2S)[Fe(CO)_3]_2$
2Na	$Na(\mu\text{-}SCH_2N(C_6H_4SO_3)CH_2S)[Fe(CO)_3][Fe(CO)_2(P(OMe)_3)]$
3Na	$Na(\mu\text{-}SCH_2N(C_6H_4SO_3)CH_2S)[Fe(CO)_3][Fe(CO)_2PTA]$
4Na	$Na(\mu\text{-}SCH_2N(C_6H_4SO_3)CH_2S)[Fe(CO)_3][Fe(CO)_2PPh_3]$
5Na	$Na(\mu\text{-}SCH_2N(C_6H_4SO_3)CH_2S)[Fe(CO)_2PMe_3]_2$
1	$(\mu\text{-}SH)_2[Fe(CO)_3]_2$
2	$(\mu\text{-}SAuPPh_3)_2[Fe(CO)_3]_2$

TABLE OF CONTENTS

LIST OF FIGURES

Page

CHAPTER I

INTRODUCTION AND LITERATURE REVIEW[*]

Introduction

Hydrogen has been viewed as a potential fuel source due to growing global energy concerns and the improved methods of producing "solar" electrons. It offers numerous advantages as an alternate energy source because it may be derived from renewable sources, obtainable from energy sources such as solar and wind, and its combustion generates no toxic by-products. For its use in fuel cells a catalyst is needed, which currently is platinum based. Unfortunately platinum is an expensive and rare precious metal, which makes it non-sustainable for long-term use on a wide scale.[1,2] Nature has developed enzymes that utilize the base metals, iron and nickel, in sulfur-rich environments, capable of performing the same catalysis, i.e., the conversion of protons and electrons into hydrogen, and vice versa, eq I-1.[3] The natural catalysts are called hydrogenases.

$$2H^+ \;+\; 2e^- \;\rightleftharpoons\; H_2 \qquad\qquad (eq\ I\text{-}1)$$

The three classes of hydrogenase enzymes are based on the composition of the active site: [NiFe]-, [FeFe]-, and mono-Fe hydrogenase.[4-8] The [FeFe]-hydrogenase is typically biased towards H_2 production, and under mild conditions, displays rates of 6000-9000 molecules of H_2 s^{-1} per site.[9]

The reproduction of metalloenzyme active sites as small molecule models is typically challenging to synthetic inorganic chemists as the first coordination sphere donor atoms, covalently attached to the metals, may be derived from a diverse pool of amino acid residues in the three-dimensional protein matrix. Their arrangement about the metal is achieved through a balance of metal coordination sphere preferences and protein folding requirements; the latter may induce notable distortions on the thermodynamically favored coordination geometry observed in compositional synthetic analogues. This is assumed to be the reason that small molecule models of enzyme active sites are only rarely catalytically active. In contrast, the organometallic active site of diiron hydrogenase, [FeFe]-H_2ase, Figure I-1, a site rich in diatomic ligands, has several H-bonding interactions but only one covalent attachment to the protein, and displays intrinsic metal-ligand preferred coordination properties.[10,11] Thus the influence of the protein lies mainly in outer coordination sphere effects.
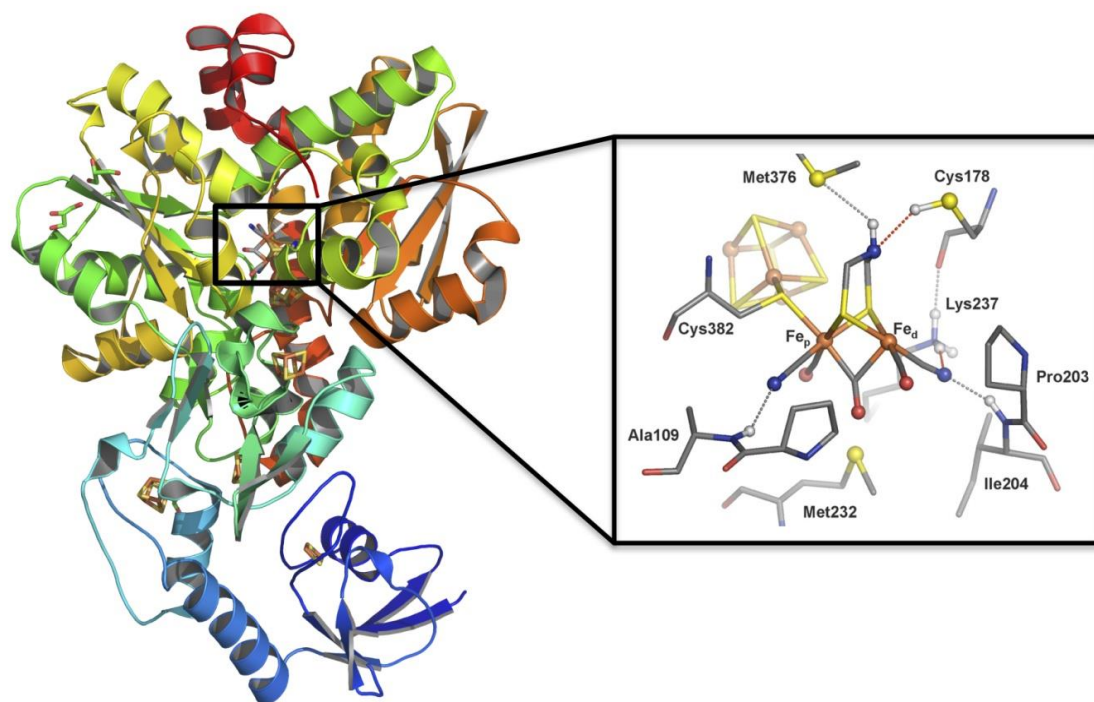
Figure I-1. Structure of the [FeFe]-hydrogenase from *Clostridium pasteurianum* with the active site enlarged showing hydrogen bonding interactions between the [2Fe]-subsite and surrounding amino acids.[12] Adapted with permission from Lubitz, W.; Ogata, H.; Rüdiger, O.; Reijerse, E. *Chemical Reviews* **2014**, *114*, 4081. Copyright **2014** American Chemical Society.

[FeFe]-Hydrogenase Active Site

The topology of the active site of the [FeFe]-H_2ase enzyme was first unveiled in the late twentieth century.[10,11] The active site, referred to as the H-cluster, contains two iron atoms coordinated to five diatomic ligands and bridged by a non-protein dithiolate linker ($S-CH_2-X-CH_2-S$), Figure I-2. The possibilities for the central X atom are NH, CH_2, or O, however spectroscopic studies give convincing evidence that the linker is dithiomethylamine, where the X atom is nitrogen.[13,14] Later studies of hybrid enzymes, in which the apo-[FeFe]-hydrogenase protein was loaded with synthetic diiron units, found that only the synthetic active site with an azadithioate bridge was fully active, vide infra.[15,16] The active site is bound to the enzyme through a cysteine sulfur, which connects to a Fe_4S_4 cluster, itself an intimate part of the catalytic site. The [2Fe]-subsite is isolated in a mixed valent Fe^IFe^{II} state with each iron bound to two terminal diatomic ligands, a CO and a CN. A third CO is found in a semi-bridging position, which gives the proximal iron, that nearest the Fe_4S_4 cluster, a square pyramidal geometry and the distal iron an inverted square pyramidal geometry. This geometry of the active site is called the "rotated" structure, which is supported by the bridging CO.[11,17]

The "rotated" structure of the active site is enforced through a semi-bridging carbonyl and hydrogen bonding, which occurs through the cyanide to various amino acid residues of the protein matrix. This unique geometry of the active site facilitates the high reactivity due to the open site on the distal iron, i.e., the iron furthest from the Fe_4S_4 cluster. Analysis of the enzyme active site suggests that H_2 oxidation and H^+ reduction occurs at the open site found on the distal iron;[18,19] the proposed mechanism is seen in

Figure I-3.[12,20] The surrounding protein usually contains several FeS clusters in addition to the one attached to the active site. These clusters transport electrons to and from the active site. Also found in the protein matrix is a hydrophobic tunnel that directs H_2 to or away from the active site.[21] All these features help facilitate the catalytic cycle.
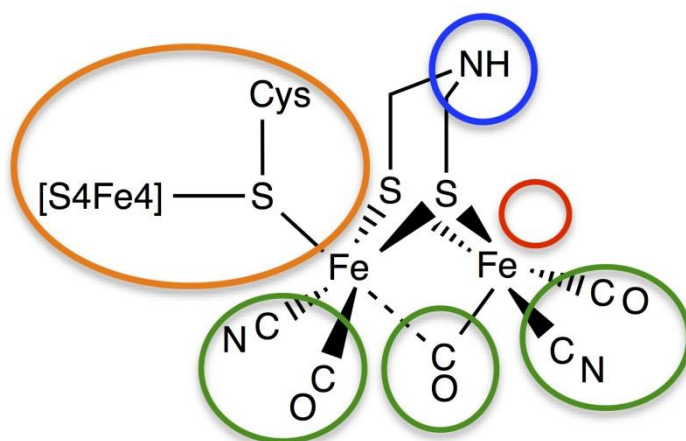
Figure I-2. Depiction of the 6Fe H-cluster of the [FeFe]-H_2ase active site with essential features related to the [2Fe]-subsite highlighted. Azadithiolate linker (blue) relays protons to and from the iron distal to the 4Fe4S cluster. Open site (red) allows for proton oxidative addition or dihydrogen binding. Diatomic ligands (green) stabilize the redox states of the irons. The 4Fe4S cluster (orange) shuttles electrons to and from the [2Fe]-subsite.

The proposed catalytic cycle begins with a mixed valent $Fe^{I}Fe^{II}$ species (H_{ox}) that undergoes a one-electron reduction to the $Fe^{I}Fe^{I}$ state (H_{red}). This step is a proton-coupled electron transfer process but the position of the proton has yet to be identified; however it is postulated that the nitrogen is protonated at this step. H_{red} can then undergo a one-electron reduction to form H_{sred}, which has recently been identified through EPR and FTIR spectroscopies.[22-24] The reduction at this step occurs at the [4Fe4S] cluster and the Fe site distal to the 4Fe4S cluster is assumed to form a terminal hydride. The nitrogen can then be protonated and a Fe^{II}-$(\eta^2$-$H_2)$ species is formed. This is followed by release of dihydrogen to return to the H_{ox} species. Each step is reversible therefore the heterolytic cleavage of H_2 is proposed to use the same steps in the opposite direction.
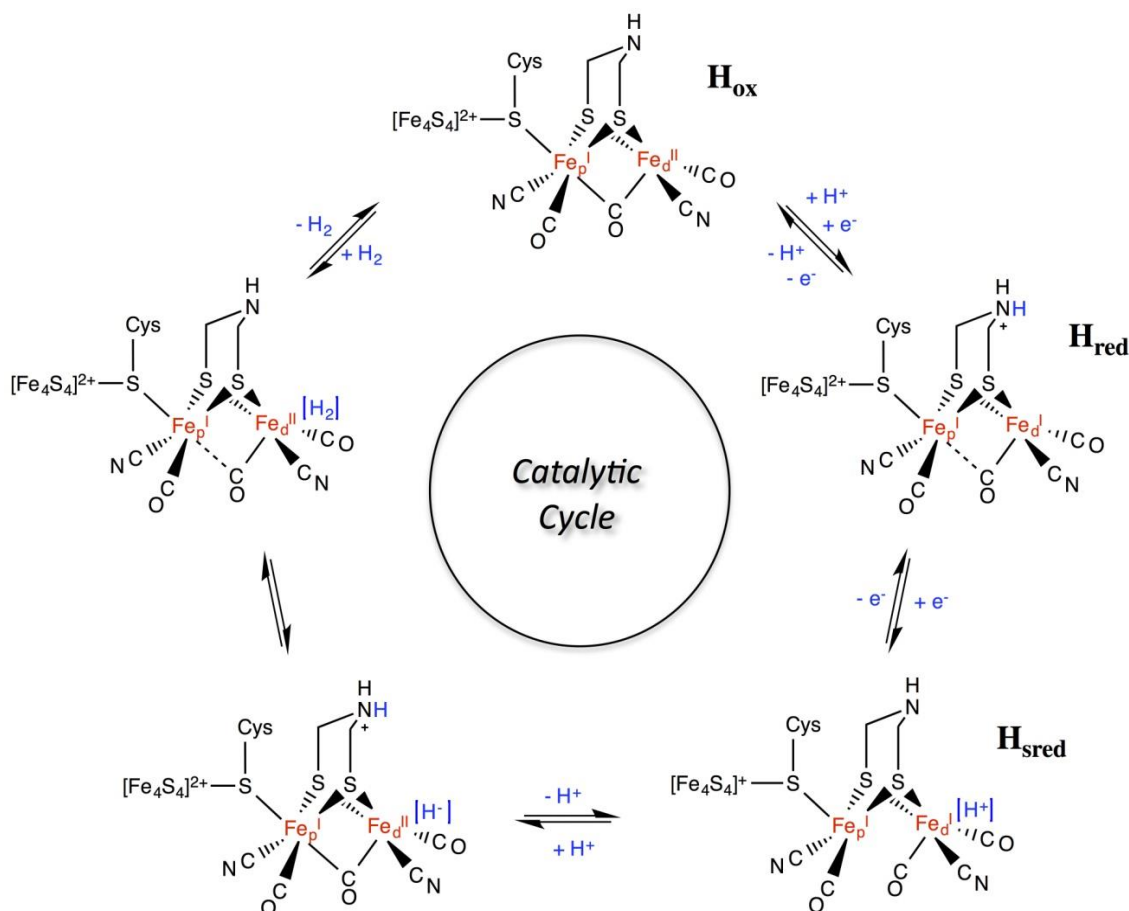
Figure I-3. Proposed catalytic cycle for the [FeFe]-hydrogenase that reversible produces (clockwise) and oxidizes (counter clockwise) H_2.[12] Adapted with permission from Lubitz, W.; Ogata, H.; Rüdiger, O.; Reijerse, E. *Chemical Reviews* **2014**, *114*, 4081. Copyright **2014** American Chemical Society.

Simple Synthetic Models of the Active Site

Although the [FeFe]-H$_2$ase protein structure was revealed in the late twentieth century, [2Fe2S] compounds with similar structural characteristics as the active site, (µ-SR)$_2$[Fe(CO)$_3$]$_2$, were first synthesized in the late 1920's by Reihlen.[25] A very simple synthetic analogue, (µ-pdt)[Fe(CO)$_3$]$_2$, pdt = propane dithiolate or S(CH$_2$)$_3$S, Figure I-4 (A), has achieved wide-spread attention as a stable, readily accessible biomimetic with interpretable spectroscopic features, especially FTIR.[26-28] Furthermore it has at least a modest ability to serve as an electrocatalyst for hydrogen production. Chemical features include the possibility of systematic modifications by CO/L exchange and within the S to S linker. While structure (A) of Figure I-4 is the most common model, structure (B) is the analogous (µ-adt)[Fe(CO)$_3$]$_2$, adt = azadithiolate, containing a bridgehead nitrogen in the FeS$_2$C$_2$N cyclohexane-like metallacycle, as does the enzyme active site.[13,29,30] Other simple model complexes such as (µ-odt)[Fe(CO)$_3$]$_2$, odt = oxadithiolate, and (µ-tdt)[Fe(CO)$_3$]$_2$, tdt = thiadithiolate, containing a bridgehead oxygen and sulfur, respectively, have also been synthesized, Figure I-4 (C) and (D).
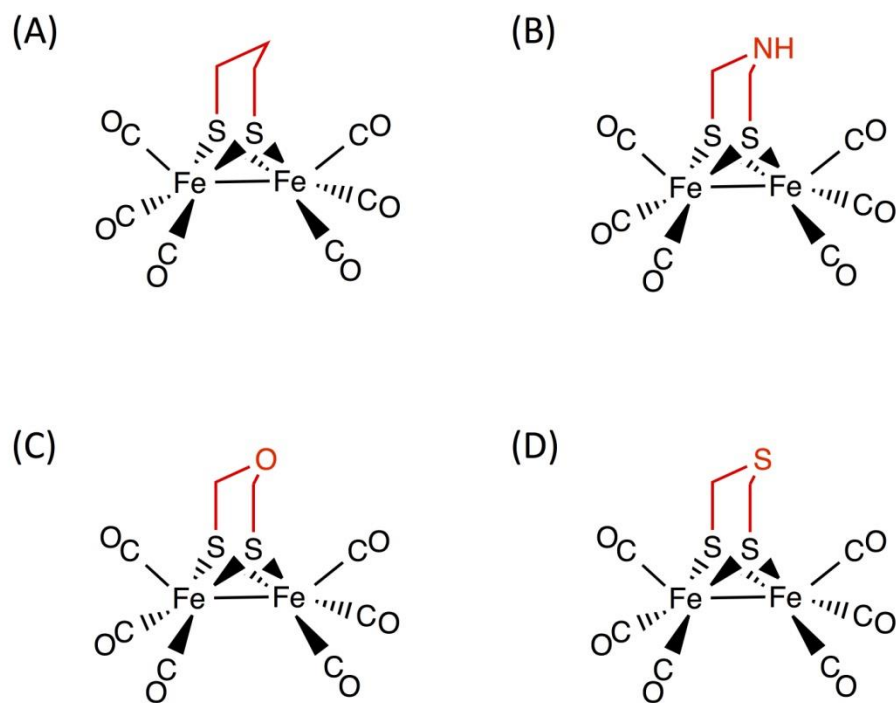
Figure I-4. Depictions of (A) the "parent" $(\mu\text{-pdt})[Fe(CO)_3]_2$ biomimetic, pdt = propane dithiolate; (B) the analogous $(\mu\text{-adt})[Fe(CO)_3]_2$, adt = azadithiolate; (C) $(\mu\text{-odt})[Fe(CO)_3]_2$, odt = oxadithiolate; (D) $(\mu\text{-tdt})[Fe(CO)_3]_2$, tdt = thiadithiolate.

There are several different methods to synthesize these simple hexacarbonyl model compounds involving two different iron carbonyl starting materials, Figure I-5. One method involves reacting dithiols or disulfides with an iron carbonyl source, $Fe_3(CO)_{12}$, at reflux conditions in toluene to afford the model complexes.[31-35] The other methods involve a starting material, $(\mu\text{-S}_2)[Fe(CO)_3]_2$, which was identified in early 2000 as a parent model compound for the [FeFe]-H_2ase active site; however this compound has also been known in chemistry for decades.

9
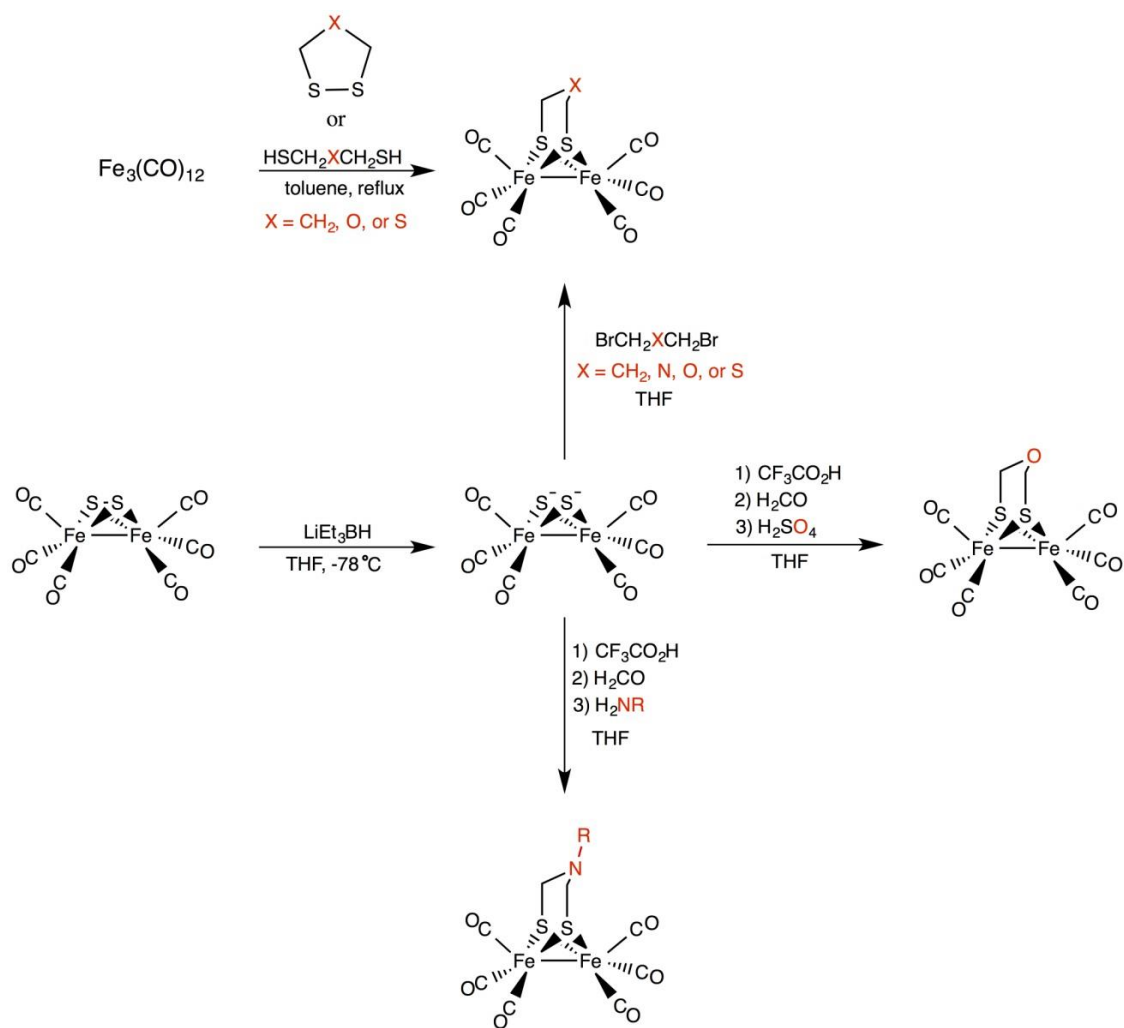
Figure I-5. Reaction scheme for the synthesis of (μ-pdt)[Fe(CO)$_3$]$_2$, (μ-adt)[Fe(CO)$_3$]$_2$, (μ-odt)[Fe(CO)$_3$]$_2$, and (μ-tdt)[Fe(CO)$_3$]$_2$ analogues.

The bridging persulfide iron carbonyl, $(\mu\text{-}S_2)[Fe(CO)_3]_2$, was first synthesized by Hieber and Gruber in 1958.[36] Seyferth, et al. and other groups carried out further studies of this complex, which involved reducing the disulfide bond prior to metallation or alkylation of the sulfurs, Figure I-6.[37-40] Rauchfuss et al. exploited this complex and its reactivity in 2001 and introduced the condensation method to synthesize the azadithiolate derivatives. This method, bottom reaction of Figure I-5, involves protonation of the sulfurs to form a dihydrosulfide complex, $(\mu\text{-}SH)_2[Fe(CO)_3]_2$. The dihydrosulfide complex efficiently condenses with aqueous formaldehyde in the presence of primary amines to give azadithiolate complexes in high yields (~70-90%).[41] The other model complexes can also be synthesized utilizing the bridging persulfide precursor through the electrophilic addition of alkyl halides to the doubly reduced persulfide complex, $(\mu\text{-}S)_2[Fe(CO)_3]_2^{2-}$. This synthetic route has led to a wide assortment of [FeFe]-H_2ase model complexes.
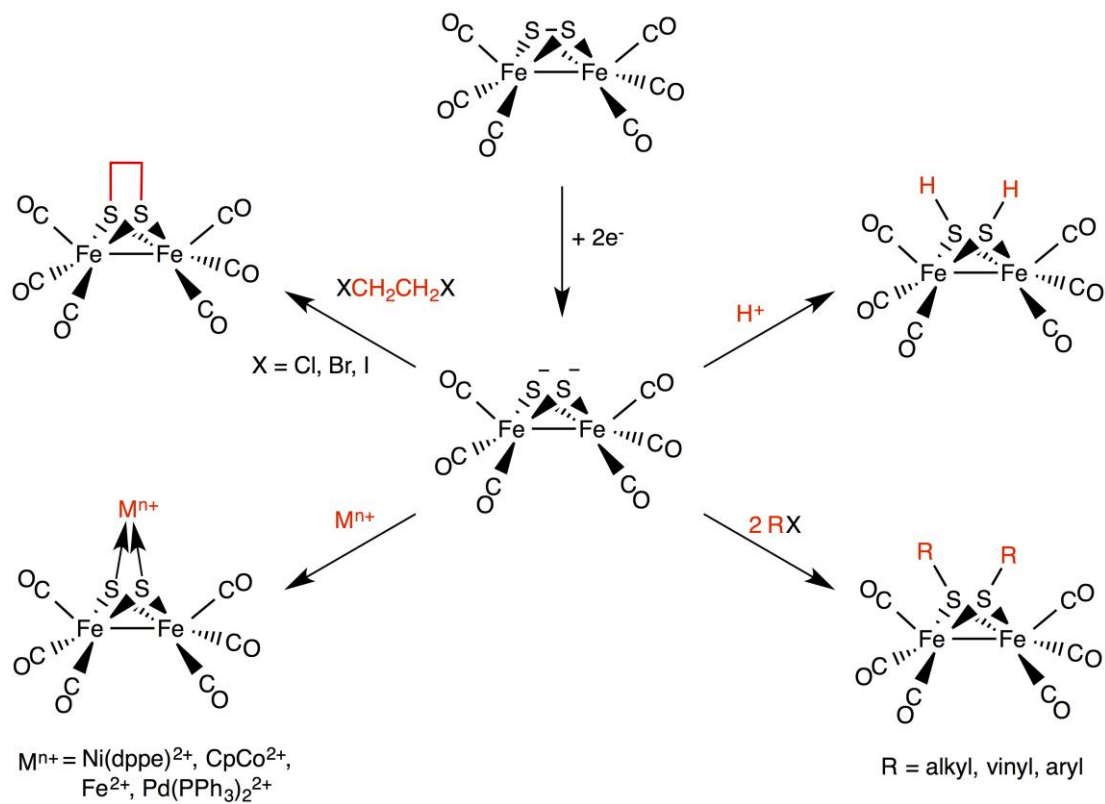
Figure I-6. Reactivity of the bridging persulfide iron carbonyl, $(\mu\text{-}S_2)[Fe(CO)_3]_2$.

The hexacarbonyl complexes are precursors to a host of model compounds because of their stability and ease of modification. Further functional groups in both L and the bridging dithiolate have permitted attachment to constructs for applications appropriate to technological development, such as solar hydrogen production, biofuel cell technology, surface-modified electrodes, etc.[42-44] While elegant diphosphine complexes have enhanced understanding as to the functional mechanism of these diiron complexes as electrocatalysts, the simpler all-carbonyl (μ-SRS)[Fe(CO)$_3$]$_2$ complexes have become standards for developing applications, examples of which are shown in Figure I-7.[45-48]

Two examples of the stability of the hexacarbonyl complexes are shown through the incorporation of a simple hexacarbonyl model, (μ-dcbdt)[Fe(CO)$_3$]$_2$ dcbdt = dicarboxyl benzenedithiolate, into a Zr(IV) based metal-organic framework, MOF, and through the assembly of (μ-S$_2$)[Fe(CO)$_3$]$_2$ to the surface of CdSe quantum dots. Both systems show photochemical hydrogen evolution in water.[46,47]
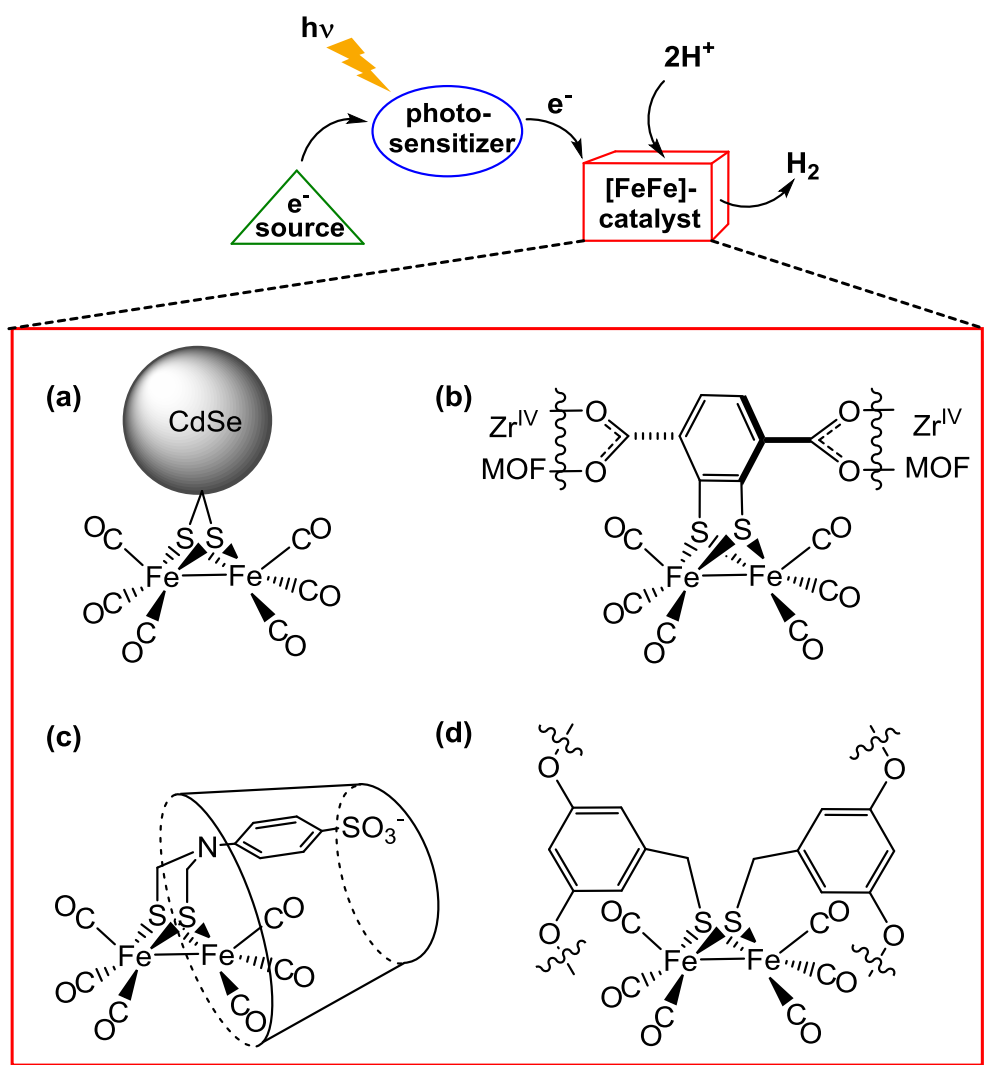
Figure I-7. Development of photocatalytic hydrogen production with diiron hexacarbonyl attached to or imbedded in supports. Depiction of (a) immobilized (μ-S$_2$)[Fe(CO)$_3$]$_2$ complex on the surface of CdSe quantum dots, producing a water soluble photocatalyst for H$_2$ evolution with a turnover frequency of ca. 600 h^{-1};[46] (b) a diiron electrocatalyst stabilized through incorporation into a robust Zr(IV) MOF;[47] (c) a photocatalytic H$_2$-producing, cyclodextrin host / diiron guest that operates in the presence of organic dyes in aqueous media;[45] (d) a dendritic hydrogenase photocatalyst for H$_2$ evolution with a turnover frequency ranging from 6190-7240 h^{-1} depending on the size of the dendritic stucture.[48]

Fluxional Processes

An intrinsic feature of (μ-SRS)[Fe(CO)$_3$]$_2$ complexes is their flexibility. Variable temperature ^{1}H and ^{13}C nmr studies of (μ-pdt)[Fe(CO)$_3$]$_2$ found two fluxional processes that characterize the flexibility of the complex: 1) boat/chair interconversion of the FeS$_2$C$_3$ 6-membered ring; and 2) the apical/basal CO site exchange of the Fe(CO)$_3$ rotor, Figure I-8 (A).[49] The fluxionality of the Fe(CO)$_3$ units of the (μ-SRS)[Fe(CO)$_3$]$_2$ complexes occurs by apical/basal CO site exchange through a turnstile rotation and does not involve the exchange of CO groups between the two irons. Modifications to the bridgehead and ligand substitution have both been shown to alter these fluxional processes.
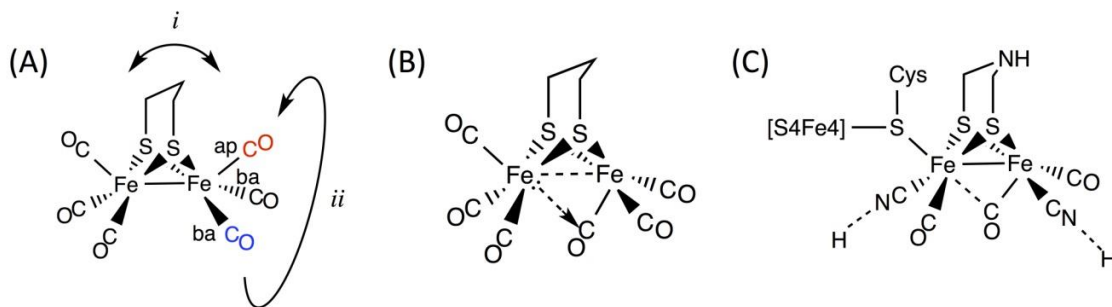
Figure I-8. Structures of (A) (μ-pdt)[Fe(CO)$_3$]$_2$ and its fluxional processes: *i.* chair/boat interconversion *ii.* apical/basal CO site exchange; (B) transition state of Fe(CO)$_3$ rotation in (μ-pdt)[Fe(CO)$_3$]$_2$; (C) the [FeFe]H$_2$ase active site.

The ^{1}H variable temperature nmr studies of (μ-pdt)[Fe(CO)$_3$]$_2$ show that the bridgehead (-SCH$_2$CH$_2$CH$_2$S-) is interconverting between the chiar/boat conformers at room temperature.[49] This process slows at low temperature (-60 °C) displaying the nonequivalency of the axial and equatorial hydrogen atoms in the bridgehead. However, when the S to S linker is a phenylene, (μ-SCH$_2$C$_6$H$_4$CH$_2$)[Fe(CO)$_3$]$_2$, the bridgehead is fixed, even at temperatures up to 75 °C. The decrease in flexibility is attributed to the arene ring. The (μ-dmpdt)[Fe(CO)$_3$]$_2$, dmpdt = 2,2-dimethylpropanedithiolate, complex displayed an opposite effect where the chair/boat interconversion occurs at temperatures as low as -120 °C, showing the fluxional process is affected by steric bulk on the bridgehead.[50]

At room temperature the (μ-pdt)[Fe(CO)$_3$]$_2$ displays only one [13]CO signal, indicating the high degree of configuration mobility of the Fe(CO)$_3$ units. [49] At low temperatures (-80 °C) four signals are seen, distinguishing the two Fe(CO)$_3$ units, as well as, the apical and basal COs. The two Fe(CO)$_3$ units are differentiated by the slowing of the interconversion of the bridgehead. The CO site exchange of (μ-dmpdt)[Fe(CO)$_3$]$_2$ slows at -110 °C displaying only two signals due to the fact that the Fe(CO)$_3$ units are equivalent.[50] This demonstrated that the bridgehead fluxionality has effects on the apical/ basal CO site exchange.

The energy barrier of the Fe(CO)$_3$ CO interchange process has been calculated at ~9.8 kcal/mol for (μ-pdt)[Fe(CO)$_3$]$_2$ and ~7.41 kcal/mol for (μ-dmpdt)[Fe(CO)$_3$]$_2$ indicating that steric bulk at the bridgehead lowers the CO site exchange barrier. Density Functional Theory (DFT) calculations suggest that the CO site exchange proceeds

through a transition state where one of the basal CO ligands rotates to a bridging position between the two irons and the apical CO moves into the square plane, Figure I-8 (B). This transition state is significant due to the similarity in geometry to the [FeFe]-H$_2$ase enzyme active site, Figure I-8 (C), as well as the similarity to the postulated transition state/intermediate in CO/ligand substitution reactions, Figure I-9.[51]
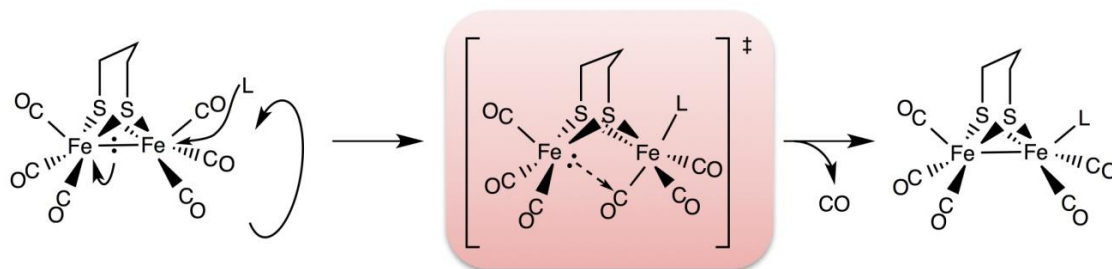
Figure I-9. The proposed mechanism for nucleophilic CO substitution highlighting the transition state.[52]

17

Function of Pendent Base

As stated previously the nature of the bridgehead has been under scrutiny since the protein crystal structure of [FeFe]-H_2ase was introduced due to the available crystallographic resolution. It could not be deciphered whether the central atom in the dithiolate bridge was a C, N, or O; however several groups have proposed that the central atom is a nitrogen. The likely function of this built-in pendent base in the active site is to assist in proton shuttling to the open position on iron, resulting in a terminal iron-hydride. For this to happen in the $Fe^I Fe^I$ model complexes, or one-electron reduced $Fe^I Fe^0$ species, a structural isomerization from the common symmetrical, eclipsed form, to the "rotated" or inverted square pyramidal configuration must occur.[53] This is shown in Figure I-10 (A), combined with the presumed pendent base function. The rotated structure is an isomeric form that involves diminishing the Fe—Fe bond order in the stable, eclipsed $Fe^I Fe^I$ parent complex structure and replacing it with a bridging carbonyl. The result is a shift of electron density, building Fe^0 character on the open-faced iron that apparently works in concert with the pendent bridgehead-N base to facilitate protonation at that iron, Figure 1-10 (A).

Until recently the only examples of rotated structural isomers reported were of mixed-valent (μ-SRS)$Fe^I Fe^{II}$ complexes.[54-57] In 2013 Zampella et al. showed that a dissymetrically substituted complex, (μ-SCH$_2$N(CH$_2$C$_6$H$_5$)CH$_2$S)[Fe^I(CO)$_3$][Fe^I(CO)dmpe], (dmpe = dimethylphosphino ethane), was in the rotated isomeric form in the solid state, Figure 1-10 (B).[58] A quasi-rotated $Fe^I Fe^I$ structure was observed in the crystalline form of (μ-

$SCH_2C(Et_2)CH_2S[Fe(CO)_2PMe_3]_2$, Figure 1-10 (C).[53] Thus the fact that even ground state rotated structures of Fe^IFe^I complexes are possible lends credibility to the mechanistic proposal of Hall, et al.[59]
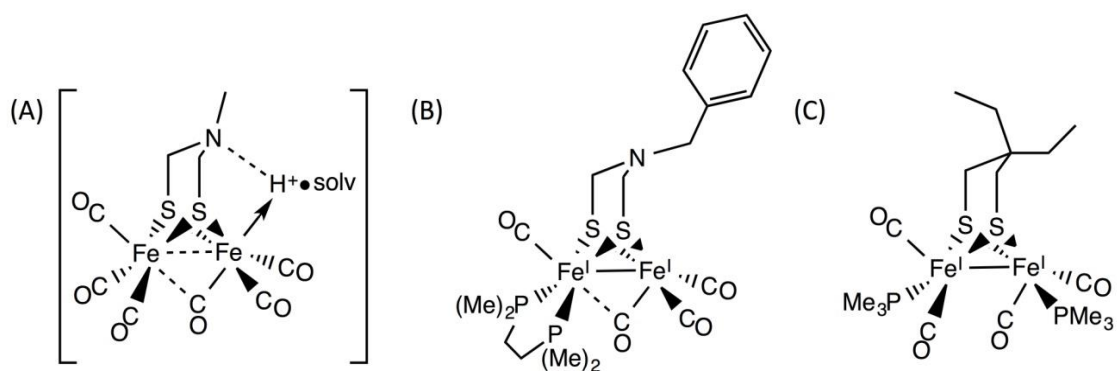
Figure I-10. Structure of (A) expected transition state during protonation of reduced (μ-adt)$[Fe(CO)_3]_2^{n-}$; (B) (μ-$SCH_2N(CH_2C_6H_5)CH_2S)[Fe^I(CO)_3][Fe^I(CO)dmpe]$, a rotated Fe^IFe^I complex;[58] (C) (μ-$SCH_2C(Et_2)CH_2S)[Fe(CO)_2PMe_3]_2$, a quasi-rotated Fe^IFe^I complex.[53]

The role of a pendent base has been demonstrated as a key factor for the extraordinary turnover numbers in the square planar nickel complexes of the DuBois catalyst, Figure I-11 (A).[60] The addition of an amine to a diphosphine ligand resulted in intramolecular heterolytic cleavage of H_2, whereas without the amine an external base was required for heterolytic cleavage of H_2. The importance of the pendent base has also

19

been established in a diiron electrocatalyst (μ-SCH$_2$N(H)CH$_2$S)[Fe(CO)(dppv)]$_2$, (dppv = diphenylphosphino ethylene), in which the diphosphine ligands provide a substantial electron-rich environment along with the steric encumbrance needed to promote the "rotated" structure (as described above), a semi-bridging CO, and protonation, yielding a terminal hydride, Figure I-11 (B).[61] This species is found to be a superior proton reduction electrocatalyst as compared to the (μ-pdt)[Fe(CO)(dppv)]$_2$ analogue.
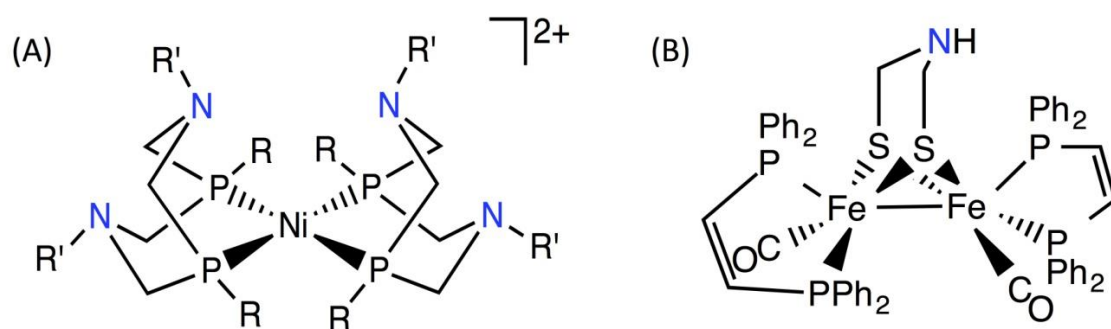
Figure I-11. Structure of (A) the DuBois catalyst featuring PNP ligands;[60] (B) (μ-SCH$_2$N(H)CH$_2$S)[Fe(CO)(dppv)]$_2$, (dppv = diphenylphosphino ethylene), which shows a higher catalytic response compared to the carbon bridgehead analogue.[61]

Hybrid [FeFe]-H$_2$ase

Recent reports of the constitution of an [FeFe]-H$_2$ase enzyme with an active site derived from small molecule model compounds, (μ-SCH$_2$XCH$_2$S)[Fe(CO)$_2$CN]$_2^{2-}$, containing either CH$_2$, NH, or O bridgeheads have shown hybrid enzymes that were indistinguishable by FTIR spectroscopy with the wild type catalyst generated by the natural maturation machinery.[16] The synthetic compounds contain one CN$^-$ and two CO ligands on each iron differing only by the central bridgehead atom. Fontecave et al. introduced these synthetic models to HydF, which is a scaffold protein that contains a [4Fe-4S] cluster, to form a hybrid HydF with the model compounds bound to the [4Fe-4S] cluster through a CN ligand, Figure I-12. HydF is one of three hydrogenase specific maturases, the others being HydE and HydG, required for the biosynthesis of the [2Fe] subcluster. The hybrid HydF was then used to transfer the model complex to the apo-HydA, hydrogenase protein without the [2Fe] subcluster. The apo-HydA was activated to form the holo-HydA hydrogenase protein with the synthetic model complex. Hydrogen evolution was monitored and was only observed with the azadithiolate complex, doing so at a rate comparable to the native enzyme.[16] A further study demonstrated the spontaneous activation of apo-HydA through direct incorporation without the help of HydF, Figure I-12.[15] These studies confirm previous speculations of nitrogen being the central atom in the bridgehead of the [FeFe]-H$_2$ase active site.
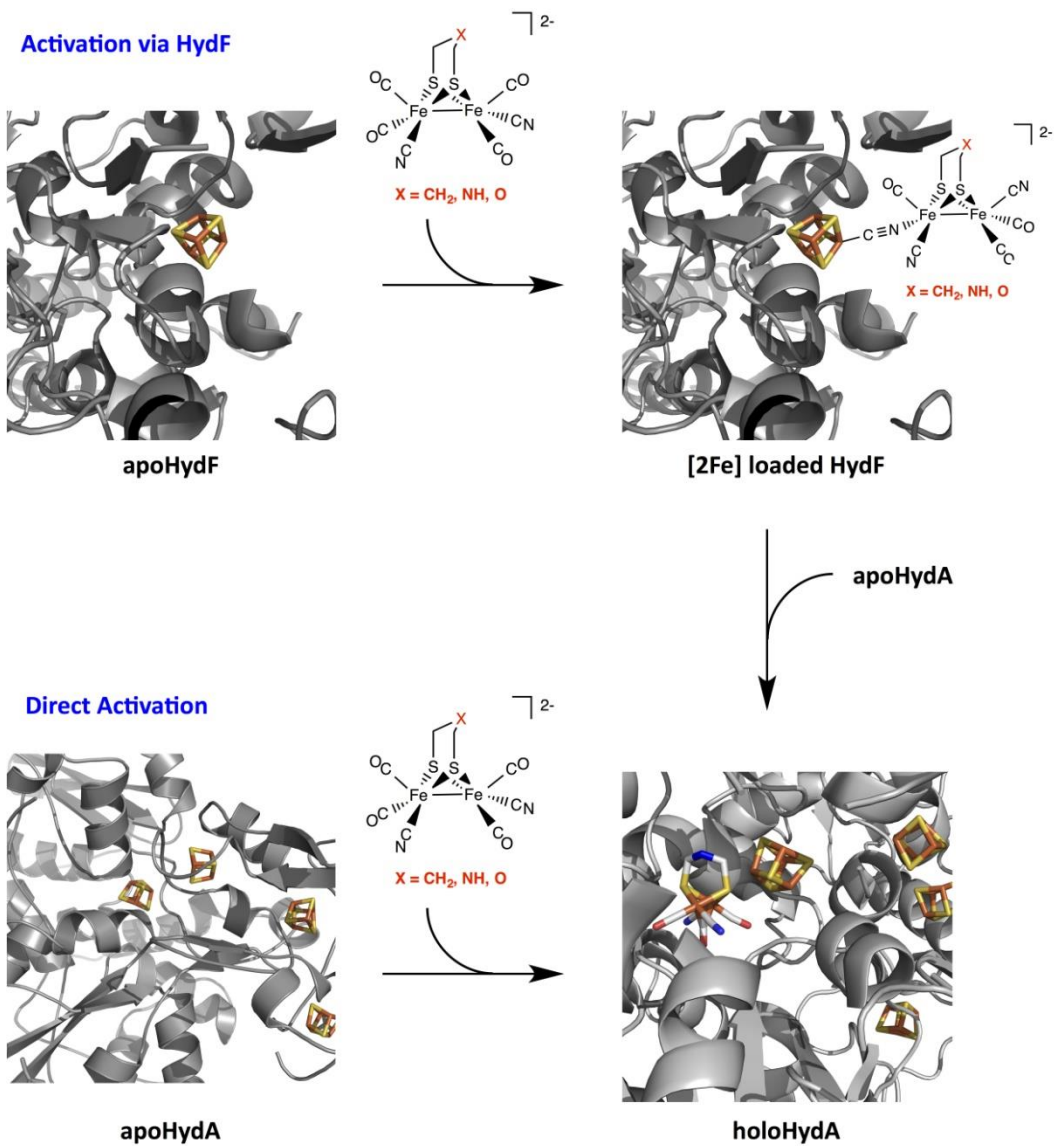
Figure I-12. Activation of apoHydA via the HydF maturase loaded with the [2Fe] synthetic compound (top) or through direct incorporation of the [2Fe] synthetic compound without aid of the Hyd F maturase protein (bottom).

Thus, this dissertation will focus on understanding the essential features of the [FeFe]-Hydrogenase active site required for catalysis through structural and functional model complexes. Specifically, the natural catalyst for which the enzyme active site differs from the model complexes by the restrictive environment within the protein as compared to the molecular catalyst dissolved in solution. In order to optimize the latter we have attempted to deconvolute certain possible factors. The fundamental properties of structural rearrangements for the model complexes that are required in the proton-reduction mechanism are discussed in Chapter III. Simple hexacarbonyl model complexes, containing carbon or nitrogen in the bridgehead, were investigated to determine any effect of the nitrogen on conformation mobility and the correlation to the catalytic efficiency utilizing variable temperature NMR and electrochemistry.

In Chapter IV, substituted azadithiolate complexes were characterized to investigate the effects of nitrogen in the bridgehead on the photochemistry of the complexes compared to the carbon bridgehead analogues. The synthesis of water-soluble diiron models was explored in Chapter V through the addition of a sulfonate group incorporated into the dithiolate linker. The water-solublity of the parent compound, $Na(\mu\text{-}SCH_2N(C_6H_4SO_3)CH_2S)[Fe(CO)_3]_2$, and several phosphine substituted complexes were analyzed. A possible abiotic analogue of the diiron hydrogenase is discussed in Chapter VI. The Ph_3PAu^+ cation was used as a proton surrogate to form a very stable Au_2Fe_2 complex, $(\mu\text{-}SAuPPh_3)_2[Fe(CO)_3]_2$, which can be used to synthesize various azadithiolate derivatives, i.e., $(\mu_2\text{-}SCH_2N(R)CH_2S)[Fe(CO)_3]_2$.

CHAPTER II

GENERAL EXPERIMENTAL DETAILS

General Procedures

All syntheses and manipulations were performed using standard Schlenk-line and syringe/rubber septa techniques under N_2 or in an Ar atmosphere glovebox. Solvents were purified according to published procedures, and freshly distilled under N_2 prior to use or purified and degassed via a Bruker solvent system. Reagents were purchased from commercial sources and used as received. Hexacarbonyl complexes, $(\mu\text{-}S_2)[Fe(CO)_3]_2$,[62] $(\mu\text{-}SCH_2N(Me)CH_2S)[Fe(CO)_3]_2$ **(NMe)**,[63] $(\mu\text{-}SCH_2N(^tBu)CH_2S)[Fe(CO)_3]_2$ **(NtBu)**,[62] $(\mu\text{-}SCH_2N(Ph)CH_2S)[Fe(CO)_3]_2$ **(NPh)**,[63] $(\mu\text{-}SCH_2N(H)CH_2S)[Fe(CO)_3]_2$ **(NH)**,[62] $(\mu\text{-}S(CH_2)_3S)[Fe(CO)_3]_2$ **(pdt)**,[27] $Na(\mu\text{-}SCH_2N(C_6H_4SO_3)CH_2S\text{-})[Fe(CO)_3]_2$ **(1Na)**,[64] $(\mu\text{-}SH)_2[Fe(CO)_3]_2$ **(1)**[38] as well as the $CDFCl_2$ used for low temperature NMR[65] experiments were synthesized according to published procedures. Elemental analyses were performed by Atlantic Microlab, inc., Norcross, Georgia, United States. Infrared spectra were recorded on a Matteson Galaxy Series 6021 FTIR spectrometer or a Bruker Tensor 37 spectrometer in CaF_2 solution cells of 0.1 mm path length.

NMR Studies. ^1H and ^{13}C NMR spectra were recorded on an Inova 500 MHz superconducting NMR instrument operating at 500.6, and 125.9 MHz respectively. ^{31}P NMR spectra were recorded an Inova 300 MHz operating at 121.4 MHz. ^1H and ^{13}C variable-temperature NMR spectra were recorded on a Unity+ 500 MHz

superconducting NMR instrument operating at 125.9 MHz. Variable–temperature ^{31}P NMR spectra were recorded on an Inova 300 MHz operating at 121.4 MHz, respectively.

Electrochemical Studies. Cyclic voltammograms were obtained on a BAS-100A electrochemical analyzer using a three-electrode cell: a glassy carbon disk (0.071 cm^2), the working electrode; reference electrode, Ag/AgNO$_3$; and a platinum wire, the counter electrode. All experiments were performed either under an Ar atmosphere or CO-saturated solutions of CH$_3$CN containing 0.1 M nBu$_4$NPF$_6$ at room temperature. Ferrocene, Fc, served as the internal reference and all potentials are reported relative to the Fc/Fc$^+$ couple set at 0.00 V. Glacial acetic acid was added in molar equivalent increments via microsyringe.

Experimental Details for Chapter III

Crystallization of (μ-SCH$_2$N(^{t}Bu)CH$_2$S)[Fe(CO)$_3$]$_2$, (NtBu). The complex **NtBu** was dissolved in a minimum amount of hexanes. Crystals of X-ray quality were obtained by cooling the solution at – 30 °C.

Variable Temperature NMR Measurement. A 275-W GE ultraviolet Sunlamp was used to prepare isotopically enriched samples with C-13 labelled CO in a solution of hexanes. The solutions were passed through a plug of silica gel and the solvent was removed in vacuo. The resulting solids were used without further purification. All

variable temperature ^{1}H and ^{13}C NMR spectra were recorded on a Unity+ 500-MHz superconducting NMR instrument operating at 500.6, and 125.9 MHz, respectively.

X-ray Structure Analysis. For the **NtBu** complex low temperature (150 K) X-ray data was obtained on a Bruker Apex-II CCD based diffractometer (Texas A&M University) (Mo sealed X-ray tube, Kα = 0.71073 Å). A crystalline sample was coated in mineral oil, affixed to a Nylon loop, and placed under streaming N_2. Space groups were determined on the basis of systematic absences and intensity statistics, and structures were solved by direct methods and refined by full-matrix least-squares on F^2. H atoms were placed at idealized positions and refined with fixed isotropic displacement parameters; anisotropic displacement parameters were employed for all non-hydrogen atoms. The following programs were used: data collection, APEX2;[66] data reduction, SAINT;[67] absorption correction SADABS;[68] cell refinement SHELXTL;[68] structure solutions, SHELXS-97;[68] and structure refinement, SHELXL-97.[68] The final data presentation and structure plots were generated in X-Seed Version 2.0.[69]

Computational Details. Geometry and frequency calculations were performed with the Gaussian 09 suite of programs[70] in the gas phase with the B3LYP,[71-73] MPW1PW91,[74] TPSSTPSS,[75] and ωB97x-D[76] functionals and the 6-311+G(d,p)[77,78] basis set on all atoms. Crystallographic coordinates were used for ground state geometries and utilized as starting geometries for optimizations. Transition state calculations of the Fe(CO)$_3$ rotor utilized starting geometry guesses from previous calculations. Transition states of the FeS$_2$C$_2$X chair/boat interconversion and the amine inversion were located through

relaxed coordinate scans of the Fe(1)-Fe(2)-X (X = bridgehead atom) and Fe(1)-N-C angles, respectively. All geometries were located with the B3LYP functional, with subsequent geometry optimizations of the other functionals using the B3LYP structure as an initial guess. Enthalpy and free energy corrections to the electronic energy of all stable geometries were calculated at 298.15 K by Gaussian, where all energies were obtained in Hartrees, then converted to kilocalories per mole. To compare to the experimental results, $\Delta G^{\ddagger}$ was recalculated at the coalescence temperature of the corresponding VT NMR experiment. Ground state geometries had no imaginary vibrational modes, while transition states were located with a single imaginary mode. The Ampac Graphical User Interface (AGUI)[79] program was used to extract geometric data as well as infrared frequency and bending and stretching vector data.

Experimental Details for Chapter IV

Synthesis of (μ-SCH$_2$N(Me)CH$_2$S)[Fe(CO)$_3$][Fe(CO)$_2$PPh$_3$], (1-PPh$_3$). To a 100 mL Schlenk flask containing **NMe** (0.300 g, 0.75 mmol), trimethylamine-N-oxide (0.062 g, 0.82 mmol) and PPh$_3$ (0.196 g, 0.75 mmol) was added MeCN (30 mL). The reaction was allowed to stir for 30 m, after which time the solvent was removed in vacuo. The resulting red solid was completely dissolved in hexanes and loaded onto the top of a silica column (4 cm x 20 cm). The red product was eluted with MeOH and solvent was removed with a rotary evaporator to yield 0.164 g (0.26 mmol, 34.5 %). Crystals of X-ray quality were obtained by slow diffusion of ether into a concentrated CH$_2$Cl$_2$ solution. IR (CH$_3$CN) ν(CO): 2044 (s), 1986 (s), 1974 (sh), 1935 (w).

Synthesis of (μ-SCH$_2$N(^{t}Bu)CH$_2$S)[Fe(CO)$_3$][Fe(CO)$_2$PPh$_3$], (2-PPh$_3$). To a 100 mL Schlenk flask containing **NtBu** (0.300 g, 0.68 mmol), trimethylamine-N-oxide (0.056 g, 0.75 mmol) and PPh$_3$ (0.178 g, 0.68 mmol) was added MeCN (30 mL). The reaction was allowed to stir for 30 m, after which time the solvent was removed in vacuo. The resulting red solid was completely dissolved in hexanes and loaded onto the top of a silica column (4 cm x 20 cm). The red product was eluted with MeOH and solvent was removed with a rotary evaporator to yield 0.166 g (0.25 mmol, 36.2 %). Crystals of X-ray quality were obtained by slow diffusion of ether into a concentrated CH$_2$Cl$_2$ solution. IR (CH$_3$CN) ν(CO): 2042 (s), 1986 (s), 1969 (m), 1933 (w).

Synthesis of (μ-SCH$_2$N(Me)CH$_2$S)[Fe(CO)$_3$][Fe(CO)$_2$PTA], (1-PTA). To a 100 mL Schlenk flask containing **NMe** (0.300 g, 0.75 mmol), trimethylamine-N-oxide (0.062 g, 0.82 mmol) and PTA (0.118 g, 0.75 mmol) was added MeCN (30 mL). The reaction was allowed to stir for 30 m, after which time the solvent was removed in vacuo. The resulting red solid was completely dissolved in hexanes and loaded onto the top of a silica column (4 cm x 20 cm). The red product was eluted with MeOH and solvent was removed with a rotary evaporator to yield 0.169 g (0.27 mmol, 42.5 %). Crystals of X-ray quality were obtained by slow diffusion of ether into a concentrated CH$_2$Cl$_2$ solution. IR (CH$_3$CN) ν(CO): 2039(s); 1983(s); 1962(sh); 1926(w).

Synthesis of (μ-SCH₂N(ᵗBu)CH₂S)[Fe(CO)₃][Fe(CO)₂PTA], (2-PTA). To a 100 mL Schlenk flask containing **NtBu** (0.500 g, 1.13 mmol), trimethylamine-N-oxide (0.093 g, 1.24 mmol) and PTA (0.177 g, 1.13 mmol) was added MeCN (30 mL). The reaction was allowed to stir for 30 m, after which time the solvent was removed in vacuo. The resulting red solid was completely dissolved in hexanes and loaded onto the top of a silica column (4 cm x 20 cm). The red product was eluted with MeOH and solvent was removed with a rotary evaporator to yield 0.2330 g (0.41 mmol, 36.0 %). Crystals of X-ray quality were obtained by slow diffusion of ether into a concentrated CH₂Cl₂ solution. IR (CH₃CN) ν(CO): 2039 (m), 1985 (s), 1968 (sh), 1927 (w).

Synthesis of (μ-SCH₂N(Ph)CH₂S)[Fe(CO)₃][Fe(CO)₂PTA], (3-PTA). To a 100 mL Schlenk flask containing **NPh** (0.200 g, 0.43 mmol), trimethylamine-N-oxide (0.036 g, 0.48 mmol) and PTA (0.068 g, 0.36 mmol) was added MeCN (30 mL). The reaction was allowed to stir for 30 m, after which time the solvent was removed in vacuo. The resulting red solid was completely dissolved in hexanes and loaded onto the top of a silica column (4 cm x 20 cm). The red product was eluted with MeOH and solvent was removed with a rotary evaporator to yield 0.073 g (0.12 mmol, 28.4 %). Crystals of X-ray quality were obtained by slow diffusion of ether into a concentrated CH₂Cl₂ solution. IR (CH₃CN) ν(CO): 2042 (m), 1989 (s), 1968 (sh), 1928 (w).

Synthesis of (μ-SCH₂N(Me)CH₂S)[Fe(CO)₃][Fe(CO)₂P(OMe)₃], (1-P(OMe)₃). To a 100 mL Schlenk flask containing **NMe** (0.300 g, 0.75 mmol), trimethylamine-N-oxide

(0.062 g, 0.82 mmol) and P(OMe)$_3$ (0.093 g, 0.75 mmol) was added MeCN (30 mL). The reaction was allowed to stir for 30 m, after which time the solvent was removed in vacuo. The resulting red solid was completely dissolved in hexanes and loaded onto the top of a silica column (4 cm x 20 cm). The red product was eluted with MeOH and solvent was removed with a rotary evaporator to yield 0.143 g (0.29 mmol, 38.4 %). Crystals of X-ray quality were obtained by slow diffusion of ether into a concentrated CH$_2$Cl$_2$ solution. IR (CH$_3$CN) ν(CO): 2048(m); 1994(s); 1970(m); 1937(w).

Synthesis of (μ-SCH$_2$N(^{t}Bu)CH$_2$S)[Fe(CO)$_3$][Fe(CO)$_2$P(OMe)$_3$], (2-P(OMe)$_3$). To a 100 mL Schlenk flask containing **NtBu** (0.300 g, 0.68 mmol), trimethylamine-N-oxide (0.054 g, 0.75 mmol) and P(OMe)$_3$ (0.084 g, 0.68 mmol) was added MeCN (30 mL). The reaction was allowed to stir for 30 m, after which time the solvent was removed in vacuo. The resulting red solid was completely dissolved in hexanes and loaded onto the top of a silica column (4 cm x 20 cm). The red product was eluted with MeOH and solvent was removed with a rotary evaporator to yield 0.154 g (0.29 mmol, 42.1 %). Crystals of X-ray quality were obtained by slow diffusion of ether into a concentrated CH$_2$Cl$_2$ solution. IR (CH$_3$CN) ν(CO): 2047(m); 1991(s); 1968(m); 1932(w).

Synthesis of (μ-SCH$_2$N(Ph)CH$_2$S)[Fe(CO)$_3$][Fe(CO)$_2$P(OMe)$_3$], (3-P(OMe)$_3$). To a 100 mL Schlenk flask containing **NPh** (0.300 g, 0.65 mmol), trimethylamine-N-oxide (0.054 g, 0.71 mmol) and P(OMe)$_3$ (0.080 g, 0.65 mmol) was added MeCN (30 mL). The reaction was allowed to stir for 30 m, after which time the solvent was removed in

vacuo. The resulting red solid was completely dissolved in hexanes and loaded onto the top of a silica column (4 cm x 20 cm). The red product was eluted with MeOH and solvent was removed with a rotary evaporator to yield 0.117 g (0.21 mmol, 32.2 %). Crystals of X-ray quality were obtained by slow diffusion of ether into a concentrated CH_2Cl_2 solution. IR (CH_3CN) ν(CO): 2045(m); 1993(s); 1969(m); 1938(w).

Synthesis of (μ-SCH$_2$N(Me)CH$_2$S)[Fe(CO)$_2$PMe$_3$]$_2$, (1-[PMe$_3$]$_2$). To a 100 mL Schlenk flask equipped with a reflux condenser and containing **NMe**, (0.300 g, 0.75 mmol), was added 50 mL of dry toluene. PMe$_3$ (0.15 mL) was added and the solution was heated to 100 °C. The reaction was monitored by IR and showed complete reaction after 0.5 hours. Solvent was removed in vacuo and the resulting solid recrystallized from MeOH to give a dark red microcrystalline solid. (Yield: 0.310 g, 0.61 mmol, 81%). Crystals of X-ray quality were obtained from a concentrated MeOH solution stored at -4 °C. IR (toluene) ν(CO): 1983 (m); 1946 (s); 1911 (m); 1902 (m); ^{31}P NMR (CD$_3$CN): δ = 24.3 ppm.

Synthesis of (μ-SCH$_2$N(^{t}Bu)CH$_2$S)[Fe(CO)$_2$PMe$_3$]$_2$, (2-[PMe$_3$]$_2$). To a 100 mL Schlenk flask equipped with a reflux condenser and containing **NtBu**, (0.300 g, 0.68 mmol), was added 50 mL of dry toluene. PMe$_3$ (0.15 mL) was added and the solution was heated to 100 °C. The reaction was monitored by IR and showed complete reaction after 1.5 hours. Solvent was removed in vacuo and the resulting solid recrystallized from MeOH to give a dark red microcrystalline solid. (Yield: 0.311 g, 0.56 mmol, 83%).

Crystals of X-ray quality were obtained from a concentrated MeOH solution stored at -4 °C. IR (toluene) ν(CO): 1983 (w); 1948 (s); 1903 (m); 1892 (sh); ^{31}P NMR (CD$_3$CN): δ = 23.7 ppm.

Synthesis of (μ-SCH$_2$N(Me)(H)CH$_2$S)[Fe(CO)$_2$PMe$_3$]$_2$$^+$, ([1H]$^+$). To a 100 mL Schlenk flask containing **1-[PMe$_3$]$_2$** (0.200 g, 0.50 mmol) in MeOH (30 mL), HBF$_4$□O(CH$_2$CH$_3$)$_2$ (0.5 mL) was added. The reaction was allowed to stir for 30 m, after which time the solvent was removed in vacuo. The resulting orange solid was washed with hexanes and ether. (Yield: 0.161 g, 0.27 mmol, 54%). IR (CH$_3$CN) ν(CO): 2000(w); 1965(s); 1924(m); ^{31}P NMR (CD$_3$CN): δ = 31.2 ppm, 19.1 ppm.

Synthesis of (μ-SCH$_2$N(^{t}Bu)(H)CH$_2$S)[Fe(CO)$_2$PMe$_3$]$_2$$^+$, ([2H]$^+$). To a 100 mL Schlenk flask containing **2-[PMe$_3$]$_2$** (0.200 g, 0.45 mmol) in MeOH (30 mL), HBF$_4$□O(CH$_2$CH$_3$)$_2$ (0.5 mL) was added. The reaction was allowed to stir for 30 m, after which time the solvent was removed in vacuo. The resulting orange solid was washed with hexanes and ether. (Yield: 0.162 g, 0.29 mmol, 65%). Crystals of X-ray quality were obtained by slow diffusion of ether into a concentrated CH$_2$Cl$_2$ solution. IR (CH$_3$CN) ν(CO): 2001(w); 1964(s); 1925(m)); ^{31}P NMR (CD$_3$CN): δ = 30.1 ppm, 18.9 ppm.

Synthesis of (μ-H)(μ-SCH$_2$N(Me)CH$_2$S)[Fe(CO)$_2$PMe$_3$]$_2$$^+$, ([1Hy]$^+$). To a 100 mL Schlenk flask containing **1-[PMe$_3$]$_2$** (0.200 g, 0.50 mmol) in CH$_2$Cl$_2$/EtOH (2

mL/15mL), HCl (1.5 mL) was added. The reaction was allowed to stir for 30 m, after which time a few drops of saturated aqueous NH_4PF_6 solution was added. The orange solid was filtered and washed with water and ether successively. The resulting orange solid was dried in vacuo. (Yield: 0.167 g, 0.25 mmol, 51%). IR (CH_3CN) ν(CO): 2034(s); 1994(m); ^{31}P NMR (CD_3CN): $\delta = 22.5$ ppm.

Synthesis of (μ-H)(μ-SCH$_2$N(^{t}Bu)CH$_2$S)[Fe(CO)$_2$PMe$_3$]$_2^+$, ([2Hy]$^+$). To a 100 mL Schlenk flask containing **1-[PMe$_3$]$_2$** (0.200 g, 0.45 mmol) in CH_2Cl_2/EtOH (2 mL/15mL), HCl (1.5 mL) was added. The reaction was allowed to stir for 30 m, after which time a few drops of saturated aqueous NH_4PF_6 solution was added. The orange solid was filtered and washed with water and ether successively. The resulting orange solid was dried in vacuo. (Yield: 0.155 g, 0.22 mmol, 48%). Crystals of X-ray quality were obtained by slow diffusion of ether into a concentrated CH_2Cl_2 solution. IR (CH_3CN) ν(CO): 2032(s); 1992(m); ^{31}P NMR (CD_3CN): $\delta = 21.1$ ppm.

Synthesis of (μ-H)(μ-SCH$_2$N(Me)(H)CH$_2$S)[Fe(CO)$_2$PMe$_3$]$_2^{2+}$, ([1HHy]$^{2+}$). To a 100 mL Schlenk flask containing **1-[PMe$_3$]$_2$** (0.200 g, 0.50 mmol) in CH_3CN (30 mL), HBF$_4$□O(CH$_2$CH$_3$)$_2$ (0.5 mL) was added. The reaction was allowed to stir for 30 m, after which time the solvent was removed in vacuo. The resulting orange solid was washed with hexanes and ether. (Yield: 0.156 g, 0.26 mmol, 52%). IR (CH_3CN) ν(CO): 2049(s); 2011(m); ^{31}P NMR (CD_3CN): $\delta = 25.2$ ppm, 21.1 ppm.

Synthesis of (μ-H)(μ-SCH₂N(ᵗBu)(H)CH₂S)[Fe(CO)₂PMe₃]₂²⁺, ([2HHy]²⁺). To a 100 mL Schlenk flask containing **2-[PMe₃]₂** (0.200 g, 0.45 mmol) in CH₃CN (30 mL), HBF₄☐O(CH₂CH₃)₂ (0.5 mL) was added. The reaction was allowed to stir for 30 m, after which time the solvent was removed in vacuo. The resulting orange solid was washed with hexanes and ether. (Yield: 0.139 g, 0.22 mmol, 48%). IR (CH₃CN) ν(CO): 2047(s); 2008(m); ³¹P NMR (CD₃CN): δ = 24.9 ppm, 20.3 ppm.

Experimental Details for Chapter V

Crystallization of Na(μ-SCH₂N(C₆H₄SO₃)CH₂S-)[Fe(CO)₃]₂, (1Na). 1Na was synthesized according to the recently described procedure.[12] Wet **1Na** was dissolved to saturation in THF. Crystals of X-ray quality were obtained by cooling this solution at 5 °C overnight.

Synthesis of Na(μ-SCH₂N(C₆H₄SO₃)CH₂S-)[Fe(CO)₃][Fe(CO)₂PTA], (3Na). To a slurry of **1Na**, (0.200 g 0.355 mmol) in MeOH (20 mL) was added PTA, (0.111 g, 0.704 mmol). The solution was then heated to 60 °C and the reaction was monitored by IR spectroscopy. The reaction mixture was stirred overnight (~20 h) after which time IR analysis of the solution indicated that it contained primarily the mono-substituted diiron complex as well as a small amount of the starting material. The solvent was removed in vacuo and the residue was dissolved in THF and loaded onto the top of a silica column (4 cm x 20 cm). Elution with methanol gave two bands which contained, in order, the unreacted starting material and then the product **3Na**. The fractions containing the

second band were concentrated to ~3-5 mL on a rotary evaporator and ether was added resulting in a red precipitate. The solid was dried under vacuum to yield 0.108 g (0.156 mmol, 43.8 %) of **3Na**. The Et_4N^+ salt (**3TEA**), was synthesized by counterion exchange using Et_4NCl in CH_2Cl_2. Crystals of X-ray quality were obtained by slow diffusion of ether into a concentrated CH_2Cl_2 solution of **3TEA**. IR (THF) $\nu(CO)$: 2042 (m); 1986 (s); 1967 (sh); 1930 (w) cm^{-1}; ^{1}H NMR (DMSO): 4.05 (s, 6H); 4.21 (d, J = 13.2 Hz, 2H); 4.38 (d, J = 12.7 Hz, 3H); 4.46 (d, J = 12.7 Hz, 3H); 4.51 (d, J = 13.2 Hz, 2H); 6.76 (d, J = 8.8 Hz, 2H); 7.44 (d, J = 8.8 Hz, 2H) ppm; Electronic absorption spectrum (H_2O): λ_{max} (ε, M^{-1} cm^{-1}) 500 (540), 346 (2880), 275 (5560); HRMS (ESI) m/z calcd for $C_{19}H_{20}Fe_2N_4O_8PS_3^{1-}$ Theoretical Mass: 670.8880 g/mol; Found Mass: 670.8847 g/mol.

Synthesis of Na(μ-SCH$_2$N(C$_6$H$_4$SO$_3$)CH$_2$S-)[Fe(CO)$_3$][Fe(CO)$_2$PPh$_3$], (4Na). To a 100 mL Schlenk flask containing **1Na** (0.100 g, 0.177 mmol), trimethylamine-N-oxide (0.015 g, 0.200 mmol) and PPh$_3$ (0.051 g, 0.195 mmol) was added MeCN (20 mL) and the solution was heated to 60 °C. IR analysis of the solution showed bands as follows: $\nu(CO)$ in MeCN: 2048 m, 1990 sh, 1931 w. The reaction was allowed to stir for 30 m, after which time the solvent was removed in vacuo. The resulting red solid was completely dissolved in THF and loaded onto the top of a silica column (4 cm x 20 cm). The dark red product was eluted with MeOH and solvent was removed with a rotary evaporator. The dried residue was triturated with H_2O and dried under vacuum to yield 0.049 g (0.061 mmol, 34.5 %) of the pure product. The Et_4N^+ salt (**4TEA**) was obtained in an analogous manner starting from **1TEA**. Crystals of X-ray quality were obtained by

cooling a saturated MeOH solution of **4TEA** at -5 °C for 2 weeks. IR (THF) ν(CO): 2046 (m); 1990 (s); 1975 (m); 1936 (w), cm^{-1}; ^{1}H NMR (DMSO): 4.28 (d, J = 12.7, 2H); 6.65 (d, J = 8.8 Hz, 2H); 7.40 (d, J = 8.8 Hz, 2H); 7.47 (m, 3H); 7.55 (m, 6H); 7.63 (m, 6H) ppm; Electronic absorption spectrum (H$_2$O): λ_{max} (ε, M^{-1} cm^{-1}) 489 (1260), 330 (9330), 303 (14210), 229 (15130), HRMS (ESI) m/z calcd for C$_{31}$H$_{23}$Fe$_2$NO$_8$PS$_3$$^{1-}$ Theoretical Mass: 775.9022 g/mol; Found Mass: 775.8988 g/mol.

Electrochemical Studies. Voltammograms were obtained using a standard three electrode cell under argon at room temperature using a Bioanalytical System (BAS) 100 electrochemical workstation with a glassy carbon working electrode and a platinum wire auxiliary electrode. For aqueous work, a saturated KCl Ag/AgCl reference electrode was used and the supporting electrolyte solution was 0.01 M NaCl. Samples were run at a concentration of ~0.1 mM due to their low solubility in the NaCl buffer solution. Between each scan the glassy carbon electrode was removed and polished using a 1 μm polycrystalline diamond suspension and rinsed with both acetone and deionized water to remove any adsorbed material. All aqueous potentials are reported relative to the Ag/AgCl couple as 0.00 V. For work done in MeCN, a saturated Ag/AgNO$_3$ reference electrode was used and the supporting electrolyte solution was 0.1 M Et$_4$NBF$_4$. All samples in MeCN were run at a concentration of 2 mM and potentials are reported relative to the Fc/Fc^{+} couple as 0.00 V.

X-ray Structure Analysis. For complexes **1Na**, **3TEA** and **4 TEA** low-temperature (110 K) X-ray data were obtained on a Bruker-D8 Adv GADDS general-purpose three-circle X-ray diffractometer (Texas A&M University) (Cu sealed X-ray tube, Kα = 1.54184 Å). Space groups were determined on the basis of systematic absences and intensity statistics and structures were solved by direct methods and refined by full-matrix least squares on F^2. All non-hydrogen atoms were refined with anisotropic thermal parameters. H atoms were placed at idealized positions and refined with fixed isotropic displacement parameters; anisotropic displacement parameters were employed for all non-hydrogen atoms. Complexe **1Na** was found as a racemic twin (BASF = 0.23126). The following programs were used: data collection, APEX2[66] and GADDS,[80] data reduction, SAINT;[67] absorption correction and twin refinement, *SADABS*[67] *and TWINABS*; [67] cell refinement *SHELXTL*; [67] structure solutions, *SHELXS-97*[67] (Sheldrick); and structure refinement, *SHELXL-97*[67] (Sheldrick). The final data presentation and structure plots were generated in X-Seed Version 1.5.[69]

UV-vis. Water solubility studies of the diiron complexes were performed using a Shimadzu UV-2450 UV-Vis spectrometer. Deaerated water was added to known amounts of each complex until no solid material was visible in solution. This stock solution was then used to generate several samples of known concentrations allowing the molar absorptivities for each absorption band in the UV-Vis spectra to be calculated. Maximum concentrations were obtained by adding enough of each complex to 20 mL of deaerated water that solid remained even after sonicating each sample for 10 minutes.

The slurry was then centrifuged for 30 minutes or until no suspended solid was visible in solution. The UV-Vis spectrum of the supernatant was recorded and Beer's law was used to calculate the concentration.

Experimental Details for Chapter VI

Crystallization of (μ-SH)$_2$[Fe(CO)$_3$]$_2$, (1). Complex **1** was dissolved in a minimum amount of hexanes. Crystals of X-ray quality were obtained by cooling the solution at -30°C.

Synthesis of (μ-SAuPPh$_3$)$_2$[Fe(CO)$_3$]$_2$, (2). A red solution of 0.10 g (0.29 mmol) of (μ-S$_2$)[(Fe(CO)$_3$]$_2$ in THF (15 mL) cooled to **-**78 °C was treated with 0.6 mL of a 1.0 M THF solution of LiEt$_3$BH (0.6 mmol). The resulting green solution was allowed to stir for 30 minutes, after which time a THF solution of PPh$_3$AuCl (0.288 g, 0.62 mmol) was added and allowed to warm to room temperature. Solvent was concentrated to ~5 mL in vacuo, and 30 mL of hexanes was added to precipitate the product. The solid was filtered in air and washed with hexanes. (Yield: 0.15 g, 0.12 mmol, 42%). IR (THF) ν(CO): 2045, 2008, 1965, 1960 cm^{-1}; ^{31}P NMR (toluene-d8): 36.40 ppm; Elem. Anal. Calculated (found) for **2** (Fe$_2$Au$_2$S$_2$P$_2$O$_6$H$_{30}$C$_{42}$) (MW 1262 = g/mol): C, 39.74 (39.96); H, 2.31 (2.40). Crystals of X-ray quality were obtained from a concentrated THF solution stored at -30 °C.

X-ray Structure Analysis. Low temperature (150 K) X-ray data was obtained on a Bruker Apex-II CCD based diffractometer (Texas A&M University) (Mo sealed X-ray tube, Kα = 0.71073 Å) for complexes **1** and **2**. Crystal samples were coated in mineral oil, affixed to a Nylon loop, and placed under streaming N_2. Space groups were determined on the basis of systematic absences and intensity statistics, and structures were solved by direct methods and refined by full-matrix least-squares on F^2. All non-hydrogen atoms were refined with anisotropic thermal parameters. H atoms were placed at idealized positions and refined with fixed isotropic displacement parameters; anisotropic displacement parameters were employed for all non-hydrogen atoms. The following programs were used: data collection, APEX2;[66] data reduction, SAINT;[67] absorption correction SADABS;[67] cell refinement SHELXTL;[67] structure solutions, SHELXS-97;[67] and structure refinement, SHELXL-97.[67] The final data presentation and structure plots were generated in X-Seed Version 2.0.[69]

Computational Details. Geometry and frequency calculations were performed with the Gaussian 09 suite of programs[70] in the gas-phase with the B3LYP[81] functional. The Stuttgart-Dresden ECP basis set was utilized for the Fe (SDD-ECP10MDF)[82] atoms and gold atoms (SDD-ECP60MDF-VTZ),[83,84] with the 6-311+G(d,p)[85-87] basis set on C and O atoms, 6-311+G(2d,p) basis[85-87] set on S and N atoms, and 6-311++G(d,p) basis set on H atoms.[85-87] One exception is, for those phenyl C and H atoms that are not directly attached to the phosphorus atoms in PPh$_3$, the 6-31G[85,88] basis set was applied to save resources. Crystallographic coordinates were used for ground state geometries of all

39

diiron complexes and utilized as starting geometries for optimizations with the hydrogen and methyl carbon atom positions selected for each of the three possible geometries. Transition state calculations of the S-H and S-Me inversion were located through relaxed coordinate scans of the S(1)−S(2)−X(2) and S(2)−S(1)−X(1) angles, where X = H or Au. Gibbs free energy corrections to the electronic energy of all stable geometries were calculated at 298.15 K by Gaussian, where all energies were obtained in hartrees and then converted to kcal/mol. There were no imaginary vibrational modes for ground state geometries, while transition states were located with a single imaginary mode. Solvation correction by SMD model[89] was computed based on optimized structure in vacuum.

CHAPTER III

CONFORMATIONAL MOBILITY AND PENDENT BASE EFFECTS ON

ELECTROCHEMISTRY OF SYNTHETIC ANALOGUES OF THE [FeFe]-

HYDROGENASE ACTIVE SITE[*]

Introduction

An obvious feature that appears to contribute to the superior function of the [FeFe]-H_2ase enzyme is the azadithiolate S to S linker that can relay protons to and from the open iron site. Several studies have reported that the aza-bridgehead, (μ-SCH_2NRCH_2S), influences the electrochemistry and catalysis, but the quantitative effect on catalytic responses is ambiguous. According to the review of Felton, Evans, Lichtenberger, et al., there is no clear correlation of E_{pc} and the nature of NR in the ca. 40 azadithiolates that have been measured.[90]

_____

Dynamic NMR (^{13}C and ^{1}H) studies of (μ-SCH$_2$XCH$_2$S)[Fe(CO)$_3$]$_2$ complexes, X = CR$_2$ or NR, were utilized to examine the fluxional processes, Figure III-1, that are important in the [FeFe]-hydrogenase active site models, where an open site for proton/hydrogen binding, achieved by configurational mobility of the Fe(CO)$_3$ unit, is required for electrocatalysis of proton reduction. In order to interrogate the effects of fluxional mobility on electrochemical response to added acid, energy barriers for the CO site exchange in Fe(CO)$_3$ rotors were determined for nitrogen and carbon-based bridgehead complexes. Herein we ask whether the dynamic processes, interrogated by variable temperature ^{1}H- and ^{13}CNMR spectroscopy, relate to differences in C- vs N-bridgehead species for electrocatalysis of proton reduction.
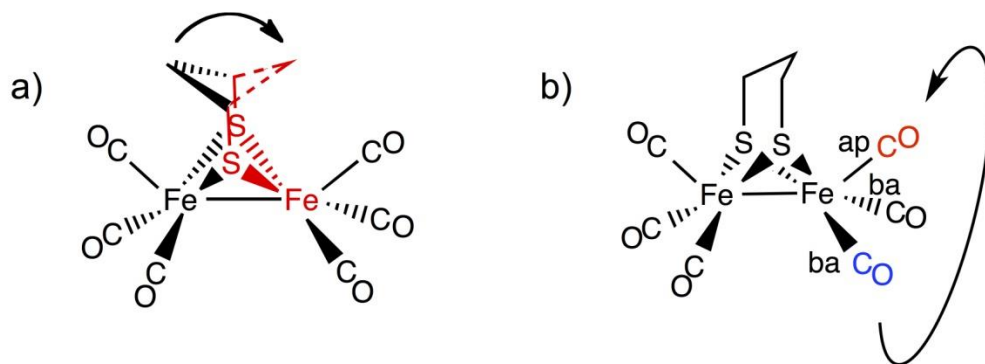
Figure III-1. The "parent" (μ-pdt)[Fe(CO)$_3$]$_2$ biomimetic, pdt = propane dithiolate, and its fluxional processes a) chair/boat interconversion and b) apical/basal CO site exchange.

Synthesis of Hexacarbonyl Complexes

The three azadithiolate complexes used in this study were synthesized according to literature, Figure III-2. Complex **NH**, $(\mu\text{-SCH}_2\text{N(H)CH}_2\text{S})[\text{Fe(CO)}_3]_2$, was synthesized through the addition of aqueous formaldehyde and ammonium carbonate to a THF solution of $(\mu\text{-SH})_2[\text{Fe(CO)}_3]_2$ leading to moderate yields (~40%).[62] High yields (~80%) of **NMe**, $(\mu\text{-SCH}_2\text{N(Me)CH}_2\text{S})[\text{Fe(CO)}_3]_2$, were afforded through the addition of a trimeric imine, $1,3,5\text{-(CH}_2)_3(\text{NMe})_3$, to $(\mu\text{-SH})_2[\text{Fe(CO)}_3]_2$.[63] **NtBu**, $(\mu\text{-SCH}_2\text{N}(^t\text{Bu})\text{CH}_2\text{S})[\text{Fe(CO)}_3]_2$, was synthesized through the condensation reaction of aqueous formaldehyde, H_2NtBu, and $(\mu\text{-SH})_2[\text{Fe(CO)}_3]_2$ in a THF solution giving yields ~60%.[62]

With the exception of **NtBu**, the solid-state structures of the compounds for this study are known.[27,41,50,92,93] To complete the series, **NtBu** was crystallized by cooling a saturated hexanes solution at -30 °C. The crystals were analyzed by X-ray diffraction and selected metric parameters are given in Table III-1 along with ν(CO) IR data.
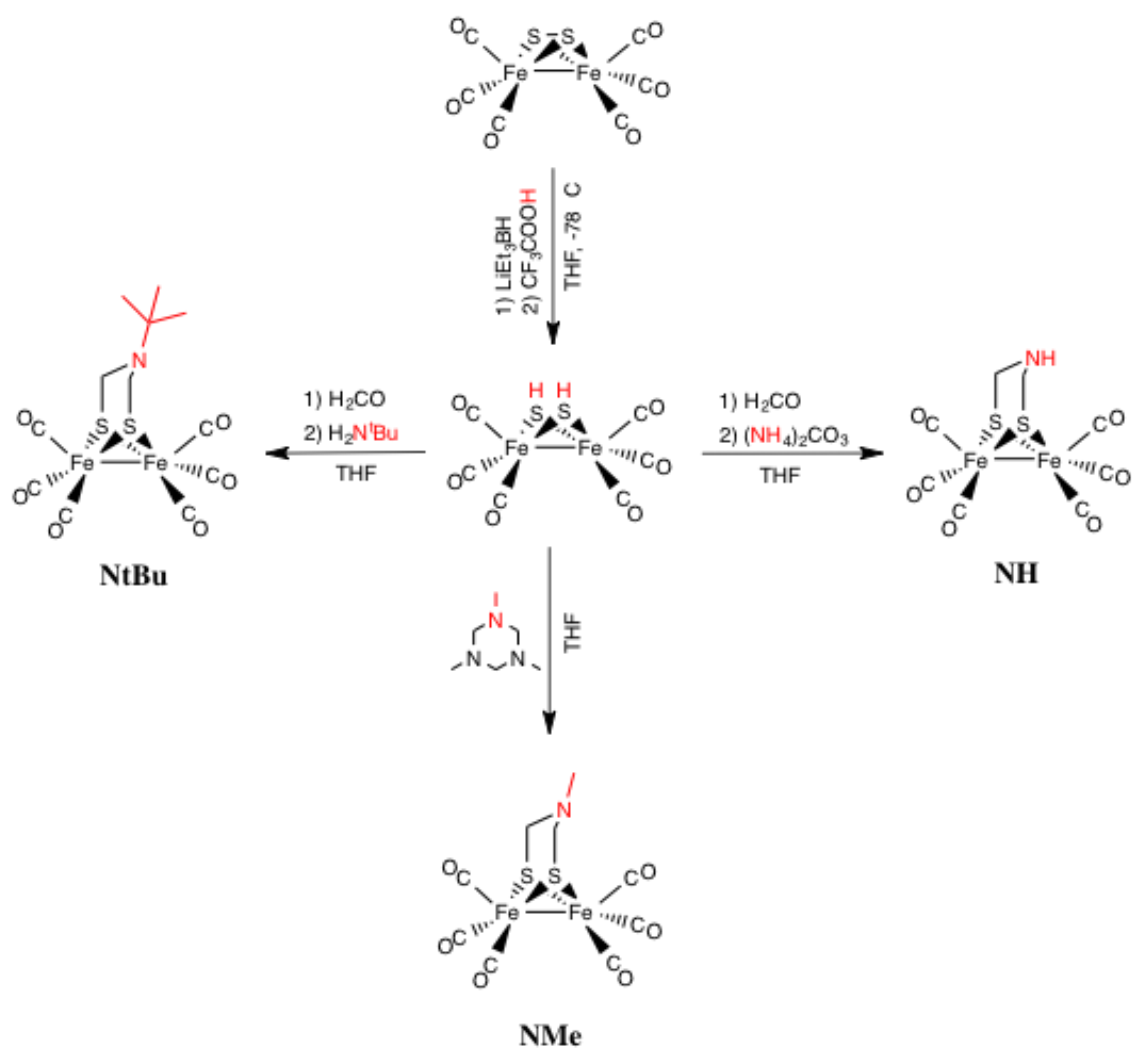
Figure III-2. Reaction scheme for the synthesis of azadithiolate hexacarbonyl complexes (μ-SCH$_2$N(H)CH$_2$S)[Fe(CO)$_3$]$_2$ **(NH),**[62] (μ-SCH$_2$N(Me)CH$_2$S)[Fe(CO)$_3$]$_2$ **(NMe),**[63] and (μ-SCH$_2$N(^{t}Bu)CH$_2$S)[Fe(CO)$_3$]$_2$ **(NtBu).**[62]

Table III-1. Spectroscopic and metric parameters of $(\mu\text{-S}(CH_2XCH_2S)[Fe(CO)_3]_2$ complexes.

Complex	ν(CO) IR (cm^{-1})[a]	Fe-Fe (Å)	Flap Angle (°)[b]	Torsion (°)[c]	C/N--Fe (Å)[d]	E_{pa} (V)[e]
disulfide	2084, 2044, 2007	2.556(1)	-	0.0	-	-
pdt	2076, 2035, 2005, 1992, 1981	2.5105(8)	137.09	0.0(2)	3.50	-1.68
dmpdt	2075, 2034, 2005, 1992, 1980	2.4939(4)	135.74	6.5(2)	3.74	-1.61
NH	2075, 2036, 2007, 1990, 1981	2.5150(3)	131.95	0.00(9)	3.48	-1.58
NMe$_{ax}$	2075, 2036, 2002, 1990, 1984	2.4924(7)	128.57	0.0(4)	3.59	-1.67
NMe$_{eq}$	-[f]	-[f]	120.48	-[f]	3.27	-[f]
NtBu	2075, 2036, 2002, 1994, 1982	2.5172(9)	118.46	6.1(2)	3.32	-1.69

[a] IR spectra obtained in hexanes.
[b] Refers to the dihedral angle formed through the intersection of the XC_2 (X = C or N) and C_2S_2 planes in the FeS_2C_2X ring.
[c] Refers to the CO_{ap}-Fe-Fe -$CO_{ap'}$ angle.
[d] The distance from the central atom in the bridgehead (C or N) to the closest iron.
[e] Potentials vs. Fc/Fc$^+$ in CH_3CN.
[f] The spectroscopic and metric parameters are the same for both the axial and equatorial isomers.

Structural Features

The molecular structure of **NtBu,** Figure III-3 (A), shows a pyramidal nitrogen in the bridgehead with the *t-Bu* group in the equatorial position, i.e., oriented away from the nearest apical CO group while the N-lone pair is directed towards that CO. The steric bulk of the *t*-Bu group has little effect on the $Fe(CO)_3$ units, as seen in the torsion angles, defined as $\angle CO_{ap}$-Fe-Fe$^{'}$-$CO_{ap'}$, Table III-1. The two $Fe(CO)_3$ units are largely in an eclipsed configuration with a torsion angle of 6.1°. As noted in Table III-1, this slight distortion is similar to that found for the **dmpdt** complex.[50] There are also variations in the angle formed from the intersection of the XC_2 and C_2S_2 planes within the FeS_2C_2X ring, which we define as the flap angle. The azadithiolate complexes have a smaller flap angle; see the overlay of the **dmpdt** and **NtBu** structures, Figure III-3 (B).

(A)   (B)
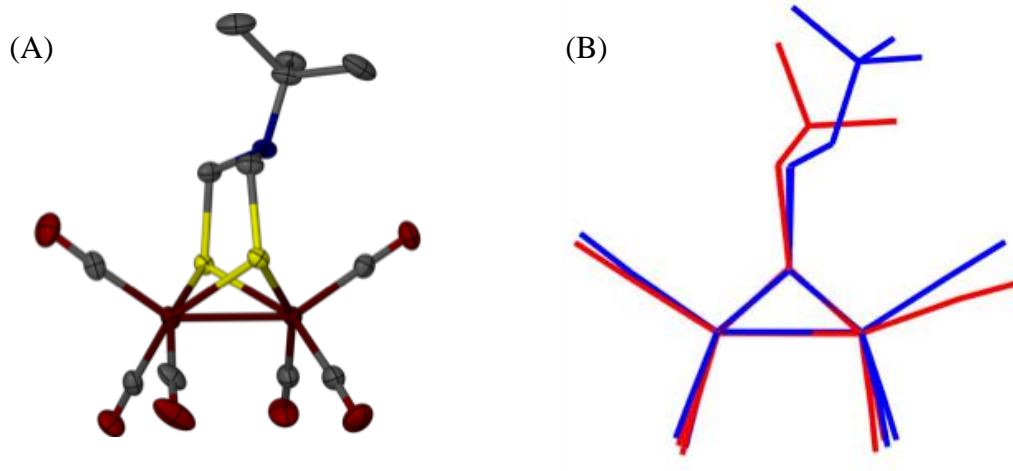
Figure III-3. (A) Structure of **NtBu** with thermal ellipsoids drawn at 50% probability level. (B) Overlay of **dmpdt** (red) and **NtBu** (blue) showing the difference between steric bulk at the carbon versus nitrogen.

As reported in the literature, two conformers of the **NMe** molecule co-crystallize; these are displayed as space-filling structures in Figure III-4.[92] The axial orientation of the methyl group on the nitrogen, Figure III-4 (A), places the methyl C-H in close contact with the adjacent apical carbonyl, similar to that seen with the methyl substituent of the **dmpdt** derivative, Figure III-4 (B). The N-inverted conformer of (A), with the methyl in the equatorial position, Figure III-4 (A'), shows a distinct spatial gap between the methyl substituent and the apical CO, as is also seen in the **NtBu** derivative, Figure III-4 (C). The **NMe** isomers show flap angles corresponding to each orientation of the methyl substituent, the larger (128.6°) relating to the axial isomer, (A), and the smaller (120.5°) belonging to the equatorial isomer, (A'). The **NtBu** derivative, (C), which crystallizes exclusively in the equatorial form of the FeS_2C_2NR metallacycle positioning the *tert*-butyl group away from the $Fe(CO)_3$ unit, has the smallest flap angle yet shows the minimal steric effect from the bridgehead. It is noteworthy that the observation of only one **NtBu** conformer is consistent with computational data, which did not converge for the axial orientation of the *tert*-butyl group, *vide infra*.

As indicated by almost identical ν(CO) values, Table III-1, the electron density on the iron centers is the same throughout the carbon and nitrogen bridgehead complexes of the series. The reduction potentials $(Fe^IFe^I \rightarrow Fe^IFe^0)$ are within 110 mV of each other ranging from -1.58 to -1.69 V, however there is no obvious trend, see Table III-1.[90]
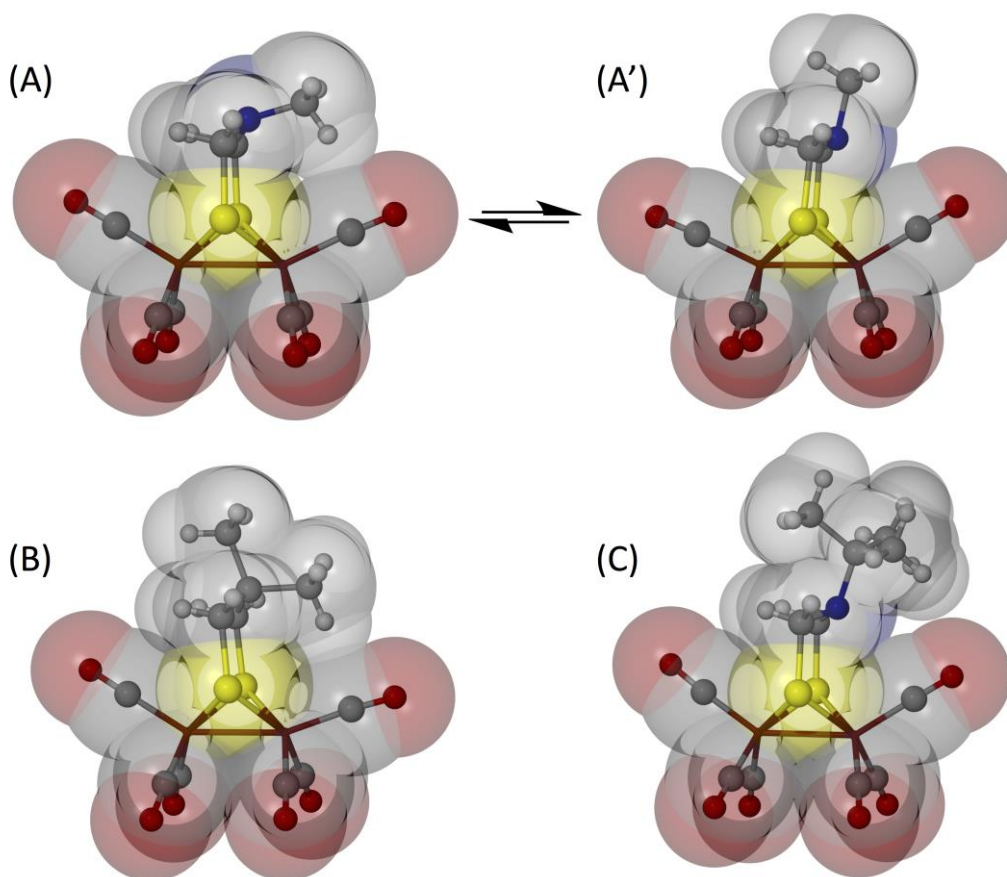
Figure III-4. Ball and stick representations featuring van der Waals spheres rendered from X-ray crystal structures of (A) **NMe**$_{axial}$, (A') **NMe**$_{equatorial}$, (B) **dmpdt**, and (C) **NtBu**.

^{1}H NMR Studies

Variable-temperature (VT) NMR spectra of the complexes were obtained to compare energy barriers of the fluxional processes, Figure III-1. At 25 °C two singlets are seen in the ^{1}H NMR spectra for both **NMe** and **NtBu**, corresponding to the rapidly equilibrating methylene (elbow carbon) protons (3.23 for the **NMe** and 3.12 ppm for the

NtBu) and the methyl (2.35 ppm) or *tert*-butyl (0.98 ppm) protons, respectively. For both complexes, the slow exchange regime, -50 °C in CD_2Cl_2 solvent, finds the methylene protons are resolved into two broad resonances reflecting the nonequivalency of the axial and equatorial H atoms, Figure III-5 (A) and (B). Coalescence occurs at -20 °C for **NtBu** and at -30 °C for **NMe**.

For **NH**, coalescence is seen at a higher temperature of 15 °C, Figure III-5 (C). In contrast, the analogous process in the **pdt** complex in CD_2Cl_2 is at -60 °C, and the lowest accessible temperature did not achieve the cessation of chair/boat interconversion in the **dmpdt** case.[50] We conclude that the N-bridgehead species have higher barriers to the chair/boat interconversion that would position the amine base further away or closer to the iron. For this series the chair/boat interconversion barrier increases in the order **dmpdt < pdt < NtBu ≤ NMe < NH**; computational values are in agreement with this trend, Table III-2.
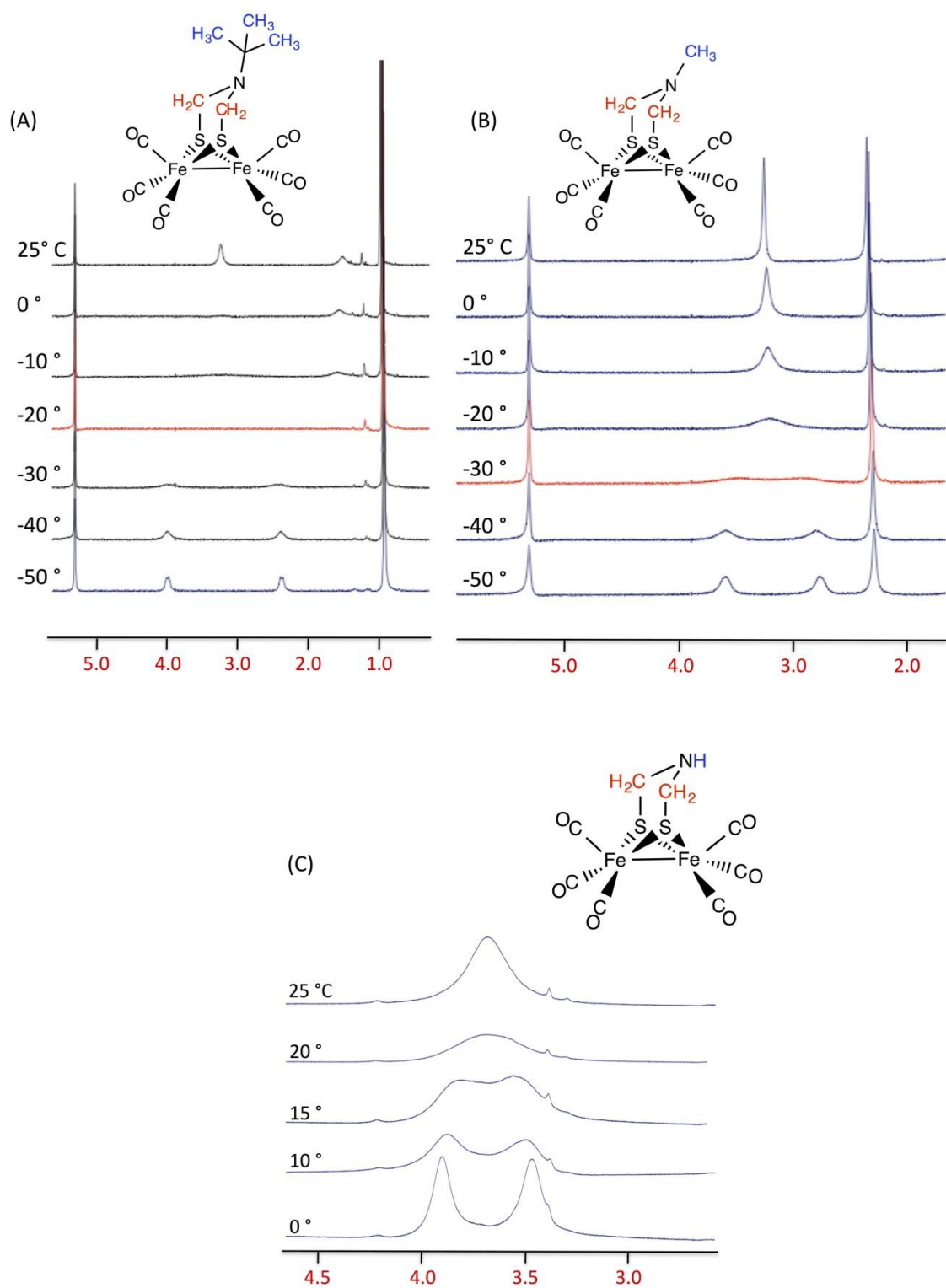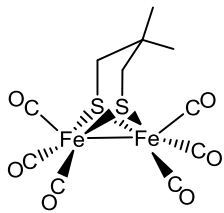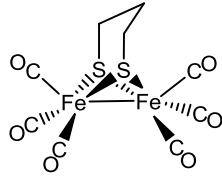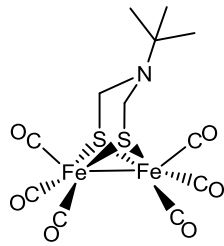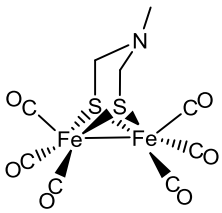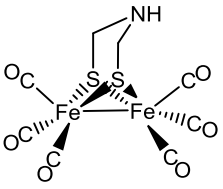
Figure III-5. Variable-temperature ^{1}H NMR spectra at 300 MHz in CD$_2$Cl$_2$ of (A) **NH**, (B) **NMe**, and (C)**NtBu**.

Table III-2. Experimental and computational chair/boat energy barriers (kcal/mol).

	dmpdt	pdt	NtBu	NMe	NH
Experimental[a]	-[b]	9.63(±0.24)	11.23(±0.24)	11.33(±0.24)	13.29(±0.24)
Computational[c]	5.21[d]	8.83	10.43	10.81	15.08

[a] Error estimated using ± 5 °C for detected coalescence temperature
[b] Experimental data could not be obtained as coalescence temperature < -120 °C[50]
[c] Computational free energy obtained at coalescence temperature utilizing TPSSTPSS functional
[d] Coalescence temperature of $Fe(CO)_3$ rotation, -87 °C, used to estimate bridgehead free energy[50]

^{13}C NMR Studies

The VT ^{13}C NMR spectra in the CO region were used to establish the $Fe(CO)_3$ rotor fluxionality. At room temperature a single ^{13}C resonance is seen at $\delta = 208.3$ ppm for **NH**, Figure III-6, indicating both $Fe(CO)_3$ units are freely rotating. Upon cooling to 0 °C, the bridgehead has slowed chair/boat interconversion leading to a distinction between $Fe(CO)_3$ units. At -60 °C three ^{13}C CO resonances are seen at $\delta = 208.3$, 208.2, and 206.8 ppm, showing that one $Fe(CO)_3$ unit has ceased motion and the other $Fe(CO)_3$ unit is in fast exchange. On the basis of relative intensities, the resonances at $\delta = 208.2$ and 206.8 ppm are assigned respectively to the apical and basal CO's on one $Fe(CO)_3$ unit. Four resonances are seen at -80 °C indicating that all fluxional processes have ceased.
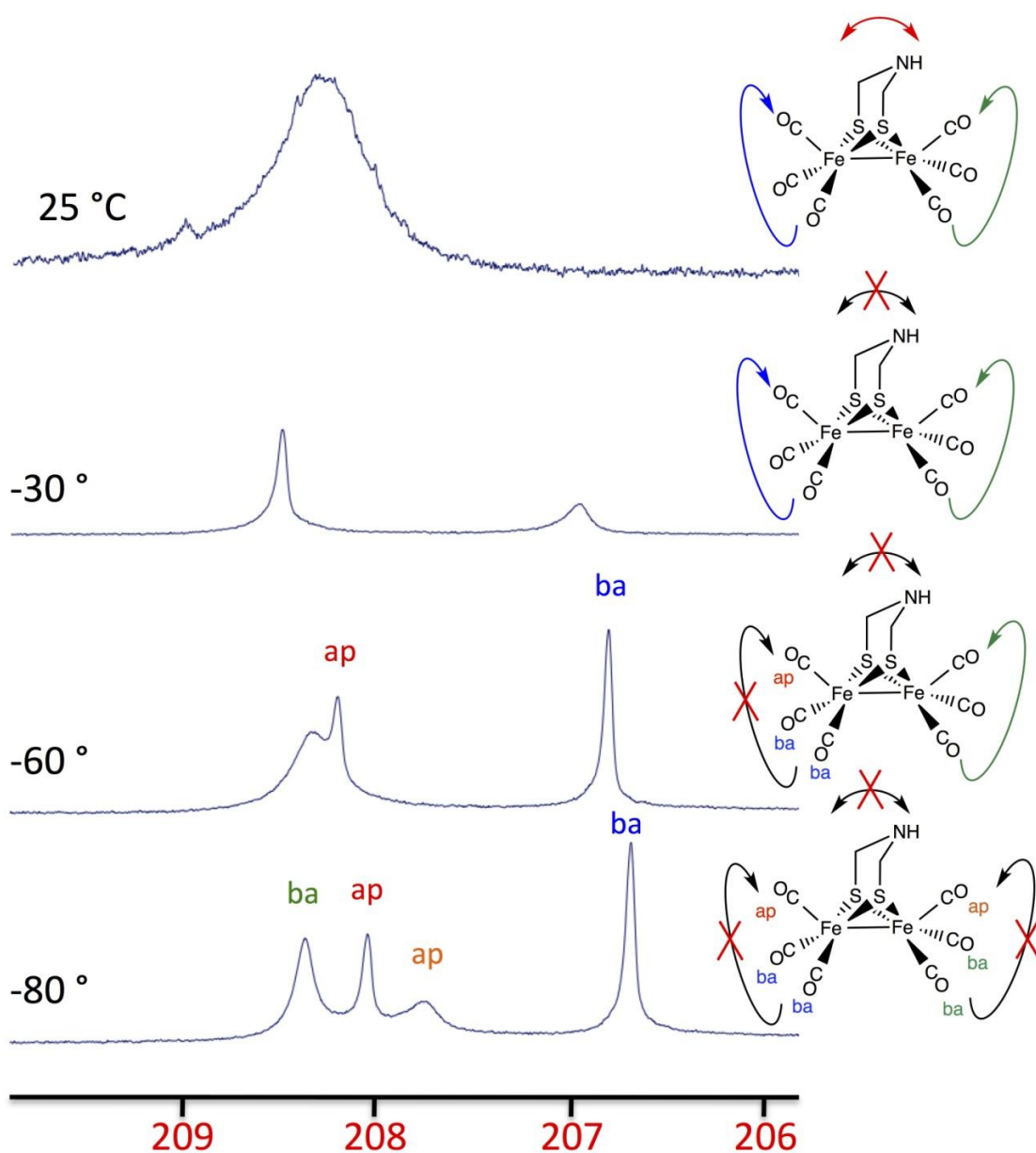
Figure III-6. Variable-temperature ^{13}C NMR spectra at 500 MHz in CD_2Cl_2 of **NH** in the low-field CO region with depiction of the fluxional processes at the various temperatures.

Upon cooling the **NMe** sample in CD_2Cl_2, the single room temperature ^{13}C resonance at $\delta = 208.4$ ppm splits in a manner indicating distinctions in the two $Fe(CO)_3$ units, panel (A) in Figure III-7. The broad lower field resonance does not collapse into the base line until -80 °C, whereas the higher field resonances become distinct between -40 and -50 °C, and remain sharp on further cooling. On the basis of relative intensities, the resonances at $\delta = 208.0$ and 207.1 ppm, are assigned to the basal and apical CO's on one $Fe(CO)_3$ unit. This indicates that one $Fe(CO)_3$ unit has ceased CO site exchange within the accessible temperature range while the other unit remains in motion, needing temperatures lower than -80 °C to resolve into separate signals. At -120 °C, using $CDFCl_2$ as the NMR solvent, four ^{13}C resonances are seen at 209.5, 208.4, 207.7, and 207.5 ppm indicating that both $Fe(CO)_3$ units have ceased rotation, Figure III-8.
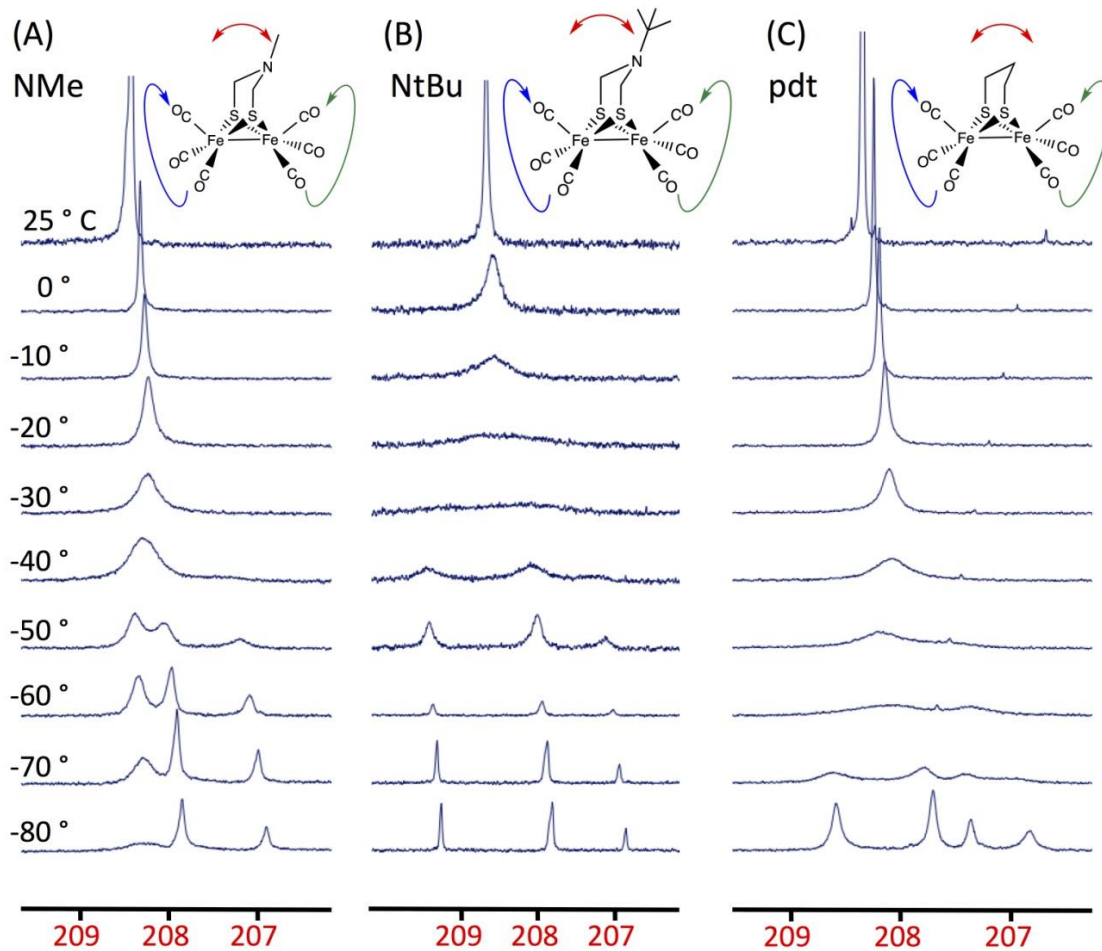
Figure III-7. Variable-temperature ^{13}C NMR spectra at 500 MHz in CD$_2$Cl$_2$ in the low-field CO region (A) **NMe**, (B) **NtBu**, and (C) **pdt**.
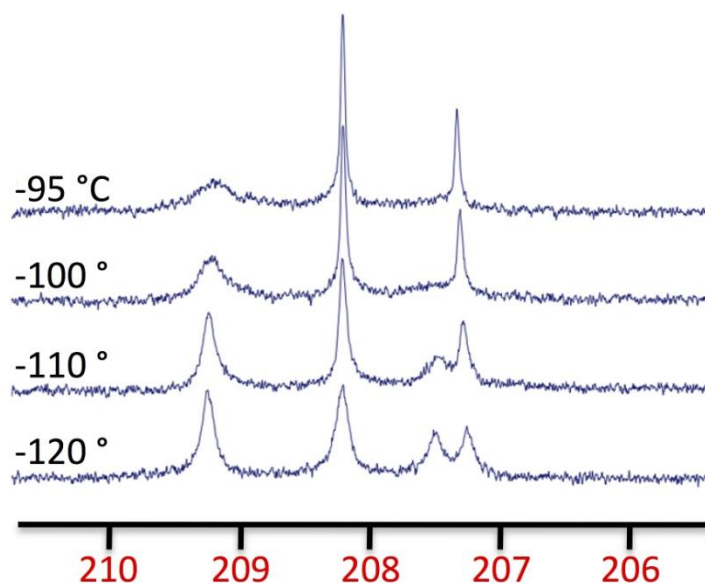
Figure III-8. Variable-temperature ^{13}C NMR spectra of **NMe** at 500 MHz in CDFCl$_2$ in the low-field CO region.

In contrast to **NMe**, the single ^{13}C CO resonance of **NtBu** at 25 °C, panel (B) of Figure III-7, broadens and collapses at -30 °C, reforming into three sharp resonances at δ = 209.3, 207.8, and 206.8 ppm, integrating as 2:3:1. This pattern is consistent with two possibilities: 1) both Fe(CO)$_3$ units simultaneously cease rotation and apical/basal CO signals from separate Fe(CO)$_3$ units overlap; or 2) one Fe(CO)$_3$ unit is fixed while the other is still in flux similar to the behaviour of **NMe**. Due to the sharpness of all three resonances at temperatures as low as -80 °C, the first option is favored. Computational (DFT) studies also support the first option in that the calculated barriers of rotation in the Fe(CO)$_3$ units of **NtBu** are within 0.2 kcal/mol of each other. Concurrent coalescence of both Fe(CO)$_3$ rotors is also seen with **pdt**, where the single room temperature resonance

broadens and collapses at -60 °C, reforming as four resonances at -80 °C, Figure III-7

(C). Thus in the **NH** and **NMe** complexes the individual $Fe(CO)_3$ units coalesce at

different rates, whereas the individual $Fe(CO)_3$ units of the **pdt** and **NtBu** complexes

coalesce at the same rate, *vide infra*.

One ^{13}CO resonance at $\delta = 208.9$ ppm is seen at room temperature for **disulide**,

$(\mu\text{-}S_2)[Fe(CO)_3]_2$, Figure III-9. Upon cooling the sample in CD_2Cl_2 to -80 °C two signals

appear at $\delta = 210.8$ and 204.4 ppm assigned to the basal and apical CO's, respectively.

Two signals are seen for disulfide instead of four because the two $Fe(CO)_3$ units are

indistinguishable due to the lack of a bridgehead. This is also seen with **dmpdt,** as the

chair/boat interconversion barrier is too low to differentiate the two $Fe(CO)_3$ units.[50]

Values for the CO intramolecular site exchange energy barriers for these

complexes were obtained using the formulas $\Delta G^{\ddagger} = -(RT)\ln[k_t h/k_b T_{coal}]$ and $k_t =$

$(\pi \Delta v)/2^{1/2}$, where the coalescense temperature (T_{coal}) and peak separation (Δv) are taken

from the VT NMR spectra.[94] The experimental $Fe(CO)_3$ rotational barriers are given

along with values from the DFT study (*vide infra*) in Table III-3. The experimental

$Fe(CO)_3$ rotational barriers for individual $Fe(CO)_3$ units in **NH** are 9.4 and 11.4

kcal/mol, those for **NMe** are 8.0 and 11.0, and those for **NtBu** are 11.0 and 11.2

kcal/mol. The computational data found that the lower energy barrier is that of the

encumbered $Fe(CO)_3$ unit, i.e., the $Fe(CO)_3$ unit positioned under the bridgehead. For

each complex the higher energy barrier is assigned to the unencumbered $Fe(CO)_3$ unit.

For this series the encumbered $Fe(CO)_3$ rotational barrier increases in the order **dmpdt** <

NMe < **NH** < **pdt** < **NtBu**.
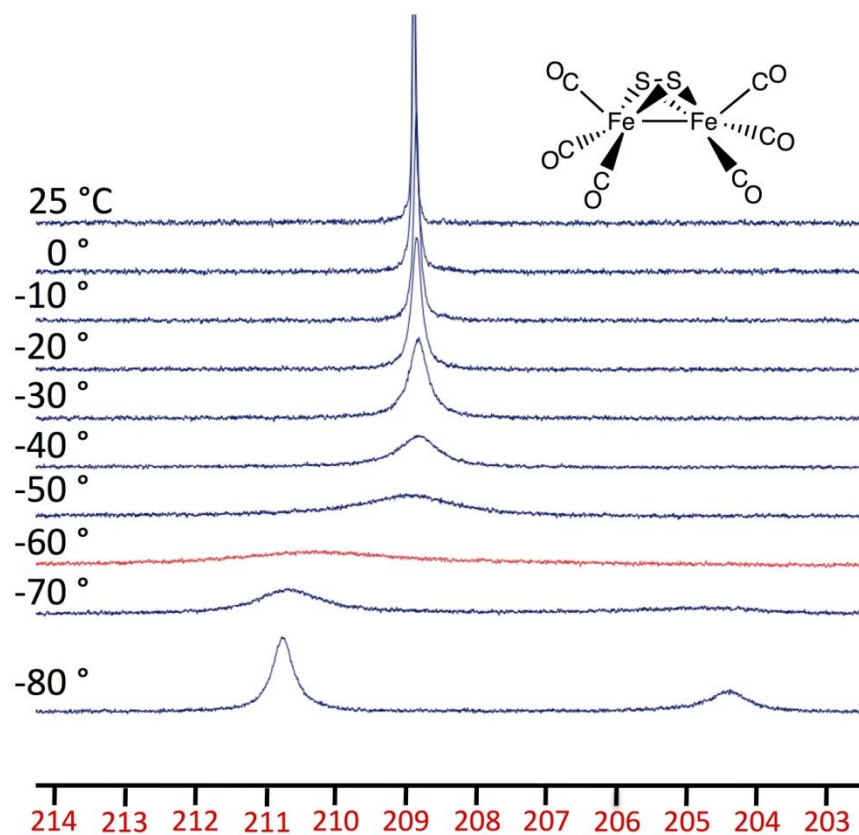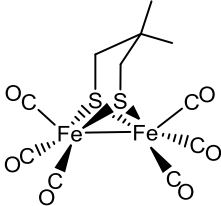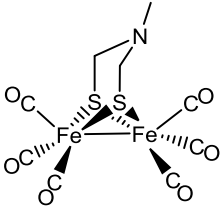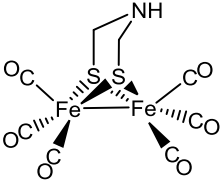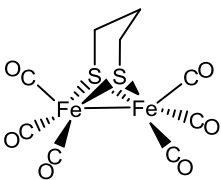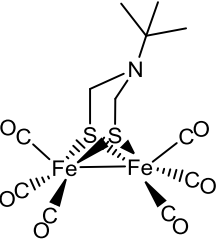
Figure III-9. Variable-temperature ^{13}C NMR spectra of $(\mu\text{-}S_2)[Fe(CO)_3]_2$ at 500 MHz in CDFCl$_2$ in the low-field CO region.

Table III-3. Experimental and computational energy barriers (kcal/mol) for the encumbered $Fe(CO)_3$ unit.

	dmpdt	NMe	NH	pdt	NtBu
Experimental[a]	7.41(±0.24)	7.95(±0.24)	9.36(±0.24)	9.86(±0.24)	11.01(±0.24)
Computational[b]	6.58	6.55[c] /11.43[d]	9.54[c] /15.81[d]	9.61	10.54[d]

[a] Error estimated using ± 5°C for detected coalescence temperature
[b] Computational free energy obtained at coalescence temperature utilizing TPSSTPSS functional
[c] Energy barriers were calculated for the structure with the substituent on the bridgehead nitrogen in the axial position, pointed towards the $Fe(CO)_3$ unit to achieve steric effect similar to dmpdt
[d] Energy barrier was calculated with the substituent in the equatorial position, pointed away the $Fe(CO)_3$ unit

Earlier we found that, in comparison to **pdt,** addition of the bridgehead steric bulk in **dmpdt** lowered the CO site exchange barrier of $Fe(CO)_3$ by stabilizing the rotated form, Table III-3.[49,50] Similar differences are seen in the $Fe(CO)_3$ rotation barrier of the nitrogen bridgehead substituents in complexes **NH** and **NMe**, where the addition of steric bulk of the latter lowered the energy barrier by 1.4 kcal/mol. Assuming an experimental error of $\pm$ 0.24 kcal/mol (based on $\pm$ 5 °C estimate of coalescence temperature), we conclude a steric effect exists for the bridgehead N substituent. This is reasonable, as inversion at the nitrogen has a lower energy barrier than does the chair/boat configurational interchange.[95] The ease of N-inversion is further indicated by the fact that both conformers, Figure III-4 (A) and (A'), are seen in the X-ray crystal structure of **NMe**.[92] Thus, space-filling models in Figure III-4 show similar close contacts of the bridgehead methyl groups in **NMe** (in axial conformation) and **dmpdt**. As the transition state/energy barrier for $Fe(CO)_3$ rotation benefits from (is lowered by) proximate steric bulk, the similarities are rationalized.

Addition of a *tert*-butyl group to the nitrogen in **NtBu**, however, *increases* the energy barrier for $Fe(CO)_3$ rotation compared to **NH**, from 9.4 to 11.0 kcal/mol. Despite the steric bulk of the *tert*-butyl group, it furnishes little steric encumbrance on the $Fe(CO)_3$ unit, at least in the solid state crystal structure Figure III-4 (C). In fact, there is no indication of nitrogen inversion in the **NtBu** complex either by experiment or from computations, as the DFT computational approach could not locate a minimum for the axial isomer shown in Figure III-10. Therefore, an energy barrier could not be found for the $Fe(CO)_3$ rotation which would alleviate steric strain underneath an inverted N-tBu

site. Thus, we conclude that, in the case of the massive *tert*-butyl group, steric encumbrance that might influence the rotational barrier is actually alleviated in comparison to the smaller methyl substituent for which N-inversion is allowed.
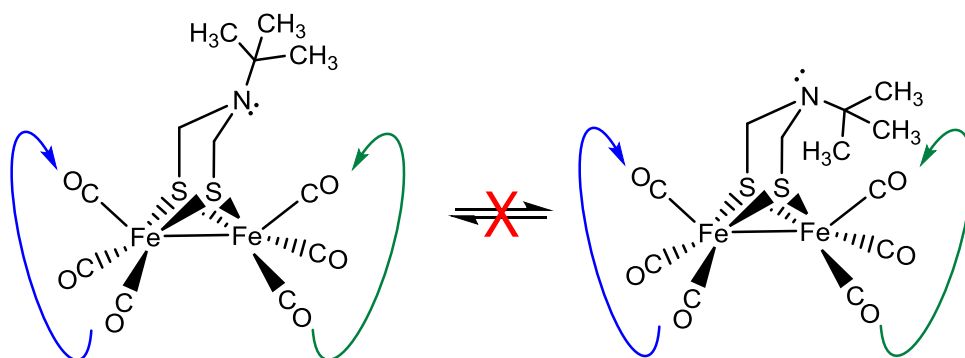
Figure III-10. Equatorial conformer of **NtBu** (left) does not undergo nitrogen inversion to generate the axial conformer (right). The separate $Fe(CO)_3$ units are distinguishable by ^{13}C NMR at low temperature and coalesce at the same rate, Figure III-7.

Electrochemical Studies

Cyclic voltammograms of the $(\mu\text{-SCH}_2\text{XCH}_2\text{S})[Fe(CO)_3]_2$ complexes, X = NR or CR_2, in CH_3CN are remarkably similar with an irreversible oxidative event at ca. +0.7 V and a quasi-reversible reduction at ca. -1.6 V (referenced to Fc/Fc^+ couple = 0.00 V), Figure III-11. This has been reported in several studies.[90,96] While the **NMe** and **NtBu**

complexes show no further reductive events, the carbon-based bridgehead derivatives, X = CH_2 and $C(Me)_2$, show a small event at -2.35 at a scan rate of 100 mV/s in CO-saturated CH_3CN. This event has been assigned by computations to the uptake of a second electron by the intact $(\mu\text{-SRS})[Fe(CO)_3]_2$;[97] however, other possibilities include reduction of a different species arising from CO loss and rearrangement.[96] Regardless of its origin or identity, it is this more negative wave that responds in an electrocatalytic manner to added amounts of HOAc.

.
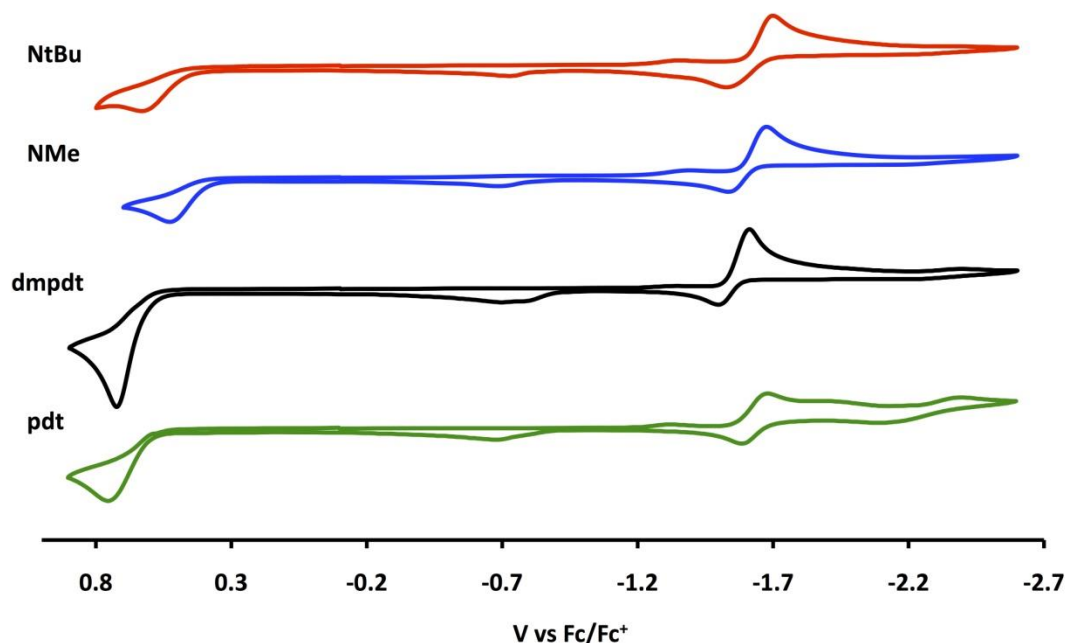
Figure III-11. Cyclic voltammograms of **NtBu** (red), **NMe** (blue), **dmpdt** (black), and **pdt** (green) in CO-saturated CH_3CN solution in the presence of 0.1 M Bu_4NPF_6 at a scan rate of 100 mV/s.

In order to compare the carbon to nitrogen-based bridgehead derivatives, with respect to iron-based protonation, the weak acid, HOAc, was used for electrocatalytic proton reduction. Figure III-12 and Figure III-13 present overlays of the cyclic voltammograms of **pdt**, **dmpdt**, **NH**, **NMe**, and **NtBu** in acetonitrile in the presence of added equivalents of acetic acid, under an Ar atmosphere. The compounds all show a response to acetic acid ca. -1.9 V. Figure III-14 presents overlays of the cyclic voltammograms of **pdt**, **dmpdt**, **NH**, **NMe**, and **NtBu** in acetonitrile in the presence of added equivalents of acetic acid, under a CO atmosphere. The response seen at ca. -1.9 V under an Ar atmosphere is suppressed and a response is seen at ca. -2.3 V.

Figure III-12 (B) and Figure III-14 (B) compare the cyclic voltammograms of **pdt**, under an atmosphere of Ar and CO, respectively. The broad, ill-defined features that build up after the first reductive event, Figure III-13 (A), are largely suppressed under the CO atmosphere, Figure III-14 (B). Under CO, there is a clear definition of the event at -2.3 V which is the electrocatalytic response producing H_2 via an EECC meachanism.[98,99] The species at this event is assumed to represent the two-electron reduced species deriving from $(\mu\text{-pdt})[Fe(CO)_3]_2$. The electrocatalytic activity is 250 mV more positive than the proton reduction of HOAc at the glassy carbon electrode in the absence of the diiron complex.

Figure III-12 (F) and Figure III-14 (F) are analogous to Figure III-12 (B) and Figure III-14 (B), however with the **NMe** complex as solution electrocatalyst for proton reduction. Note that with a CO atmosphere the current response at -1.93 V (under Ar) is

completely suppressed by CO with a sole current response at -2.3 V. The overpotential for both the carbon and nitrogen-based bridgehead complexes is ca. 0.84 V, as the standard potential for reduction of HOAc in CH_3CN is -1.46 and the complexes show a catalytic response at -2.3 V. With HBF_4 as a proton source, protonation of the nitrogen bridgehead results in a positive shift of the reduction potential to -1.2 V. Since the standard potential for reduction of HBF_4 in acetonitrile is -0.28 V, the overpotential for the nitrogen-bridged complexes is ca. 1.0 V, interestingly greater for HBF_4 than HOAc. As mentioned earlier the reduction of H^+ from HBF_4 overlaps with the first reduction of the **pdt** or the **dmpdt** complexes, hence electrocatalytic ability of the carbon bridgehead species can not be assessed using HBF_4.
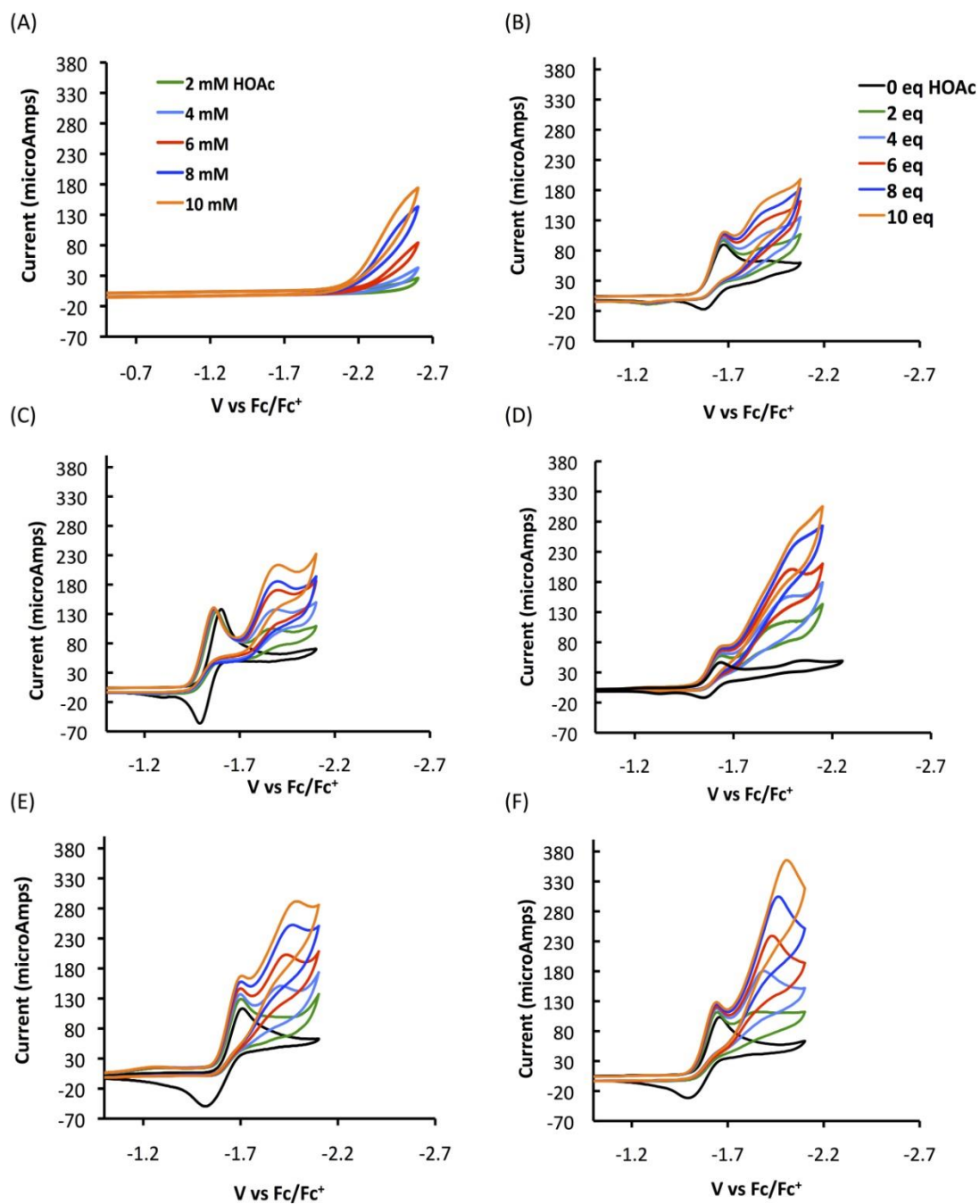
Figure III-12. Cyclic voltammograms in CH$_3$CN in the presence of 0.1 M Bu$_4$NBF$_4$ at a scan rate of 200 mV/s under an Ar atmosphere. Concentration of all samples is 2 mM. (A) Reduction of H$^+$ from glacial acetic acid in the absence of electrocatalyst; (B) **pdt** with equivalents of acetic acid; (C) **dmpdt** with equivalents of acetic acid; (D) **NH** with equivalents of acetic acid; (E) **NtBu** with equivalents of acetic acid; (F) **NMe** with equivalents of acetic acid.
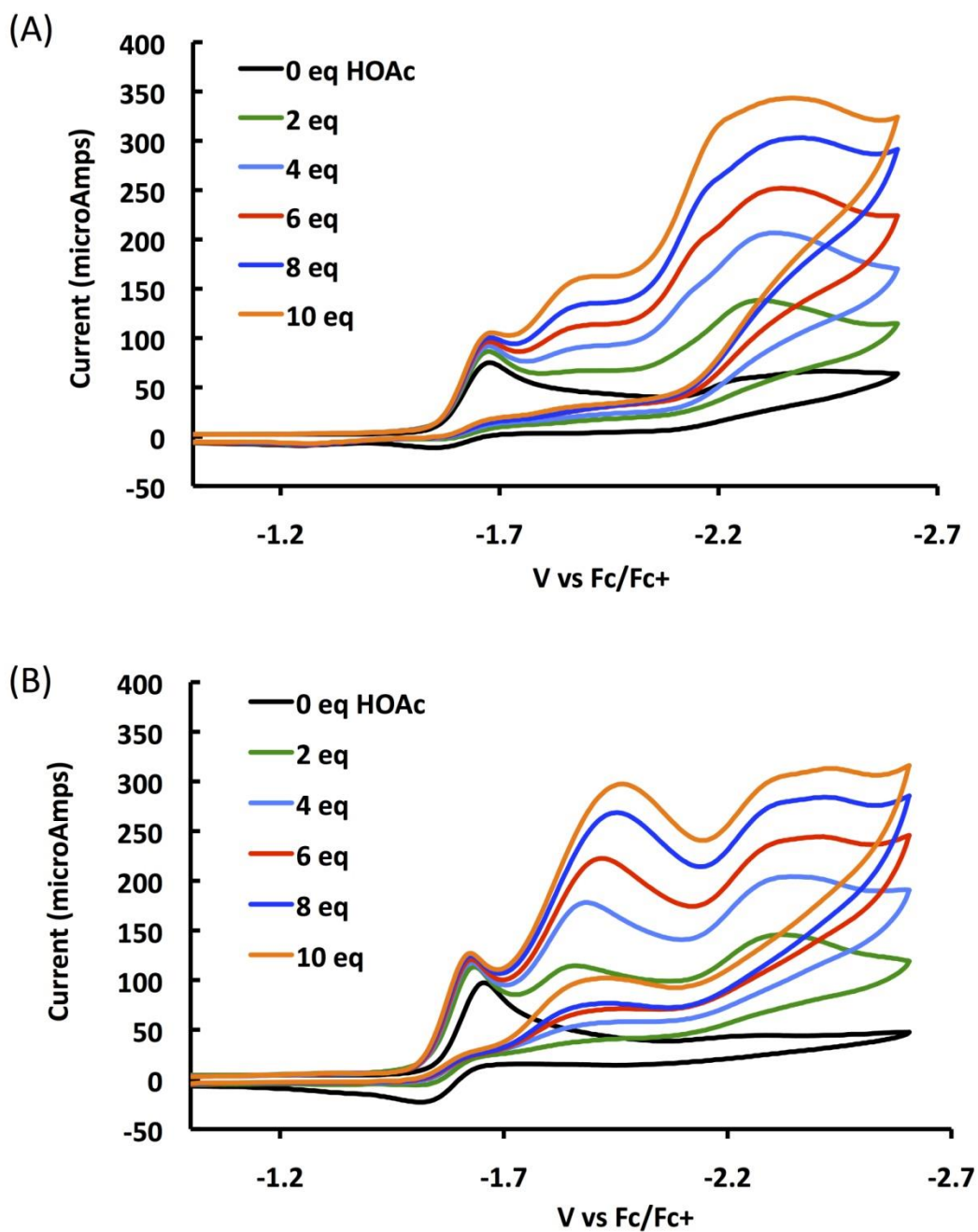
Figure III-13. Cyclic voltammograms in CH_3CN in the presence of 0.1 M Bu_4NBF_4 at a scan rate of 200 mV/s under an Ar atmosphere extended to -2.6 V. Concentration of all samples is 2 mM. (A) **pdt** with equivalents of acetic acid and (B) **NMe** with equivalents of acetic acid.
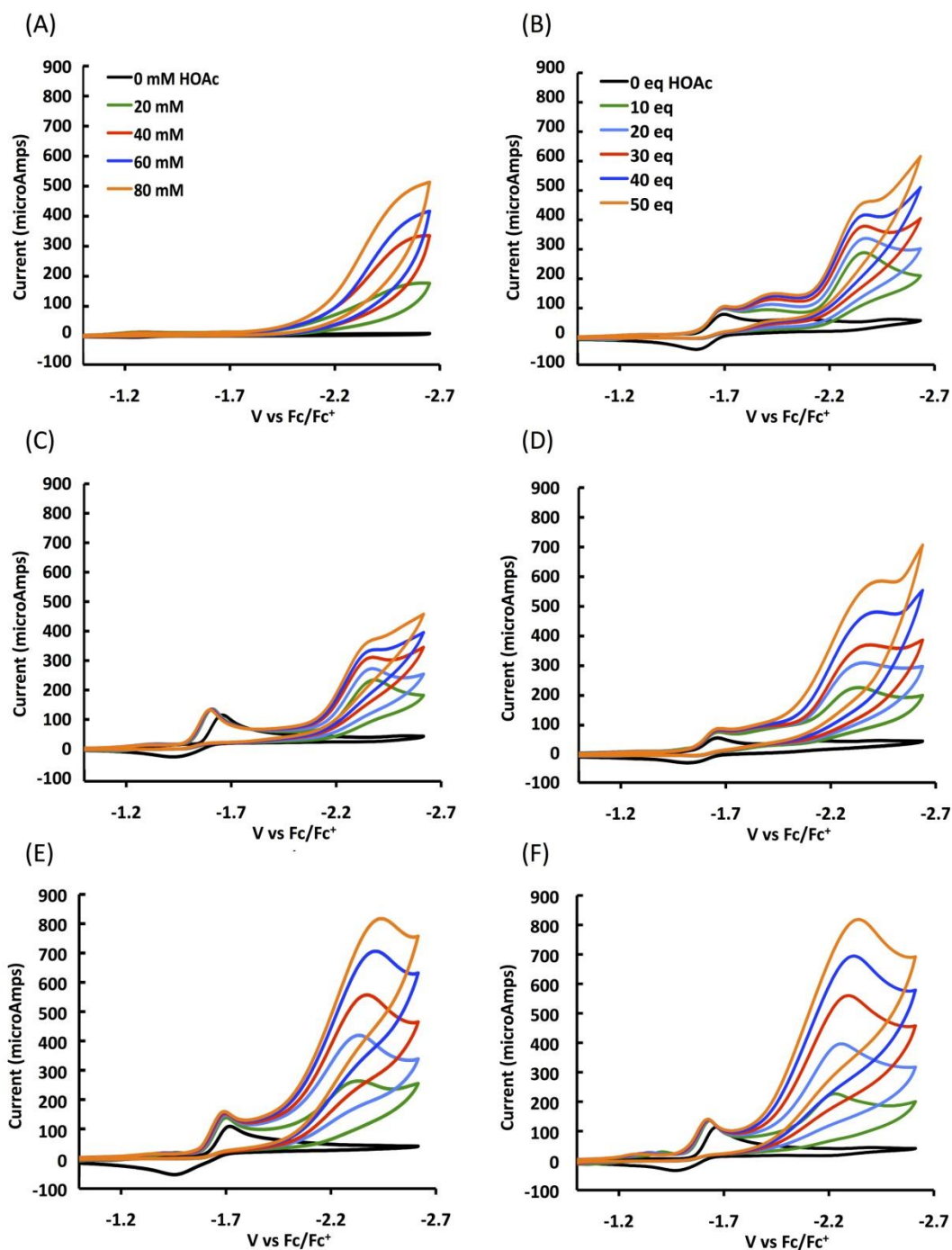
Figure III-14. Cyclic voltammograms in CH_3CN in the presence of 0.1 M Bu_4NBF_4 at a scan rate of 200 mV/s under a CO atmosphere. Concentration of all samples is 2 mM. (A) Reduction of H^+ from glacial acetic acid in the absence of electrocatalyst; (B) **pdt** with equivalents of acetic acid; (C) **dmpdt** with equivalents of acetic acid; (D) **NH** with equivalents of acetic acid; (E) **NtBu** with equivalents of acetic acid; (F) **NMe** with equivalents of acetic acid.

The catalytic response sensitivity, i.e., the increase in current of the complexes to acetic acid, was plotted vs. the [HOAc]/[cat] ratio and the slope taken as a measure of comparative catalytic ability, Figure III-15. Under an Ar atmosphere all there nitrogen bridgehead complexes, **NH**, **NMe**, and **NtBu**, show a two-fold greater response at -1.9 V to acetic acid over the carbon complexes, **pdt** and **dmpdt,** Figure III-14 (A). Under a CO atmosphere the nitrogen bridgehead complexes, **NMe** and **NtBu**, showed about a two-fold greater response at -2.3 V to the weak HOAc proton source in CH_3CN over that of the **pdt** or **dmpdt** analogs, while the **NH** complex showed only a 1.5 fold greater response. Unlike electrocatalysts, such as the $[Ni(P^R_2N^{R'})_2]^{2+}$ with pendent bases built into the PNP ligand, addition of small amounts of water (up to 10 equivalents) had no effect on the catalytic wave position or response to added acid, Figure III-16.[100] This is attributed to greater hydrophobicity of the $(\mu\text{-SRS})[Fe(CO)_3]_2$.
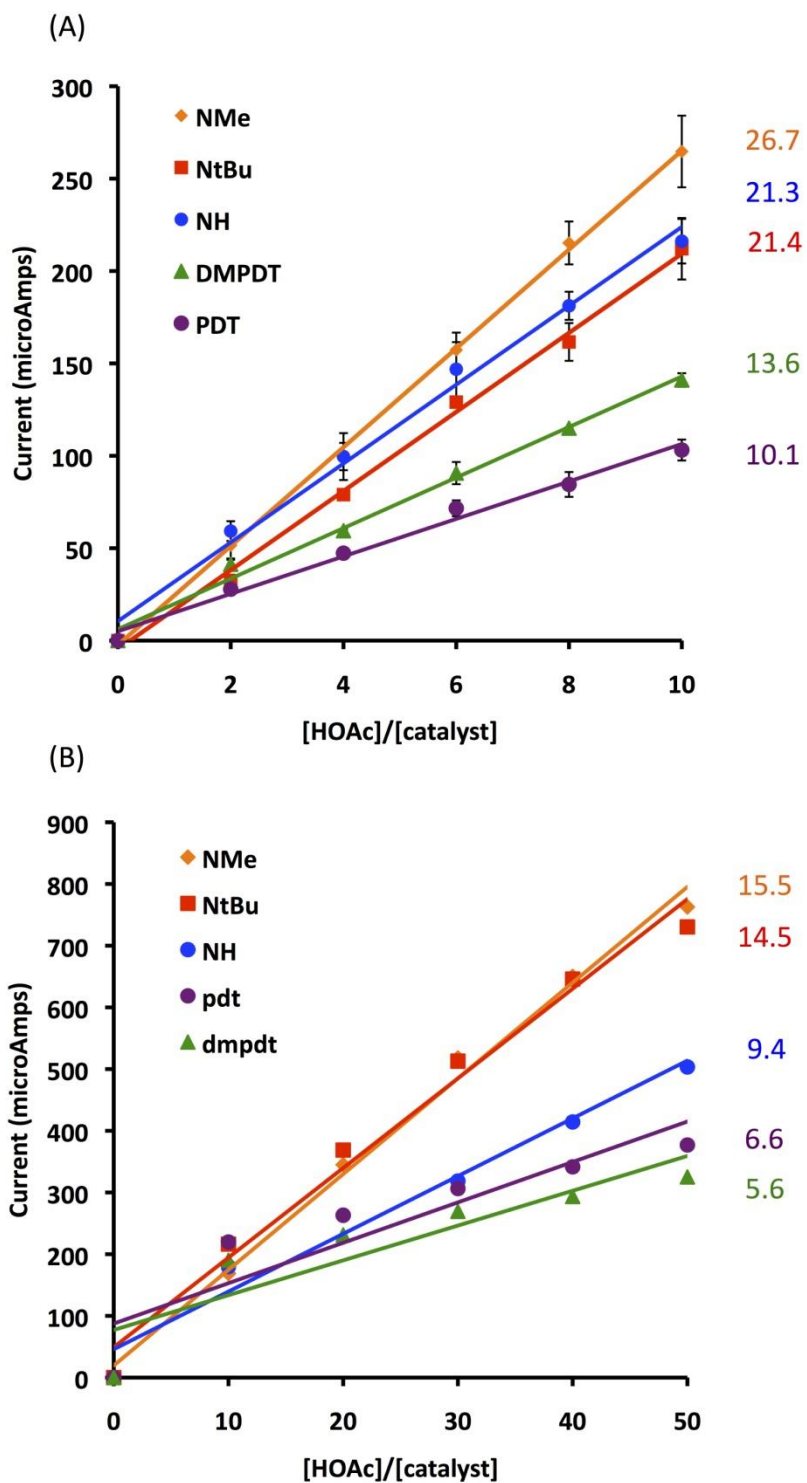
Figure III-15. Dependence of current heights of electrocatalytic waves for hexacarbonyl complexes (2 mM) on acid concentration (A) in Ar-saturated CH_3CN and (B) in CO-saturated CH_3CN.
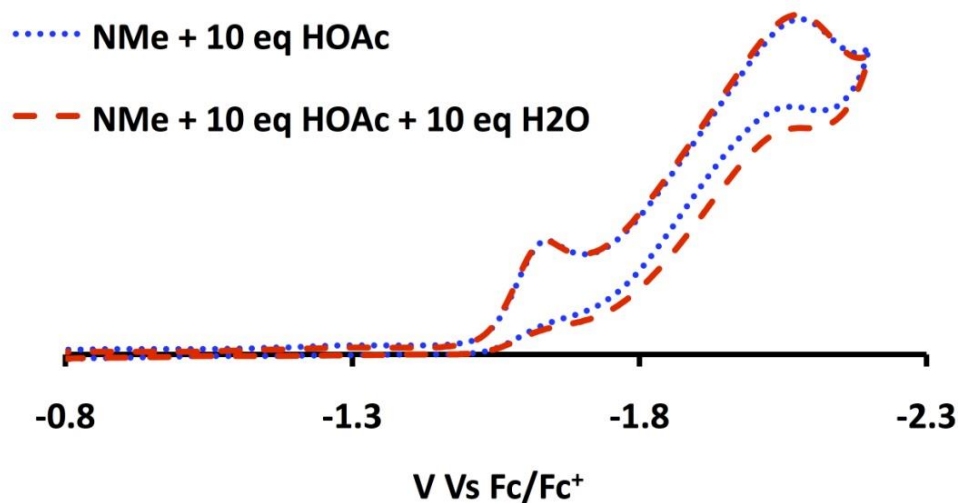
Figure III-16. Cyclic voltammogram of **NMe** at a scan rate of 200 mV/s with additions of acetic acid and water**.**

Conclusion

Our study finds that while steric hindrance at the bridgehead position of (μ-SCH$_2$XCH$_2$S)[Fe(CO)$_3$]$_2$ enhances Fe(CO)$_3$ rotation thus making the electron density within the Fe-Fe bond more accessible to oxidative addition of a proton, there is no evidence that this feature enhances proton uptake as assigned by electrochemical response to added HOAc in the aprotic CH$_3$CN solvent. The catalytic response varies as listed in Chart 1, with the three azadithiolates used in this study superior to both of the carbon bridgehead complexes. Hence we are led to the conclusion that the mobility of the Fe(CO)$_3$ unit, as influenced by the bridgehead substituent, has no effect on the proton uptake/electrochemical process when using a weak acid.

Catalytic response: **NMe ≥ NtBu > NH > pdt ≥ dmpdt**

Rotational barrier: **dmpdt < NMe < NH < pdt < NtBu**

Figure III-17. Chart showing the order of catalytic response and rotational energy barrier for compounds **NMe**, **NtBu**, **NH**, **pdt**, and **dmpdt**.

The question of whether there is a steric effect caused by substituents on the pyramidal nitrogen is answered in the affirmative according to the VT NMR studies, the experimental and computational barrier to $Fe(CO)_3$ rotation, and the computational barrier for N-inversion. The low barrier to N-inversion generates a similar steric effect in the **NMe** as is found for the **dmpdt**, $C(CH_3)_2$, bridgehead. Notably the **NtBu** bridgehead, with a large barrier to inversion, leads to a small steric encumbrance at the adjacent $Fe(CO)_3$ unit and in our study, the largest barrier to $Fe(CO)_3$ rotation. That is, steric bulk at the bridgehead of the S to S linker interfering with the apical carbonyl of the $Fe(CO)_3$ unit underneath that bridgehead, see Figure 4, lowers the barrier to the rotated structure. The possibility of isolating this "rotated" isomer of the $(\mu\text{-SRS})[Fe(CO)_3]_2$ with only bridgehead effects becomes closer on consideration of the $(\mu\text{-} SCH_2N(CH_2C_6H_5)CH_2S)[Fe^I(CO)_3][Fe^I(CO)dmpe]$ complex of Zampella et al.[58]

The subtle effects seen for the $(\mu\text{-SRS})[Fe(CO)_3]_2$ complexes are small in comparison to the huge effect observed for the different bridgehead atoms in the hybrid enzymes comprised of $(\mu\text{-SCH}_2XCH_2S)[Fe(CO)_2CN]_2^{2-}$, where only the X = NH yields functional H_2-production catalysts when inserted into the protein matrix.[15,16] In nature,

the steric assist from protein residues in close proximity constitute a third coordination sphere effect. We conclude that the deceptively simple diiron hexacarbonyls as models of the [FeFe]-H$_2$ase active site continue to provide fundamental information regarding the manifold of processes available to the dithiolate-bridged unit, that are certainly of significance to nature's evolved choice of this unit for hydrogen production catalysis. To enhance functionality in man-made catalysts, such studies must be coupled with development of host materials providing outer coordination sphere interactions analogous to the protein.

CHAPTER IV

LIGAND MODIFIED AZADITHIOLATE [FeFe]-HYDROGENASE ENZYME

ACTIVE SITE MODELS

Introduction

An important feature of the $(\mu\text{-SRS})[Fe(CO)_3]_2$ complexes is the ability to be modified through the dithiolate bridgehead and CO/L ligand substitution. The route for CO substitution for a new ligand depends on the type of incoming ligand and the degree of substitution desired. In general, monosubstitution occurs with one to two equivalents of the new ligand to the hexacarbonyl parent complex under conditions involving elevated temperatures, photolysis, or the aid of a CO labilizing agent, usually trimethylamine N-oxide. Disubstitution of the hexacarbonyl starting materials normally occurs with excess ligand at elevated temperatures. Typically disubstitution for PR_3 and CN^- occurs on different irons and only with bidentate ligands, such as diphenylphosphinoethane, dppe, are two phosphine donors placed on a single metal. Higher degrees of substitution can take place through photolysis of the hexacarbonyl starting material in the presence of excess ligand, for example $(\mu\text{-edt})[Fe(CO)(PMe_3)_2]_2$.[101] There are several conformational isomers possible for monosubstituted and disubstituted complexes, which depend on the donor strength and size of the ligand, Figure IV-1. A large range of ligands have been reported, such as

phosphines, cyanide, amines, carbenes, etc, with a variety of dithiolate bridgehead modifications.[90]
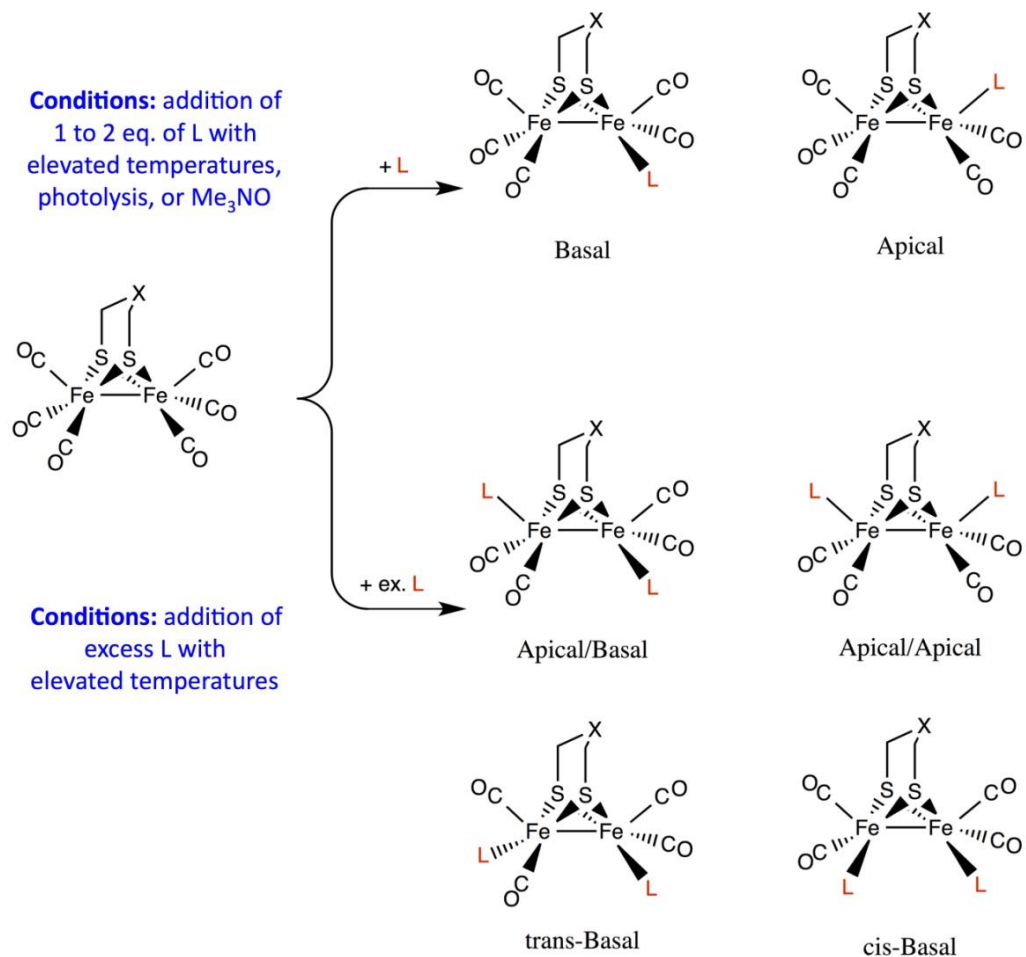
Figure IV-1. Conditions and possible conformational isomers for mono and di-substituted complexes.

Protonation of the substituted complexes has been under investigation for decades to determine the ability of the model complexes to undergo proton reduction via

the formation of a terminal hydride, propsoed in the mechanism of the [FeFe]-H$_2$ase.[12] Direct protonation at the 2Fe core in the Fe^{I}Fe^I model complexes with carbon in the S to S linker, -SCH$_2$C(R)CH$_2$S-, is limited to complexes that are disubstituted or have higher degrees of substitution with ligands that are strongly electron donating. The hexacarbonyl and monosubstituted complexes exhibit no signs of reaction under acidic conditions in most cases. The exceptions to this are complexes containing a basic site in the substituent ligands, such as the nitrogen in CN$^-$ and PTA.[99,102] However, the azadithiolate complexes, containing a basic site in the dithiolate linker (-SCH$_2$N(R)CH$_2$S-), exhibit both nitrogen protonation and, when suitably electron rich through strong donor ligands, protonation at the Fe-Fe bond.[103-106]

The photolability of CO on the hexacarbonyl complexes has led to many studies investigating the binding of weak and strong donor ligands.[107-112] It is known that (μ-pdt)[Fe(CO)$_3$]$_2$ undergoes photolysis, losing CO and leaving an open site capable of binding various substrates.[113] A study by the Bengali laboratory at TAMU-Qatar, utilizing time-resolved infrared spectroscopy (TRIR), analyzed the solution photochemistry of (μ-pdt)[Fe(CO)$_3$]$_2$, (μ-pdt = μ-S(CH$_2$)$_3$S), in the presence of weakly binding ligands, such as cyclohexene, THF, 3-hexyne, and dihydrofuran.[113] It was concluded that subsequent ligand substitution of the weakly bound ligands by pyridine or cyclooctene occurs via a dissociative mechanism and affords a more stable complex. Due to the fact that the [FeFe]-H$_2$ase active site has been determined to contain an azadithiolate linker (-SCH$_2$NHCH$_2$S-), a series of ligand substituted azadithiolate complexes were synthesized and characterized by the author so that the photochemistry

could be investigated in TAMU-Qatar in order to determine the effect of nitrogen in the bridgehead.

This chapter will be divided into three sections: 1) PR$_3$ monosubstituted azadithiolate complexes, 2) disubstituted PMe$_3$ azadithiolate complexes, and 3) protonation of the bis-PMe$_3$ azadithiolate complexes. Each section will discuss the synthesis and characterizations of the complexes. This chapter reports 9 new solid state structures whose XRD was performed by Jason Denny.

Synthesis of Monosubstituted Phosphine Complexes

Various mono-substituted phosphine complexes were obtained through the treatment of the (μ-SCH$_2$N(R)CH$_2$S)[Fe(CO)$_3$]$_2$ starting materials, (μ-SCH$_2$N(Me)CH$_2$S)[Fe(CO)$_3$]$_2$ (**NMe**), (μ-SCH$_2$N(^{t}Bu)CH$_2$S)[Fe(CO)$_3$] (**NtBu**), and (μ-SCH$_2$N(Ph)CH$_2$S)[Fe(CO)$_3$] (**NPh**), with one equivalent of Me$_3$NO followed by addition of the P-donor ligand, P(OMe)$_3$, PPh$_3$, or PTA (phosphatriazaadamantane), Figure IV-2. All of the mono-substituted complexes are obtained as air-stable red solids in moderate yields (30-40%). ^{1}H-NMR analysis of the complexes shows two signals for the methylene protons in the dithiolate linker of the mono-phosphine complexes, resulting from the loss of symmetry between the two irons upon substitution of a single CO.

The ν(CO) infrared stretching frequencies of the monosubstituted phosphine complexes are presented in Table IV-1. As expected from π–backbonding arguments, the ν(CO) IR bands of the hexacarbonyl precursors shift by ca. 30 cm^{-1} to lower wave numbers upon substitution of a CO ligand, indicating that one CO ligand has been

replaced by a stronger donor. The slightly stronger electron-donating ability of PTA relative to the PPh$_3$ and P(OMe)$_3$ ligands is shown by the lower v(CO) IR values. The intensity patterns seen for the monosubstituted complexes vary slightly due to the ligand arrangement, apical vs. basal, on the irons, Figure IV-1.
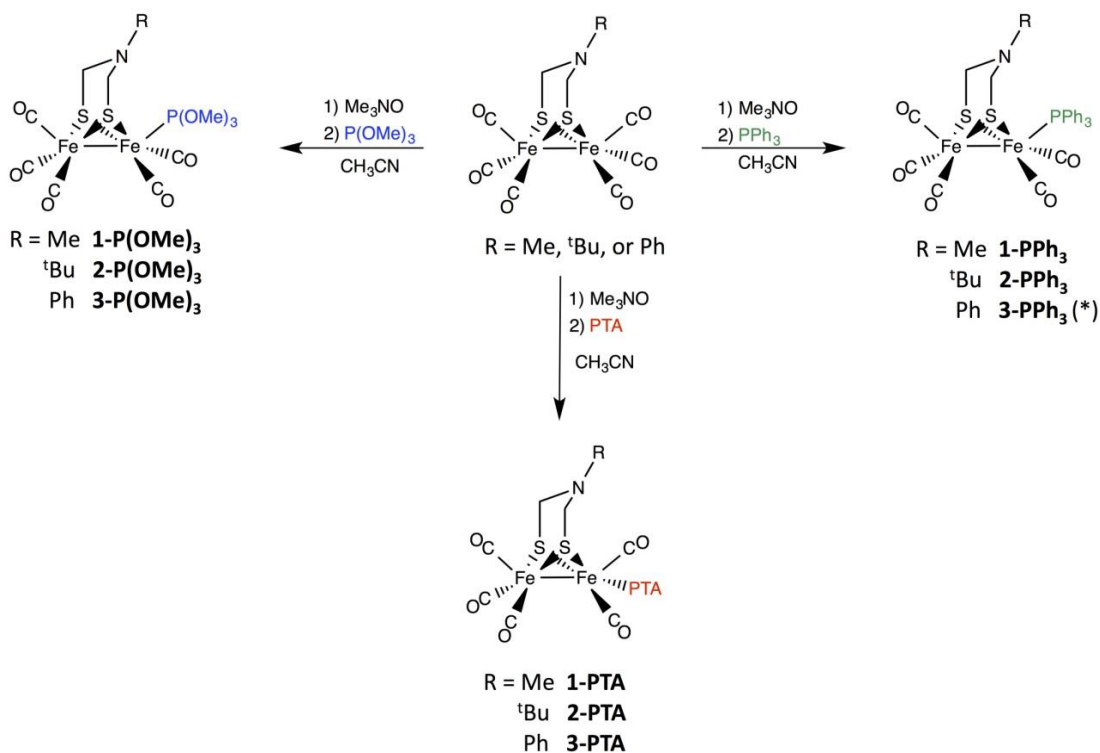
Figure IV-2. Synthesis of monosubstituted phosphine derivatives of azadithiolate model complexes. * Previously synthesized.[114]

Table IV-1. ν(CO) stretching frequencies for the monosubstituted phosphine complexes.

Complex	ν(CO) cm^{-1}[a]
(μ-SCH$_2$N(Me)CH$_2$S)[Fe(CO)$_3$][Fe(CO)$_2$PPh$_3$], **1-PPh$_3$**	2044(s); 1986(s); 1974(sh); 1935(w)
(μ-SCH$_2$N(^{t}Bu)CH$_2$S)[Fe(CO)$_3$][Fe(CO)$_2$PPh$_3$], **2-PPh$_3$**	2042(m); 1986(s); 1969(m); 1933(w)
(μ-SCH$_2$N(Ph)CH$_2$S)[Fe(CO)$_3$][Fe(CO)$_2$PPh$_3$], **3-PPh$_3$**	2046(s); 1990(s); 1974(m); 1934(w)
(μ-SCH$_2$N(Me)CH$_2$S)[Fe(CO)$_3$][Fe(CO)$_2$PTA], **1-PTA**	2039(s); 1983(s); 1962(sh); 1926(w)
(μ-SCH$_2$N(^{t}Bu)CH$_2$S)[Fe(CO)$_3$][Fe(CO)$_2$PTA], **2-PTA**	2044(w); 1984(s); 1970(m); 1927(w)
(μ-SCH$_2$N(Ph)CH$_2$S)[Fe(CO)$_3$][Fe(CO)$_2$PTA], **3-PTA**	2039(m); 1985(s); 1968(m); 1927(w)
(μ-SCH$_2$N(Me)CH$_2$S)[Fe(CO)$_3$][Fe(CO)$_2$P(OMe)$_3$], **1-P(OMe)$_3$**	2048(m); 1994(s); 1970(m); 1937(w)
(μ-SCH$_2$N(^{t}Bu)CH$_2$S)[Fe(CO)$_3$][Fe(CO)$_2$P(OMe)$_3$], **2-P(OMe)$_3$**	2047(m); 1991(s); 1968(m); 1932(w)
(μ-SCH$_2$N(Ph)CH$_2$S)[Fe(CO)$_3$][Fe(CO)$_2$P(OMe)$_3$], **3-P(OMe)$_3$**	2045(m); 1993(s); 1969(m); 1938(w)

[a] IR spectra obtained in CH$_3$CN.

78

X-ray Diffraction Studies of Monosubstituted Phosphine Complexes

The monosubstituted phosphine complexes, **1-PPh₃**, **2-PPh₃**, **2-PTA**, **2-P(OMe)₃**, and **3-PTA**, were crystallized through slow diffusion of ether into a CH_2Cl_2 solution. The crystals were subjected to X-ray diffraction analysis and the resultant structures are shown in Figure IV-3 and IV-4; Table IV-3 lists selected metric parameters. Despite repeated attempts, crystals of X-ray quality were not obtained for the **1-PTA**, **1-P(OMe)₃**, and **3-P(OMe)₃** complexes. The **3-PPh₃** complex was previously crystallized and the metric parameters are listed in Table IV-3 for comparison.[114]

The molecular structures of all the azadithiolate complexes show a pyramidal nitrogen in the bridgehead except for **3-PPh₃** which contains a planar nitrogen. The overall structures of the mono-substituted complexes, edge-bridged square pyramids, are similar to their $(\mu\text{-SRS})[Fe(CO)_3]_2$ precursors with the Fe---Fe distances within bonding range. Notably the PTA derivatives have slightly longer Fe-Fe distances.

The PPh₃ ligand in **1-PPh₃**, **2-PPh₃**, and **3-PPh₃** occupies the apical rather than basal position as was found for $(\mu\text{-pdt})[Fe(CO)_3][Fe(CO)_2PPh_3]$ and $(\mu\text{-dmpdt})[Fe(CO)_3][Fe(CO)_2PPh_3]$.[50] The bridgehead N of the FeS_2C_2N ring of **1-PPh₃** is oriented towards the $Fe(CO)_2PPh_3$ unit as also seen in $(\mu\text{-pdt})[Fe(CO)_3][Fe(CO)_2PPh_3]$. In contrast, in the solid state the bridgehead N of **2-PPh₃** and **3-PPh₃** is oriented away from the $Fe(CO)_2PPh_3$ unit and towards the $Fe(CO)_3$ unit as was seen for $(\mu\text{-dmpdt})[Fe(CO)_3][Fe(CO)_2PPh_3]$.[50] The structural arrangement of **2-PPh₃** is also observed for **2-P(OMe)₃**, where the P(OMe)₃ ligand adopts an apical position and the

bridgehead N points towards the $Fe(CO)_3$ unit. The PTA ligand in **2-PTA** and **3-PTA** adopts a basal position, also seen for $(\mu\text{-pdt})[Fe(CO)_3][Fe(CO)_2PTA]$ and $(\mu\text{-depdt})[Fe(CO)_3][Fe(CO)_2PTA]$.[50,99] Similar to **2-PPh₃** and **2-P(OMe)₃**, the bridgehead N in **2-PTA** points away from the $Fe(CO)_2PTA$ unit. The bridgehead N in **3-PTA** points toward the $Fe(CO)_2L$ unit, as seen in $(\mu\text{-pdt})[Fe(CO)_3][Fe(CO)_2PTA]$ and $(\mu\text{-depdt})[Fe(CO)_3][Fe(CO)_2PTA]$.[50,99]

The torsion angle, C_{ap}-Fe-Fe-L_{ap}, between the $Fe(CO)_3$ and $Fe(CO)_2L_{ap}$ (L = CO, PPh₃, and P(OMe)₃) units on the monosubstituted complexes varies, Figure IV-4. The PPh₃ substituted complexes show an increase in torsion angle compared to the analogous hexacarbonyl precursors. The increase of 20° in the torsion angle for **1-PPh₃** and **3-PPh₃** could be due to the bridgehead pointing towards the $Fe(CO)_2PPh_3$ unit adding steric pressure to the unit. The steric influence of the N-phenyl group on **3-PTA** also leads to an increase in torsion angle, 10°. However, only a slight increase, ca. 5°, in torsion angle is observed for all the *tert*-butyl bridgehead substituted complexes, **2-PPh₃**, **2-PTA**, and **2-P(OMe)₃**. The orientation of the *tert*-butyl group, as well as the bridgehead pointing away from the apical phosphines likely accounts for the lack of steric influence from the bridgehead.
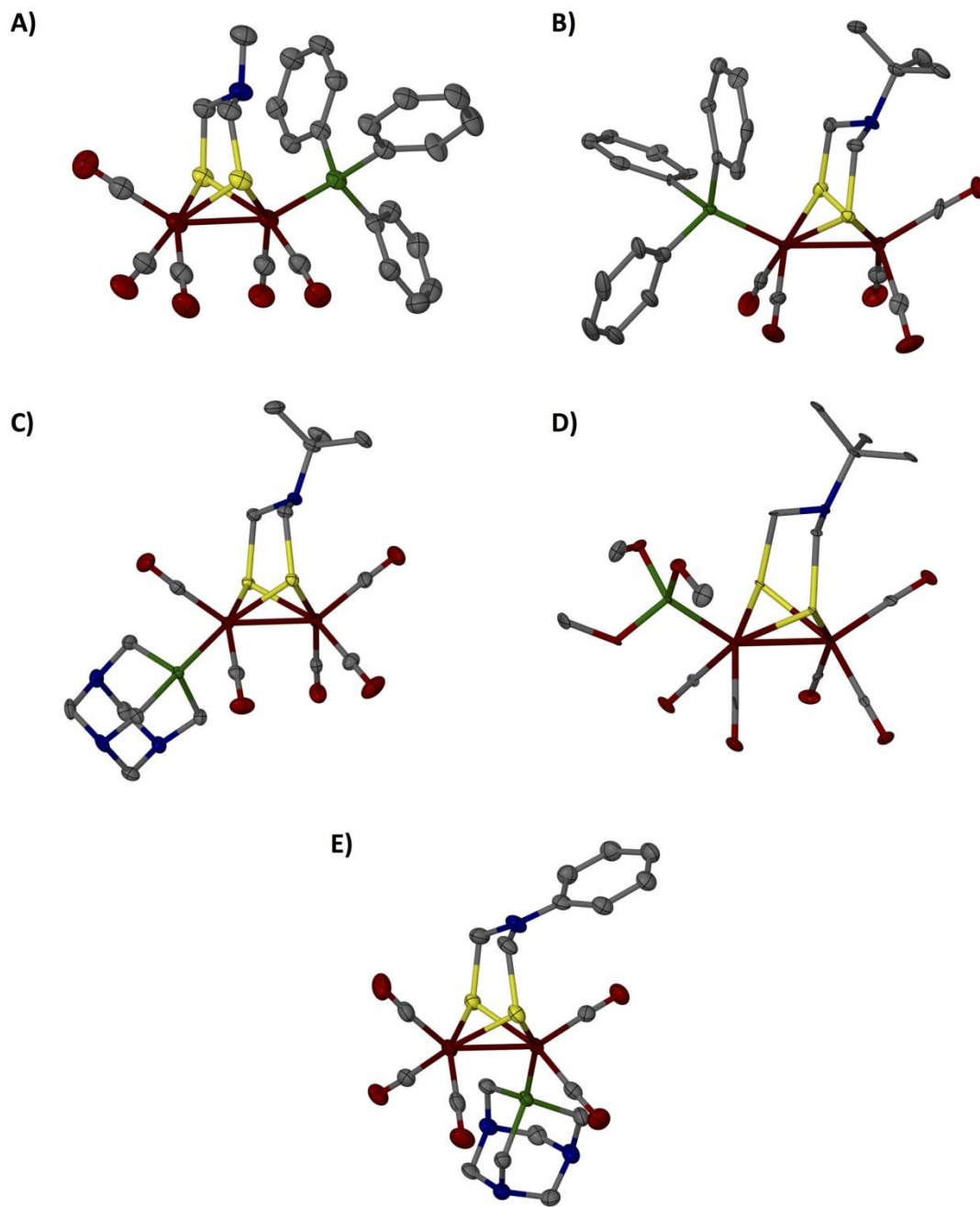
Figure IV-3. Structures of A) **1-PPh₃**, B) **2-PPh₃**, C) **2-PTA**, D) **2-P(OMe)₃,** and E) **3-PTA** with thermal ellipsoids drawn at 50% probability level. Selected metric parameters listed in Table IV-2.
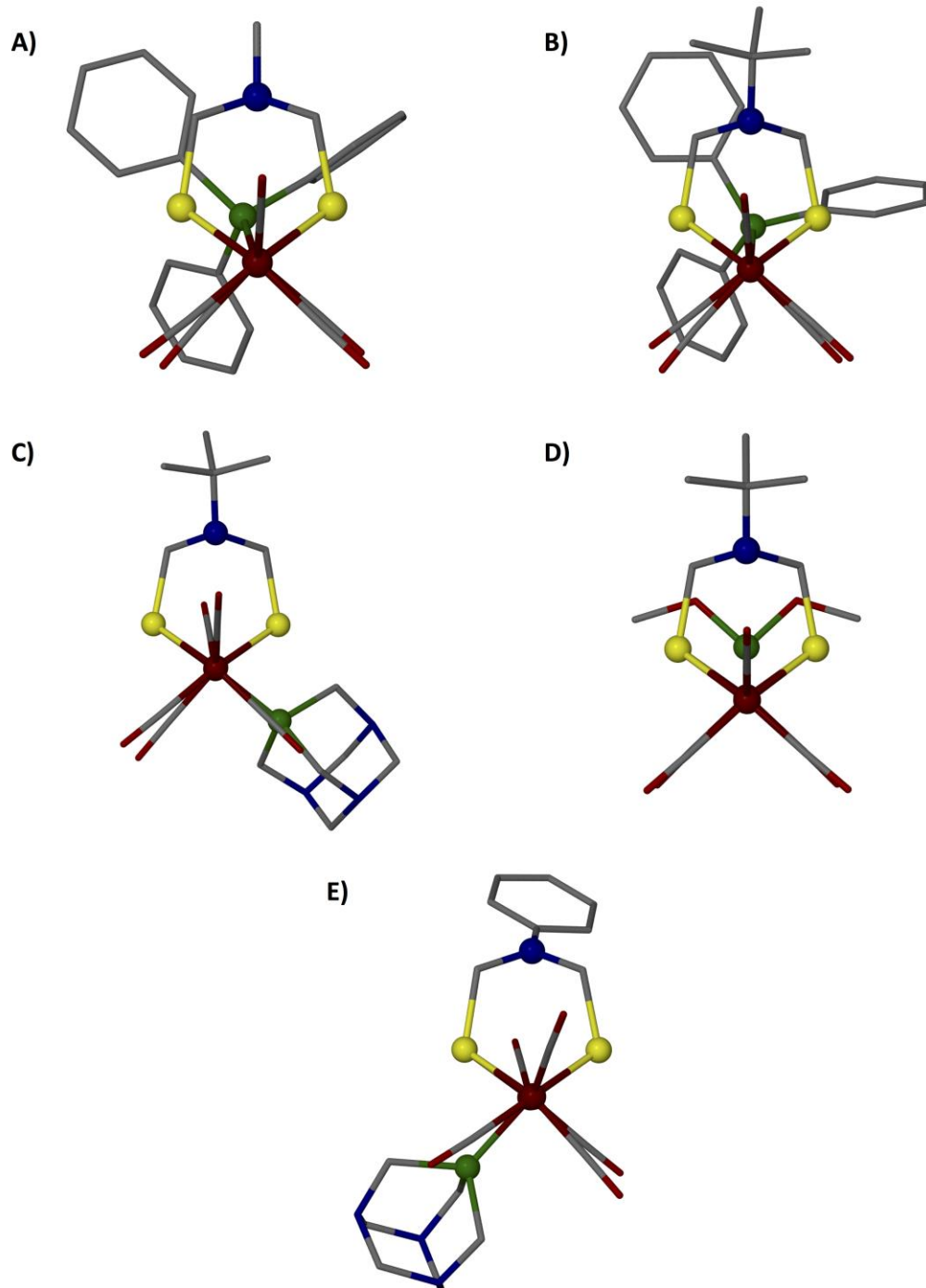
Figure IV-4. Ball and stick representation of the X-ray determined structure viewed along the FeFe bond vector of A) **1-PPh₃**, B) **2-PPh₃**, C) **2-PTA**, D) **2-P(OMe)₃**, and E) **3-PTA**.

Table IV-2. Metric parameters of (μ-S(CH$_2$XCH$_2$S)[Fe(CO)$_3$][Fe(CO)$_2$L] (X = CH$_2$, C(CH$_3$)$_2$, NMe, NtBu, or NPh; L = PPh$_3$, PTA, or P(OMe)$_3$)

Complex	Fe-Fe (Å)	Flap Angle (°)[a]	Torsion (°)[b]	C/N--Fe (Å)[c]
(μ-pdt)[Fe(CO)$_3$][Fe(CO)$_2$PPh$_3$][50]	2.5247(7)	133.82	9.3(3)	3.61
(μ-dmpdt)[Fe(CO)$_3$][Fe(CO)$_2$PPh$_3$][50]	2.498(1)	138.72	9.7(6)	-
(μ-SCH$_2$N(Me)CH$_2$S)[Fe(CO)$_3$][Fe(CO)$_2$PPh$_3$], **1-PPh$_3$**	2.523(1)	120.58	19.0(4)	3.42
(μ-SCH$_2$N(^{t}Bu)CH$_2$S)[Fe(CO)$_3$][Fe(CO)$_2$PPh$_3$], **2-PPh$_3$**	2.513(2)	117.88	10.7(8)	3.25
(μ-SCH$_2$N(Ph)CH$_2$S)[Fe(CO)$_3$][Fe(CO)$_2$PPh$_3$], **3-PPh$_3$**[114]	2.502(1)	122.37	40.1(3)	3.41
(μ-SCH$_2$N(^{t}Bu)CH$_2$S)[Fe(CO)$_3$][Fe(CO)$_2$P(OMe)$_3$], **2-P(OMe)$_3$**	2.5225(9)	116.63	0.0(3)	3.26
(μ-pdt)[Fe(CO)$_3$][Fe(CO)$_2$PTA][50]	2.542(2)	123.66	6(1)	3.45
(μ-SCH$_2$N(^{t}Bu)CH$_2$S)[Fe(CO)$_3$][Fe(CO)$_2$PTA], **2-PTA**	2.5635(7)	119.17	9.2(2)	3.30
(μ-SCH$_2$N(Ph)CH$_2$S)[Fe(CO)$_3$][Fe(CO)$_2$PTA], **3-PTA**	2.5518(8)	123.56	30.1(4)	3.42

[a] Refers to the dihedral angle formed through the intersection of the XC$_2$ (X = C or N) and C$_2$S$_2$ planes in the FeS$_2$C$_2$X ring.
[b] Refers to the CO$_{ap}$-Fe-Fe -CO$_{ap'}$ angle.
[c] The distance from the central ato in the bridehead (C or N) to the closest iron.

Electrochemical Studies of Monosubstituted Phosphine Complexes

Cyclic voltammograms of the monosubstituted phosphine complexes in CH_3CN solution display similar events to each other as well as the $(\mu$-pdt$)[Fe(CO)_3][Fe(CO)_2L]$ derivatives, with an irreversible oxidative event in the range of $+0.16$ to $+0.34$ V and an irreversible reduction at ca. -1.9 V, Table IV-3. Based on previously reported $(\mu$-pdt$)[Fe(CO)_3][Fe(CO)_2L]$ derivatives, the irreversible reduction event is assigned to $Fe^I Fe^I \rightarrow Fe^I Fe^0$.[50,98] The electrochemical data for the phosphine substituted complexes show a ca. 200 mV shift to more negative potentials for the irreversible $Fe^I Fe^I / Fe^0 Fe^I$ reduction as compared to the hexacarbonyl precursors. This is consistent with substitution of CO with a more electron donating ligand. As expected, due to the slightly poorer donor ability of PPh_3 over PTA, the PTA complexes have a ca. 40 mV cathodic shift of the irreversible reduction compared to the PPh_3 complexes.

Table IV-3. Electrochemical potentials of monosubstituted complexes.

Complex	E_{pc} $E_1 : Fe^I Fe^I \rightarrow Fe^0 Fe^I$	E_{pa} $Fe^I Fe^I \rightarrow Fe^{II} Fe^I$
1-PPh$_3$[a]	-1.84	+0.22
2-PPh$_3$[a]	-1.88	+0.30
3-PPh$_3$[a]	-1.83	+0.31
1-PTA[a]	-1.90	+0.18
2-PTA[a]	-1.91	+0.16
3-PTA[a]	-1.87	+0.25

[a] Ar deaerated CH_3CN solution (0.1 M $^nBu_4NPF_6$). All experiments were recorded using a glassy carbon working electrode (A = 0.071 cm^2) referenced to Cp_2Fe/Cp_2Fe^+ as an internal standard and a Pt counter electrode at a scan rate of 100 mV/s.

Synthesis of Disubstituted (μ-SCH$_2$N(R)CH$_2$S)[Fe(CO)$_2$PMe$_3$]$_2$ Complexes

The reaction of (μ-SCH$_2$N(R)CH$_2$S)[Fe(CO)$_3$]$_2$, R = Me, ^{t}Bu, or Ph, with excess PMe$_3$ in toluene at 100 °C for 0.5 − 1.5 h gives the disubstituted complexes **1-[PMe$_3$]$_2$**, **2-[PMe$_3$]$_2$**, and **3-[PMe$_3$]$_2$** in ~60 % yield, Figure IV-5. Unlike the monosubstituted complexes, the bis-PMe$_3$ complexes degrade rapidly when exposed to air. The ^{1}H NMR spectrum of the complexes show one signal for the methylene protons in the dithiolate linker indicating that each iron has one phosphine and that the bridgehead is undergoing fast chair/boat interconversion at room temperature.

The time required to fully convert the hexacarbonyl complex to the bis-PMe$_3$ complex is dependent on the hexacarbonyl precursor. The carbon bridgehead analogues,

(μ-pdt)[Fe(CO)$_2$PMe$_3$]$_2$ and (μ-dmpdt)[Fe(CO)$_2$ PMe$_3$]$_2$, have reaction times of 4 hr and 48 h, respectively.[57,98] However, the reaction time for (μ-SCH$_2$N(^{t}Bu)CH$_2$S)[Fe(CO)$_2$PMe$_3$]$_2$, **2-[PMe$_3$]$_2$**, and (μ-SCH$_2$N(Ph)CH$_2$S)[Fe(CO)$_2$PMe$_3$]$_{22}$, **3-[PMe$_3$]$_2$**, is 1.5 h. The (μ-SCH$_2$N(Me)CH$_2$S)[Fe(CO)$_3$]$_2$ complex completely converts to the bis-PMe$_3$ complex, (μ-SCH$_2$N(Me)CH$_2$S)[Fe(CO)$_2$PMe$_3$]$_2$ **(1-[PMe$_3$]$_2$)**, in 0.5 h.
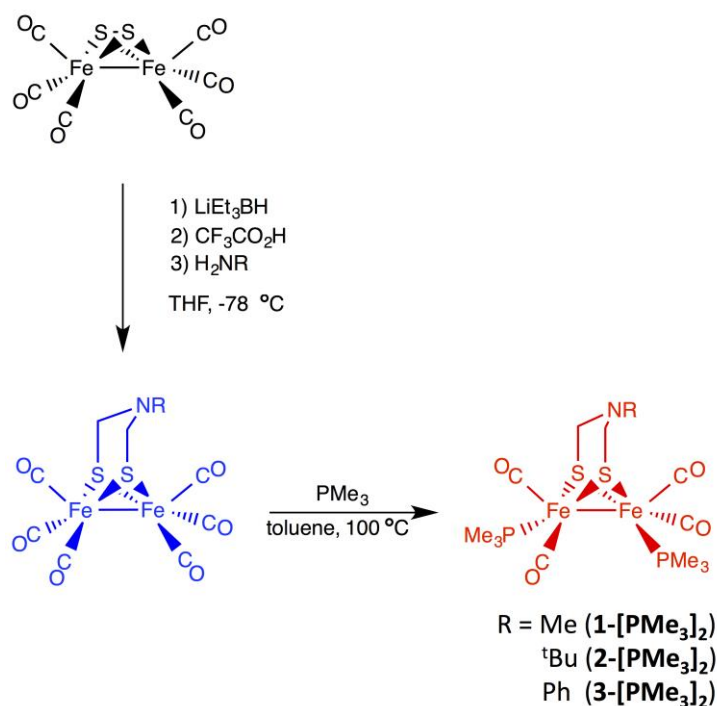
Figure IV-5. Reaction scheme for the synthesis of the (μ-SCH$_2$N(R)CH$_2$S)[Fe(CO)$_2$PMe$_3$]$_2$ complexes **1-[PMe$_3$]$_2$**, **2-[PMe$_3$]$_2$**, and **3-[PMe$_3$]$_2$**.

The ν(CO) IR values are nearly identical for **1-[PMe₃]₂**, **2-[PMe₃]₂**, and **3-[PMe₃]₂**, however a difference is seen in the intensity patterns, Figure IV-6 and Table IV-4. The intensity pattern seen for **2-[PMe₃]₂** and **3-[PMe₃]₂** (weak, strong, medium) is also observed for (μ-pdt)[Fe(CO)₂PMe₃]₂ and (μ-dmpdt)[Fe(CO)₂PMe₃]₂ indicating these complexes have similar structures. The **1-[PMe₃]₂** complex has an intensity pattern (medium, strong, medium) that is similar to disubstituted complexes with an apical/basal ligand arrangement in the solid-state structure, Figure IV-1.[57]

Table IV-4. ν(CO) stretching frequencies and intensity patterns for the bis-PMe₃ complexes.

Complex	ν(CO) cm^{-1a}
1-[PMe₃]₂	1983 (m); 1946 (s); 1911 (m); 1902 (m)
2-[PMe₃]₂	1983 (w); 1948 (s); 1903 (m); 1892 (sh)
3-[PMe₃]₂	1982 (w); 1949 (s); 1905 (m); 1897 (sh)

a IR spectra obtained in toluene.
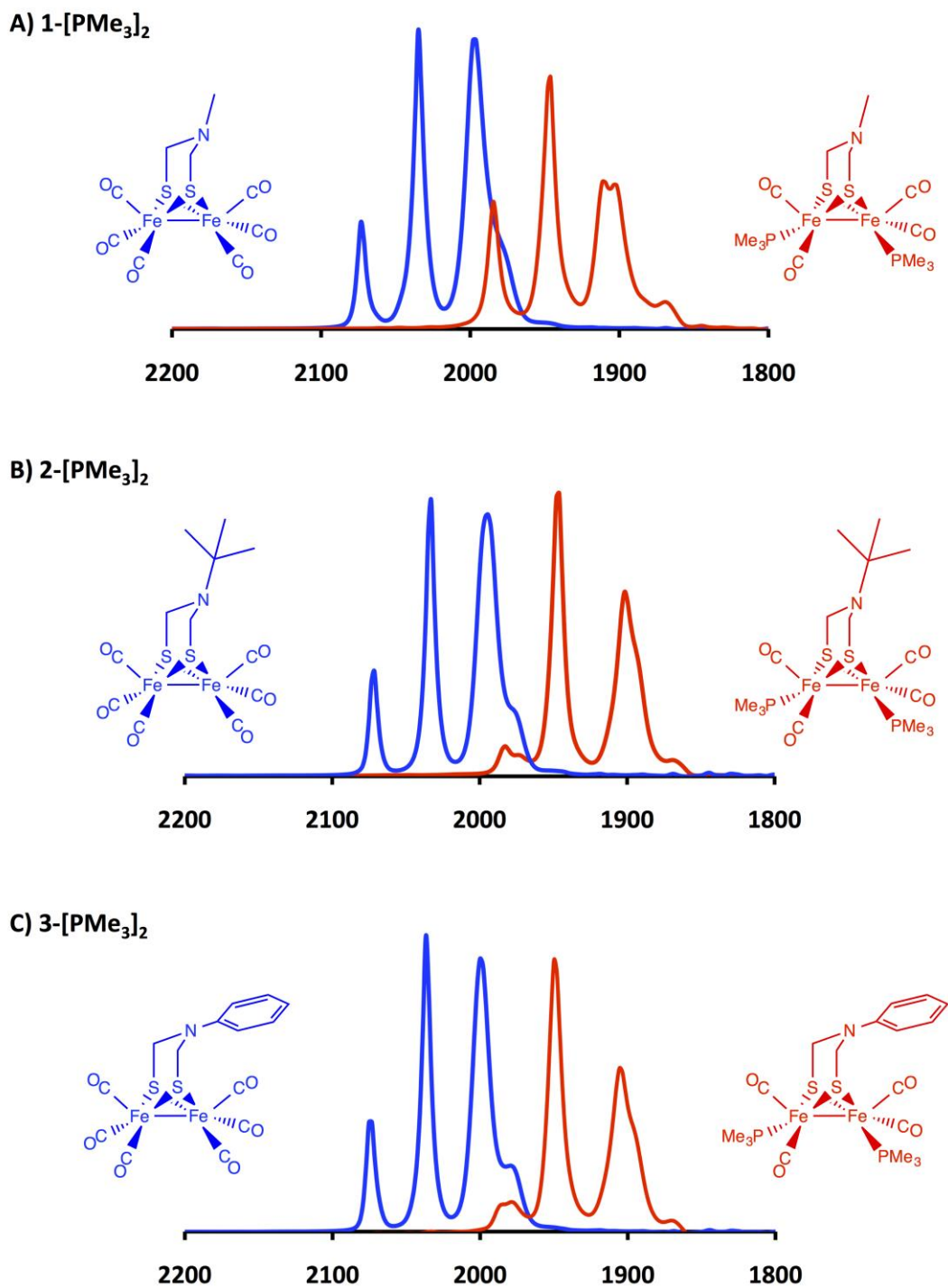
Figure IV-6. ν(CO) IR spectra in toluene of A) **1-[PMe₃]₂**, B) **2-[PMe₃]₂**, and C) **3-[PMe₃]₂**. The bis-PMe₃ complex is shown in red and the respective hexacarbonyl precursor is shown in blue.

X-ray Diffraction Studies of Disubstituted Phosphine Complexes

The disubstituted phosphine complexes, **1-[PMe$_3$]$_2$ and 2-[PMe$_3$]$_2$**, were crystallized from a concentrated MeOH solution stored at -4 $^\circ$C. The crystals were subjected to X-ray diffraction analysis and the molecular structures are shown in Figure IV-7. Table IV-5 lists selected metric parameters of (μ-pdt)[Fe(CO)$_2$PMe$_3$]$_2$,[98] (μ-dmpdt)[Fe(CO)$_2$PMe$_3$]$_2$,[57] **1-[PMe$_3$]$_2$**, **2-[PMe$_3$]$_2$**,and **3-[PMe$_3$]$_2$**.

The structure of **2-[PMe$_3$]$_2$** is similar to the carbon bridgehead analogues, (μ-pdt)[Fe(CO)$_2$PMe$_3$]$_2$[98] and (μ-dmpdt)[Fe(CO)$_2$PMe$_3$]$_2$. [57] Both of the PMe$_3$ ligands adopt basal positions in the FeS$_2$(CO)$_2$L square pyramids and are transoid to each other in the diiron structure. However, the PMe$_3$ ligands in the structure of **1-[PMe$_3$]$_2$** adopt an apical/basal arrangement that was indicated by the ν(CO) IR intensity patterns. The bridgehead N of the FeS$_2$C$_2$N ring of **1-[PMe$_3$]$_2$** is oriented towards the Fe(CO)$_2$PMe$_3$ unit with the apical PMe$_3$. Unlike (μ-dmpdt)[Fe(CO)$_2$PMe$_3$]$_2$, the addition of steric bulk to the bridgehead had little to no effect on the torsion angle. In both **1-[PMe$_3$]$_2$ and 2-[PMe$_3$]$_2$** the Fe(CO)$_3$ units are essentially eclipsed, with only a 1-2° torsion angle, C$_{ap}$-Fe-Fe-L$_{ap}$. This is due to the orientation of the methyl and *tert*-butyl substituents on the nitrogen in **1-[PMe$_3$]$_2$** and **2-[PMe$_3$]$_2$**, respectively, which points away from the Fe(CO)$_2$(PMe$_3$) unit. That is, the nitrogen is substantially pyramidal with the lone pair directed inwardly towards the adjacent iron.
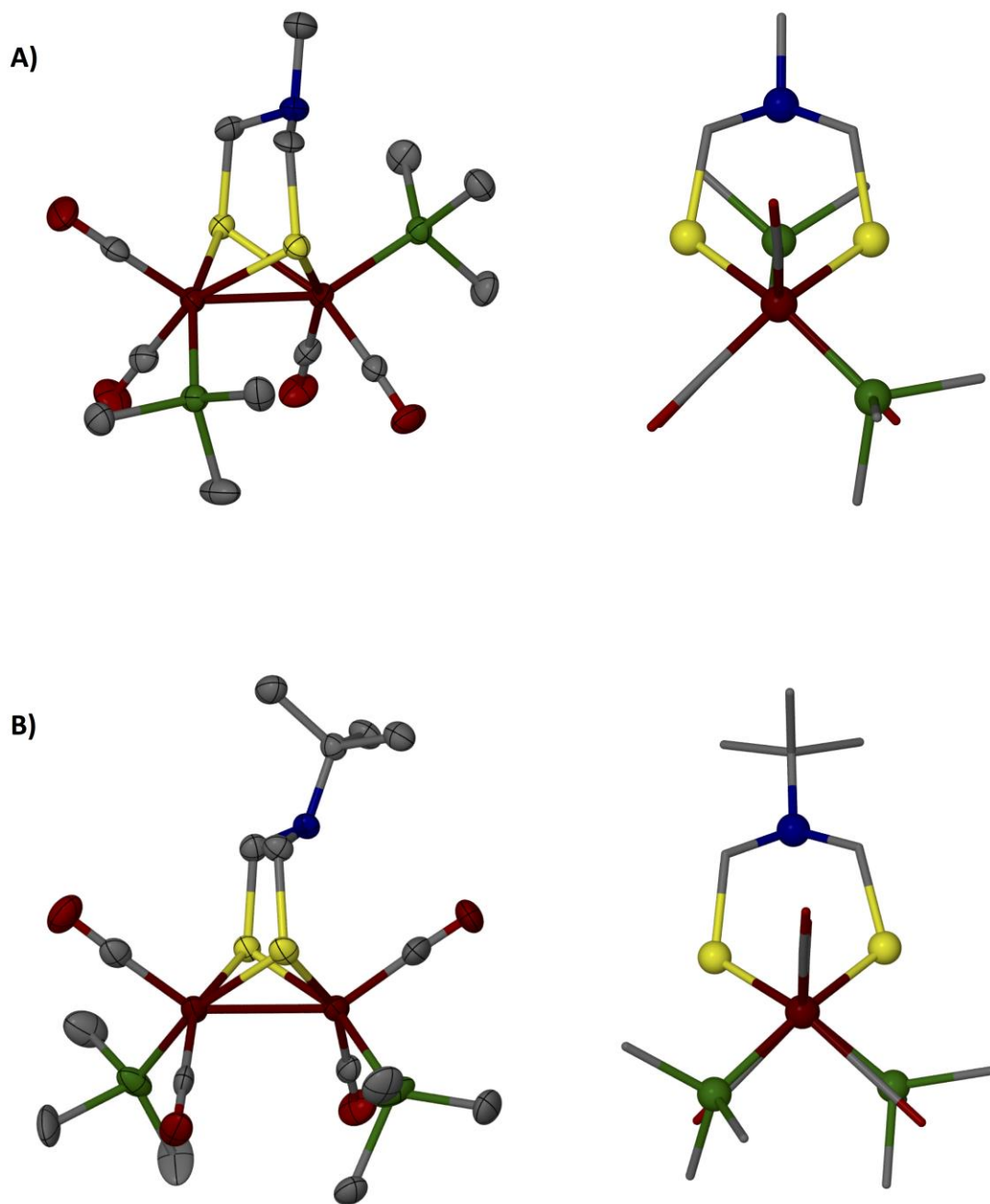
Figure IV-7. Molecular structures of complexes (a) **1-[PMe₃]₂** and (b) **2-[PMe₃]₂**: (left) side view of thermal ellipsoids drawn at 50% probability level; (right) ball-and-stick view down the iron-iron bond.

Table IV-5. Metric parameters of $(\mu\text{-S(CH}_2\text{XCH}_2\text{S)[Fe(CO)}_3]_2$ complexes.

(μ-pdt)[Fe(CO)₂PMe₃]₂	**(μ-dmpdt)[Fe(CO)₂PMe₃]₂**	**1-[PMe₃]₂**	**2-[PMe₃]₂**
trans-basal	**trans-basal**	**apical-basal**	**trans-basal**

Complex	Fe-Fe (Å)	Flap Angle (°)ᵃ	Torsion (°)ᵇ	C/N--Fe (Å)ᶜ
(μ-pdt)[Fe(CO)₂PMe₃]₂[98]	2.5554(2)	129.91	9.1(5)	3.45
(μ-dmpdt)[Fe(CO)₂PMe₃]₂[57]	2.5690(3)	141.47	28.9(4)	3.71
(μ-SCH₂N(Me)CH₂S)[Fe(CO)₃]₂, **1-[PMe₃]₂**	2.526(1)	122.24	2.1(3)	3.40
(μ-SCH₂N(ᵗBu)CH₂S)[Fe(CO)₃]₂, **2-[PMe₃]₂**	2.5586(2)	119.14	1.0(9)	3.30
(μ-SCH₂N(Ph)CH₂S)[Fe(CO)₃]₂, **3-[PMe₃]₂**	2.573(4)	121.28	10(2)	3.43

ᵃ Refers to the dihedral angle formed through the intersection of the XC_2 (X = C or N) and C_2S_2 planes in the FeS_2C_2X ring.
ᵇ Refers to the CO_{ap}-Fe-Fe -$CO_{ap'}$ angle.
ᶜ The distance from the central atom in the bridgehead (C or N) to the closest iron.

Electrochemical Studies of Disubstituted Phosphine Complexes

Figure IV-8 displays the cyclic voltammograms of **1-[PMe$_3$]$_2$** and **2-[PMe$_3$]$_2$** in CH$_2$Cl$_2$. The Fe^{I}Fe^I/Fe^{I}Fe^0 reduction of both bis-phosphine complexes show up at slightly more negative potentials (~ -2.4 V) than (μ-pdt)[Fe(CO)$_2$PMe$_3$]$_2$ and (μ-dmpdt)[Fe(CO)$_2$PMe$_3$]$_2$ (~ -2.3 V), Table IV-6. The Fe^{I}Fe^I/Fe^{II}Fe^I oxidation event for **1-[PMe$_3$]$_2$** (E$_{1/2}$ = -0.120 V) is quasi-reversible similar to (μ-pdt)[Fe(CO)$_2$PMe$_3$]$_2$, however this event is irreversible for **2-[PMe$_3$]$_2$** (E$_{pa}$ = +0.169 V). The addition of steric bulk through the *gem*-dimethyl groups on (μ-dmpdt)[Fe(CO)$_2$PMe$_3$]$_2$ led to a fully reversible Fe^{I}Fe^I/Fe^{II}Fe^I oxidation.[57]

In Chapter III it was shown that the nitrogen in **NMe**, (μ-SCH$_2$N(Me)CH$_2$S)[Fe(CO)$_3$]$_2$, undergoes inversion to place the steric bulk towards the Fe(CO)$_3$ unit, observed in the solid state structure (two isomers co-crystallized in which the methyl group on the nitrogen was in the axial and equatorial orientations) and supported by computational studies.[91] However, this inversion is not observed for **NtBu**, (μ-SCH$_2$N(tBu)CH$_2$S)[Fe(CO)$_3$]$_2$, through X-ray analysis or computations, as the DFT computational approach could not locate a minimum for the axial isomer. Although the steric bulk on the nitrogen in both **1-[PMe$_3$]$_2$** and **2-[PMe$_3$]$_2$** is pointing away from the Fe(CO)$_3$ units in the solid state structures, it can be assumed from the previous study described above that the nitrogen in **1-[PMe$_3$]$_2$**, derivative of **NMe**, can invert leading to an isomer where the steric bulk of the methyl group would be oriented towards the Fe(CO)$_2$(PMe$_3$) unit. The study also implies that the sterically bulky *tert*-butyl group in **2-[PMe$_3$]$_2$**, derivative of **NtBu**, is locked in the outward position and unable to enforce

steric strain on the Fe(CO)$_2$(PMe$_3$) unit. As steric strain has been found to enhance the reversibility, this would account for the difference observed between the reversibility of **1-[PMe$_3$]$_2$** and **2-[PMe$_3$]$_2$**, Figure IV-8.[57] Although a quasi-reversible Fe^{I}Fe^I/Fe^{II}Fe^I oxidation event was observed for **1-[PMe$_3$]$_2$**, a bridging CO species was not detected in the product of oxidation of **1-[PMe$_3$]$_2$**.
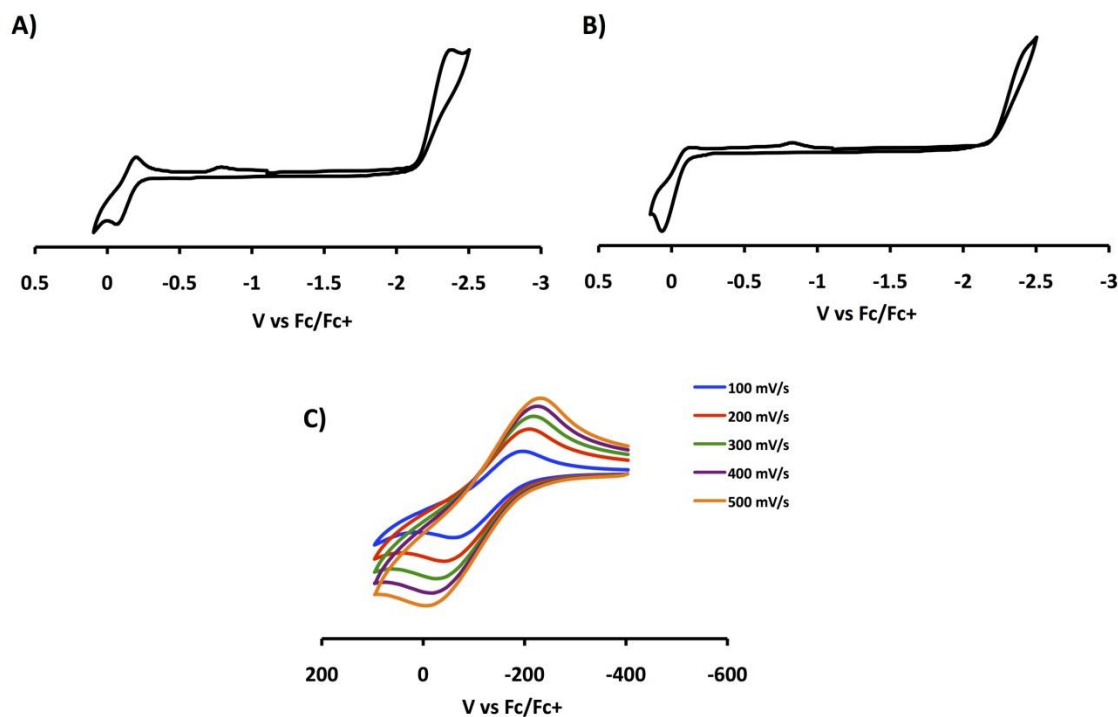
Figure IV-8. Cyclic voltammetry of A) **1-[PMe$_3$]$_2$**, B) **2-[PMe$_3$]$_2$**, and C) multiple scan rates of the Fe^{I}Fe^I/Fe^{II}Fe^I oxidation event of **1-[PMe$_3$]$_2$**. Concentrations were 2 mM in CH$_2$Cl$_2$ with 0.1 M ^{n}Bu$_4$NBF$_4$ as an electrolyte.

Table IV-6. Electrochemical potentials of bis-PMe₃ derivatives.

Complex	E_{pc} $E_1 : Fe^IFe^I \rightarrow Fe^0Fe^I$	E_{pa} $Fe^IFe^I \rightarrow Fe^{II}Fe^I$
1-[PMe₃]₂[a]	-2.36	-0.120[b]
2-[PMe₃]₂[a]	-2.41	+0.169
(μ-pdt)[Fe(CO)₂PMe₃]₂[98]	-2.28	-0.096 [b]
(μ-dmpdt)[Fe(CO)₂PMe₃]₂[57]	-2.29	-0.335 [b]

[a]Ar deaerated CH₂Cl₂ solution (0.1 M $^nBu_4NBF_4$). All experiments were recorded using a glassy carbon working electrode (A = 0.071 cm^2) referenced to Cp₂Fe/Cp₂Fe$^+$ as an internal standard and a Pt counter electrode at a scan rate of 100 mV/s. [b] Potential for $E_{1/2}$

Protonation of (μ-SCH₂N(R)CH₂S)[Fe(CO)₂PMe₃]₂ Complexes

The reaction of (μ-SCH₂N(R)CH₂S)[Fe(CO)₂PMe₃]₂, R = Me (**1-[PMe₃]₂**) or ^tBu (**2-[PMe₃]₂**), with strong acid, HBF₄ or HCl, in varying solvents affords three different protonated species, Figure IV-9. Through the addition of HBF₄ to **1-[PMe₃]₂** or **2-[PMe₃]₂** in methanol the ν(CO) bands of the bis-PMe₃ complexes shift by ~ 20 cm^{-1} towards more positive values, Figure IV-10 and Table IV-7. This is indicative of a protonated nitrogen species, (μ-SCH₂N(Me)(H)CH₂S)[Fe(CO)₂PMe₃]₂$^+$ (**[1H]$^+$**) and (μ-SCH₂N(^tBu)(H)CH₂S)[Fe(CO)₂PMe₃]₂$^+$ (**[2H]$^+$**).{Dong, 2006 #148;Dong, 2007 #147;Wang, 2007 #32} The addition of HCl to a CH₂Cl₂/EtOH (3:1) solution of **1-[PMe₃]₂** and **2-[PMe₃]₂**, respectively, results in ~ 90 cm^{-1} shift in the ν(CO) bands to higher frequencies. This shift observed in the IR spectra suggests that a bridging hydride

species was synthesized, $(\mu\text{-}H)(\mu\text{-}SCH_2N(Me)CH_2S)[Fe(CO)_2PMe_3]_2^+$ (**[1Hy]⁺**) and $(\mu\text{-}H)(\mu\text{-}SCH_2N(^tBu)CH_2S)[Fe(CO)_2PMe_3]_2^+$ (**[2Hy]⁺**).{Georgakaki, 2003 #213} The addition of HBF₄ to **1-[PMe₃]₂** and **2-[PMe₃]₂** in CH_3CN resulted in shifts of the $\nu(CO)$ bands of the bis-PMe₃ complexes by ~ 100 cm⁻¹ towards more positive values. This is indicative of protonation of both the nitrogen and iron-iron bond affording a doubly protonated species, $(\mu\text{-}H)(\mu\text{-}SCH_2N(Me)(H)CH_2S)[Fe(CO)_2PMe_3]_2^{2+}$ (**[1HHy]²⁺**) and $(\mu\text{-}H)(\mu\text{-}SCH_2N(^tBu)(H)CH_2S)[Fe(CO)_2PMe_3]_2^{2+}$ (**[2HHy]²⁺**).
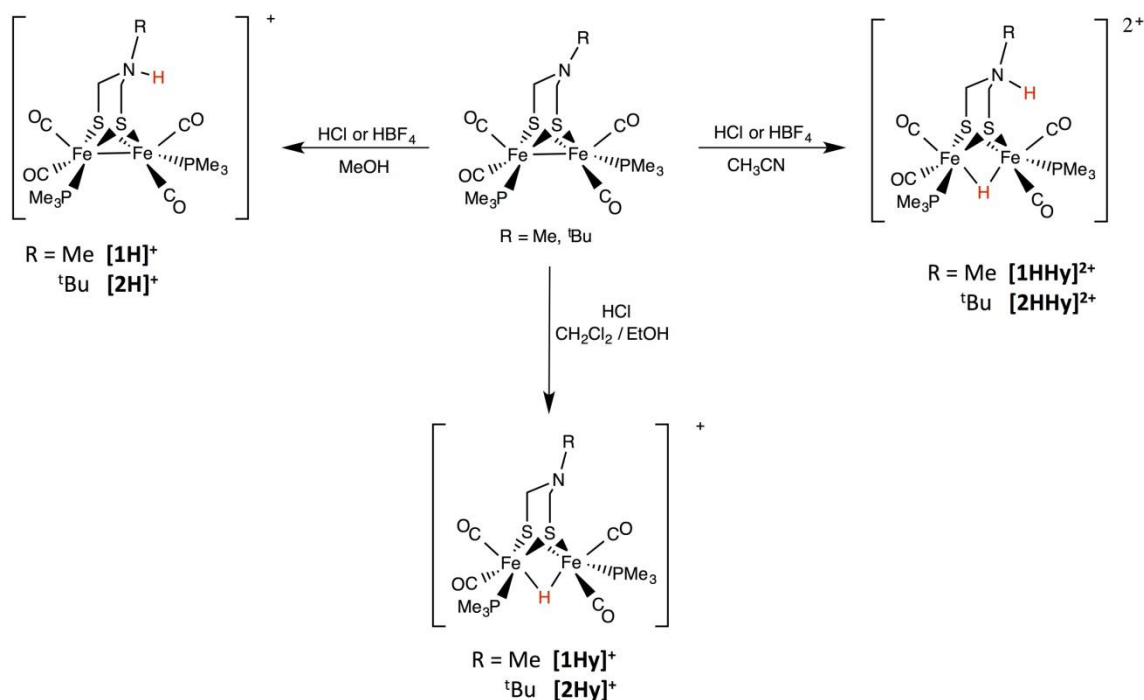
Figure IV-9. Reaction scheme for the synthesis of three protonated species of **1-[PMe₃]₂** and **2-[PMe₃]₂**.
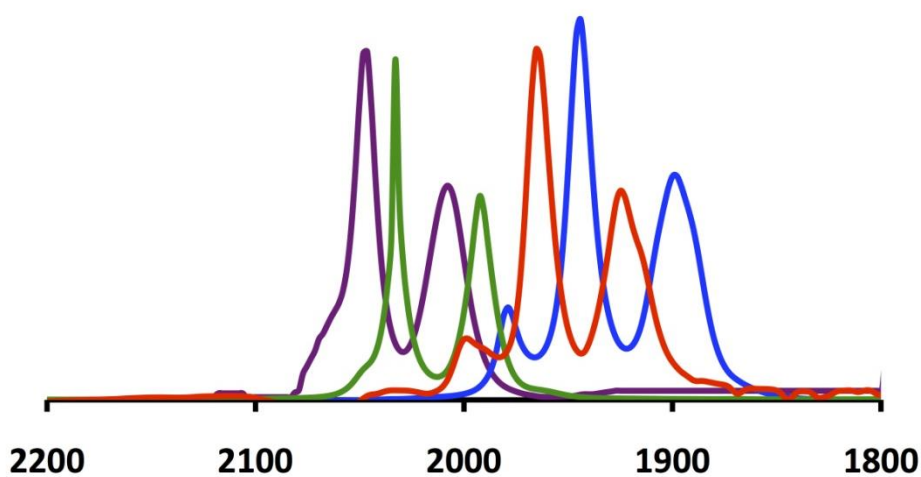
Figure IV-10. ν(CO) IR spectra recorded in CH$_3$CN of **2-[PMe$_3$]$_2$** (blue), **[2H]$^+$** (red), **[2Hy]$^+$** (green), and **[2HHy]$^{2+}$** (purple).

Table IV-7. ν(CO) IR stretching frequencies recorded in CH$_3$CN.

Complex	ν(CO) cm^{-1}
1-[PMe$_3$]$_2$	1980(w); 1941(s); 1908(m)
2-[PMe$_3$]$_2$	1981(w); 1944(s); 1899(m)
[1H]$^+$	2000(w); 1965(s); 1924(m)
[2H]$^+$	2001(w); 1964(s); 1925(m)
[1Hy]$^+$	2034(s); 1994(m)
[2Hy]$^+$	2032(s); 1992(m)
[1HHy]$^{2+}$	2049(s); 2011(m)
[2HHy]$^{2+}$	2047(s); 2008(m)

^{1}H and ^{31}P NMR Studies

The ^{31}P NMR room temperature spectra of **1-[PMe$_3$]$_2$** and **2-[PMe$_3$]$_2$** display only one signal at δ = 24.3 and 23.7 ppm, respectively, indicating the Fe(CO)$_2$(PMe$_3$) units are freely rotating in solution, Figure IV-11. However upon nitrogen protonation, **[1H]$^+$** and **[2H]$^+$** have two ^{31}P signals at 25 °C suggesting the bridgehead chair/boat interconversion has slowed resulting in an asymmetric complex. The ^{1}H NMR spectrum of **[2H]$^+$** displays two doublets at δ = 1.58 and 1.56 ppm for the PMe$_3$ protons as the two ligands are nonequivalent. One ^{31}P signal is observed for the bridging hydride, **[1Hy]$^+$** and **[2Hy]$^+$**, observed at δ = 22.5 and 21.1 ppm, respectively, indicating the PMe$_3$ ligands on each Fe units are symmetrical. This is similar to the ^{31}P NMR spectrum of (μ-H)(μ-pdt)[Fe(CO)$_2$PMe$_3$]$_2$$^+$ which displays a single resonance at δ = 22.3.[115] The ^{1}H NMR spectra for the bridging hydride species, **[1Hy]$^+$** and **[2Hy]$^+$**, have a prominent feature at -15.8 (J_{H-P} = 22 Hz) and -15.6 (J_{H-P} = 22 Hz) ppm, respectively, that is assigned to the hydride, Figure IV-12. This signal appears as a triplet therefore it is concluded that the hydride is in the bridging position and it couples to two equivalent phosphorus atoms. Again this is similar to (μ-H)(μ-pdt)[Fe(CO)$_2$PMe$_3$]$_2$$^+$ that displays a triplet at δ = -15.3 (J_{H-P} = 22 Hz).[115] The doubly protonated complexes, **[1HHy]$^{2+}$** and **[2HHy]$^{2+}$**, display two ^{31}P signals indicating the phosphorus atoms are nonequivalent, as seen with the nitrogen protonated species. The bridging hydride in the dication species appears as a doublet of doublets at δ = -15.5 (J_{H-P} = 21 Hz) for **[2HHy]$^{2+}$**. This is also observed for (μ-H)(μ-SCH$_2$N(benzyl)(H)CH$_2$S)[Fe(CO)$_2$PMe$_3$]$_2$$^{2+}$.[116]
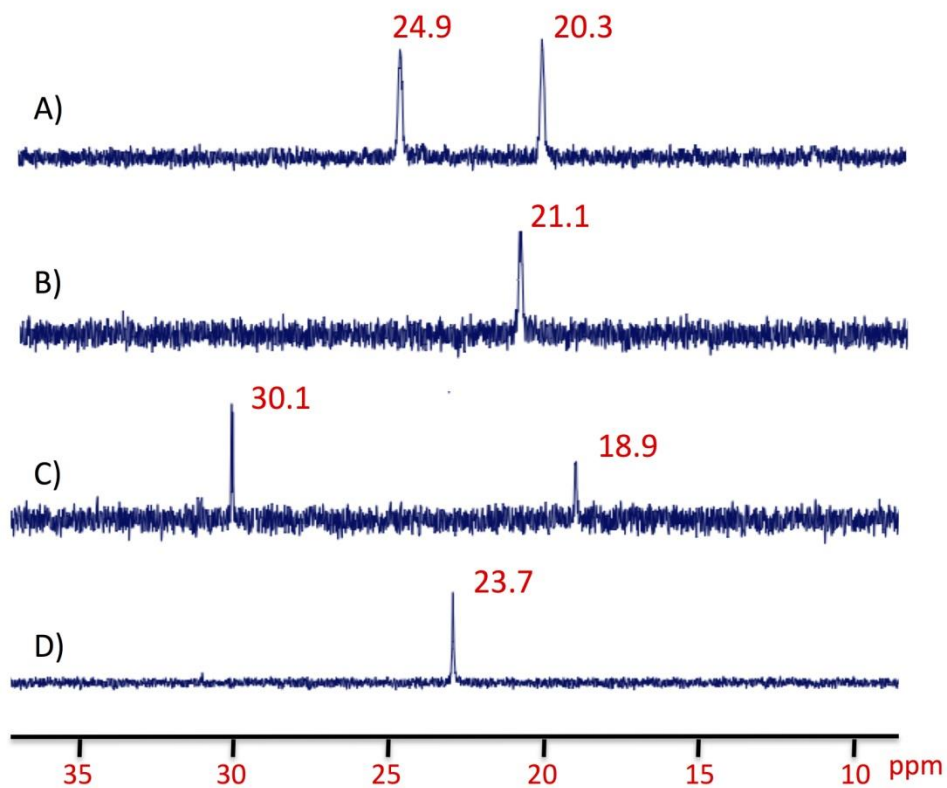
Figure IV-11. Proton-decoupled ^{31}P NMR spectra in CD$_3$CN of (A) **[2HHy]$^{2+}$**, (B) **[2Hy]$^{+}$**, (C) **[2H]$^{+}$**, and (D) **2-[PMe$_3$]$_2$**.
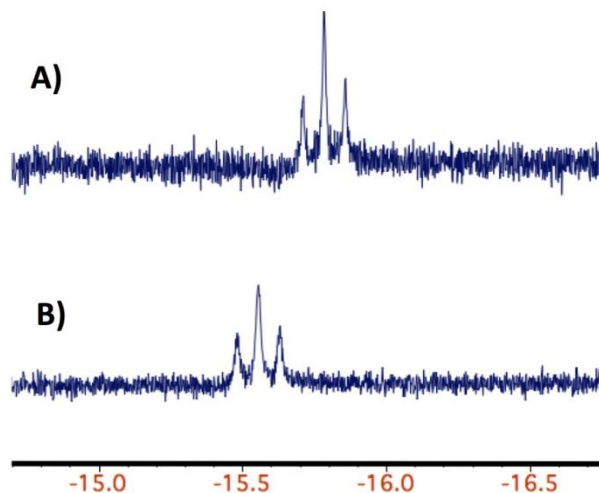
Figure IV-12. High field region of the ^{1}H NMR spectra at 300 MHz in CD$_3$CN of (A) **[1Hy]**$^+$ and (B) **[2Hy]**$^+$.

X-ray Diffraction Studies of the Protonated Species

Complexes **[2H]**$^+$ and **[2Hy]**$^+$ were crystallized through slow diffusion of ether into a CH$_2$Cl$_2$ solution. The crystals were subjected to X-ray diffraction analysis and the resulting structures are shown in Figure IV-13. Table IV-6 lists selected metric parameters of **2-[PMe$_3$]$_2$**, **[2H]**$^+$, and **[2Hy]**$^+$. Despite repeated attempts, crystals of X-ray quality were not obtained for **[1H]**$^+$, **[1Hy]**$^+$, **[1HHy]**$^{2+}$, and **[2HHy]**$^{2+}$.

Both of the PMe$_3$ ligands adopt basal positions in the FeS$_2$(CO)$_2$L square pyramids of **2-[PMe$_3$]$_2$**, however upon nitrogen protonation, **[2H]**$^+$, the phosphine ligands have an apical/basal arrangement. As observed with other complexes, the *tert*-butyl group on the nitrogen is oriented away from the Fe(CO)$_2$(PMe$_3$) unit leaving the proton on the nitrogen pointing towards the Fe(CO)$_2$(PMe$_3$) unit. The Fe(CO)$_2$(PMe$_3$)

units are staggered in **[2H]**[+] resulting in a C_{ap}-Fe-Fe-L_{ap} torsion angle of 39° compared to the 1° torsion angle observed in **2-[PMe$_3$]$_2$**. This staggering is attributed to the steric bulk of the proton on the nitrogen, which is in close contact with the adjacent apical carbonyl, Figure IV-14. Upon protonation of the Fe-Fe bond (**[2Hy]**[+]), the PMe$_3$ ligands adapt a transoid basal configuration, seen in starting material **2-[PMe$_3$]$_2$**. This configuration is also found in (μ-pdt)[Fe(CO)$_2$PMe$_3$]$_2$ and (μ-H)(μ-pdt)[Fe(CO)$_2$PMe$_3$]$_2$[+]. The Fe(CO)$_3$ units are essentially eclipsed in **[2Hy]**[+], with only a 5° torsion angle similar to **2-[PMe$_3$]$_2$**. An overlay of **2-[PMe$_3$]$_2$** and **[2Hy]**[+] showing little difference between the two structures, Figure IV-15.
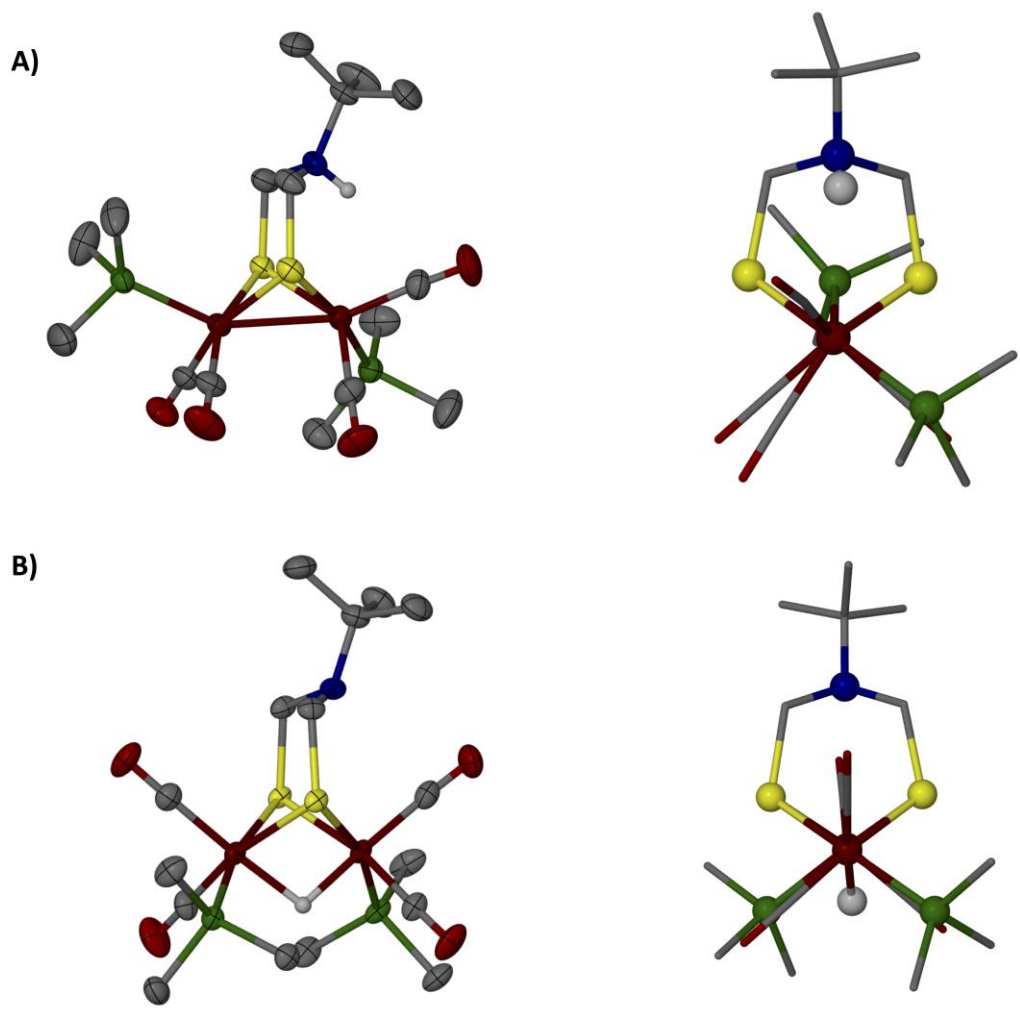
Figure IV-13. Molecular structures of complexes (A) **[2H]**[+] and (b) **[2Hy]**[+]: (left) side view of thermal ellipsoids drawn at 50% probability level; (right) ball-and-stick view down the iron-iron bond.
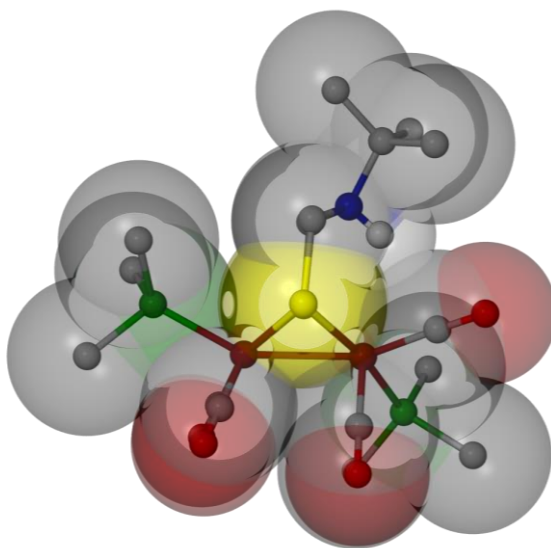
Figure IV-14. Ball and stick representations featuring van der Waals spheres rendered from the X-ray crystal structure of **[2H]**[+].
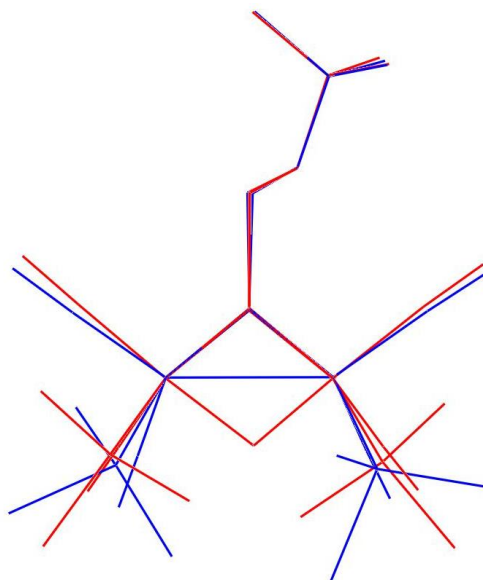
Figure IV-15. Overlay of the crystal structures of **2-[PMe₃]₂** (blue) and **[2Hy]**[+] (red).

Table IV-8. Spectroscopic and metric parameters of disubstituted phosphine complexes.

| 2-[PMe₃]₂ | [2H]⁺ | [2Hy]⁺ |
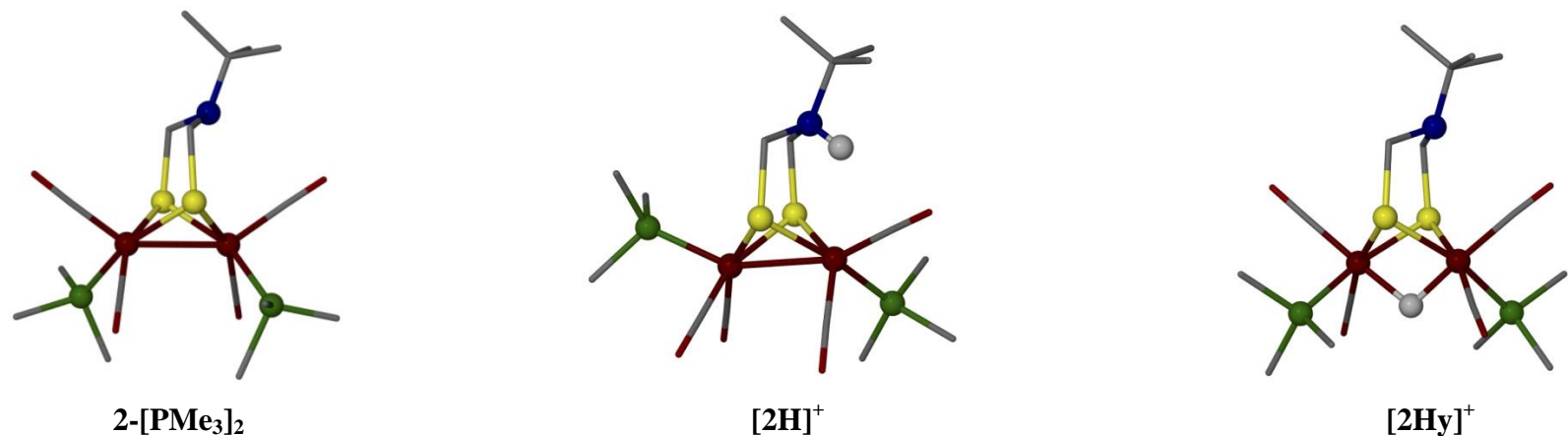
Complex	Fe-Fe (Å)	Flap Angle (°)[a]	Torsion (°)[b]	N--Fe (Å)[c]	Fe-H (Å)	³¹P NMR
2-[PMe₃]₂	2.5860(2)	118.46	1.0(9)	3.298	-	23.7
[2H]⁺	2.540(1)	115.91	38.8(4)	3.223(4)	2.610(1)	30.1, 18.9
[2Hy]⁺	2.5842(9)	117.21	5.4(3)	3.302(3)	1.61(4)/ 1.72(4)	21.1

[a] Refers to the dihedral angle formed through the intersection of the XC_2 (X = C or N) and C_2S_2 planes in the FeS_2C_2X ring.
[b] Refers to the CO_{ap}-Fe-Fe -$CO_{ap'}$ angle.
[c] The distance from the central atom in the bridgehead (C or N) to the closest iron.

Conclusion

Azadithiolate diiron compounds were synthesized and characterized for future photochemical studies. Phosphine substituted complexes were synthesized to model the CN$^-$ ligands found in the [FeFe]-hydrogenase active site. The monosubstituted phosphine (PPh$_3$, PTA, and P(OMe)$_3$) complexes show similar ν(CO) infrared stretching frequencies with different intensity patterns. The intensity patterns were indicative of the ligand arrangement in the molecular structures. Similarly, the disubstituted PMe$_3$ complexes had varying intensity patterns indicative of the apical/basal and trans-basal arrangement of the ligands. The Fe^{I}Fe^I/Fe^{II}Fe^I oxidation event for (μ-SCH$_2$N(Me)CH$_2$S)[Fe(CO)$_3$]$_2$, **1-[PMe$_3$]$_2$**, showed a quasi-reversible wave, however the oxidation event of (μ-SCH$_2$N(^{t}Bu)CH$_2$S)[Fe(CO)$_3$]$_2$, **2-[PMe$_3$]$_2$**, was irreversible due to the lack of steric influence from the *tert*-butyl substituent on the nitrogen.

The electron donating ability of the PMe$_3$ ligands increases the electron density on the iron centers allowing for protonation of the Fe-Fe bond, seen with both the nitrogen and the carbon bridgehead analogues. However, the addition of a basic site in the bridgehead, i.e. nitrogen, permits another protonation site. The proton affinity of these sites is clearly similar as small changes in solvent or proton source results in different selectivity. Three different species were isolated depending on the site of protonation 1) nitrogen protonation; 2) iron-iron bond; and 3) doubly protonated species containing both nitrogen protonation and protonated iron-iron bond. The bridging hydride species forms a stable Fe^{II}Fe^{II} complex ideal for photochemical studies.

CHAPTER V

SULFONATED DIIRON COMPLEXES AS WATER-SOLUBLE MODELS OF

THE [FeFe]-HYDROGENASE ENZYME ACTIVE SITE[*]

Introduction

The synthesis of new small molecule models of the diiron hydrogenase enzyme active site is driven by a desire to better understand a unique biological system capable of producing hydrogen at rates comparable to platinum.[7,117] In doing so the ultimate goal is the development of iron- and sulfur-based molecular catalysts for use in the cathode of solar powered water electrolysis cells.[118] To date hundreds of these small molecule models of the form (μ-SCH$_2$XCH$_2$S)[Fe(CO)$_{3-n}$L$_n$]$_2$ (X = CR$_2$, NR, O, or S) have been synthesized and their proton reduction capabilities analyzed through a combination of electrochemical and spectroscopic techniques.[90,119] While it would seem reasonable to conduct these assays in water in order to match the ideal environment of the hydrolysis cells, the proton reduction experiments conducted on the diiron model systems have been limited almost entirely to organic solvents or mixtures of water and MeCN. This limitation is due to the inherent insolubility of the majority of small molecule models in water, which results from their hydrophobic nature. In fact, over the last ten years only a handful of water soluble complexes have been described.

_____
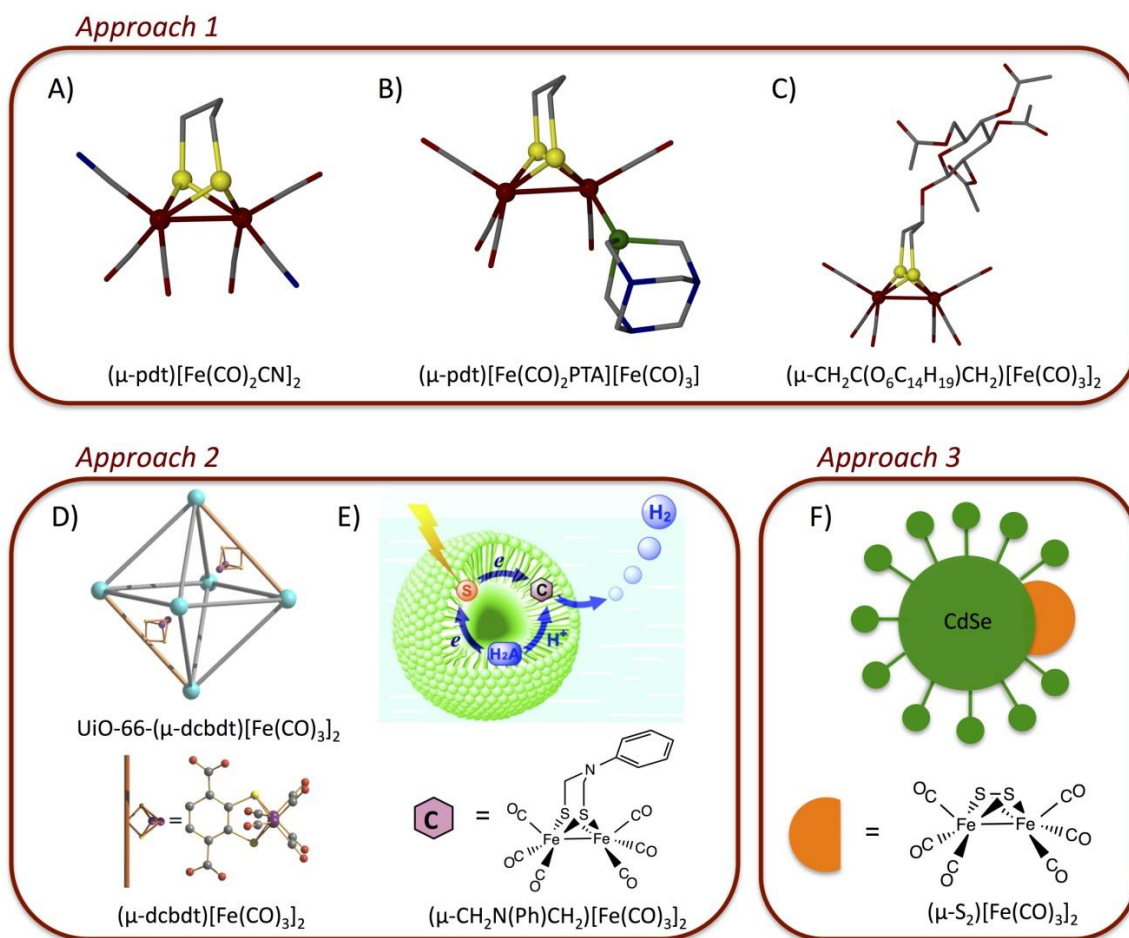
Figure V-1. Examples of [FeFe]-hydrogenase models with improved water solubility. Depiction of (A) a highly water-soluble diiron model with two CN$^-$ ligands;[26] (B) a diiron model with a water-soluble ligand, 1,3,5-triaza-7-phosphaadamantane (PTA);[99] (C) a sugar residue incorporated into the bridgehead of a diiron model;[121] (D) a diiron electrocatalyst stabilized through incorporated into a robust Zr(IV) MOF that catalyzes hydrogen evolution in water;[47] (E) the incorporation of a diiron model into an aqueous sodium dodecyl sulfate micelle solution;[122] (F) immobilized (μ-S$_2$)[Fe(CO)$_3$]$_2$ complex on the surface of CdSe quantum dots, producing a water soluble photocatalyst for H$_2$ evolution with a turnover frequency of ca. 600 h^{-1}.[46]

The efforts to improve water solubility of the diiron models can be categorized into three approaches: 1) addition of water-soluble substituents onto the diiron models,[26,99,121] 2) encapsulating the diiron models into a hydrophobic pocket with a hydrophilic exterior,[47,122] and 3) interface-directed assembly of diiron models onto quantum dots.[46] Examples of each approach are given in Figure V-1.

The (μ-pdt)[Fe(CO)$_2$CN]$_2^{2-}$ complex, reported from three research groups almost simultaneously,[26,27] was used in 1999 by Pickett and coworkers as a water-soluble dianionic complex, synthesized by substituting two CO ligands with CN$^-$. In the interim there have been no further reports of work exploring the aqueous, proton reduction catalysis capability of the cyanide-containing diiron complexes, likely due to the sensitivity of these compounds to both air and acid. There have however been several approaches towards developing more hydrophilic complexes that exhibit greater stability than the cyanide derivatives.

Phosphine ligands have long been used in the [Fe-Fe]-hydrogenase model systems as a synthetic substitute for the naturally occurring CN$^-$ ligands.[7] The degree of substitution has been shown to play an important role in fine tuning the proton reduction capabilities of hundreds of models of the enzyme active site. Disubstituted (μ-pdt)[Fe(CO)$_2$L]$_2$ complexes typically reduce protons from HOAc at the initial Fe^{I}Fe^I/Fe^{I}Fe^0 reduction, but with a large overpotential.[123] Mono-substituted complexes on the other hand can still reduce protons at the first reduction event but at a lower overpotential than disubstituted complexes.[99] Specialized ligands such as phosphatriazaadamantane (PTA), tris(hydroxymethyl)Phosphine, and Ph$_2$P(C$_6$H$_4$SO$_3^-$)

have been shown to increase water solubility in a variety of metal complexes.[99,124,125] Both the Darensbourg and Sun groups have utilized the PTA ligand to increase the hydrophilicity of the diiron system.[99,125] While the PTA ligand alone did not impart significant solubility in pure water it did permit studies in mixtures of MeCN/H_2O of up to a 1:3 ratio where the proton reduction capabilities of the complexes were observed to shift to significantly more positive potentials with increasing amounts of water.[99] Sun and co-workers further used the di-N-acetylated phosphatriazaadamantane (DAPTA) ligand to impart moderate solubility of ((μ-pdt)[Fe(CO)$_2$(DAPTA)]$_2$ in water which allowed the first electrochemical studies in 100% water (0.05 M n-Bu$_4$NPF$_6$ solution).[124,125] These studies indicated that water played a significant role in altering both the reduction potential and electrocatalytic response of the model complexes, with the reduction of protons occurring more positive than the initial Fe^{I}Fe^I/Fe^{I}Fe^0 reduction as a result of the protonation of the amines in the PTA and DAPTA ligands.

While successful for developing less hydrophobic diiron model systems, the ligand-based solubilization technique limits the variety of complexes that might be synthesized. In contrast, incorporation of a water-solublizing group into the dithiolate linker would appear to offer more versatility. By modifying D-glucopyranoside to include a dithiolate unit Weigand and co-workers were able to obtain sugar functionalized diiron models.[121] These species, initially synthesized as the protected tetra-O-acetyl derivatives, showed greatly increased hydrophilicity upon deprotection of the hydroxyl units. Unfortunately, the deprotected species was not stable in protic solvents, thus limiting its applicability.

Dr. Mike Singleton, a former group member, reported in 2010 a diiron model complex containing an aryl sulfonate modified azadithiolate linker, $Na^+(\mu\text{-}SCH_2N(C_6H_4SO_3^-)CH_2S\text{-})[Fe(CO)_3]_2$, **1Na,** Figure V-2.[64] The aryl sulfonate-functionalized [FeFe]-hydrogenase model complex was synthesized through the condensation reaction of formaldehyde, an amine, and $(\mu\text{-}SH)_2[Fe(CO)_3]_2$ to give $(\mu\text{-}SCH_2N(R)CH_2S)[Fe(CO)_3]_2$, as reported by Rauchfuss and coworkers.[63] While the addition of this moiety into the parent hexacarbonyl complex renders it insoluble in most non-polar organic solvents, it does impart moderate solubility (~1.1 mM) in pure water. The complex remains stable for an extended period of time in deaereated water (up to several months when stored in the refrigerator), allowing study of the diiron complex in water by NMR, IR, UV-Vis and electrochemical methods.
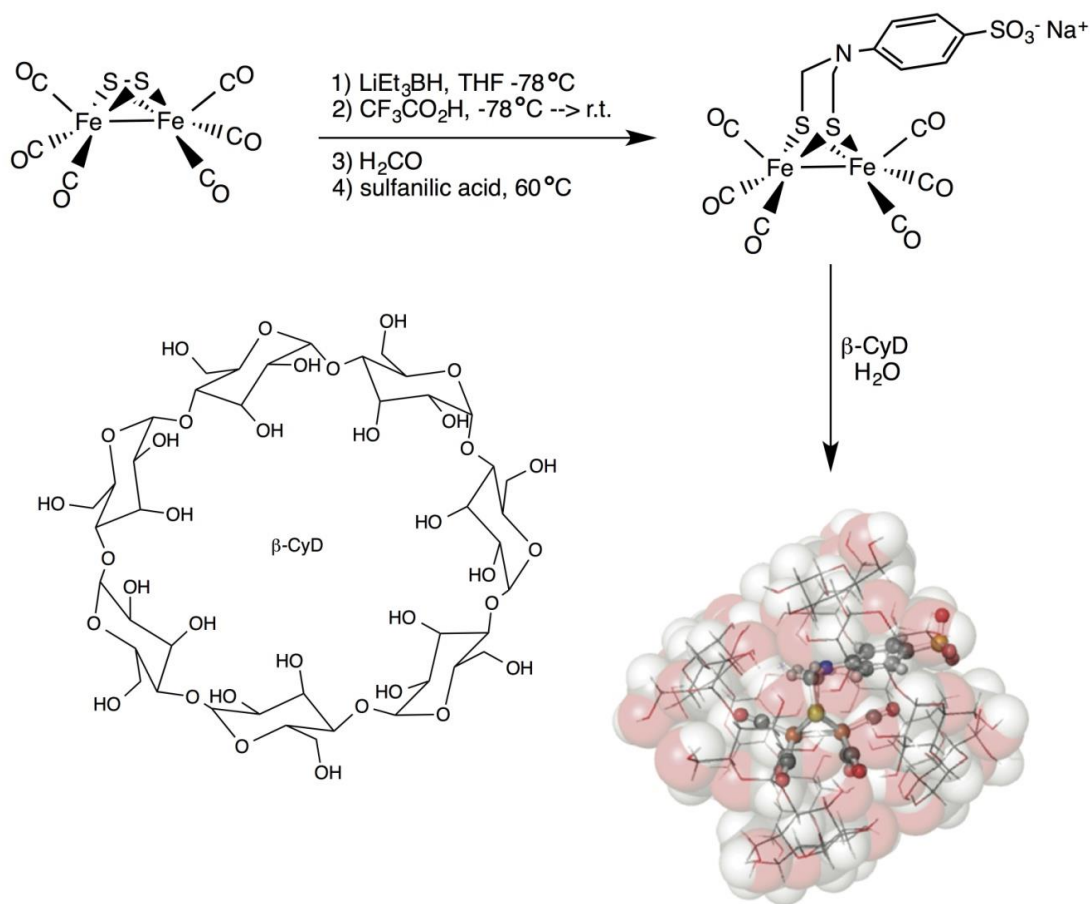
Figure V-2. Synthesis of Na⁺(μ-SCH$_2$N(C$_6$H$_4$SO$_3$⁻)CH$_2$S-)[Fe(CO)$_3$]$_2$ and the β-cyclodextrin inclusion complex.[64]

Additionally, the aryl sulfonate group promoted inclusion of the complex in β-cyclodextin leading to the structural characterization of a **1Na**·2 β-cyclodextrin inclusion complex, which showed the aryl sulfonate group penetrating through the cavity of one of the cyclodextrins, Figure V-2. As expected, the interaction with the cyclodextrin greatly increased the water solubility of **1Na** and opened the possibility for using the inclusion

in the cavity to mimic the protein environment of the enzyme. This study gives rise to a few questions.

- Can greater water solubility be induced through the addition of hydrophilic ligands to the sulfonated hexacarbonyl complex, **1Na**?

- Will the addition of the sulfonate group and hydrophilic ligands alter the structural or electrochemical properties?

In this chapter the sulfonated hexacarbonyl complex, **1Na**, was used as a precursor to generate a series of phosphine-substituted complexes of the type Na(μ-SCH$_2$N(C$_6$H$_4$SO$_3$)CH$_2$S-)[Fe(CO)$_3$][Fe(CO)$_2$L] (L = P(OMe)$_3$ (**2Na**); PTA (**3Na**); and PPh$_3$ (**4Na**) and Na(μ-SCH$_2$N(C$_6$H$_4$SO$_3$)CH$_2$S-)[Fe(CO)$_2$PMe$_3$]$_2$ (**5Na**), that have varying degrees of water solubility. Through structural analysis and electrochemical studies in MeCN/H$_2$O we show that the sulfonate group can impart modest water solubility to complexes **2Na**, **3Na** and **5Na** without drastically altering their structural or electrochemical properties. The addition of the large hydrophobic PPh$_3$ ligand however, overwhelms the effects of the sulfonate group and renders the model complex insoluble in H$_2$O.

Synthesis of Monosubstituted Phosphine Complexes

Dr. Mike Singleton demonstrated that sulfanilic acid can be used in a condensation reaction to introduce an aryl sulfonate group into the dithiolate linker of the model complexes to give the anionic (μ-SCH$_2$N(p-C$_6$H$_4$SO$_3^-$)CH$_2$S)[Fe(CO)$_3$]$_2$.[63]

This compound acts as precursor to a series of water soluble phosphine-substituted complexes through the synthetic routes shown in Figure V-3.

The synthesis of these various phosphine-substituted complexes required different methods. Treatment of **1Na** with one equivalent of Me_3NO followed by either $P(OMe)_3$ or PPh_3 yielded the monosubstituted complexes **2Na** and **4Na**, respectively. The PTA derivative, **3Na**, was synthesized by heating a solution of **1Na** and multiple equivalents of the PTA ligand overnight. All of the monosubstituted complexes are obtained as air-stable red solids in moderate yield (35-43%) and can be isolated as the Na^+ salt as depicted in Figure V-3 or as the Et_4N^+ salt by direct synthesis from **1TEA** or by counterion exchange using Et_4NCl. ^{1}H-NMR analysis of the complexes shows two signals for the methylene protons in the dithiolate linker of the monophosphine complexes, resulting from the loss of symmetry between the two irons upon substitution of a single CO. The reaction of **1Na** with excess PMe_3 at 60 °C in THF gives the disubstituted complex **5Na** in ~60 % yield. Unlike the monosubstituted complexes, the disubstituted PMe_3 complex is air sensitive and degrades rapidly when exposed to air. ^{1}H-NMR displays a single signal for the methylene protons in the dithiolate linker at room temperature indicating that one phosphine has substituted onto each iron. Additionally, this single signal indicates that the dithiolate bridgehead is undergoing chair/boat interconversion, as is seen in the case of the $(\mu\text{-pdt})[Fe(CO)_3]_2$.[49]
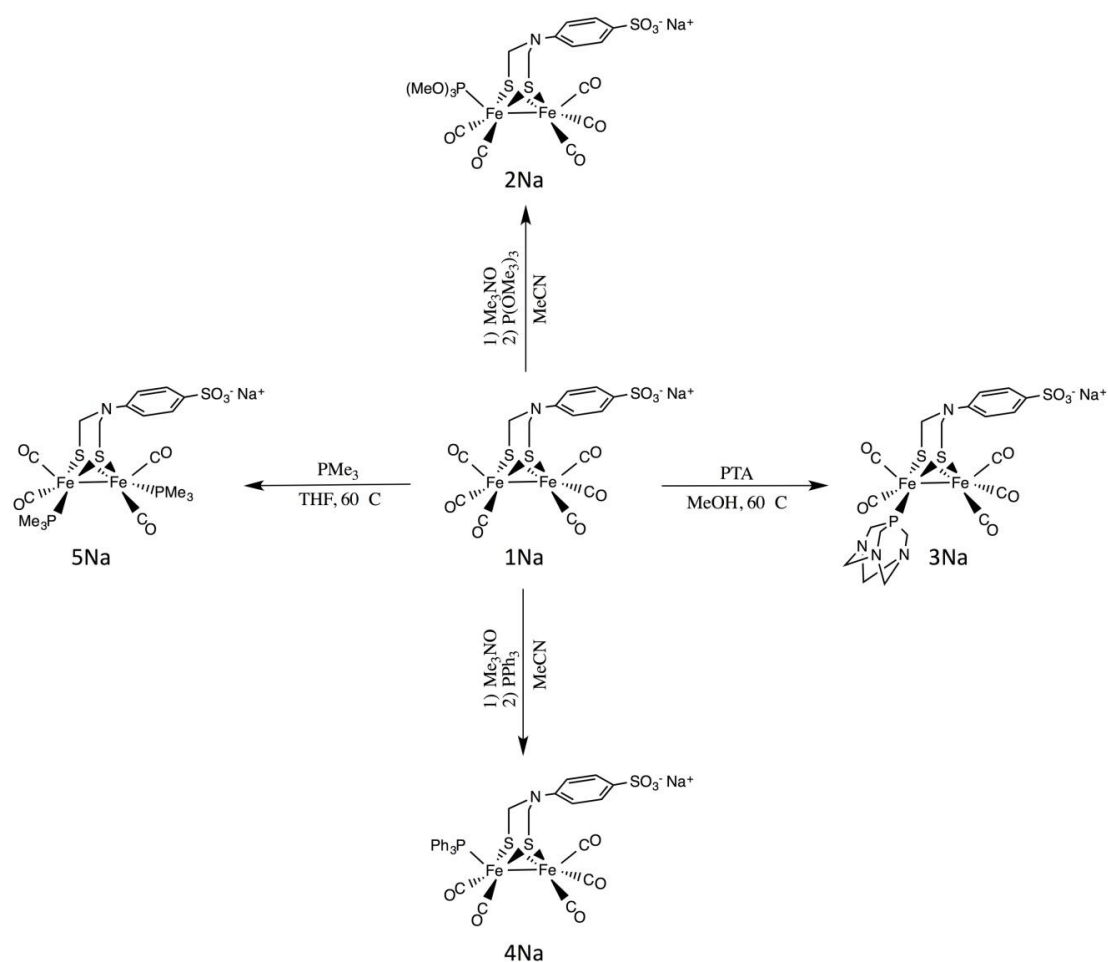
Figure V-3. Reaction scheme for the synthesis of phosphine substituted complexes $Na^+(\mu\text{-}SCH_2N(C_6H_4SO_3^-)CH_2S)[Fe(CO)_3][Fe(CO)_2P(OMe)_3]$ (**2Na***), $Na^+(\mu\text{-}SCH_2N(C_6H_4SO_3^-)CH_2S)[Fe(CO)_3][Fe(CO)_2PTA]$ (**3Na**), $Na^+(\mu\text{-}SCH_2N(C_6H_4SO_3^-)CH_2S)[Fe(CO)_3][Fe(CO)_2$ $PPh_3]$ (**4Na**), and $Na^+(\mu\text{-}SCH_2N(C_6H_4SO_3^-)CH_2S)[Fe(CO)_2PMe_3]_2$(**5Na***). *Synthesized by Dr. Mike Singleton.

IR analysis of the monosubstitued phosphine complexes show lower v(CO) stretching frequencies compared to the hexacarobonyl starting material, **1Na**. This is consistent with the increased donation into the Fe atoms by the phosphine ligands versus CO; the increased electron density on Fe based on the □(CO) values is in the order **3Na** > **4Na** > **2Na**. The IR v(CO) stretching frequencies for **5Na** are significantly lower as compared to the monosubstituted complexes, consistent with a higher degree of substitution and greater electron donation into the irons, Figure V-4.
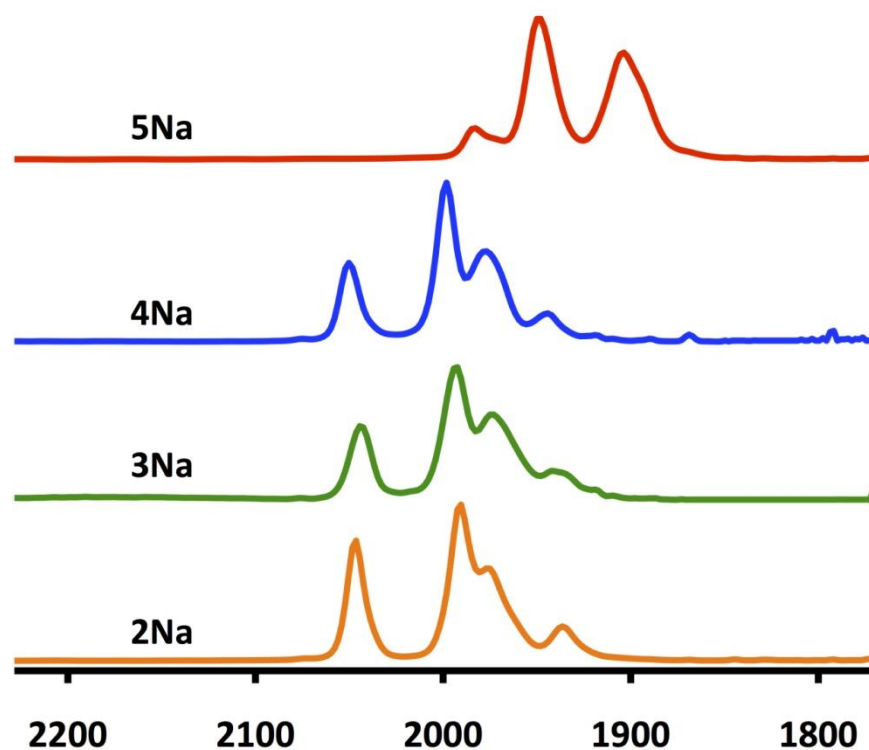
Figure V-4. Stacked v(CO) IR spectra of **2Na**-**5Na** recorded in THF.

Table V-1. IR stretching frequencies in THF for complexes **1Na** - **5Na**.

Complex	$\nu(CO)$ cm^{-1}
1Na	2074 (w); 2035 (s); 1996 (m)
2Na	2048 (m); 1992 (s); 1971 (m); 1942 (w)
3Na	2042 (m); 1986 (s); 1967 (sh); 1930 (w)
4Na	2046 (m); 1990 (s); 1975 (m); 1936 (w)
5Na	1982 (w); 1948 (s); 1903 (m)

Water Solubility of 2Na – 5Na

The sulfonate group endows a degree of water solubility on (μ-SCH$_2$N(C$_6$H$_4$SO$_3^-$)CH$_2$S-)[Fe(CO)$_2$L]$_2$ (L = CO or PR$_3$) that varies depending on the ligands, Table V-2. In the case of the parent hexacarbonyl complex, **1Na**, the maximum obtainable concentration was ~1.1 mM at 22 °C. Upon substitution, the solubilities vary depending on the nature of the ligands. Both complexes **2Na** and **5Na** show slightly higher maximum concentrations, c.a. 1.4 – 1.9 mM at 22 °C, than complex **1Na**. For complex **4Na**, the hydrophobic PPh$_3$ ligand dramatically reduces solubility and lowers the maximum concentration to < 0.1 mM, making it the least water soluble of the complexes. Conversely when the more hydrophilic PTA ligand is used the maximum concentration is greatly increased, with **3Na** dissolution of up to ~3 mM in pure water. The significantly greater water solubility of the **3Na** complex makes it one of the most

water-soluble diiron complexes reported to date. The CN-containing complexes are expected to be even more water soluble based on the original report by Pickett and co-workers,[26] however no quantitative data on their solubilities has been described. It should be noted that the solubilities for all of the complexes are measured in pure water; the addition of small amounts of salt (NaCl, KCl, or Et_4NCl) results in the partial precipitation of the complexes from solution.

Table V-2. Concentrations of **1Na** - **5Na** in H_2O at 22 °C.

Complex	Concentration in H_2O
1Na	~ 1.1 mM
2Na	~ 1.4-1.9 mM
3Na	3 mM
4Na	<0.1 mM
5Na	~ 1.4-1.9 mM

X-ray Diffraction Studies of 1Na and 3TEA and 4TEA

Table V-3 lists the crystal data for the five structures. Dr. Mike Singleton reported the structure of $Et_4N^+(\mu\text{-}SCH_2N(C_6H_4SO_3^-)CH_2S)[Fe^I(CO)_3]_2$, **1TEA**, however the sodium salt, **1Na**, was not obtained crystalline in his work.[64] However, upon cooling a THF solution of **1Na** at 5 °C overnight in the presence of a small amount of water, large X-ray quality crystals grew. While similar to the Et_4N^+ structure there are key differences between the two salts. The extended packing diagram of **1Na**, Figure V-5, shows that two Na^+ ions interact with adjacent sulfonate groups and bridge between pairs of the diiron moieties. In addition to a THF solvent molecule that also binds to the Na^+, two water molecules connect each Na^+ to the Na^+ of an adjacent dimer to create a two dimensional array of the diiron molecules in the solid state. Though not within bonding distance to the Na^+, an apical carbonyl O atom interacts with Na^+ leaving it with a pseudo-square pyramidal geometry. A long range ion-dipole interaction between the Na^+ and the carbonyl oxygen could be the explanation for the increased C1-Fe1-Fe2-C6 torsion angle of **1Na**, 25.7°, compared to **1TEA**, 7.9°.

117

Table V-3. Crystallographic experimental data for the complexes **1Na**, **2TEA** - **5TEA**.

Complex	1Na	2TEA	3TEA	4TEA	5TEA
Formula Weight	655.20	768.41	801.49	906.60	796.48
Temperature (K)	110(2)	110(2)	110(2)	110(2)	110(2)
Wavelength (Å)	1.54178	0.71073	1.54178	1.54178	0.71073
Z	2	4	4	2	4
$D_{calc'd}$ (Mg/cm^3)	1.753	0.671	1.527	1.455	1.440
μ(mm^{-1})	12.436	0.509	9.241	7.838	1.092
Crystal System	triclinic	orthorhombic	monoclinic	triclinic	monoclinic
Space Group	P-1	$Pca21$	$P2/n$	P-1	$P21/c$
a(Å)	6.4151(9)	14.046(14)	14.968(2)	10.11(18)	10.311(2)
b(Å)	12.6371(9)	33.262(15)	7.6777(11)	11.29(19)	34.159(7)
c(Å)	15.6834(16)	16.28(3)	30.718(4)	18.607(3)	10.437(2)
α	96.703(2)	90.00	90.00	102.336	90
β	95.498(9)	90.00	99.042(7)	93.946(6)	91.713(2)
γ	98.239(10)	90.00	90.00	90.895(6)	90
$R_1{}^a$, $wR_2{}^b$(%) [I>2σ(I)]	0.0840, 0.2325	0.0738, 0.1362	0.0806, 0.1543	0.0521, 0.0982	0.0428, 0.1036
$R_1{}^a$, $wR_2{}^b$(%) all data	0.1020, 0.2550	0.1649, 0.1692	0.1598, 0.1828	0.0937, 0.1080	0.0560, 0.1094

[a] $R_1 = \Sigma||F_o| - |F_c||/\Sigma|F_o|$

[b] $wR_2 = [\Sigma w(F_o{}^2 - F_c{}^2)^2/ \Sigma w(F_o{}^2)^2]^{1/2}$

Table V-4 lists selected metric parameters of (μ-pdt)[Fe(CO)$_3$]$_2$ (**pdt**),[27] **1TEA**,[64] and **1Na**. In **1** the Fe(CO)$_3$ units are eclipsed and there is only a slight increase in the C1-Fe1-Fe2-C6 torsion angle between the apical carbonyl units for **1TEA**. However, when the Et$_4$N$^+$ counterion is exchanged for a Na$^+$, this torsion angle increases by ~18 ° (25 ° > **1**). In the [Fe-Fe]-hydrogenase enzyme active site, a number of dipole-dipole and hydrogen bonding interactions are purported to stabilize the unique geometry and semi-bridging carbonyl. The possibility that an ion dipole interaction in the model complexes could be used to enforce structural changes is thus intriguing. Nevertheless, UV spectroscopic studies showed no discernable difference between **1TEA** and **1Na** in the solvents used in this study indicating that these interactions in **1Na** exist only in the confines of the solid state.
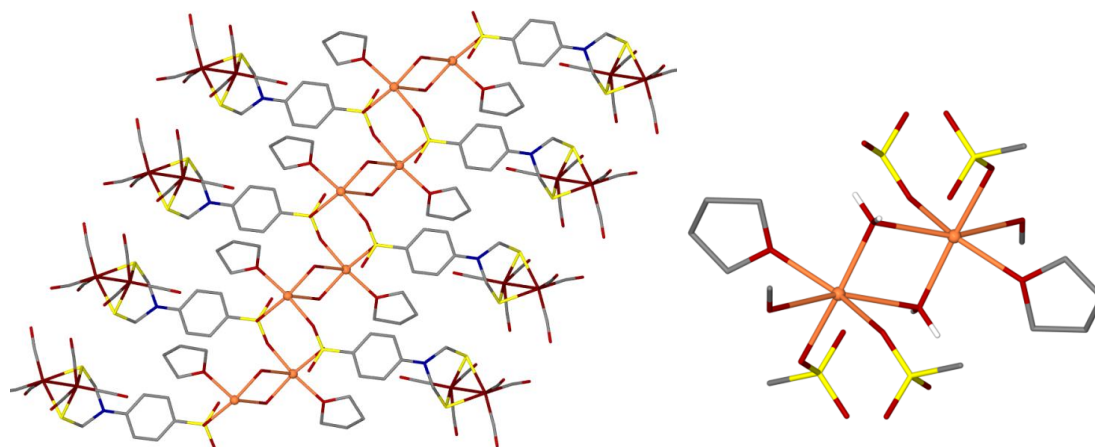
Figure V-5. (Left) Extended structure of **1Na** as a stick model showing the sodium ion-controlled array in the solid state. (Right) Close up view of the Na$^+$ ions showing the coordination environment around them. All protons except the water protons have been removed for clarity.

Table V-4. Comparison of selected metric data for **pdt**,[27] **1TEA**,[64] and **1Na.**

	pdt[27]	**1TEA**	**1Na**
Fe-Fe (Å)	2.510(1)	2.498(1)	2.512(6)
Fe-C $_{avg}$ (Å)	1.800	1.797	1.786
C-O$_{avg.}$ (Å)	1.136	1.140	1.155
Fe(1)-S(1) (Å)	2.254(1)	2.251(1)	2.259(8)
Fe(1)-S(2) (Å)	2.249(1)	2.269(1)	2.282(7)
Fe(2)-S(1) (Å)	2.254(1)	2.257(1)	2.280(8)
Fe(2)-S(2) (Å)	2.249(1)	2.278(1)	2.275(8)
S(1)-C(7) (Å)	1.823(4)	1.860(5)	1.86(3)
S(2)-C(8) (Å)	1.818(4)	1.861(5)	1.79(3)
Fe(1)-S(1)-Fe(2) (°)	67.67(4)	66.97(4)	66.8(2)
Fe(1)-S(2)-Fe(2) (°)	67.85(4)	67.02(4)	67.3(2)
Fe(2)-Fe(1)-C(1) (°)	148.3	147.4(1)	155.7(9)
Fe(1)-Fe(2)-C(6) (°)	148.3	155.8(2)	148.1(1)
C(1)-Fe(1)-Fe(2)-C(6) (°)	0	7.9(5)	25.7(1)

Despite repeated attempts, crystals of X-ray quality were not obtained for the Na^+ salts of the substituted complexes. However, Dr. Mike Singleton crystallized the respective Et_4N^+ salts of **2TEA** and **5TEA** through slow diffusion of ether into a CH_2Cl_2 solution. The Et_4N^+ salts of **3TEA** and **4TEA** were crystallized by the author through slow diffusion of ether into a CH_2Cl_2 solution and by cooling saturated MeOH solutions, respectively. The core structure of all four molecules contains the familiar 2Fe2S butterfly motif common to this class of compounds.[126] Additionally, both irons have a square based pyramidal geometry with the two sulfurs defining the shared edge between them. As is the normal case with the structures of most Fe^IFe^I model complexes the CO ligands are all terminal. The pyramidalization of the N in the dithiolate linker is very modest (ca. 0.1 to 0.2 Å above the C_3 plane around it) throughout the series of complexes and is similar to that observed for **1Na** and the corresponding aniline derivative that lacks the sulfonate group.[64]

The solid state structures of the monosubstituted complexes are consistent with the degrees of substitution indicated by the spectral data and are overall structurally similar to the analogous propanedithiolate complexes.[99,127] For **3TEA** and **4TEA** the phosphine ligands are situated on the iron distal to the aryl sulfonate group, likely to minimize steric repulsions between the ligand and the aryl group of the dithiolate, Figure V-6. The PPh_3 ligand in **4TEA** adopts an apical position, similar to $P(OMe)_3$ in **2TEA**. The PTA ligand in 3**TEA** assumes a basal orientation consistent with its stronger donor ability and small size. The Fe-Fe bond distances for **2TEA** − **4TEA** remain similar throughout the series, Table V-5, with only an ~0.03 Å change from the weaker donor-

containing complexes **2TEA** and **4TEA** to complex **3TEA**; they fall within the typical range for Fe-Fe bond distances found in the diiron model complexes, 2.49 - 2.56.[50] The similarities to previously reported systems means that the sulfonate group, while altering the solubilities, is far enough removed from the diiron unit to have influence on significant changes in the core structure and reactivity of the complexes.
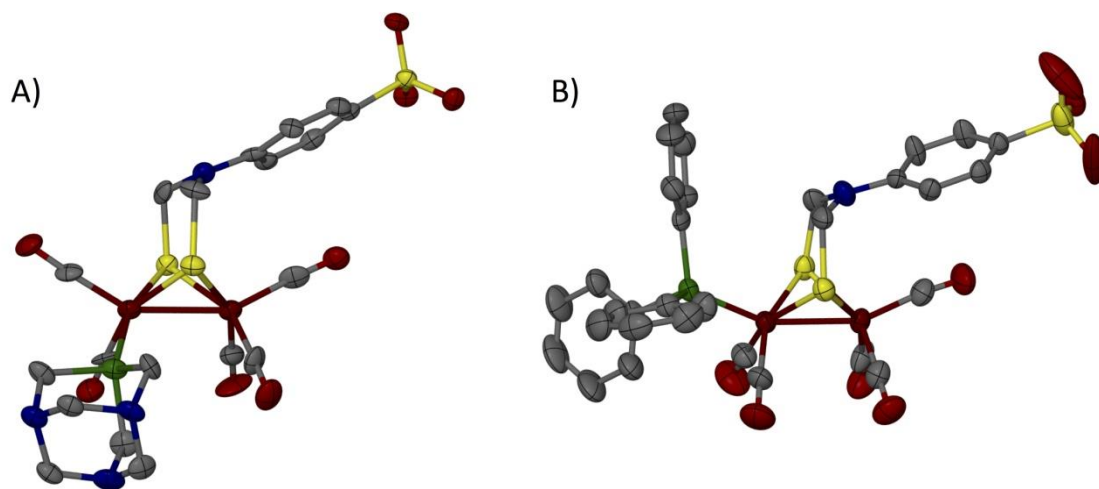
Figure V-6. Structures of A) **3TEA** and B) **4TEA** with thermal ellipsoids drawn at 50% probability level. Protons and the Et_4N^+ counter ions have been omitted for clarity.

Table V-5. Comparison of selected metric data for **2TEA - 5TEA**.

	2TEA*	3TEA	4TEA	5TEA*
Fe-Fe (Å)	2.504(3)	2.532(2)	2.506(1)	2.600(1)
Fe-C $_{avg}$ (Å)	1.836	1.759	1.768	1.763
C-O$_{avg.}$ (Å)	1.106	1.169	1.143	1.154
Fe(1)-S(1) (Å)	2.572(3)	2.260(2)	2.274(1)	2.250(1)
Fe(1)-S(2) (Å)	2.571(2)	2.281(3)	2.269(1)	2.269(1)
Fe(2)-S(1) (Å)	2.186(3)	2.255(3)	2.271(1)	2.252(1)
Fe(2)-S(2) (Å)	2.170(2)	2.256(2)	2.281(1)	2.257(1)
S(1)-C(7) (Å)	1.984(7)	1.985(8)	1.852(5)	1.857(3)
S(2)-C(8) (Å)	1.984(8)	1.982(8)	1.854(5)	1.852(3)
Fe(1)-S(1)-Fe(2) (°)	67.3(1)	68.23(8)	66.92(4)	70.57(3)
Fe(1)-S(2)-Fe(2) (°)	68.3(1)	67.86(7)	66.83(4)	70.35(3)
Fe(2)-Fe(1)-C(1) (°)	154.1(3)	152.6(3)	156.1(2)	152.6(1)
Fe(1)-Fe(2)-L$_{apical}$ (°)	149.0(1)	148.9(3)	156.19(5)	142.7(1)
C(1)-Fe(1)-Fe(2)L$_{apical}$ (°)	5.0(7)	10.5(8)	9.8(5)	11.3(3)

* Crystallized by Dr. Mike Singleton

Electrochemical Studies in MeCN

In MeCN, the complexes show similar electrochemical events as have been reported for the analogous diiron systems with different dithiolates,[90] with both an irreversible Fe^IFe^I/Fe^IFe^0 reduction and irreversible Fe^IFe^I/Fe^IFe^{II} oxidation, Figure V-7. While all of the oxidative events follow the expected trend based on the donor abilities of the ligands as established from $\nu(CO)$ infrared studies, the reductive events do not. The mono-substituted complexes are all reduced at ~ -1.8 V. The stronger donor containing complex, **3Na**, is reduced at slightly more positive potentials than either **2Na** or **4Na,** Table V-6. For complexes **2Na** and **3Na**, a second oxidative event appears at ca. 100 mV. This event is not present when the reductive scan is stopped prior to the Fe^IFe^I/Fe^IFe^0 reduction and is thus attributed to a degradation product of the first reduction. While all of the oxidative events follow the expected trend based on the donor abilities of the ligands as established from $\nu(CO)$ infrared studies, the reductive events do not, and instead the mono-substituted complexes are all reduced at ~ -1.8 V. More interesting is the fact that the stronger donor containing complex, **3Na**, is reduced at slightly more positive potentials than either **2Na** or **4Na**. The differences are more pronounced in their electrochemical response to HOAc, added as a proton source for electrocatalytic reduction of H^+ to H_2.

Table V-6. Electrochemical data for **2Na - 5Na** in MeCN.

Complex	Ep$_c$ (V)*	Ep$_a$ (V)*
1Na	-1.61	0.59
2Na	-1.85	0.40
3Na	-1.81	0.22
4Na	-1.85	0.31
5Na	-2.24	-0.19

*Referenced to Cp$_2$Fe/Cp$_2$Fe$^+$
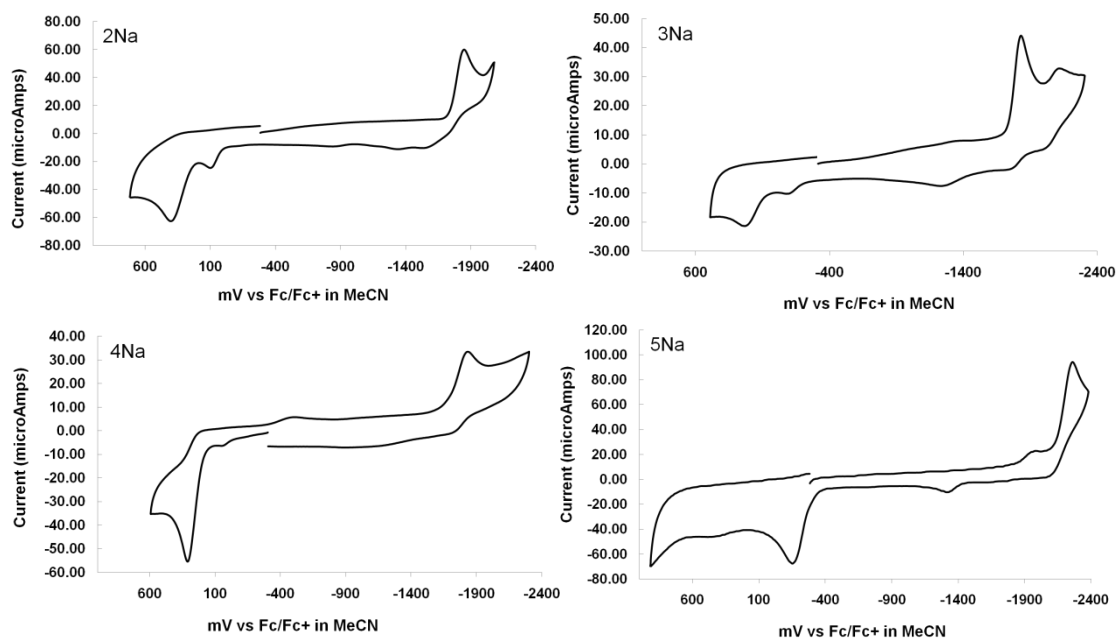
Figure V-7. Cyclic voltammograms of complexes **2Na**, **3Na**, **4Na** and **5Na** in MeCN with 0.1 M Bu$_4$NBF$_4$ at a scan rate of 200 mV/s. Concentration of all samples is 2mM.

For complex **2Na** dissolved in MeCN, upon addition of HOAc an increase in the current response of the reductive event around -2.10 V is observed and distinguishable from the event attributed to reduction of HOAc on glassy carbon, Figure V-8. The fact that this response occurs at potentials past the initial reduction of **2Na** is consistent with trends reported for the less electron rich model complexes.[96-98,106,128,129] Similarly, complexes **3Na** and **4Na** exhibit an increase in the current well beyond their first reductive events, -2.24 and -2.15 V respectively. While both **2Na** and **3Na** show an anodic shift for this event at higher concentrations of HOAc, the increase observed in **4Na** shifts to more positive potentials with incremental addition of the acid similar to the behavior observed in **5Na**. Unlike the other substituted complexes **5Na** shows a response to HOAc at the first reduction potential, which follows a ECEC mechanism.
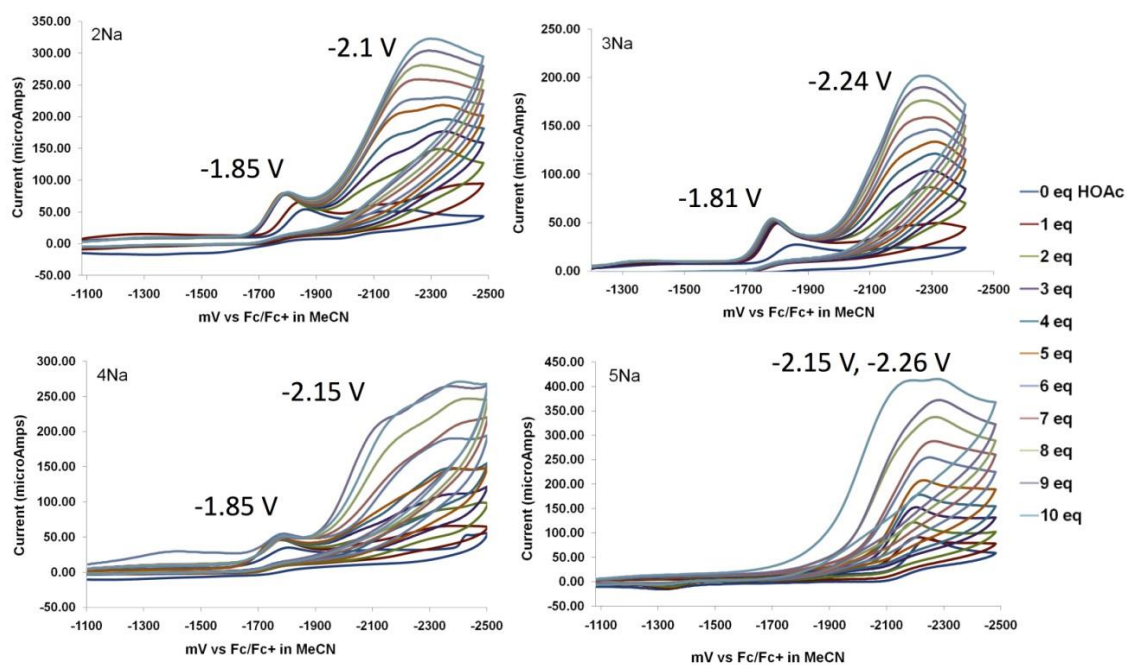
Figure V-8. Cyclic voltammograms of complexes **2Na**, **3Na**, **4Na** and **5Na** in MeCN with 0.1 M Bu$_4$NBF$_4$ at a scan rate of 200 mV/s showing the effect of added HOAc. Concentration of all samples is 2mM.

Electrochemical Studies of 2Na – 5Na in H$_2$O

The increased water solubility of the complexes permits electrochemical examination in aqueous solutions, Figure V-9. Similar to MeCN solutions, most of the compounds in H$_2$O show both an irreversible oxidation and reduction, Table V-7. Similar to what was observed in MeCN the reductive events of **2Na** and **4Na** are in a similar range, -1.39 to -1.45 V, and are not entirely consistent with expected changes resulting from the donor abilities of the ligands. For complex **5Na** the reductive event seen in MeCN solution is not observed and is likely beyond the solvent window. While the data for comparison of the aqueous electrochemistry to other diiron model

128

complexes is still strongly limited by the scarcity of water soluble systems, comparison of **3Na** to the similar ligand substituted DAPTA complex by Sun and co-workers shows that the two compounds have similar reductive events at -1.45 and -1.5 respectively.[125] Complexes **2Na** and **5Na** adsorb onto the surface of the glassy carbon electrode, resulting in changes in the observed potentials for the redox events, and require continual cleaning of the electrode to reproduce the events of the initial scan. At no point do the sulfonate species react with water; they are surprisingly stable, showing no change in the electrochemical response after being left in deaerated solution for several hours. Dr. Mike Singleton showed that in the presence of β-cyclodextrin, all of the complexes show noted decreases in the current intensity associated with both the reductive and oxidative events. This is commonly seen in other electrochemical studies of inclusion complexes and is attributed to the slower diffusion of the host-guest complex relative to the free guest.[130]

Table V-7. Electrochemical data for **2Na - 5Na** in H_2O.

Complex	Ep_c (V)[a]	Ep_a (V)[a]
1Na	-1.22	0.78
2Na	-1.45	0.71
3Na	-1.39	0.54
5Na	------[b]	0.13

[a]Referenced to Ag/AgCl.
[b]Reduction is beyond the solvent window.
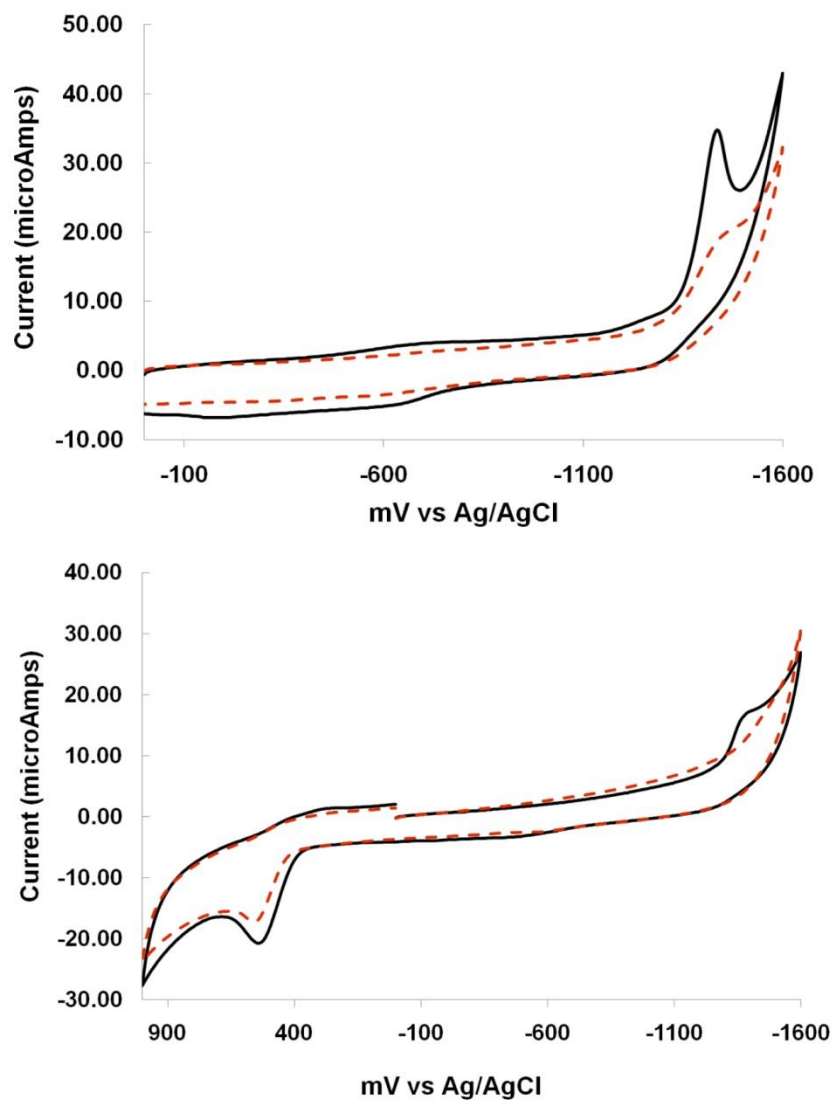
Figure V-9. Cyclic voltammograms of complexes **2Na** (top) and **3Na** (bottom) in 0.01 M aqueous NaCl in the absence (black line) and presence (red line) of 1 mM β-cyclodextrin. Scans were run at 200 mV/s with sample concentration of 0.1 mM.

The electrochemical response to HOAc was also studied for the water-soluble complexes in aqueous solutions. Because the first reduction is beyond the solvent window and complex **5Na** does not react with HOAc, the changes in its voltammograms with added HOAc are indistinguishable from voltammograms of pure HOAc increments itself. However, for complexes **2Na** and **3Na** show notable changes in the current intensities for the reductive events similar to that observed for the parent complex **1Na**. Upon addition of HOAc to a solution of **2Na**, there is an increase in current for the Fe^IFe^I/Fe^IFe^0 reduction at -1.45 mV, Figure V-9. This is also a second event ca. 100 mV more cathodic. The presence of multiple events for proton reduction is not surprising as this is generally the case when such studies are carried out in MeCN. Evans and co-workers have proposed that these separate events, observed in MeCN for (μ-pdt)[Fe(CO)$_3$]$_2$, are due to conformational changes that occur upon reduction resulting in multiple conformers that reduce protons at different potentials.[131]
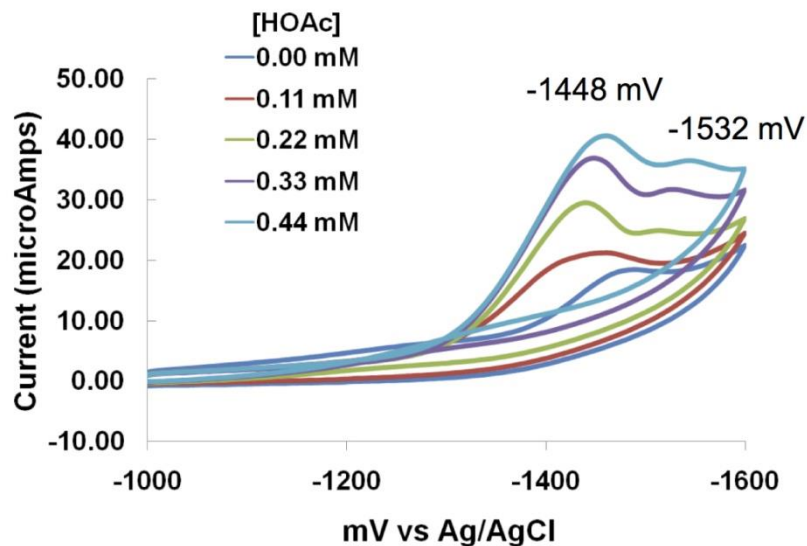
Figure V-10. Aqueous cyclic voltammograms of complexes **2Na** showing the response to incremental addition of HOAc. Scans were run at 200 mV/s with samples concentration of 0.1 mM.

Conclusion

The incorporation of the sulfonate group into the dithiolate of the diiron hexacarbonyl and P-donor ligand substituted derivatives has resulted in greatly increased water solubility as compared to the widely studied propane dithiolate analogs. The aryl sulfonate method shows significant advantages over reported methods for developing water soluble diiron complexes including 1) the facile synthesis of a variety of water-soluble, CO- substituted derivatives, and 2) the stability of resulting complexes in oxygen free water for several hours. Through structural analys

is and electrochemical studies, it was shown that the sulfonate group can impart modest water solubility to the $P(OMe)_3$, PTA, and PMe_3 derivatives without drastically altering their structural or electrochemical properties. The addition of the large hydrophobic PPh_3 ligand however, overwhelms the effects of the sulfonate group and renders the model complex insoluble in H_2O.

CHAPTER VI

A REDUCED 2Fe2S CLUSTER PROBE OF SULFUR-HYDROGEN VS.

SULFUR-GOLD INTERACTIONS[†]

Introduction

Transition metal sulfide clusters are presumed to have played an important role in energy metabolism even before the proliferation of life on planet Earth and before the paleoatmosphere became enriched in oxygen. An appealing hypothesis is that in the presence of CO the simplest of iron-sulfur clusters, Fe_2S_2, developed and detached in a molecular form as $(\mu\text{-}S_2)[Fe(CO)_3]_2$, or possibly its hydrogenated form, $(\mu\text{-}HS)_2[Fe(CO)_3]_2$, from a precursor mineral surface, such as iron pyrite, Figure VI-1.[132-135] As such, these could represent an early abiotic analogue of the diiron hydrogenase, [FeFe]-H_2ase, active site to be later replaced by biosynthetic paths required for protection of the organism from the toxic diatomic ligands in the [FeFe]-H_2ase active site.. In fact $(\mu\text{-}S_2)[Fe(CO)_3]_2$ enjoys current fame as the synthetic precursor to a host of small molecules that are biomimetics of the active site, [FeFe]-H_2ase. It is also a likely candidate for connecting the inorganic to the biological world, via organometallic chemistry, Figure VI-1.

_____

[†]The computational results and their description presented in this chapter was performed by Shengda Ding. Likewise the X-ray diffraction studies were carried out by Jason Denny.
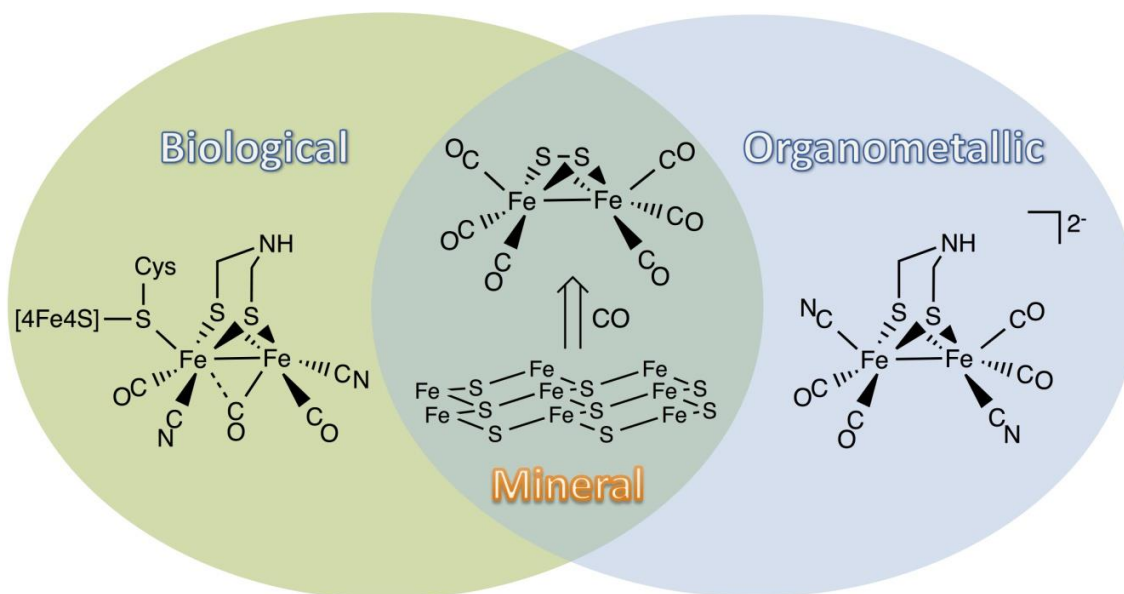
Figure VI-1. Diagram of the biological [FeFe]-hydrogenase active site and the organometallic [FeFe]-hydrogenase active site model connected through the precursor $(\mu\text{-}S_2)[Fe(CO)_3]_2$.

Bona fide studies of SH$^-$ as a ligand are of importance to the bioinorganic chemistry of iron, however studies of isolated Fe-SH units are sparse.[136,137] The direct addition of H_2S to low valent, complexed metals is known to proceed with H_2 loss and incorporation of the SH unit as an anionic ligand to the partially oxidized metal.[136] It has been proposed by Schoonen, et al. that dissociation of H_2S absorbed onto a pyrite suface results in SH binding to pyrite at elevated temperatures.[138,139] Discrete hydrosulfido complexes can also be synthesized through protonation of sulfido ligands, an example of

which is the protonation of the reduced, anionic sulfido-bridged species, $(\mu$-S$)_2$[Fe(CO)$_3$]$_2^{2-}$, to form $(\mu$-SH$)_2$[Fe(CO)$_3$]$_2$.

The spectroscopic signatures (ν(CO) and NMR spectra) of $(\mu$-SH$)_2$[Fe(CO)$_3$]$_2$ have been defined for decades, however its X-ray crystal structure is until now unreported.[38] Interestingly its ^{1}H NMR spectrum displays four resonances, in the range of 0.2 to -2.5 ppm, representing the three isomers shown in Figure VI-2. Two of these isomeric forms, syn_{eq} and anti, are also known for the analogous alkyl thiolates (μ-SR$)_2$[Fe(CO)$_3$]$_2$. The steric hindrance of nearby alkyl groups in the syn_{ax}, or the *up, up* orientation of the alkyl groups on sulfur, is apparently sufficient to prohibit that form, although S to S connective bridges such as –CH$_2$CH$_2$- and –CH$_2$CH$_2$CH$_2$- are easily synthesized and stable.[38,140] In fact, through a condensation reaction, the hydrosulfido groups in the $(\mu$-SH$)_2$[Fe(CO)$_3$]$_2$ complex are synthons for the μ-SCH$_2$NHCH$_2$S unit that is a known requirement for the catalytic activity of the diiron hydrogenase, Figure VI-1.[63]
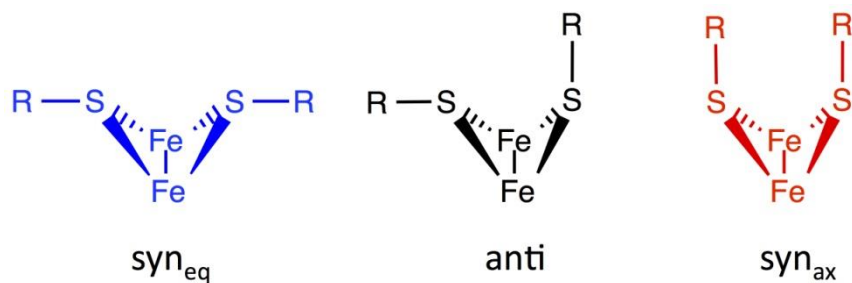
Figure VI-2. Three possible stereo-isomers of bis-alkylthiolate- and hydrosulfido-bridged diiron complexes.

As highlighted by F.G.A. Stone in 1984, and further explored by Hoffmann and Mingos, the Ph_3PAu^+ ion may serve as a surrogate for the proton in many organometallic compounds containing transition metal hydrides.[141,142] The Ph_3PAu^+ unit has also been used to model the protonation of metal bound thiolates, thereby generating thiolate-bridged $M(\mu\text{-}SR)Au^I$ moieties.[143,144] Examples of complexes of this type often show aurophilic interactions that further organize structures.[145] Hence, we were mindful of the possibility that aurolation of the sulfurs of the deprotonated form of the dihydrosulfide complex, $(\mu\text{-}S)_2[Fe(CO)_3]_2^{2-}$, might result in higher order aggregates. Nevertheless, application of the isolobal analogy of Ph_3PAu^+ ⇌ H^+ resulted in the isolation of the analogues, $(\mu\text{-}SAuPPh_3)_2[Fe(CO)_3]_2$ and $(\mu\text{-}SH)_2[Fe(CO)_3]_2$ complexes, which have been characterized by X-ray diffraction. The spectroscopic properties and chemical reactivity were compared for the two as well as the "nickelated" complex, $(\mu_3\text{-}S)_2Ni(dppe)[Fe(CO)_3]_2$.[39,146] Interestingly, gold has been used in explorations of heterometallic sulfides, derived from co-precipitation of Au(I) with pyrite from hydrothermal fluids, presumably generating some form of $[Fe(\mu\text{-}S)Au^I]_y$ aggregates.[139]

Synthesis of $(\mu\text{-}SH)_2[Fe(CO)_3]_2$ and $(\mu\text{-}PPh_3AuS)_2[Fe(CO)_3]_2$

Reduction of the disulfide bond of $(\mu\text{-}S_2)[Fe(CO)_3]_2$ by two equivalents of $LiEt_3BH$ in THF at -78 °C produces the $(\mu\text{-}S)_2[Fe(CO)_3]_2^{2-}$ dianion, whose versatility has been amply demonstrated by the preparation of myriad derivatives containing features of the [FeFe]-H_2ase active site.[63,119,147] Following the method described by Seyferth, et al., protonation of the dianion with 2 equivalents of trifluoroacetic acid leads to the

formation of $(\mu\text{-}SH)_2[Fe(CO)_3]_2$, **1**, and shifts the $\nu(CO)$ bands of the dianion (2029(w), 2003(s), 1956(s)) by $\sim +50$ cm^{-1} as expected for the formation of the neutral SH derivative.[38] The product **1** is an air-sensitive red solid which has similar $\nu(CO)$ stretching frequencies as its persulfide precursor, $(\mu\text{-}S_2)[Fe(CO)_3]_2$, Figure VI-3.
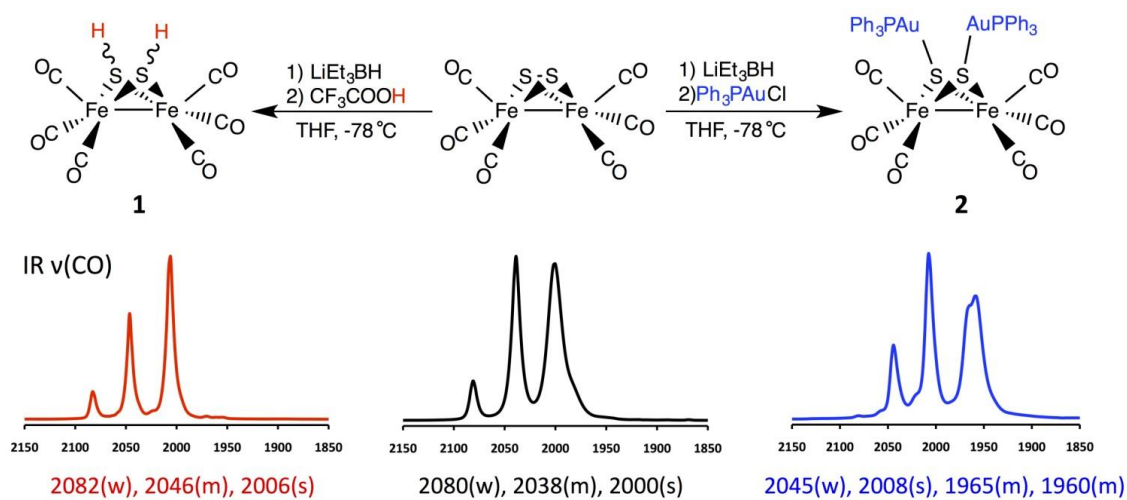
Figure VI-3. Synthesis and IR spectra (THF) of $(\mu\text{-}SH)_2[Fe(CO)_3]_2$ (right), $(\mu\text{-}S_2)[Fe(CO)_3]_2$ (middle), and $(\mu\text{-}PPh_3AuS)_2[Fe(CO)_3]_2$ (left).

138

Complex **2**, $(\mu\text{-SAuPPh}_3)_2[\text{Fe(CO)}_3]_2$, an analog of **1**, was isolated as a thermally

and air stable red solid from the addition of 2 equiv. of Ph_3PAuCl to $(\mu\text{-S})_2[\text{Fe(CO)}_3]_2^{2-}$.

The ν(CO) values in the IR spectrum of **2** show a shift in the ν(CO) bands from the

dianion by only ~ +10 cm^{-1}; whereas there is a ~40 cm^{-1} difference as compared to **1**,

Figure VI-3. This implies there is more negative character on the 2Fe core in **2**, as seen

in other S-bridged polymetallic diiron complexes such as $(\mu_3\text{-S})_2\text{Ni(dppe)}[\text{Fe(CO)}_3]_2$

(also prepared by addition of $(\text{dppe})\text{NiCl}_2$ to $(\mu\text{-S})_2[\text{Fe(CO)}_3]_2^{2-}$).[39,146] In contrast to **1**

and most other $(\mu\text{-SRS})[\text{Fe(CO)}_3]_2$ complexes which are highly soluble in hexanes,

complex **2** as well as the $(\mu_3\text{-S})_2\text{Ni(dppe)}[\text{Fe(CO)}_3]_2$ complex are insoluble. The

indication of greater ionicity in the metallated diiron sulfides as signified by the low

ν(CO) values is consistent with this solubility difference.

Molecular Structures

Complexes **1** and **2** were crystallized by slowly cooling concentrated solutions of

hexanes and THF, respectively. The molecular structures of complexes **1** and **2** were

determined by X-ray diffraction analysis and are compared in Figure VI-4. Complexes **1**

and **2** were refined to R_1 factors of 3.17% and 3.76%, respectively. Complex **1** co-

crystallized with the starting material, $(\mu\text{-S})_2[\text{Fe(CO)}_3]_2$, in a 93:7 ratio. According to the

area of maximum electron densities, the hydrogen atoms on the thiolates in complex **1**

were found in the anti configuration positions, analogous to the gold atoms in complex

2. The $\text{Fe}_2(\text{CO})_6$ units in **1** and **2** are almost superimposable, Figure VI-5.
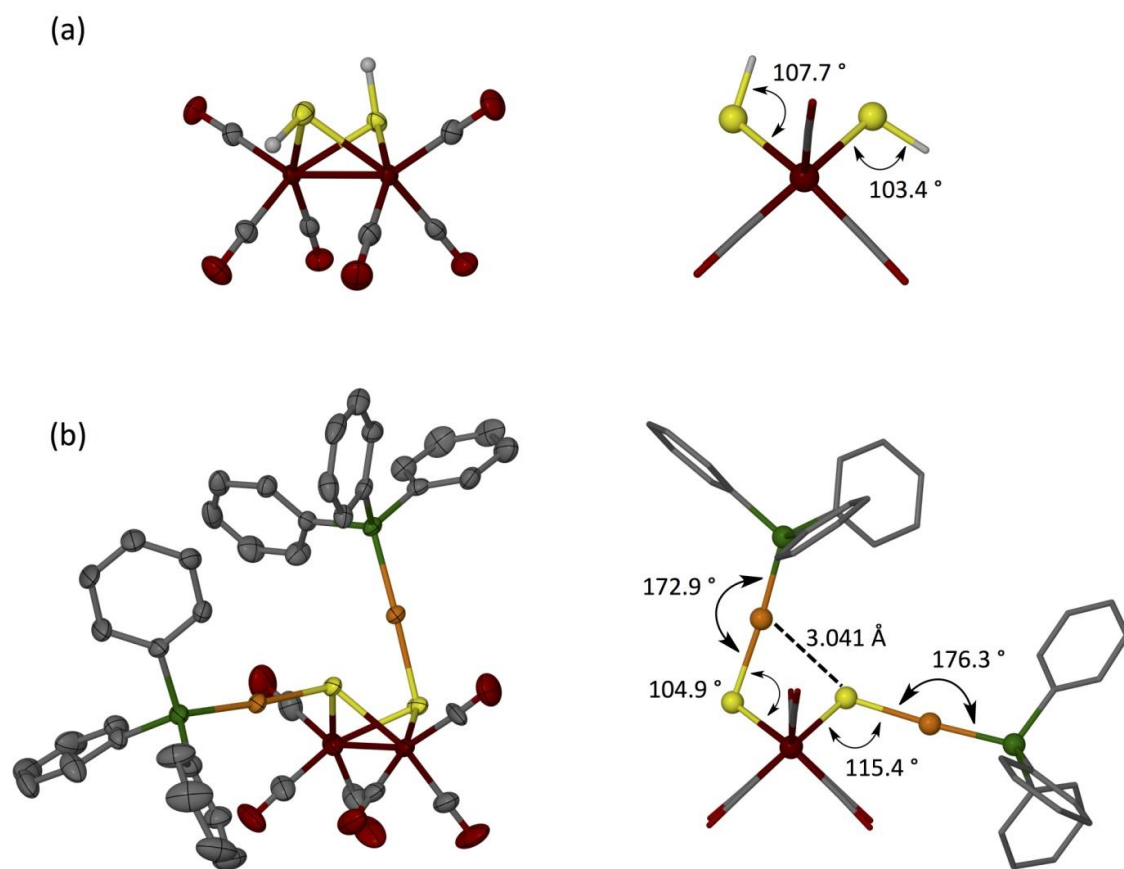
Figure VI-4. Molecular structures of complexes (a) **1** and (b) **2**: (left) side view of thermal ellipsoids drawn at 50% probability level; (right) ball-and-stick view down the iron-iron bond. Average ∠Fe-S-Au are given.
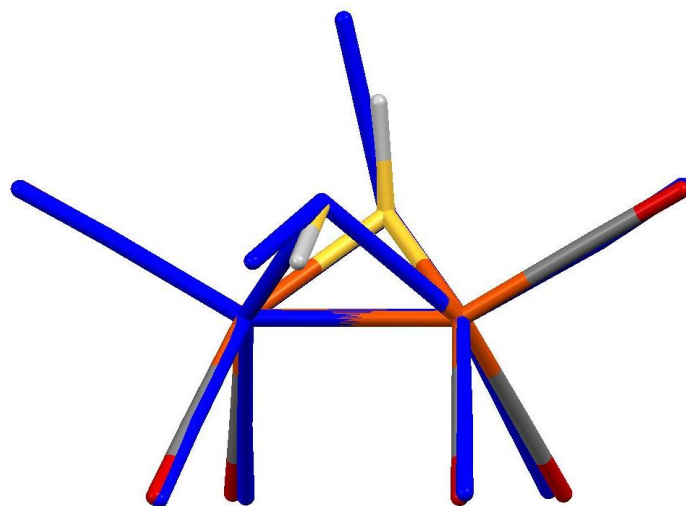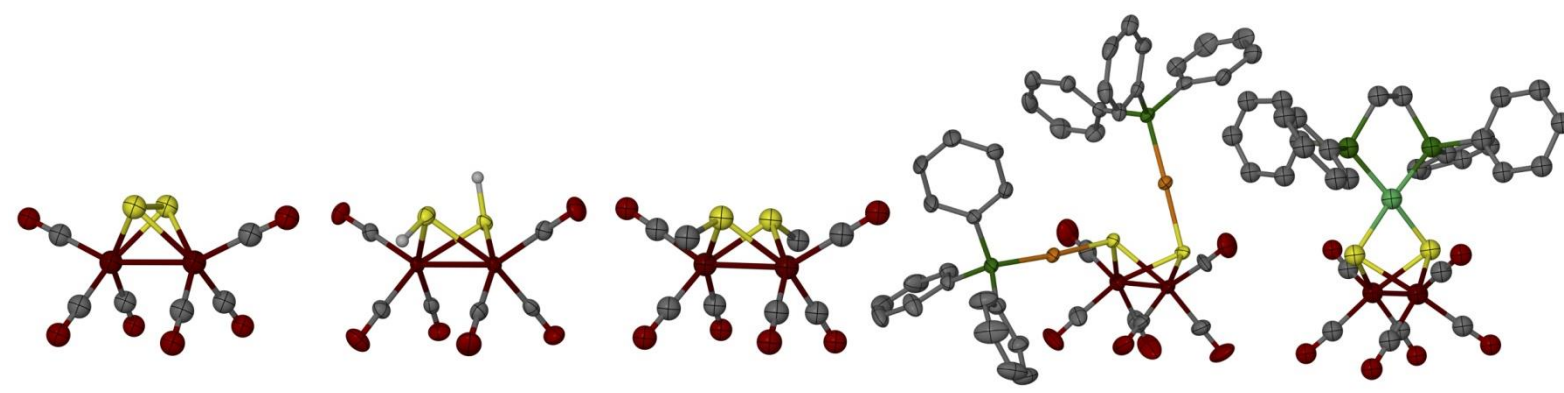
Figure VI-5. Overlay of complexes **1** and **2** (blue) shown in capped stick form with phenyl rings removed for clarity.

Table VI-1. Comparison of selected spectroscopic and metric parameters.

Complex	IR ν(CO)[a]	Fe-Fe (Å)	S---S (Å)	S-Fe-S (°)	Ref
$(\mu\text{-}S)_2[Fe(CO)_3]_2$	2084, 2044, 2007	2.556(1)	2.021	53.76(8)	63
$(\mu\text{-}SH)_2[Fe(CO)_3]_2$ **(1)**	2082, 2046, 2006	2.4962(8)	2.880	79.09(7)	-[b]
$(\mu\text{-}SMe)_2[Fe(CO)_3]_2$	2075, 2040, 2000, 1995	2.516(1)	2.759	75.03	140
$(\mu\text{-}pdt)[Fe(CO)_3]_2$	2073, 2032, 1998	2.511(1)	3.060	85.60(3)	27
$(\mu\text{-}SAuPPh_3)_2[Fe(CO)_3]_2$ **(2)**	2045, 2008, 1965, 1956	2.494(2)	2.977	80.75(8)	-[b]
$(\mu_3\text{-}S)_2Ni(dppe)[Fe(CO)_3]_2$	2047, 2006, 1968, 1956	2.485(6)	2.870	77.2(3)	146

[a] IR spectra obtained in THF.
[b] This work.

Table VI-1 lists selected spectroscopic and metric parameters for complexes **1**, **2**, (μ-S$_2$)[Fe(CO)$_3$]$_2$, (μ-SMe)$_2$[Fe(CO)$_3$]$_2$, (μ-pdt)[Fe(CO)$_3$]$_2$, and (μ_3-S)$_2$Ni(dppe)[Fe(CO)$_3$]$_2$. As shown by the v(CO) stretching frequencies, the electron density on the iron centers varies throughout the series of compounds. As stated previously, complex **1** and its persulfide precursor, (μ-S$_2$)[Fe(CO)$_3$]$_2$, have almost identical v(CO) that are the highest within the series. The two alkylated sulfur compounds, (μ-SMe)$_2$[Fe(CO)$_3$]$_2$ and (μ-pdt)[Fe(CO)$_3$]$_2$, have similar v(CO) values and have shifts in v(CO) bands of ~ -10 cm^{-1} compared to complex **1** and (μ-S$_2$)[Fe(CO)$_3$]$_2$. The two metallated complexes, **2** and (μ_3-S)$_2$Ni(dppe)[Fe(CO)$_3$]$_2$, also have similar v(CO) stretching frequencies and differ from the alkylated complexes by ~ -30 cm^{-1} and complex **1** and (μ-S$_2$)[Fe(CO)$_3$]$_2$ by ~ -40 cm^{-1}. For this series the electron density on the 2Fe core increase in the order of complex **1** ≈ (μ-S$_2$)[Fe(CO)$_3$]$_2$ < (μ-SMe)$_2$[Fe(CO)$_3$]$_2$ ≈ (μ-pdt)[Fe(CO)$_3$]$_2$ < complex **2** ≈ (μ_3-S)$_2$Ni(dppe)[Fe(CO)$_3$]$_2$.

Although the electron density on the 2Fe core differs in this series of compounds, all show similar Fe-Fe distances, ~2.5 Å, with the longest bond exhibited by the starting material, (μ-S$_2$)[Fe(CO)$_3$]$_2$, 2.56 Å. The S---S distance increases from 2.02 Å in (μ-S$_2$)[Fe(CO)$_3$]$_2$, to ~2.9 Å for the other complexes consistent with the loss of the disulfide bond, Figure VI-6. The complex with the largest S---S distance, 3.05 Å, is the bridging dithiolate with a three carbon linker, (μ-pdt)[Fe(CO)$_3$]$_2$, which is similar to complex **2**, 2.98 Å. Accordingly, these two complexes have the largest ∠S-Fe-S as well. The Fe(CO)$_3$ units are eclipsed in the case of (μ-S$_2$)[Fe(CO)$_3$]$_2$, (μ-pdt)[Fe(CO)$_3$]$_2$, and (μ-SH)$_2$[Fe(CO)$_3$]$_2$ (**1**); for example the ∠CO$_{ap}$-Fe-Fe-CO$_{ap'}$ torsion angles are 0°. The

torsion angles for $(\mu\text{-SMe})_2[\text{Fe(CO)}_3]_2$, $[(\text{dppe})\text{Ni}](\mu_3\text{-S})_2[\text{Fe(CO)}_3]_2$, and $(\mu\text{-SAuPPh}_3)_2[\text{Fe(CO)}_3]_2$ (**2**) range from 5.3-7.7°.

The aurolation of sulfurs by Ph_3PAu^+ in complex **2** results in the anti isomer configuration in the solid state structure. The Au---Au distance of 5.19 Å within the complex is beyond that expected for intramolecular aurophilic interactions, as most occur ~3 Å.[148] Likewise the shortest intermolecular Au---Au distance is 7.81 Å, Figure VI-7. The geometry about the gold is largely linear, with $\angle$S-Au-P = 172.9° and 176.3°. The $\angle\text{Fe}_{avg}$-S-Au is 115.4° for the equatorial gold and 104.9° for the axial gold. This contrasts slightly to complex **1** with $\angle\text{Fe}_{avg}$-S-H_{eq} = 103.4 and $\angle\text{Fe}_{avg}$-S-H_{ax} = 107.7°.
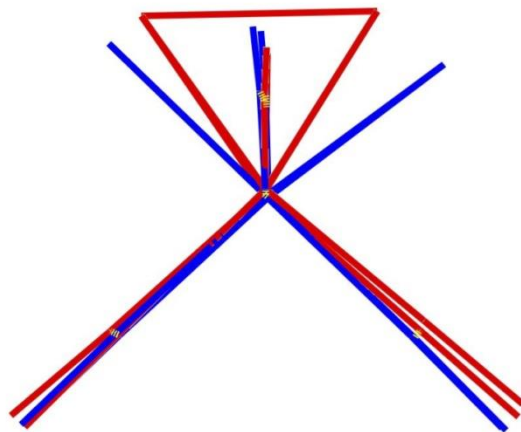
Figure VI-6. Overlay of $(\mu\text{-S}_2)[\text{Fe(CO)}_3]_2$ (red) and $(\mu\text{-SH})_2[\text{Fe(CO)}_3]_2$ (blue) crystal structures.

144
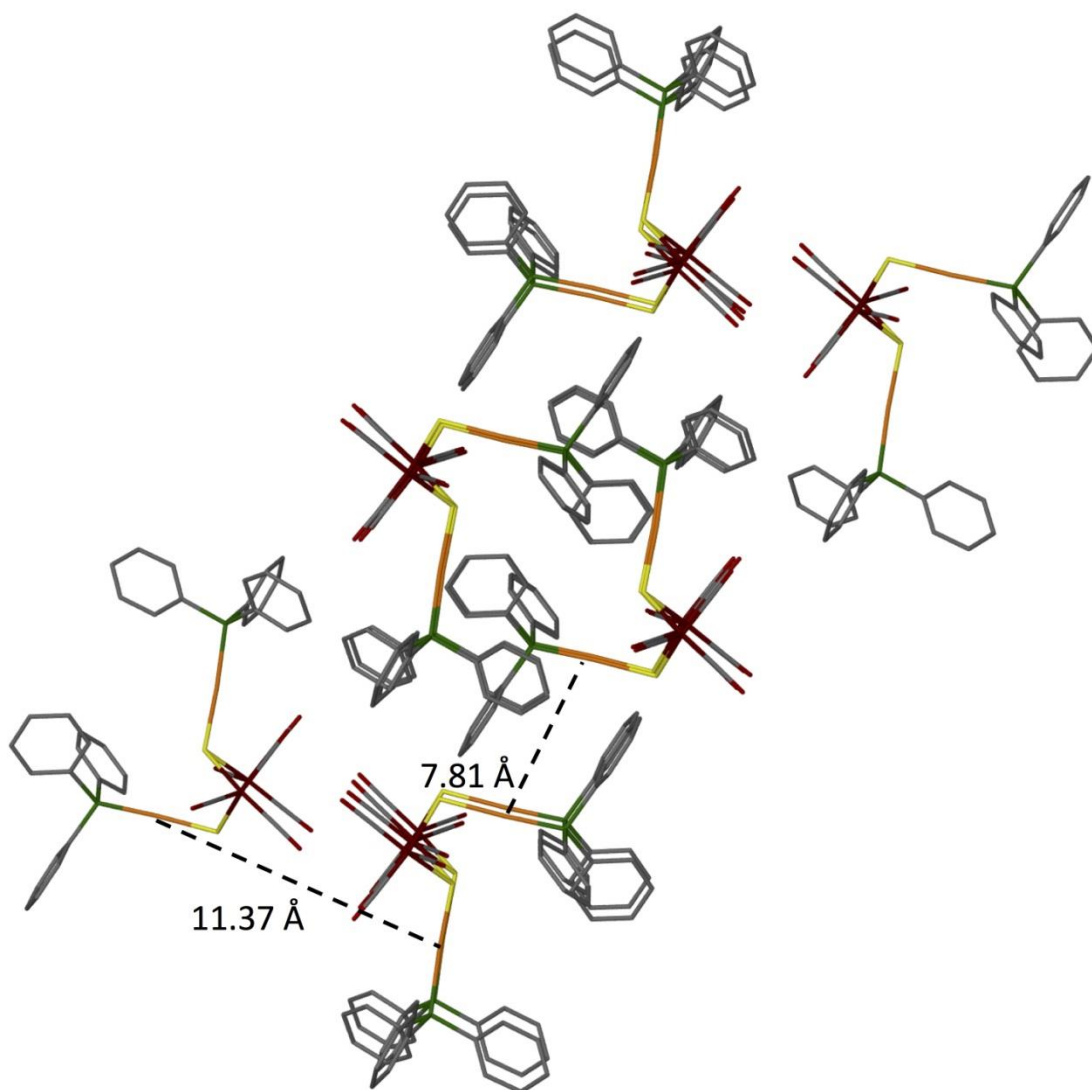
Figure VI-7. X-ray crystal structure packing diagram of complex **2** viewed down the a axis, displaying the intermolecular Au---Au distances.

The molecular structures may provide clues as to the lack of the syn_{eq} isomer for

complex **2**. While the average Au-S bond distance is 2.315 Å, the observed distance of

gold to the adjacent sulfur within the anti isomer is of 3.041(2) Å, i.e., shorter than the sum of the van der Waals radii of 3.24 Å. Space-filling models indicate the overlap and presumed interaction, Figure VI-8. This Au---S interaction is also seen in other dinuclear gold complexes, where one ∠S-Au-P is largely linear (~ 172°) and the other possesses an irregular trigonal planar geometry (~ 163°).[149,150] The difference in the ∠S-Au-P is caused by the Au---S interaction in these complexes (~ 2.7 Å). The Au---S interaction in complex **2** appears to be much weaker, if at all, as one of the ∠S-Au-P is only slightly less linear than the other (172.9° and 176.3°) and the Au---S distance is 0.3 Å longer than other complexes in the literature.
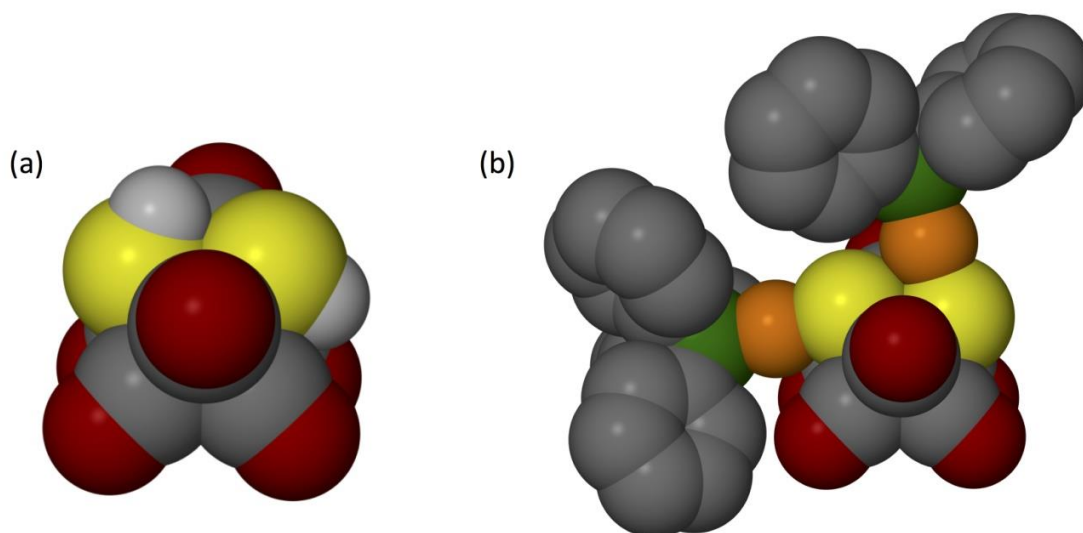
Figure VI-8. Space filling models from the crystal structure of (a) $(\mu\text{-SH})_2[\text{Fe(CO)}_3]_2$ (**1**) and (b) $(\mu\text{-PPh}_3\text{AuS})_2[\text{Fe(CO)}_3]_2$ (**2**) in the anti configuration.

NMR Studies

The ^1H NMR spectrum of $(\mu\text{-SH})_2[Fe(CO)_3]_2$ in $CDCl_3$ at 22 °C displays four resonances, indicative of three isomers present at room temperature, Figure VI-9. Consistent with earlier conclusions,[38] the resonances at δ = 0.22 and -2.21 ppm are assigned to the equatorial and axial hydrogens of the anti isomer, anti-**1**, defined in Figure VI-9. The resonances at δ = -0.40 (syn_{ax}-**1**) and -2.43 (syn_{eq}-**1**) ppm are assigned to the protons of the two syn isomers.[38] The 14:4:4 (anti:syn_{eq}:syn_{ax}) ratio of the isomers indicates that the anti isomer is the major product, which is reported by Seyferth et al., albeit with a slightly different isomer ratio, 14:2:1. Derivatives in the form $(\mu\text{-}SR)_2[Fe(CO)_3]_2$, R = Me, Et, and Ph, have been isolated and separated by chromatography into two isomers, identified as anti and syn_{eq}, in ~ 4:1 ratio.[140,151-153] In these cases the absence of the syn isomer is ascribed to steric encumbrance, which is overcome in the linked thiolates, i.e., $(\mu\text{-edt})[Fe(CO)_3]_2$ and $(\mu\text{-pdt})[Fe(CO)_3]_2$, as well as complex **1**. As might be expected, with increasing size of the R groups, the equilibrium of the isomers shifts to favor the anti isomer. Bor et al. concluded that the compromise of the repulsive forces of the R groups and the CO ligands in the syn_{eq}, and that between mutual R groups in the syn_{ax} accounts for the observed isomer ratios.[140] The balance of these forces seems to be quite delicate as various reports over the years find differences, albeit minor, in isomer ratios.
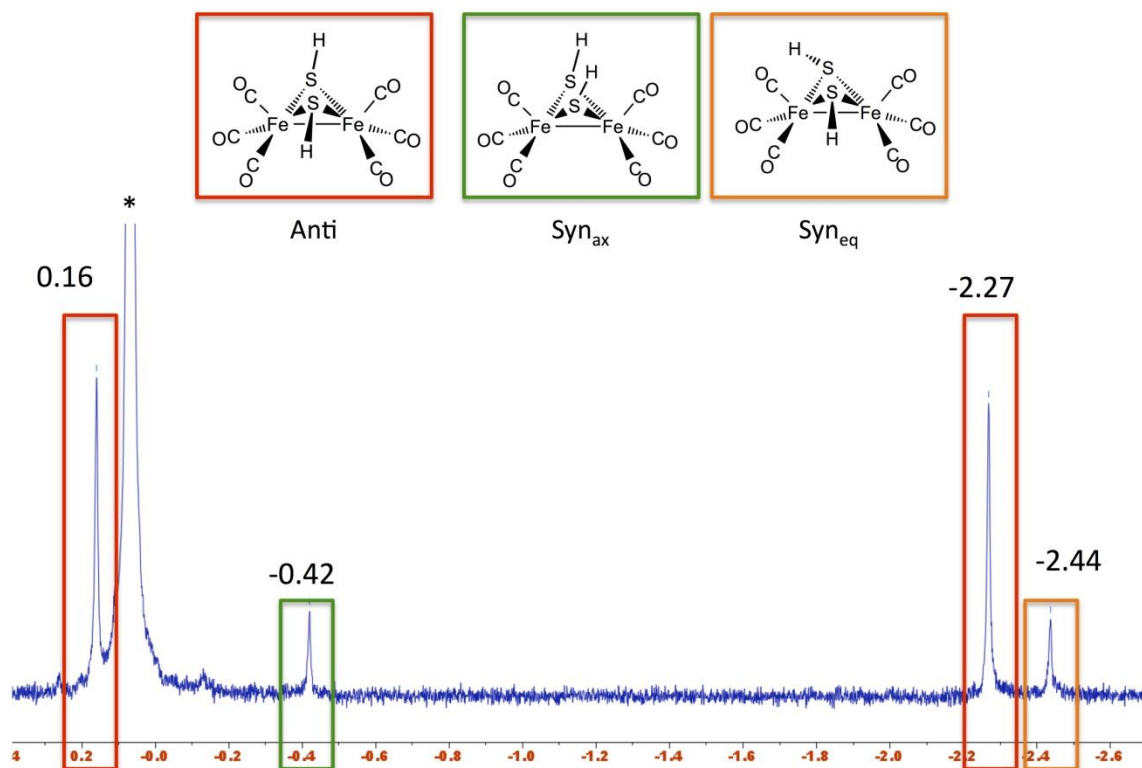
Figure VI-9. The ^{1}H NMR spectrum at 300 MHz in CDCl$_3$ at 22 °C for (μ-SH)$_2$[Fe(CO)$_3$]$_2$ (**1**), showing four resonances assigned to three isomers.

By ^{1}H and ^{31}P NMR spectroscopies we have explored the temperature dependence of the isomer ratios of complexes **1** and **2**. At 30 °C, four resonances are seen in the ^{1}H NMR spectrum for complex **1** in C_6D_6 indicating all three isomers are present, in a ratio of 12:5:4, differing from the ratio observed in $CDCl_3$. Within experimental error of measurement, the ratio was maintained upon warming to 70 °C, with no evidence of broadening of the signals, Figure VI-10. From the ratios obtained from the ^{1}H NMR spectra of complex **1** in C_6D_6, the anti isomer is thermodynamically more stable than the syn_{ax} and syn_{eq} by -0.67 and -0.56 kcal/mol, respectively. The variable-temperature NMR data for complex **1** is consistent with descriptions of the (μ-SMe)$_2$[Fe(CO)$_3$]$_2$ derivative.[140,153] Isolated pure by chromatography, the anti-isomer of (μ-SMe)$_2$[Fe(CO)$_3$]$_2$ is reported to equilibrate into the thermodynamic mixture of anti- and syn_{eq} isomers over the course of several days at 40 °C.
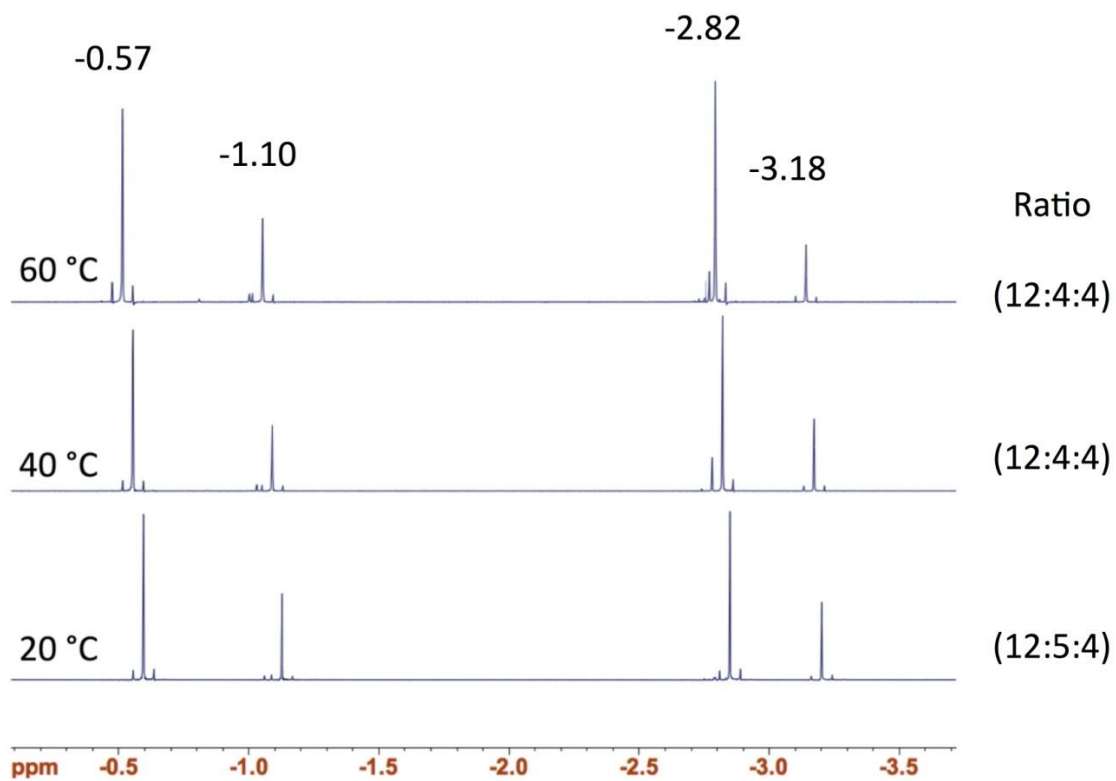
Figure VI-10. Variable-temperature ^{1}H NMR spectra at 500 MHz in C_6D_6 for (μ-SH)$_2$[Fe(CO)$_3$]$_2$ (**1**), showing the ratio of isomers (Anti:Syn$_{eq}$:Syn$_{ax}$) on the right for each spectrum.

At room temperature a single broad ^{31}P resonance is seen at δ 34.8 ppm for complex **2** in CDCl$_3$, indicating equilibration of the two P nuclei, or the fast exchange of the two gold-phosphine moieties, Figure VI-11. This differs from complex **1**, as there is no site exchange of the hydrogens detected at room temperature in the ^{1}H NMR. Upon cooling the sample of complex **2** to -50 °C, two signals are seen at δ 35.6 and 33.6 ppm. Although the signal at 35.6 ppm is broad compared to the sharp signal at 33.6 ppm, the ratio of the two resonances is 1:1. Due to the ratio of the signals, the resonances are presumed to represent the non-equivalent phosphorus nuclei in the anti configuration of complex **2**. The line widths of the two signals suggest that one AuPPh$_3$ unit is undergoing a faster motion than the other. Coalescence of the two signals occurs at ~10 °C. The experimental energy barrier for this exchange was calculated from peak separation and coalescence temperature to be 13.0 kcal/mol, Table VI-2. The intramolecular site exchange energy barrier for complex **2** was obtained using the formulas $\Delta G^{\ddagger} = -(RT)\ln[k_t h/k_b T_{coal}]$ and $k_t = (\pi \Delta v)/2^{1/2}$, where the coalescence temperature (T_{coal}) and peak separation (Δv) are taken from the VT NMR spectra.[94]

Variable-temperature ^{31}P NMR of complex **2** was also recorded in CD$_2$Cl$_2$ and toluene-d$_8$, Figures VI-12 and 13, respectively. A similar exchange rate was seen in toluene-d$_8$ as compared to CDCl$_3$, where one peak sharpens faster than the other at low temperatures. In CD$_2$Cl$_2$ complex **2** displays two sharp peaks at -60 °C that broaden and coalesce at the same rate. Although there is a slight solvent effect on the line width of the signals, within experimental error the energy barrier for this process is not affected, 13.1 (CD$_2$Cl$_2$) and 13.6 kcal/mol (toluene-d$_8$), Table VI-2. A study by Toyota, et al. in

1995 also observed no solvent effect on the inversion barrier of their Au(I) complexes suggesting a sulfur inversion without bond dissociation.[154]
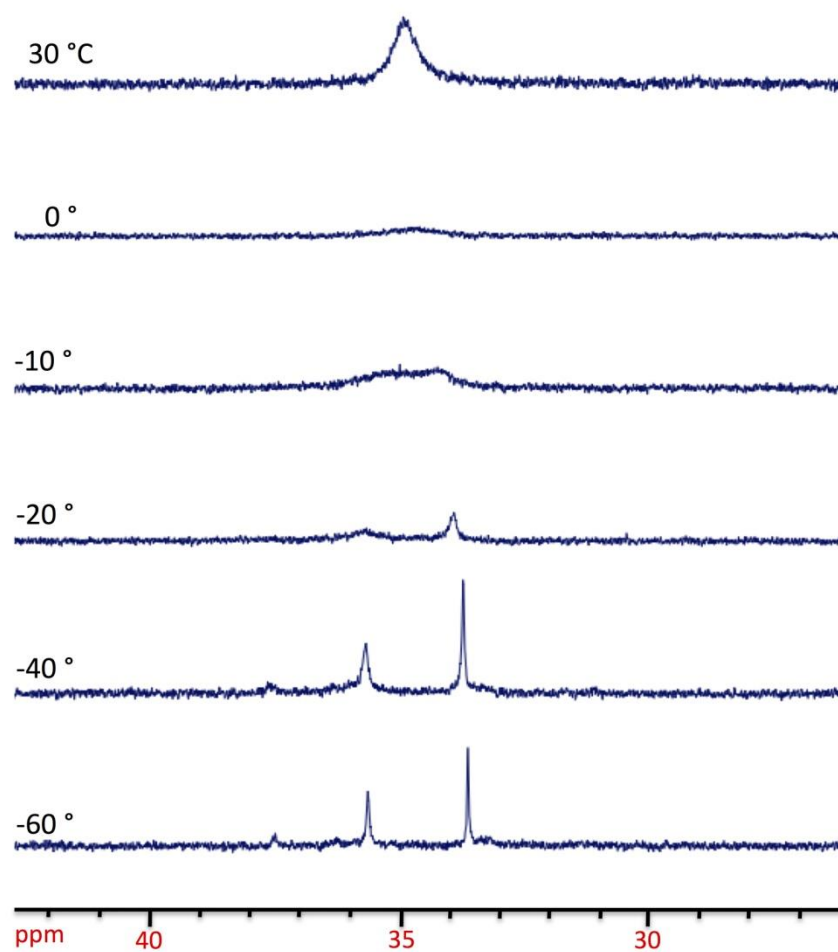
Figure VI-11. Variable-temperature ^{31}P NMR spectra at 300 MHz in CDCl$_3$ for (μ-PPh$_3$AuS)$_2$[Fe(CO)$_3$]$_2$ (**2**).
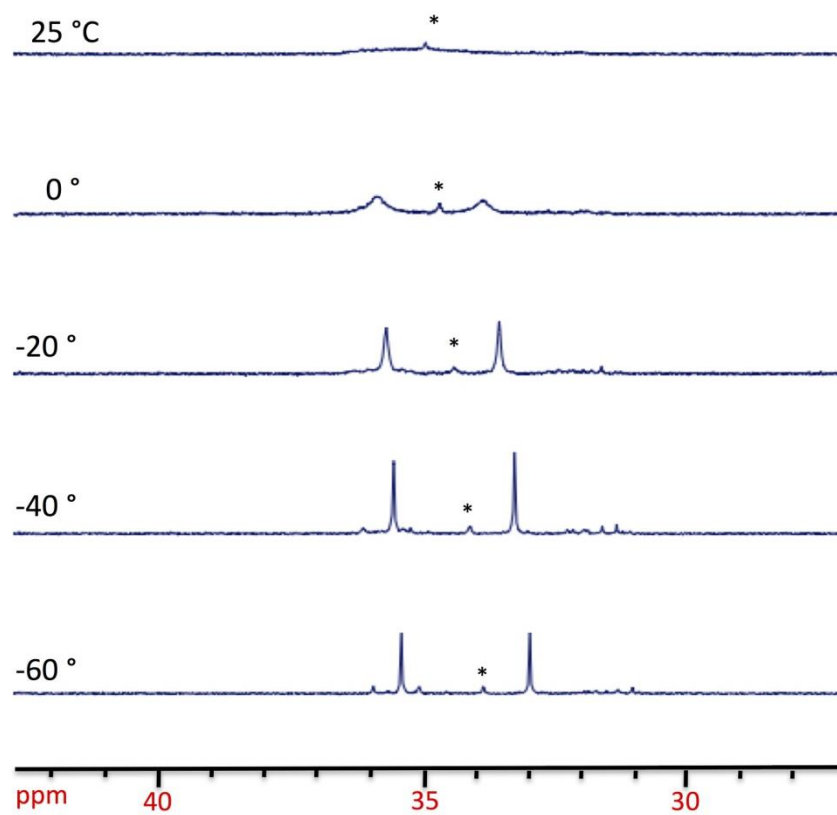
Figure VI-12. Variable-temperature ^{31}P NMR spectra at 300 MHz in CD_2Cl_2 for (μ-PPh$_3$AuS)$_2$[Fe(CO)$_3$]$_2$ (**2**). * Ph$_3$PAuCl
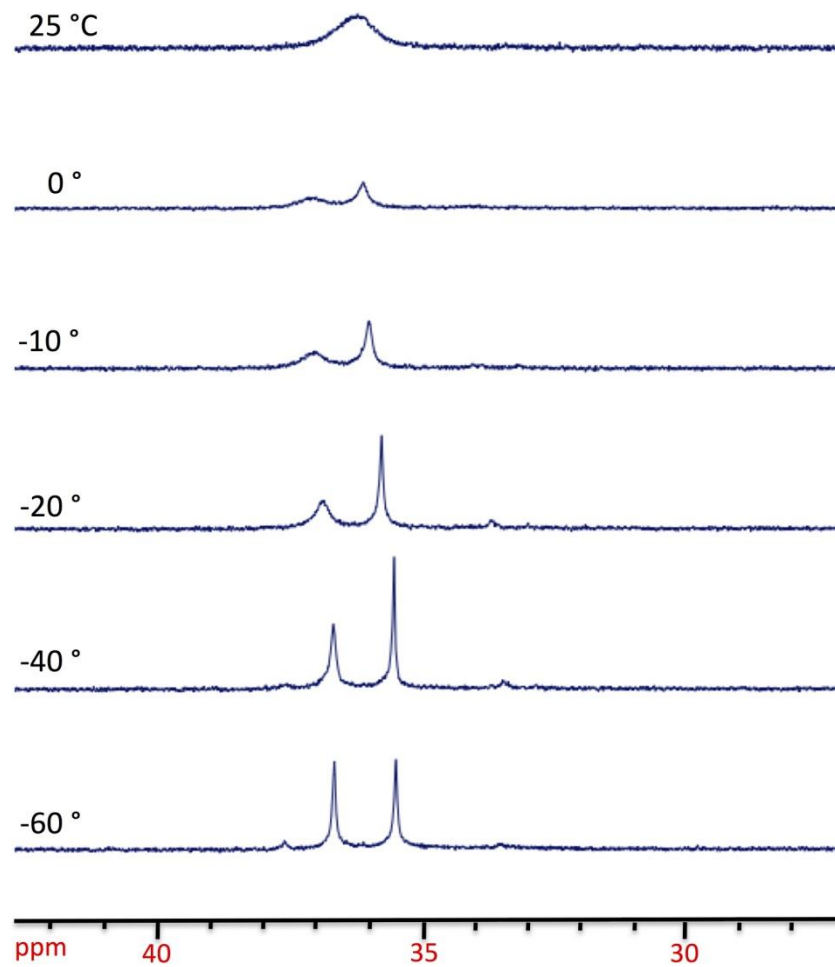
Figure VI-13. Variable-temperature ^{31}P NMR spectra at 300 MHz in toluene-d8 for (μ-PPh$_3$AuS)$_2$[Fe(CO)$_3$]$_2$ (**2**).

Table VI-2. Variable-temperature ^{31}P NMR parameters and site exchange energy barriers for complex **2** in various solvents.

	δ ^{31}P (ppm) at 25 °C	δ ^{31}P (ppm) at -60 °C	Peak Seperation (Δv)	Coalesence Temperature (T_{coal})	G (kcal/mol)[a]
CDCl₃	34.80	35.63, 33.63	2.00 ppm / 242.8 Hz	10 °C / 283.15 K	13.0 (±0.5)
CD₂Cl₂	35.61	35.49, 33.06	2.43 ppm / 295.0 Hz	15 °C / 288.2 K	13.1 (±0.5)
Toluene-d₈	36.40	36.55, 35.37	1.18 ppm / 143.3 Hz	15 °C / 288.2 K	13.6 (±0.5)

[a] Error estimated using ± 10°C for detected coalescence temperature

Computational Studies

Density functional theory (DFT) computations were performed, started by Dr. Ryan Bethel and carried out further by Shengda Ding, to calculate the Gibbs free energy of each isomer of **1** and **2** as well as the activation energy barrier for conversion between the isomers. According to Toyota's review,[154] multiple mechanisms are possible for the inversion of pyramidal sulfur. From the experimental results of Mueting et al., the isomerization between the syn_{eq} and anti isomers of $(\mu\text{-SMe})_2[Fe(CO)_3]_2$, measured in $CDCl_3$ over a range of $45 - 65$ °C, has an $\underline{E}_{act}$ barrier of 29.0 kcal/mol which was presumed to indicate a mechanism requiring Fe-S bond rupture and reformation.[155] However recent computational studies for the same system by Lichtenberger et al. concluded that a simple inversion at sulfur could account for the lowest energy pathway ($\underline{E}_{act} = 26.8$ kcal/mol).[156] Their computations also found that the syn_{ax} isomer of $(\mu\text{-SMe})_2[Fe(CO)_3]_2$ is 7.4 kcal/mol less stable than the anti isomer, thereby accounting for its absence at room temperature, Figure VI-14.
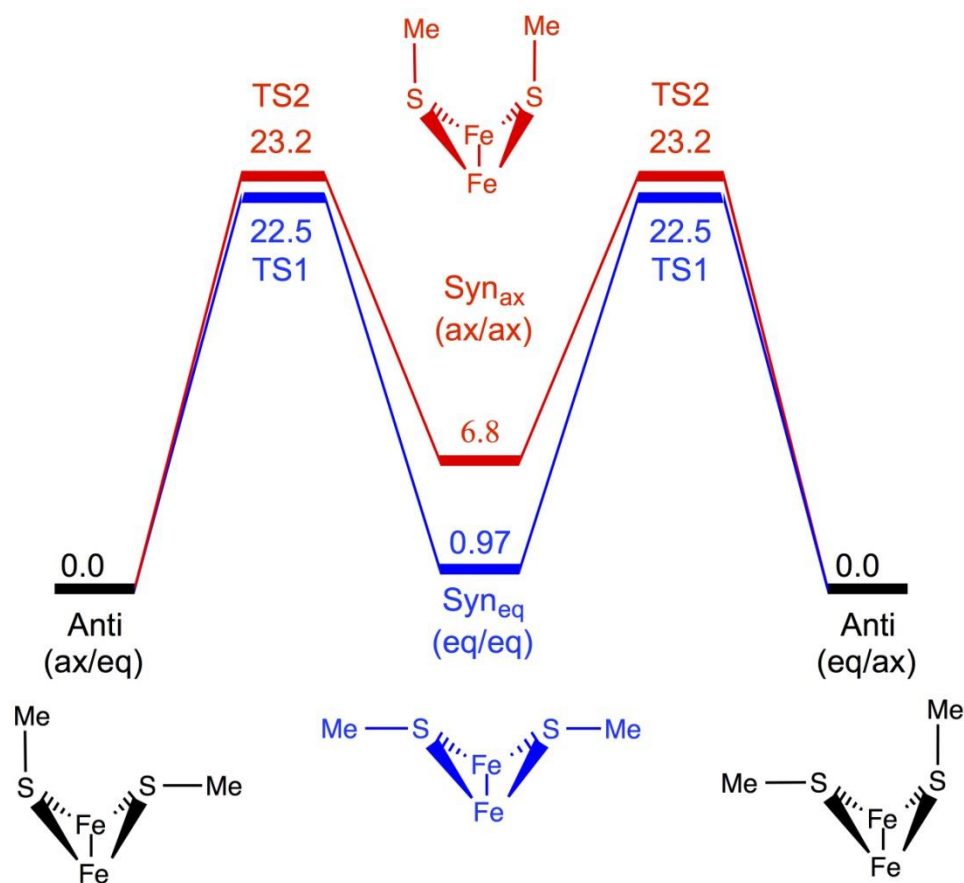
Figure VI-14. Energy profile of the transitions between the three isomers of (μ-SMe)$_2$[Fe(CO)$_3$]$_2$.

As described above, the small steric encumbrance of the SH unit, and an apparent high barrier to inversion at S, permits observation via ^{1}H NMR spectroscopy of all three isomers of **1**. DFT calculations, with thermal and solvation corrections, find similar Gibbs free energies (*G*) for these, with the syn$_{ax}$-**1** and syn$_{eq}$-**1** isomers slightly less stable than anti-**1**, by 1.4 and 0.5 kcal/mol, respectively, Figure VI-15. This is qualitatively consistent with the experimental ratios determined by the NMR studies that

find the major product to be the anti-isomer, followed by the syn_{eq} and syn_{ax}, *vide supra*. As for **2**, the calculations determined that syn_{eq}-**2** is slightly less stable than anti-**2** by 0.7 kcal/mol while syn_{ax}-**2** is 10.4 kcal/mol less stable, Figure VI-16. These values differ slightly depending on the solvent used in the computations, Table VI-3. In chloroform and dichloromethane the anti-**2** and syn_{eq}-**2** have identical calculated *G* values, though the pure electronic energies (E_{ele}) indicate anti-**2** is lower than syn_{eq}-**2** by 1.4 kcal/mol. The failure to observe syn_{eq}-**2** experimentally by ^{31}P NMR infers that the calculated solvation correction may over-stabilize the open/gold accessible structure; nevertheless the difference is still within the typical range of computational error. The high energy of syn_{ax}-**2** is attributable to the steric repulsion between two bulky triphenylphosphines, even through they are found (by computation) to interdigitate to minimize the repulsion, Figure VI-17. Additional calculations indicate the repulsion is comparable to that of a trimethylphosphine-substituted (on gold) syn_{ax}-**2**, due to the staggered arrangement of the phenyl groups.
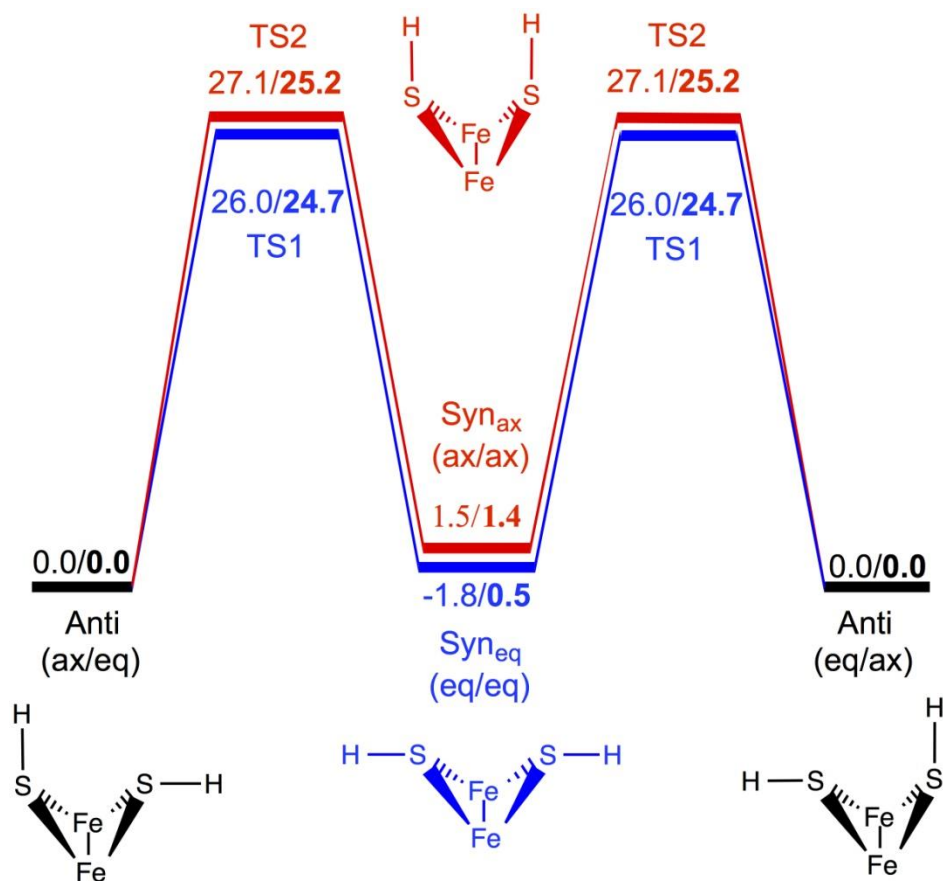
Figure VI-15. Energy profile of the transitions between the three isomers of **1**. The calculated electronic energies E_{ele} in vacuum are in plain text while the Gibbs free energies G after thermal and solvation corrections are in bold (solvent: benzene for **1**).
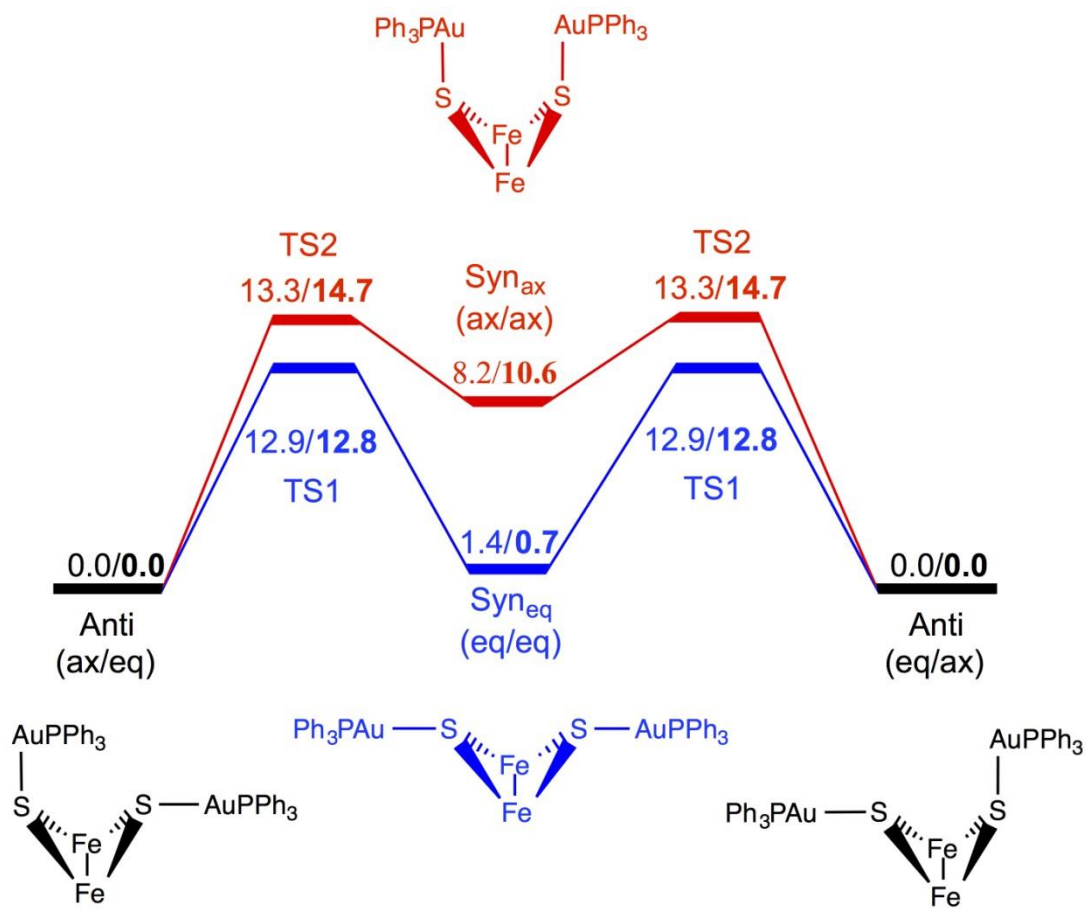
Figure VI-16. Energy profile of the transitions between the three isomers of **2**. The calculated electronic energies E_{ele} in vacuum are in plain text while the Gibbs free energies G after thermal and solvation corrections are in bold (solvent: toluene for **2**).

Table VI-3. Computational Gibbs free energies (kcal/mol) with solvent corrections.

G (kcal/mol)[a]	Syneq-**2**	TS1-**2**	Anti-**2**	TS2-**2**	Synax-**2**
Chloroform	0.0	12.0	0.0	14.3	10.2
Toluene	0.7	12.8	0.0	14.7	10.6
Dichloromethane	-0.1	11.7	0.0	14.0	10.1
Benzene	0.8	12.8	0.0	14.7	10.6

[a]Solvation correction is based on in-vacuum optimized structures.
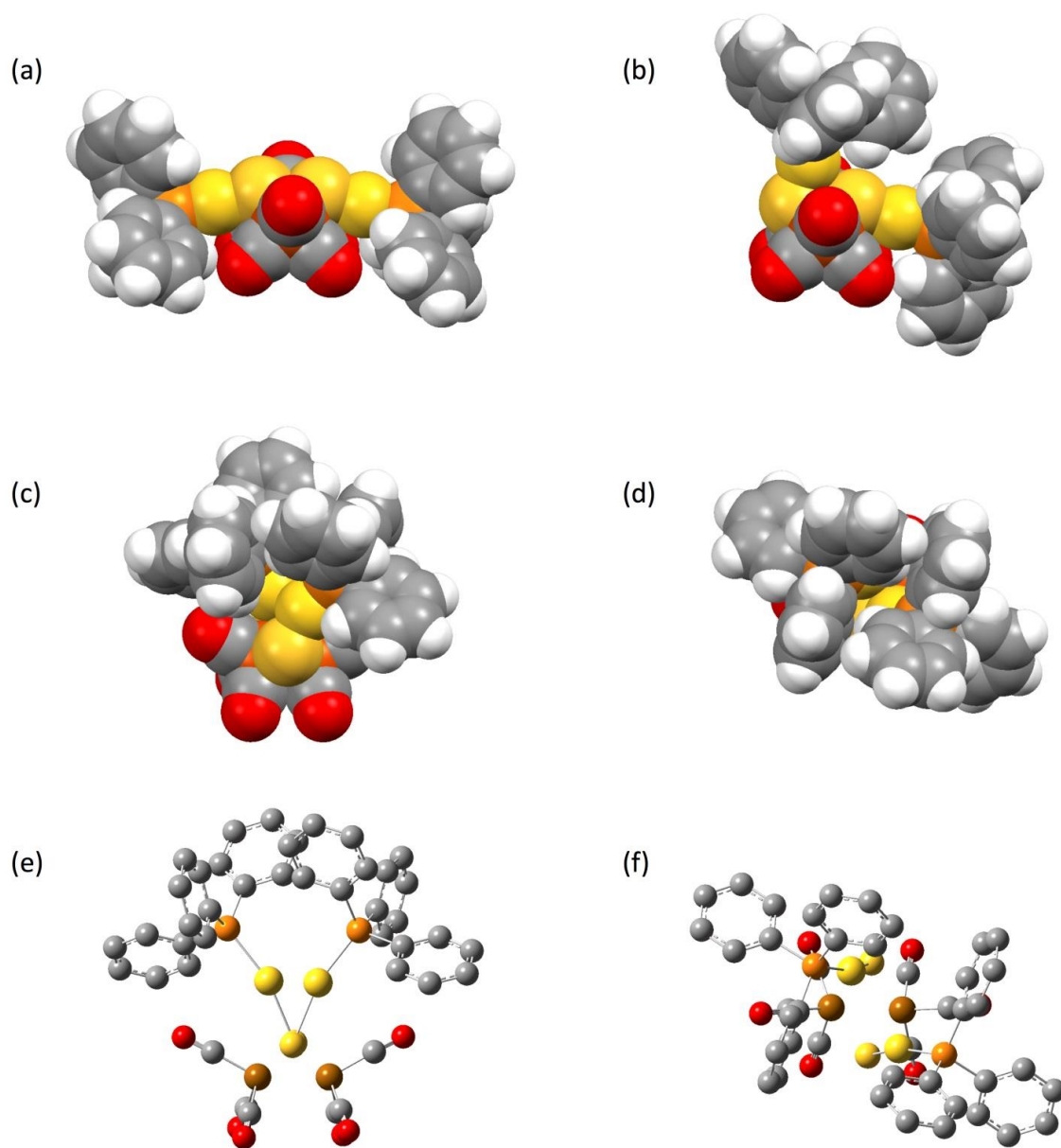
Figure VI-17. Calculated space-filling models of the three isomers of (μ-PPh$_3$AuS)$_2$[Fe(CO)$_3$]$_2$ (**2**): (a)syn$_{eq}$-**2**, (b) anti-**2**, (c) front view of Syn$_{ax}$-**2** and (d) top view of syn$_{ax}$-**2**. The calculated ball and stick model of syn$_{ax}$-**2** showing the (e) front view and (f) top view. Note the deviation of Au and S atoms from the mirror plane of the FeS$_2$(CO)$_6$ moiety and the staggered arrangement of phenyls.

Similar to the results of Lichenberger, et al. for the $(\mu\text{-SMe})_2[Fe(CO)_3]_2$ complex,[156] our calculations for the inter-conversion of isomers of complexes **1** and **2** find for both a transition state structure with a pseudo-trigonal planar sulfur, $HSFe_2$ or $AuSFe_2$, Figure VI-18. The activation energy barriers between the anti and the two syn isomers of **1** were calculated to be 24.7 kcal/mol (TS1, between anti-**1** and syn_{ax}-**1**) and 25.2 kcal/mol (TS2, between anti-**1** and syn_{eq}-**1**), while the transition states for **2** are much more accessible Gibbs free energy with barriers of 12.0 (TS1) and 14.3 (TS2) kcal/mol, Figure IV-16. The intermediate, syn_{eq}-**2** or syn_{ax}-**2**, of this exchange process depends on the order of the motions of the two moieties, through TS1 or TS2. The route featuring a lower barrier, TS1, is favored over the alternative route, TS2. The most accessible path for **2** (12.0 kcal/mol), qualitatively fits the experimental value (13.0 kcal/mol). Other mechanistic trials for the conformation exchange in **2**, which involve dissociation-association of PPh_3 or $AuPPh_3^+$, or concerted semaphore-like motions of both $AuPPh_3$ units, did not yield an acceptable route with a relatively low barrier.
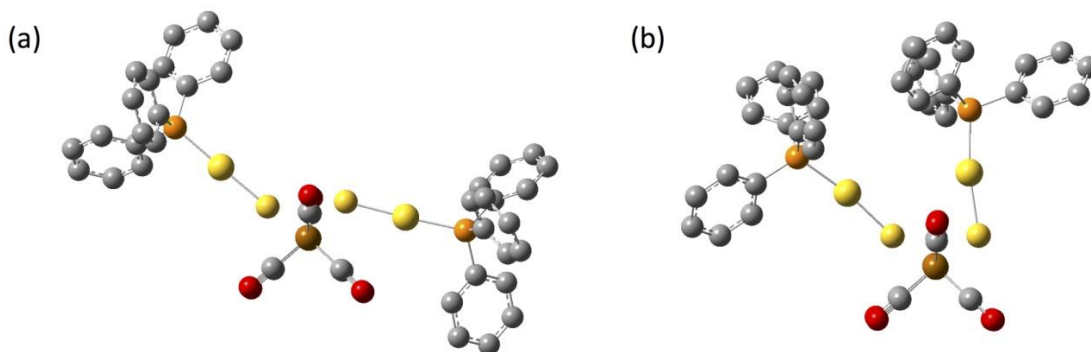
Figure VI-18. The calculated ball and stick structures of (a) TS1 and (b) TS2 for **2**. Note one of the sulfurs is planar.

It is worth noting that the high barriers (TS1 and TS2) of **1** are due to the electronic reorganization required for inversion of a pyramidal sulfur, accessing the trigonal planar, sp^2 type bonding from bonds that were largely *p3*-type.[154,157] The pyramidal sulfur in syn_{eq}-**1** mainly utilizes its p orbitals to interact with coordinating atoms while a large portion of its s character resides on the lone pair. However in TS1-**1**, the planar sulfur is forced to adapt a sp^2 hybridization with almost equivalent s contribution in each sp^2 orbital and regenerates a pure p lone pair. The 3s orbital of sulfur is more compact and harder to overlap with a coordinating atom so that the bond containing 3s contribution of sulfur is less stable. The structural transition of sulfur, from pyramidal to planar, inevitably utilizes its 3s orbital to make bonds and renders in a higher energy. Note that the inversion barrier for the simple H_3S^+ was calculated, by the

same computational methodology, to be 25 to 30 kcal/mol higher than the first row analogues, NH_3 and OH_3^+.

However, despite its analogy to the proton, the gold-phosphine moiety in **2** is able to significantly lower the planar barrier because it does not require the S to significantly rehybridize during the inversion. This interpretation is reflected by metric data and NBO analysis, Table VI-4. In the inversion (TS1-**2** and TS2-**2**), the two Fe-S bonds continue to utilize mainly *p*-contribution from S for bonding while the Au's dative bond to S changes easily from accepting the S $3p$ lone pair in the pyramidal ground state to accepting the $3s$ lone pair in the planar transition states. In conclusion, the gold perturbs the electronic structure of the Fe_2-S moiety less in the motion to the transition states and those transition states have low energies in turn.

Table VI-4. Selected NBO analysis concerning the S that undergoes structural changes.

Species	S'^{1}-H or S-Au bond	Two S'-Fe bonds	Lone pair
syn$_{eq}$-**1**	56.86% S	70.85% S	100% S
	(12% *s*, 87% *p*, 1% *d*)	(17% *s*, 83% *p*)	(53% *s*, 47% *p*)
	43.14% H	29.15% Fe	
	(100% *s*)	(14% *s*, 51% *p*, 35% *d*)	
TS1-**1**	60.85% S	74.04% S	100% S
	(26% *s*, 74% *p*)	(37% *s*, 63% *p*)	(100% *p*)
	39.15% H	25.96% Fe	
	(100% *s*)	(13% *s*, 53% *p*, 33% *p*)	
syn$_{eq}$-**2**	Detected as S lone pair	69.49% S	100% S
	100% S	(19% *s*, 81% *p*)	(54% *s*, 46% *p*)
	(8% *s*, 91% *p*)	30.51% Fe	
		(14% *s*, 50% *p*, 36% *p*)	
TS1-**2**	Detected as S lone pair	69.22% S	100% S
	100% S	(16% *s*, 84% *p*)	(100% *p*)
	(68% *s*, 32% *p*)	30.78% Fe	
		(7% *s*, 49% *p*, 44% *d*)	

Reactivity

The reactivity of the polymetallic complexes (μ-PPh$_3$AuS)$_2$[Fe(CO)$_3$]$_2$ and (μ_3-S)$_2$Ni(dppe)[Fe(CO)$_3$]$_2$ was investigated to test the validity of the theory that through a polymetallic complex an early abiotic analogue of the [FeFe]-hydrogenase active site was formed. The following four routes were be analyzed: (1) addition of dibromopropane to form (μ-pdt)[Fe(CO)$_3$]$_2$, (2) ligand/CO exchange, (3) metal trapping to produce the dianionic disulfide complex, and (4) condenstaion reaction to form the azadithiolate linker, (μ-SCH$_2$N(R)CH$_2$S)[Fe(CO)$_3$]$_2$, Figure VI-15.
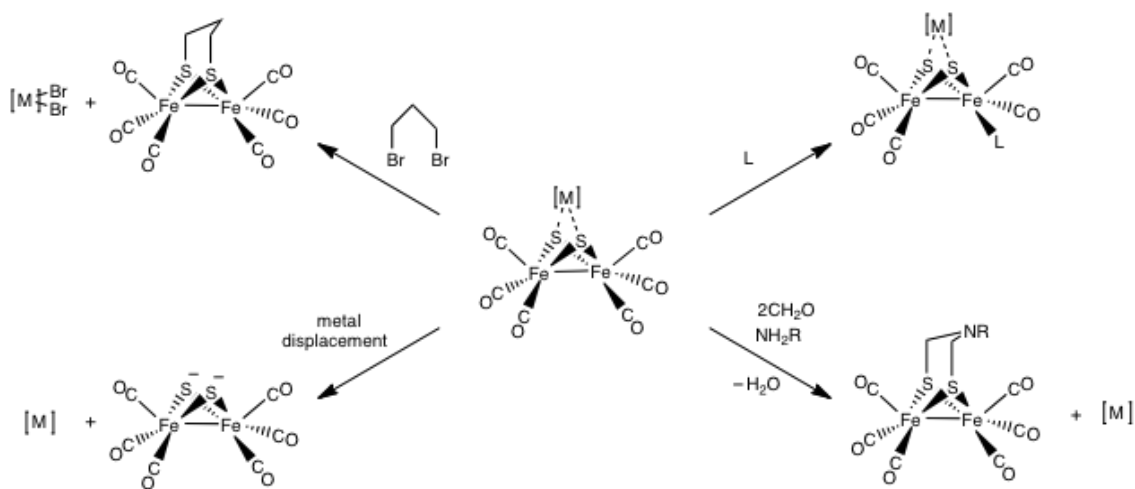
Figure VI-19. Proposed reactivity of complexes (μ-PPh$_3$AuS)$_2$[Fe(CO)$_3$]$_2$ (**2**) and (μ_3-S)$_2$Ni(dppe)[Fe(CO)$_3$]$_2$.

167

Many studies have shown that carbonyl ligand substitution, by cyanide or phosphines, readily takes place with alkylated sulfur derivatives, such as (μ-SMe)$_2$[Fe(CO)$_3$]$_2$ and especially the (μ-pdt)[Fe(CO)$_3$]$_2$.[31,52,158] Complex **1** also undergoes phosphine substitution under anaerobic conditions, however when exposed to air it immediately oxidizes to the disulfide, (μ-S$_2$)[Fe(CO)$_3$][Fe(CO)$_2$(PR$_3$)].[159] Mono-substituted phosphine derivatives of complex **2** and (μ_3-S)$_2$Ni(dppe)[Fe(CO)$_3$]$_2$ with PPh$_3$ or P(OMe)$_3$ can be obtained in low yields. However decomposition occurs on addition of PMe$_3$, a strongly donating phosphine, presumably due to [Ph$_3$P-Au-PMe$_3$]$^+$ or [(dppe)Ni(PMe$_3$)$_2$]$^{2+}$ formation and production of (μ-S)$_2$[Fe(CO)$_3$]$_2^{2-}$ which is unstable at room temperature.

In order to determine if the polymetallic, Fe$_2$Ni or Fe$_2$Au$_2$, complexes could be synthons for the azadithiolate derivative, i.e., (μ_2-SCH$_2$(NR)CH$_2$S)[Fe(CO)$_3$]$_2$, conditions that would favor the formaldehyde/amine condensation reaction were explored. While direct addition was not successful, either with **2** or the (μ_3-S)$_2$Ni(dppe)[Fe(CO)$_3$]$_2$ complex, the addition of a strong acid, i.e., HCl or HBF$_4$, to complex **2** readily yields the azadithiolate either in a one-pot reaction or following isolation of **1** from complex **2**, Figure VI-16. The synthesis of the carbon analogue was explored through the direct addition of 1,3-dibromopropane however this reaction was not successful.
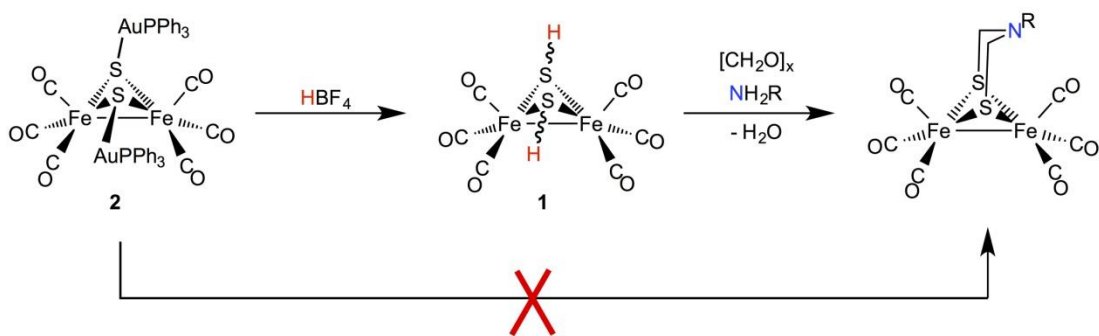
Figure VI-20. Synthesis of (μ-SCH$_2$NRCH$_2$S)[Fe(CO)$_3$]$_2$ through release of gold from (μ-PPh$_3$AuS)$_2$[Fe(CO)$_3$]$_2$ (**2**) with complex **1** as an intermediate.

Conclusion

The (μ-SAuPPh$_3$)$_2$[Fe(CO)$_3$]$_2$ complex, as an isolobal analogue of (μ-SH)$_2$[Fe(CO)$_3$]$_2$, and a molecular mimic of an aurolated or metallated FeS surface, was synthesized and crystallized with the large AuPPh$_3$ units found in the solid state in the anti-orientation, as was the hydrosulfido diiron complex. Solution NMR studies of the latter find all possible isomers, anti, syn$_{ax}$ and syn$_{eq}$. Small calculated differences in Gibbs free energies are consistent with the experimental distribution of the three isomers at room temperature reflecting a high barrier to isomerization due to substantial electronic reorganization at sulfur in the transition states. In contrast the dative character of the Fe$_2$S$^-\rightarrow$AuPPh$_3^+$ bond renders such sulfur inversion to occur with less perturbation of electronic structure. Through selective sulfur protonation with a strong acid with release of the exogenous metal, the polymetallic complexes (μ-

SAuPPh$_3$)$_2$[Fe(CO)$_3$]$_2$ and (μ$_3$-S)$_2$Ni(dppe)[Fe(CO)$_3$]$_2$ are demonstrated capable for conversion into azadithiolate derivatives, through the amine/aldehyde condensation reaction. Hence the metallated sulfide-diiron species may be viewed as protected S-reactivity centers. The significance of such inorganic protection agents for sulfur may also relate to the hypothesis expressed earlier regarding the abiotic origin of the [FeFe]-hydrogenase active site.

CHAPTER VII

CONCLUSIONS AND PERSPECTIVES

An initial debate in the [FeFe]-hydrogenase community of scientists was centered around the identity of the central atom (N, C, or O) in the dithiolate bridge of the [FeFe]-hydrogenase active site as the light atoms could not be distinguished at the available resolution of the X-ray crystal structure of the protein.[10,11] In the early 2000's several experimental and computational studies suggested that the central atom was a nitrogen, assisting in proton shuttling to and from the iron. Recent reports of hybrid [FeFe]-hydrogenase enzymes with synthetic active sites, (μ-SCH$_2$XCH$_2$S)[Fe(CO)$_2$CN]$_2^{2-}$ (X = CH$_2$, NH, or O), have solidified the identity of the central atom according to their efficacy as catalysts for H$_2$ production. Hydrogen evolution was monitored for the various hybrid enzymes and the active site with the azadithiolate linker produced hydrogen at a rate comparable to the native enzyme.[15,16]

The active site of the [FeFe]-H$_2$ase appears straightforward with simple diatomic ligands and a dithiolate bridge between the two irons, however there are several key features of the protein that lead to high activity. The "rotated" structure of the active site, formed by a bridging CO ligand giving one iron an inverted square pyramidal geometry, is enforced through hydrogen bonding between the cyanide ligands to various amino acid residues of the protein matrix. This unique geometry of the active site leaves an open site on the distal iron, i.e., the iron furthest from the Fe$_4$S$_4$ cluster, where H$_2$ oxidation and H$^+$ reduction occurs.[18,19] The active site is buried in the protein therefore

there are hydrophobic gas channels allowing access of the substrate to the active site and FeS clusters to aid in electron transfer, Figure VII-1.[21] All these features help facilitate the catalytic cycle and therefore the small molecule models of enzyme active sites are only rarely catalytically active.

Although the synthesis of a functional model capable of catalysis comparable to the enzyme active site has yet to be achieved, the hexacarbonyl diiron complexes are superb precursors to study fundamental properties of the active site due to their ease of synthesis and stability. An important aspect of the $(\mu\text{-SRS})[Fe(CO)_3]_2$ complexes is their ability to be modified through the dithiolate bridgehead and CO/L ligand substitution leading to a host of model compounds. Another intrinsic feature of $(\mu\text{-SRS})[Fe(CO)_3]_2$ complexes is their flexibility which includes the fluxionality of the $Fe(CO)_3$ units. The transition state of this process, where one of the basal CO ligands rotates to a position underneath the iron-iron vector, is significant due to the similarity in geometry to the $[FeFe]\text{-H}_2\text{ase}$ enzyme active site. These features have allowed the simple all-carbonyl $(\mu\text{-SRS})[Fe(CO)_3]_2$ complexes to become standards for developing applications.
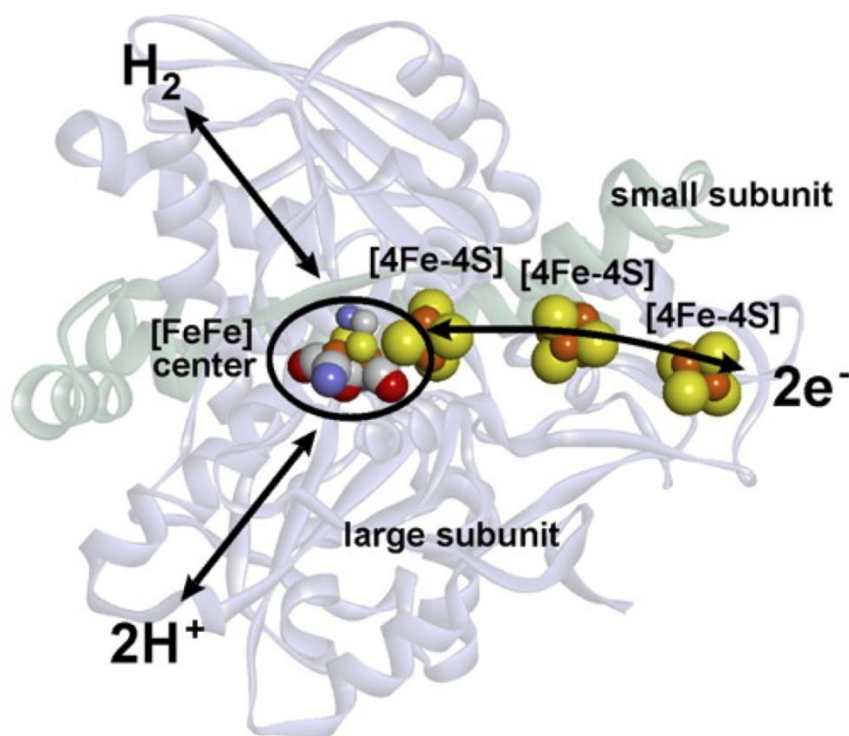
Figure VII-1. Structure of the [FeFe]-hydrogenase from *Dd*. Schematically indicated is the electron transport chain involving the FeS clusters and the pathways for dihydrogen and H^+ transfer. Reprinted with permission from Lubitz, W.; Ogata, H.; Rüdiger, O.; Reijerse, E. *Chemical Reviews* **2014**, *114*, 4081. Copyright **2014** American Chemical Society.

My graduate research at Texas A&M University has focused on understanding the effect of the nitrogen in the dithiolate linker on the structure and reactivity of the model complexes. Specifically a large portion of this work has been aimed at understanding the fundamental properties of structural rearrangements for the model complexes that are required in the proton-reduction mechanism. From work described in

Chapters III and IV the differences between the hexacarbonyl and phosphine-substituted carbon (-SCH$_2$CR$_2$CH$_2$S-) and nitrogen (-SCH$_2$NRCH$_2$S-) bridgehead model complexes could be analyzed. The proposed function of the nitrogen in these complexes is to assist in proton shuttling to the iron, Figure VII-2; however little difference is seen in hydrogen production compared to the carbon analogues.
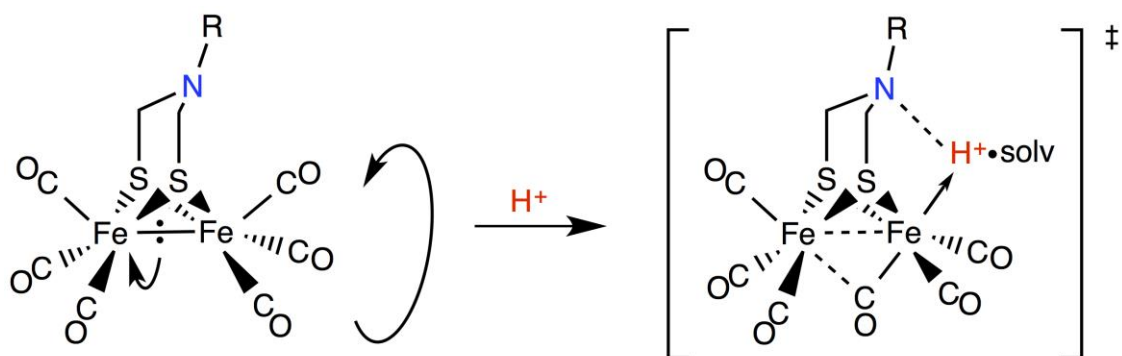
Figure VII-2. Nitrogen assisted proton relay to the open site on the iron unit.

In a previous study it was shown that addition of steric bulk to the bridgehead of the carbon analogues lowered the CO site exchange barrier of Fe(CO)$_3$ by stabilizing the rotated form.[49,50] A steric effect was also observed for the nitrogen analogues, (μ-SCH$_2$N(H)CH$_2$S)[Fe(CO)$_3$]$_2$ and (μ-SCH$_2$N(Me)CH$_2$S)[Fe(CO)$_3$]$_2$, in the variable-temperature NMR studies due to the low barrier to N-inversion. However, unlike the carbon bridgehead analogues, (μ-pdt)[Fe(CO)$_3$]$_2$ and (μ-dmpdt)[Fe(CO)$_3$]$_2$, the

substituent on the nitrogen is not always oriented towards the $Fe(CO)_3$ unit. Therefore less of an effect is seen in lowering the $Fe(CO)_3$ rotational barrier for the azadithiolate complexes. Interestingly the $(\mu\text{-}SCH_2N(^tBu)CH_2S)[Fe(CO)_3]_2$ complex was found to have the largest barrier to $Fe(CO)_3$ rotation. Computationally it was shown that the $(\mu\text{-}SCH_2N(^tBu)CH_2S)[Fe(CO)_3]_2$ complex does not undergo N-inversion, Figure VII-3. This is due to the steric repulsion between the bulky *tert*-butyl group and the $Fe(CO)_3$ unit. Therefore careful consideration should be taken when choosing steric bulk at the nitrogen in the bridgehead to lower the $Fe(CO)_3$ rotational energy barrier. For example a benzyl group on the bridgehead nitrogen, $\text{-}SCH_2N(CH_2C_6H_5)CH_2S\text{-}$, was used to achieve the first fully rotated Fe^IFe^I diiron model, Figure I-10.[58] The asymmetrically substituted complex, $(\mu\text{-}SCH_2N(CH_2C_6H_5)CH_2S)[Fe^I(CO)_3][Fe^I(CO)dmpe]$, was observed to have a remote agostic interation in the solid state helping stabilize the geometry.
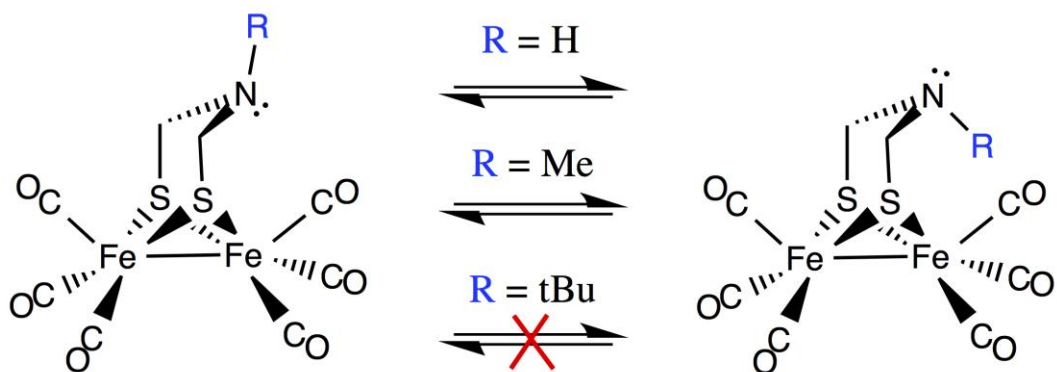
Figure VII-3. Nitrogen inversion for hexacarbonyl complexes.

Because protonation is expected to occur at a terminal Fe, lowering the $Fe(CO)_3$ rotational barrier is expected to make the electron density within the Fe-Fe bond more accessible to oxidative addition of a proton. Despite this argument, there is no experimental evidence that the mobility of the $Fe(CO)_3$ unit enhances the proton uptake as assessed by electrochemical response to added HOAc in the aprotic CH_3CN solvent. The nitrogen bridgehead complexes were found to have only a slightly higher catalytic efficiency compared to the carbon bridgehead analogues; this is in contrast to the drastic difference seen in the hybrid [FeFe]-hydrogenase enzymes with synthetic active sites.[15,16] The $(\mu\text{-SCH}_2N(^tBu)CH_2S)[Fe(CO)_3]_2$ complex should have the highest activity as the lone pair on the nitrogen is continuously positioned towards the iron unit to help with proton relay, as the nitrogen does not undergo inversion. It can be concluded that the assist of electron donating ligands, such as cyanide, and a third coordination sphere, i.e., the protein residues in the [FeFe]-H_2ase, play critical roles in hydrogen production

by locking the active site in the "rotated" structure which allows a constant open site on the distal iron.

A library of phosphine substituted azadithiolate complexes was synthesized to compare their photochemistry to the carbon bridgehead analogues. The comparison of solution photochemistry and time resolved infrared spectroscopy of the Fe^IFe^I complexes of $(\mu\text{-}SRS)[Fe^I(CO)_2L]_2$ to that of formerly explored $(\mu\text{-}S(CH_2)_3S)[Fe(CO)_3]_2$ is to be performed by TAMU-Qatar to assess ability of coordinatively-unsaturated species to bind alkenes, alkynes, and pyridines. Due to the electron donation into the iron core the disubstituted PMe_3, azadithiolate complexes can be protonated accessing the Fe-Fe bond density, thus generating a bridging hydride via oxidative addition. The additional basic site in the bridgehead, i.e. nitrogen, offers the potential of several protonated species that could be specifically synthesized and isolated. The bridging hydride species forms a stable $Fe^{II}(\mu\text{-}H)Fe^{II}$ complex ideal for photochemical studies due to more labile CO groups on Fe(II) resulting from less π-backbonding. The solution photochemistry of the $Fe^{II}(\mu\text{-}H)Fe^{II}$ complexes will be studied with the expectation that the $Fe^{II}(\mu\text{-}H)Fe^{II}$ complexes will more strongly bind olefins and other typically weak binding ligands as compared to the Fe^IFe^I complexes.

The applicability of water as a solvent for hydrogen production catalysts is a requirement for a proton-reduction electrocatalyst. The incorporation of a sulfonate group in an azadithiolate linker increased water-solubility that was further enhanced through the addition of a water-soluble ligand, PTA. Although there are several methods to increase water solubility, the aryl sulfonate method shows significant advantages as it

has a facile synthetic route and is stable in oxygen free water for several hours. This is the first system where the electrochemisty was studied in water without any organic co-solvents. This achievement of water-solubility from the incorporation of the sulfonate group should be an important consideration in the design of functional biomimetics.

Finally to help better understand the origin of the [FeFe]-hydrogenase possible intermediates in the prebiotic biosynthetic pathway way are described in Chapter VI. Mineral sulfides are found in hydrothermal and volcanic vents and are expected to have been present on primordial earth. Gunther Wachterhauser has promoted the hypothesis that iron-sulur mineral surfaces have templated the condensation of small molecues giving rise to amino acids and other molecules of life.[133] Our hypothesis is that through modifications of a mineral surface, forming a polymetallic complex, an early abiotic analogue of the [FeFe]-hydrogenase active site was formed, Figure VII-4. Evidence that metal sulfide/carbonyl clusters were formed through modifications of a mineral surface was investigated through synthesis and reactivity studies of two polymetallic compounds, $(\mu\text{-SAuPPh}_3)_2[\text{Fe(CO)}_3]_2$, original to my work, and the already published $(\mu_3\text{-S})_2\text{Ni(dppe)}[\text{Fe(CO)}_3]_2$.
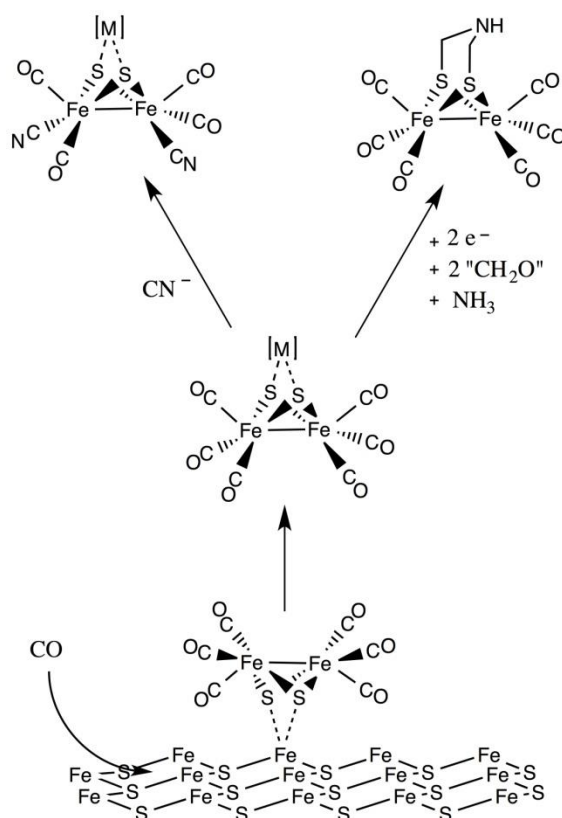
Figure VII-4. Representation of metallated disulfide released from a mineral surface.

The Ph_3PAu^+ cation, well known in the organometallic literature as an isolobal analogue of the proton, H^+, is shown to serve as a proton surrogate and form a very stable Au_2Fe_2 complex, $(\mu\text{-}SAuPPh_3)_2[Fe(CO)_3]_2$, analogous to the highly reactive di-hydrosulfide, $(\mu\text{-}SH)_2[Fe(CO)_3]_2$. Due to the non-bridging dithiolate three possible isomers are possible for $(\mu\text{-}SAuPPh_3)_2[Fe(CO)_3]_2$ and $(\mu\text{-}SH)_2[Fe(CO)_3]_2$ however only one conformation is possible for $(\mu_3\text{-}S)_2Ni(dppe)[Fe(CO)_3]_2$. Solution ^{31}P NMR studies of $(\mu\text{-}SAuPPh_3)_2[Fe(CO)_3]_2$ show that the $AuPPh_3$ units are in motion, however at low

temperature and also in the solid state the isomer present is the anti isomer. DFT studies confirmed substantial barriers to intramolecular interconversions between the three stereoisomers of $(\mu\text{-SH})_2[Fe(CO)_3]_2$, the syn_{eq}, syn_{ax}, and anti, observed at 22°C in solution. In contrast to the rigidity of the protonated sulfide, facile isomerizations of the aurolated analogue was seen. The low barrier to inversion at sulfur for $(\mu\text{-SAuPPh}_3)_2[Fe(CO)_3]_2$ is because gold does not require changes in hybridization of the sulfur atom as hydrogen does. That is, while the latter is substantially a covalent bond, the S to Au^+ interaction is largely dative.

The reactivity of the metal-protected sulfurs of $(\mu\text{-SAuPPh}_3)_2[Fe(CO)_3]_2$, and $(\mu_3\text{-S})_2Ni(dppe)[Fe(CO)_3]_2$ may be accessed by strong acid release of the gold or nickel, generating in situ the $(\mu\text{-SH})_2[Fe(CO)_3]_2$ for which condensation of amines and formaldehyde yields the azadithiolate derivative, i.e., $(\mu_2\text{-SCH}_2(NR)CH_2S)[Fe(CO)_3]_2$. This gives validity to our hypothesis that through modifications of a mineral surface an early abiotic analogue of the [FeFe]-hydrogenase active site could be formed. However due to the stability of the disulfide, the precursor to both the polymetallic species and azadithiolate derivatives, this is not the ideal approach for synthesizing [FeFe]-hydrogenase models. The synthesis of model complexes through this route adds an additional step in the condensation reaction of aurolating the sulfurs to form $(\mu\text{-SAuPPh}_3)_2[Fe(CO)_3]_2$ before protonation with acid. Starting with the disulfide, which can be produced in large quantities and is air-stable, allows direct protonation and condensation to form the azadithiolate complexes. Therefore as stated previously, the disulfide remains as the preferred precursor for [FeFe]-hydrogenase model compounds.

REFERENCES

(1) Jacques, P.-A.; Artero, V.; Pécaut, J.; Fontecave, M. *Proceedings of the National Academy of Sciences* **2009**, *106*, 20627.

(2) Le Goff, A.; Artero, V.; Jousselme, B.; Tran, P. D.; Guillet, N.; Métayé, R.; Fihri, A.; Palacin, S.; Fontecave, M. *Science* **2009**, *326*, 1384.

(3) Vignais, P. M.; Billoud, B. *Chemical Reviews* **2007**, *107*, 4206.

(4) Fontecilla-Camps, J. C. *Journal of Biological Inorganic Chemistry* **1996**, *1*, 91.

(5) Fontecilla-Camps, J. C.; Volbeda, A.; Cavazza, C.; Nicolet, Y. *Chemical Reviews (Washington, DC, United States)* **2007**, *107*, 4273.

(6) Hiromoto, T.; Warkentin, E.; Moll, J.; Ermler, U.; Shima, S. *Angewandte Chemie, International Edition* **2009**, *48*, 6457.

(7) Nicolet, Y.; Lemon, B. J.; Fontecilla-Camps, J. C.; Peters, J. W. *Trends in Biochemical Sciences* **2000**, *25*, 138.

(8) Shima, S.; Thauer, R. K. *Chemical Record* **2007**, *7*, 37.

(9) Artero, V.; Fontecave, M. *Coordination Chemistry Reviews* **2005**, *249*, 1518.

(10) Peters, J. W.; Lanzilotta, W. N.; Lemon, B. J.; Seefeldt, L. C. *Science* **1998**, *282*, 1853.

(11) Nicolet, Y.; Piras, C.; Legrand, P.; Hatchikian, C. E.; Fontecilla-Camps, J. C. *Structure* **1999**, *7*, 13.

(12) Lubitz, W.; Ogata, H.; Rüdiger, O.; Reijerse, E. *Chemical Reviews* **2014**, *114*, 4081.

(13) Silakov, A.; Wenk, B.; Reijerse, E.; Lubitz, W. *Physical Chemistry Chemical Physics* **2009**, *11*, 6592.

(14) Erdem, O. F.; Schwartz, L.; Stein, M.; Silakov, A.; Kaur-Ghumaan, S.; Huang, P.; Ott, S.; Reijerse, E. J.; Lubitz, W. *Angewandte Chemie, International Edition* **2011**, *50*, 1439.

(15) Esselborn, J.; Lambertz, C.; Adamska-Venkatesh, A.; Simmons, T.; Berggren, G.; Noth, J.; Siebel, J.; Hemschemeier, A.; Artero, V.; Reijerse, E.; Fontecave, M.; Lubitz, W.; Happe, T. *Nature Chemical Biology* **2013**, *9*, 607.

(16) Berggren, G.; Adamska, A.; Lambertz, C.; Simmons, T. R.; Esselborn, J.; Atta, M.; Gambarelli, S.; Mouesca, J.-M.; Reijerse, E.; Lubitz, W.; Happe, T.; Artero, V.; Fontecave, M. *Nature* **2013**, *499*, 66.

(17) Van der Spek, T. M.; Arendsen, A. F.; Happe, R. P.; Yun, S.; Bagley, K. A.; Stufkens, D. J.; Hagen, W. R.; Albracht, S. P. *European Journal of Biochemistry / FEBS* **1996**, *237*, 629.

(18) Nicolet, Y.; Lacey, A. L. D.; Vernéde, X.; Fernandez, V. M.; Hatchikian, E. C.; Fontecilla-Camps, J. C. *Journal of the American Chemical Society* **2001**, *123*, 1596.

(19) Frey, M. *ChemBioChem* **2002**, *3*, 153.

(20) Siegbahn, P. E. M.; Tye, J. W.; Hall, M. B. *Chemical Reviews* **2007**, *107*, 4414.

(21) Nicolet, Y.; Lemon, B. J.; Fontecill-Camps, J. C.; Peters, J. W. *Trends in BioChemical Sciences* **2002**, *25*, 138.

(22) Adamska-Venkatesh, A.; Krawietz, D.; Siebel, J.; Weber, K.; Happe, T.; Reijerse, E.; Lubitz, W. *Journal of the American Chemical Society* **2014**, *136*, 11339.

(23) Adamska, A.; Silakov, A.; Lambertz, C.; Rudiger, O.; Happe, T.; Reijerse, E.; Lubitz, W. *Angewandte Chemie, International Edition* **2012**, *51*, 11458.

(24) Silakov, A.; Kamp, C.; Reijerse, E.; Happe, T.; Lubitz, W. *Biochemistry* **2009**, *48*, 7780.

(25) Reihlen, H. G.; Hessling, G. *Justus Leibigs Annalen der Chemie* **1929**, *472*, 268.

(26) Le Cloirec, A.; C. Davies, S.; J. Evans, D.; L. Hughes, D.; J. Pickett, C.; P. Best, S.; Borg, S. *Chemical Communications* **1999**, 2285.

(27) Lyon, E. J.; Georgakaki, I. P.; Reibenspies, J. H.; Darensbourg, M. Y. *Angewandte Chemie International Edition* **1999**, *38*, 3178.

(28) Schmidt, M.; Contakes, S. M.; Rauchfuss, T. B. *Journal of the American Chemical Society* **1999**, *121*, 9736.

(29) Lubitz, W.; Reijerse, E.; van Gastel, M. *Chemical Reviews* **2007**, *107*, 4331.

(30) Pilet, E.; Nicolet, Y.; Mathevon, C.; Douki, T.; Fontecilla-Camps, J. C.; Fontecave, M. *FEBS Letters* **2009**, *583*, 506.

(31) Gloaguen, F.; Lawrence, J. D.; Schmidt, M.; Wilson, S. R.; Rauchfuss, T. B. *Journal of the American Chemical Society* **2001**, *123*, 12518.

(32) Gloaguen, F.; Lawrence, J. D.; Rauchfuss, T. B.; Benard, M.; Rohmer, M.-M. *Inorganic Chemistry* **2002**, *41*, 6573.

(33) Song, L.-C.; Yang, Z.-Y.; Hua, Y.-J.; Wang, H.-T.; Liu, Y.; Hu, Q.-M. *Organometallics* **2007**, *26*, 2106.

(34) Apfel, U.-P.; Troegel, D.; Halpin, Y.; Tschierlei, S.; Uhlemann, U.; Goerls, H.; Schmidt, M.; Popp, J.; Dunne, P.; Venkatesan, M.; Coey, M.; Rudolph, M.; Vos, J. G.; Tacke, R.; Weigand, W. *Inorganic Chemistry* **2010**, *49*, 10117.

(35) Harb, M. K.; Windhager, J.; Niksch, T.; Gorls, H.; Sakamoto, T.; Smith, E. R.; Glass, R. S.; Lichtenberger, D. L.; Evans, D. H.; El-khateeb, M.; Weigand, W. *Tetrahedron* **2012**, *68*, 10592.

(36) Darensbourg, M. Y.; Lyon, E. J.; Zhao, X.; Georgakaki, I. P. *Proceedings of the National Academy of Sciences* **2003**, *100*, 3683.

(37) Seyferth, D.; Henderson, R. S.; Gallagher, M. K. *Journal of Organometallic Chemistry* **1980**, *193*, C75.

(38) Seyferth, D.; Henderson, R. S. *Journal of Organic Chemistry* **1981**, *218*, C34.

(39) Seyferth, D.; Henderson, R. S.; Song, L. C. *Organometallics* **1982**, *3*, 327.

(40) Cowie, M.; DeKock, R. L.; Wagenmaker, T. R.; Seyferth, D.; Henderson, R. S.; Gallagher, M. K. *Organometallics* **1989**, *8*, 119.

(41) Stanley, J. L.; Heiden, Z. M.; Rauchfuss, T. B.; Wilson, S. R.; De Gioia, L.; Zampella, G. *Organometallics* **2008**, *27*, 119.

(42) Wang, M.; Chen, L.; Li, X.; Sun, L. *Dalton Transactions* **2011**, *40*, 12793.

(43) Barber, J.; Tran, P. D. *Journal of the Royal Society, Interface* **2013**, *10*, 20120984/1.

(44) Chenevier, P.; Mugherli, L.; Darbe, S.; Darchy, L.; DiManno, S.; Tran, P. D.; Valentino, F.; Iannello, M.; Volbeda, A.; Cavazza, C.; Artero, V. *Comptes Rendus Chimie* **2013**, *16*, 491.

(45) Li, X.; Wang, M.; Zheng, D.; Han, K.; Dong, J.; Sun, L. *Energy & Environmental Science* **2012**, *5*, 8220.

(46) Li, C.-B.; Li, Z.-J.; Yu, S.; Wang, G.-X.; Wang, F.; Meng, Q.-Y.; Chen, B.; Feng, K.; Tung, C.-H.; Wu, L.-Z. *Energy & Environmental Science* **2013**, *6*, 1754.

(47) Pullen, S.; Fei, H.; Orthaber, A.; Cohen, S. M.; Ott, S. *Journal of the American Chemical Society* **2013**, *135*, 16997.

(48) Tianjun, Y.; Zeng, Y.; Chen, J.; Li, Y.-Y.; Yang, G.; Li, Y. *Angewandte Chemie International Edition* **2013**, *52*, 5631.

(49) Lyon, E. J.; Georgakaki, I. P.; Reibenspies, J. H.; Darensbourg, M. Y. *Journal of the American Chemical Society* **2001**, *123*, 3268.

(50) Singleton, M. L.; Jenkins, R. M.; Klemashevich, C. L.; Darensbourg, M. Y. *Comptes Rendus Chimie* **2008**, *11*, 861.

(51) Thomas, C. M.; Liu, T.; Hall, M. B.; Darensbourg, M. Y. *Inorganic Chemistry* **2008**, *47*, 7009.

(52) Li, B.; Liu, T.; Singleton, M. L.; Darensbourg, M. Y. *Inorganic Chemistry* **2009**, *48*, 8393.

(53) Hsieh, C.-H.; Erdem, Ö. F.; Harman, S. D.; Singleton, M. L.; Reijerse, E.; Lubitz, W.; Popescu, C. V.; Reibenspies, J. H.; Brothers, S. M.; Hall, M. B.; Darensbourg, M. Y. *Journal of the American Chemical Society* **2012**, *134*, 13089.

(54) Justice, A. K.; Rauchfuss, T. B.; Wilson, S. R. *Angewandte Chemie, International Edition* **2007**, *46*, 6152.

(55) Liu, T.; Darensbourg, M. Y. *Journal of the American Chemical Society* **2007**, *129*, 7008.

(56) Justice, A. K.; De Gioia, L.; Nilges, M. J.; Rauchfuss, T. B.; Wilson, S. R.; Zampella, G. *Inorganic Chemistry* **2008**, *47*, 7405.

(57) Singleton, M. L.; Bhuvanesh, N.; Reibenspies, J. H.; Darensbourg, M. Y. *Angewandte Chemie, International Edition* **2008**, *47*, 9492.

(58) Munery, S.; Capon, J.-F.; De Gioia, L.; Elleouet, C.; Greco, C.; Petillon, F. Y.; Schollhammer, P.; Talarmin, J.; Zampella, G. *Chemistry - A European Journal* **2013**, *19*, 15458.

(59) Tye, J. W.; Darensbourg, M. Y.; Hall, M. B. *Inorganic Chemistry* **2006**, *45*, 1552.

(60) Helm, M. L.; Stewart, M. P.; Bullock, R. M.; DuBois, M. R.; DuBois, D. L. *Science* **2011**, *333*, 863.

(61) Carroll, M. E.; Barton, B. E.; Rauchfuss, T. B.; Carroll, P. J. *Journal of the American Chemical Society* **2012**, *134*, 18843.

(62) Stanley, J. L.; Rauchfuss, T. B.; Wilson, S. R. *Organometallics* **2007**, *26*, 1907.

(63) Li, H.; Rauchfuss, T. B. *Journal of the American Chemical Society* **2002**, *124*, 726.

(64) Singleton, M. L.; Reibenspies, J. H.; Darensbourg, M. Y. *Journal of the American Chemical Society* **2010**, *132*, 8870.

(65) Siegel, J. S.; Anet, F. A. L. *Journal of Organic Chemistry* **1988**, *53*, 2629.

(66) APEX2; Bruker AXS Inc., 5465 East Cheryl Parkway, Madison, WI, **2007**.

(67) SAINT; Bruker AXS Inc., 5465 East Cheryl Parkway, Madison, WI, **2007**.

(68) Sheldrick, G. M. *Acta Crystallographica, Section A* **2008**, *A63*, 112.

(69) Barbour, L. J. *Journal of Supramolecular Chemistry* **2003**, *1*, 189.

(70) Frisch, M. J. T., G. W.; Schlegel, H. B.; Scuseria, G. E.; Robb, M. A.; Cheeseman, J. R.; Scalmani, G.; Barone, V.; Mennucci, B.; Petersson, G. A.; Nakatsuji, H.; Caricato, M.; Li, X.; Hratchian, H. P.; Izmaylov, A. F.; Bloino, J.; Zheng, G.;

Sonnenberg, J. L.; Hada, M.; Ehara, M.; Toyota, K.; Fukuda, R.; Hasegawa, J.; Ishida, M.; Nakajima, T.; Honda, Y.; Kitao, O.; Nakai, H.; Vreven, T.; Montgomery, J. A., Jr.; Peralta, J. E.; Ogliaro, F.; Bearpark, M.; Heyd, J. J.; Brothers, E.; Kudin, K. N.; Staroverov, V. N.; Kobayashi, R.; Normand, J.; Raghavachari, K.; Rendell, A.; Burant, J. C.; Iyengar, S. S.; Tomasi, J.; Cossi, M.; Rega, N.; Millam, N. J.; Klene, M.; Knox, J. E.; Cross, J. B.; Bakken, V.; Adamo, C.; Jaramillo, J.; Gomperts, R.; Stratmann, R. E.; Yazyev, O.; Austin, A. J.; Cammi, R.; Pomelli, C.; Ochterski, J. W.; Martin, R. L.; Morokuma, K.; Zakrzewski, V. G.; Voth, G. A.; Salvador, P.; Dannenberg, J. J.; Dapprich, S.; Daniels, A. D.; Farkas, Ö.; Foresman, J. B.; Ortiz, J. V.; Cioslowski, J.; Fox, D. J. Gaussian 09, Revision B.01; Gaussian, Inc., Wallingford, CT, **2009**.

(71) Becke, A. D. *Journal of Chemical Physics* **1993**, *98*, 5648.

(72) Stephens, P. J.; Devlin, F. J.; Chabalowski, C. F.; Frisch, M. J. *Journal of Physical Chemistry* **1994**, *98*, 11623.

(73) Lee, C. T.; Yang, W. T.; Parr, R. G. *Physical Review B* **1988**, *37*, 785.

(74) Adamo, C.; Barone, V. *Journal of Chemical Physics* **1998**, *108*, 664.

(75) Tao, J.; Perdew, J. P.; Staroverov, V. N.; Scuseria, G. E. *Physical Review Letters* **2003**, *91*, 146401/1.

(76) Chai, J.-D.; Head-Gordon, M. *Physical Chemistry Chemical Physics* **2009**, *10*, 6615.

(77) Krishnan, R.; Binkley, J. S.; Seeger, R.; Pople, J. A. *Journal of Chemical Physics* **1980**, *72*, 650.

(78) McLean, A. D.; Chandler, G. S. *Journal of Chemical Physics* **1980**, *72*, 5639.

(79) AMPAC 9; Semichem, I., 12456 W. 62nd Terrace. Suite D, Shawnee, KS, 66216, **1992**.

(80) Bruker, G.; Bruker AXS Inc., 5465 East Cheryl Parkway, Madison, WI, 53711, **2007**.

(81) Becke, A. D. *Journal of Chemical Physics* **1993**, *98*, 5648.

(82) Dolg, M.; Wedig, U.; Stoll, H.; Preuss, H. *Journal of Chemical Physics* **1987**, *86*, 866.

(83) Figgen, D.; Rauhut, G.; Dolg, M.; H. *Chemical Physics* **2005**, *311*, 227.

(84) Peterson, K. A.; Puzzarini, C. *Theoretical Chemistry Accounts* **2005**, *114*, 283.

(85) Frisch, M. J.; Pople, J. A.; Binkley, J. S. *Journal of Chemical Physics* **1984**, *80*, 3265.

(86) Raghavachari, K.; Binkley, J. S.; Seeger, R.; Pople, J. A. *Journal of Chemical Physics* **1980**, *72*, 650.

(87) Clark, T.; Chandrasekhar, J.; Spitznagel, G. W.; Schleyer, P. V. R. *Journal of Computational Chemistry* **1983**, *4*, 294.

(88) Hehre, W. J.; Ditchfield, R.; Pople, J. A. *Journal of Chemical Physics* **1972**, *56*, 2257.

(89) Marenich, A. V.; Cramer, C. J.; Truhlar, D. G. *Journal of Physical Chemistry B* **2009**, *113*, 6378.

(90) Felton, G. A. N.; Mebi, C. A.; Petro, B. J.; Vannucci, A. K.; Evans, D. H.; Glass, R. S.; Lichtenberger, D. L. *Journal of Organometallic Chemistry* **2009**, *694*, 2681.

(91) Crouthers, D. J.; Denny, J. A.; Bethel, R. D.; Munoz, D. G.; Darensbourg, M. Y. *Organometallics* **2014**, *33*, 4747.

(92) Lawrence, J. D.; Li, H.; Rauchfuss, T. B.; Bénard, M.; Rohmer, M.-M. *Angewandte Chemie International Edition* **2001**, *40*, 1768.

(93) Wang, Z.; Liu, J.-H.; He, C.-J.; Jiang, S.; Åkermark, B.; Sun, L.-C. *Journal of Organometallic Chemistry* **2007**, *692*, 5501.

(94) Kessler, H. *Angewandte Chemie International Edition in English* **1970**, *9*, 219.

(95) Lambert, J., B.; Oliver, W. L. J.; Packard, B. S. *Journal of the American Chemical Society* **1970**, *93*, 933.

(96) Capon, J.-F.; Ezzaher, S.; Gloaguen, F.; Petillon, F. Y.; Schollhammer, P.; Talarmin, J.; Davin, T. J.; McGrady, J. E.; Muir, K. W. *New Journal of Chemistry* **2007**, *31*, 2052.

(97) Surawatanawong, P.; Tye, J. W.; Darensbourg, M. Y.; Hall, M. B. *Dalton Transactions* **2010**, *39*, 3093.

(98) Chong, D.; Georgakaki, I. P.; Mejia-Rodriguez, R.; Sanabria-Chinchilla, J.; Soriaga, M. P.; Darensbourg, M. Y. *Dalton Transactions* **2003**, 4158.

(99) Mejia-Rodriguez, R.; Chong, D.; Reibenspies, J. H.; Soriaga, M. P.; Darensbourg, M. Y. *Journal of the American Chemical Society* **2004**, *126*, 12004.

(100) Stewart, M. P.; Ho, M.-H.; Wiese, S.; Lindstrom, M. L.; Thogerson, C. E.; Raugei, S.; Bullock, R. M.; Helm, M. L. *Journal of the American Chemical Society* **2013**, *135*, 6033.

(101) Zaffaroni, R.; Rauchfuss, T. B.; Gray, D. L.; De Gioia, L.; Zampella, G. *Journal of the American Chemical Society* **2012**, *134*, 19260.

(102) Gloaguen, F.; Lawrence, J. D.; Rauchfuss, T. B. *Journal of the American Chemical Society* **2001**, *123*, 9476.

(103) Dong, W.; Wang, M.; Liu, X.; Jin, K.; Li, G.; Wang, F.; Sun, L. *Chemical Communications* **2006**, 305.

(104) Dong, W.; Wang, M.; Liu, T.; Liu, X.; Jin, K.; Sun, L. *Journal of Inorganic Biochemistry* **2007**, *101*, 506.

(105) Wang, F.; Wang, M.; Liu, X.; Jin, K.; Dong, W.; Sun, L. *Dalton Transactions* **2007**, 3812.

(106) Capon, J.-F.; Ezzaher, S.; Gloaguen, F.; Petillon, F. Y.; Schollhammer, P.; Talarmin, J. *Chemistry - A European Journal* **2008**, *14*, 1954.

(107) Marhanke, J.; Pierri, A. E.; Lomotan, M.; Damon, P. L.; Ford, P. C.; Works, C. *Inorganic Chemistry* **2011**, *50*, 11850.

(108) Kaziannis, S.; Santabarbara, S.; Wright, J. A.; Greetham, G. M.; Towrie, M.; Parker, A. W.; Pickett, C. J.; Hunt, N. T. *The Journal of Physical Chemistry B* **2010**, *114*, 15370.

(109) Brown-McDonald, J.; Berg, S.; Peralto, M.; Works, C. *Inorganica Chimica Acta* **2009**, *362*, 318.

(110) Ridley, A. R.; Stewart, A. I.; Adamczyk, K.; Ghosh, H. N.; Kerkeni, B.; Guo, Z. X.; Nibbering, E. T. J.; Pickett, C. J.; Hunt, N. T. *Inorganic Chemistry* **2008**, *47*, 7453.

(111) Silaghi-Dumitrescu, I.; Bitterwolf, T. E.; King, R. B. *Journal of the American Chemical Society* **2006**, *128*, 5342.

(112) Kania, R.; Frederix, P. W. J. M.; Wright, J. A.; Ulijn, R. V.; Pickett, C. J.; Hunt, N. T. *Journal of Chemical Physics* **2012**, *136*, 044521.

(113) Muhammad, S.; Moncho, S.; Brothers, E. N.; Darensbourg, M. Y.; Darensbourg, D. J.; Bengali, A. A. *Inorganic Chemistry* **2012**, *51*, 7362.

(114) Liu, X.-F.; Xiao, X.-W.; Shen, L.-J. *Transition Metal Chemistry* **2011**, *36*, 465.

(115) Irene P. Georgakaki, M. L. M., and Marcetta Y. Darensbourg *Inorganic Chemistry* **2003**, *42*, 2489.

(116) Eilers, G.; Schwartz, L.; Stein, M.; Zampella, G.; de Gioia, L.; Ott, S.; Lomoth, R. *Chemistry* **2007**, *13*, 7075.

(117) Hambourger, M.; Gervaldo, M.; Svedruzic, D.; King, P. W.; Gust, D.; Ghirardi, M.; Moore, A. L.; Moore, T. A. *Journal of the American Chemical Society* **2008**, *130*, 2015.

(118) Esswein, A. J.; Nocera, D. G. *Chemical Reviews* **2007**, *107*, 4022.

(119) Tard, C.; Pickett, C. J. *Chemical Reviews* **2009**, *109*, 2245.

(120) Singleton, M. L.; Crouthers, D. J.; Duttweiler, R. P., 3rd; Reibenspies, J. H.; Darensbourg, M. Y. *Inorganic Chemistry* **2011**, *50*, 5015.

(121) Apfel, U.-P.; Halpin, Y.; Gottschaldt, M.; Görls, H.; Vos, J. G.; Weigand, W. *European Journal of Inorganic Chemistry* **2008**, *2008*, 5112.

(122) Wang, H.-Y.; Wang, W.-G.; Si, G.; Wang, F.; Tung, C.-H.; Wu, L.-Z. *Langmuir* **2010**, *26*, 9766.

(123) Felton, G. A. N.; Glass, R. S.; Lichtenberger, D. L.; Evans, D. H. *Inorganic Chemistry* **2006**, *45*, 9181.

(124) Li, P.; Wang, M.; Chen, L.; Wang, N.; Zhang, T.; Sun, L. *CrystEngComm* **2008**, *10*, 267.

(125) Na, Y.; Wang, M.; Jin, K.; Zhang, R.; Sun, L. *Journal of Organometallic Chemistry* **2006**, *691*, 5045.

(126) Wei, C. H.; Dahl, L. F. *Inorganic Chemistry* **1965**, *4*, 1.

(127) Li, P.; Wang, M.; He, C.; Li, G.; Liu, X.; Chen, C.; Åkermark, B.; Sun, L. *European Journal of Inorganic Chemistry* **2005**, *2005*, 2506.

(128) Gloaguen, F.; Morvan, D.; Capon, J.-F.; Schollhammer, P.; Talarmin, J. *Journal of Electroanalytical Chemistry* **2007**, *603*, 15.

(129) Tye, J. W.; Lee, J.; Wang, H.-W.; Mejia-Rodriguez, R.; Reibenspies, J. H.; Hall, M. B.; Darensbourg, M. Y. *Inorganic Chemistry* **2005**, *44*, 5550.

(130) Matsue, T.; Evans, D. H.; Osa, T.; Kobayashi, N. *Journal of the American Chemical Society* **1985**, *107*, 3411.

(131) Felton, G. A. N.; Petro, B. J.; Glass, R. S.; Lichtenberger, D. L.; Evans, D. H. *Journal of the American Chemical Society* **2009**, *131*, 11290.

(132) McGlynn, S. E.; Mulder, D. W.; Shepard, E. M.; Broderick, J. B.; Peters, J. W. *Dalton Transactions* **2009**, 4274.

(133) Wächtershäuser, G. *Progress in Biophysics and Molecular Biology* **1992**, *58*, 85.

(134) Wächtershäuser, G. *Philosophical Transactions of the Royal Society B* **2006**, *361*, 1787.

(135) Cody, G. D.; Boctor, N. Z.; Filley, T. R.; Hazen, R. M.; Scott, J. H.; Sharma, A.; Yoder, H. S. *Science* **2000**, *289*, 1337.

(136) Kuwata, S.; Hidai, M. *Coordination Chemistry Reviews* **2001**, *213*, 211.

(137) Tsou, C.-C.; Chiu, W.-C.; Ke, C.-H.; Tsai, J.-C.; Wang, Y.-M.; Chiang, M.-H.; Liaw, W.-F. *Journal of the American Chemical Society* **2014**, *136*.

(138) Guevremont, J. M.; Strongin, D. R.; Schoonen, M. A. A. *American Mineralogist* **1998**, *83*, 1246.

(139) Murphy, R.; Strongin, D. R. *Surface Science Reports* **2009**, *64*, 1.

(140) Maresca, L.; Greggio, F.; Sbrignadello, G.; Bor, G. *Inorganica Chimica Acta* **1971**, *5*, 667.

(141) Stone, F. G. A. *Angewandte Chemie International Edition* **1984**, *23*, 89.

(142) Raubenheimer, H. G.; Schmidbaur, H. *Organometallics* **2012**, *31*, 2507.

(143) Fritsch, E.; Polborn, K.; Robl, C.; Suenkel, K.; Beck, W. *Zeitschrift Für Anorganische Und Allgemeine Chemie* **1993**, *619*, 2050.

(144) Ruiz, J.; Rodríguez, V.; Vicente, C.; Martí, J. M.; López, G. *Inorganic Chemistry* **2001**, *40*, 5354.

(145) Pinder, T. A.; Montalvo, S. K.; Lunsford, A. M.; Hsieh, C.-H.; Reibenspies, J. H.; Darensbourg, M. Y. *Dalton Transactions* **2014**, *43*, 138.

(146) Song, L.-C.; Sun, X.-J.; Jia, G.-J.; Wang, M.-M.; Song, H.-B. *Journal of Organometallic Chemistry* **2014**, *761*, 10.

(147) Darensbourg, M. Y.; Lyon, E. J.; Smee, J. J. *Coordination Chemistry Reviews* **2000**, *206-207*, 533.

(148) Schmidbaur, H.; Schier, A. *Chemical Society Reviews* **2012**, *41*, 370.

(149) Gimeno, M. C.; Jones, P. G.; Laguna, A.; Laguna, M.; Terroba, R. *Inorganic Chemistry* **1994**, *33*, 3932.

(150) Guyon, F.; Hameau, A.; Khatyr, A.; Knorr, M.; Amrouche, H.; Fortin, D.; Harvey, P. D.; Strohmann, C.; Ndiaye, A. L.; Huch, V.; Veith, M.; Avarvari, N. *Inorganic Chemistry* **2008**, *47*, 7483.

(151) King, B.; Bisnette, M. B. *Inorganic Chemistry* **1965**, *4*, 1663.

(152) King, R. B. *Journal of the American Chemical Society* **1962**, *84*, 2460.

(153) Adams, R. D.; Coton, F. A.; Cullen, W. R.; Hunter, D. L.; Mihichuk, L. *Inorganic Chemistry* **1975**, *14*, 1395.

(154) Toyota, S. *Reviews on Heteroatom Chemistry* **1999**, *21*, 139.

(155) Mueting, A.; Mattson, M. *Journal of Inorganic and Nuclear Chemistry* **1981**, *43*, 749.

(156) In-noi, O.; Haller, K. J.; Hall, G. B.; Brezinski, W. P.; Marx, J. M.; Sakamoto, T.; Evans, D. H.; Glass, R. S.; Lichtenberger, D. L. *Organometallics* **2014**, *33*, 5009.

(157) Hall, M. B. *Inorganic Chemistry* **1978**, *17*, 2261.

(158) Gloaguen, F.; Rauchfuss, T. B. *Chemical Society Reviews* **2009**, *38*, 100.

(159) Song, L.-C.; Zhao, P.-H.; Du, Z.-Q.; Tang, M.-Y.; Hu, Q.-M. *Organometallics* **2010**, *29*, 5751.